CONDENSATION OF PURE AND ZEOTROPIC MIXTURES OF HYDROCARBONS IN SMOOTH HORIZONTAL TUBES

A Dissertation
Presented to
The Academic Faculty

By

Malcolm Macdonald

In Partial Fulfillment
Of the Requirements for the Degree
Doctor of Philosophy in Mechanical Engineering

Georgia Institute of Technology

August 2015

CONDENSATION OF PURE AND ZEOTROPIC MIXTURES OF HYDROCARBONS IN SMOOTH HORIZONTAL TUBES

Approved by:

Dr. Srinivas Garimella, Advisor
G. W. Woodruff School of Mechanical Engineering
Georgia Institute of Technology

Dr. Thomas F. Fuller
School of Chemical & Biomolecular Engineering
Georgia Institute of Technology

Dr. Susan N. Thomas
G. W. Woodruff School of Mechanical Engineering
Georgia Institute of Technology

Dr. S. Mostafa Ghiaasiaan
G. W. Woodruff School of Mechanical Engineering
Georgia Institute of Technology

Dr. Peter Loutzenhiser
G. W. Woodruff School of Mechanical Engineering
Georgia Institute of Technology

Date Approved: [July 24, 2015]

To my family.

ACKNOWLEDGMENTS

I want to thank Dr. Garimella for giving me the opportunity to work with him and the Sustainable Thermal Systems Laboratory during my Ph.D, and for his guidance in my technical and professional education.

I want to especially thank all of the past and present members of the Sustainable Thermal Systems Lab. I have relied on their support and guidance throughout my PhD, and I am very grateful for their contributions to my development as a researcher. Most importantly, my past five years have been a fun experience.

I would like to thank Heat Transfer Research, Inc. for their sponsorship of this project and for their enthusiastic and informative discussions of the experimental trends and analysis throughout the study.

Finally, I would like to thank my PhD committee members for generously agreeing to serve on my committee, for reading my dissertation and for their guidance and advice.

TABLE OF CONTENTS

CHAPTER

LIST OF TABLES

Page

LIST OF FIGURES

NOMENCLATURE

Variables

A	Vertical contribution to film heat transfer coefficient, -
B	Horizontal contribution to film heat transfer coefficient, -
Bo	Bond number, -
C_p	Specific heat capacity, kJ kg^{-1} K^{-1}
D	Diameter, m
$D_{1\rightarrow 2}$	Diffusivity, m^2 s^{-1}
E	Entrained liquid fraction, -
f	Friction factor, -
Fr_So	Froude number ($1.26 \cdot \mathrm{Re}_\mathrm{L}^{1.04} \cdot \mathrm{Ga}^{-0.50} \left(1+1.09 X_{tt}{}^{0.039}\right)^{1.5} X_{tt}^{-1.5}$, -
g	Gravitational constant, m s^{-2}
G	Mass flux, kg m^{-2} s^{-1}
Ga	Galileo number $\left(gD^3\rho_\mathrm{L}^2\mu_\mathrm{L}^{-2}\right)$, -
h	Heat transfer coefficient, W m^{-2} K^{-1}
i	Enthalpy, J kg^{-1}
J	Dimensionless gas velocity $Gq \cdot \left(gD\rho_\mathrm{V}\left(\rho_\mathrm{L}-\rho_\mathrm{V}\right)\right)^{-1}$, -
j	Superficial velocity, m s^{-1}
Ja	Jakob number $\left(C_\mathrm{p,V}\Delta T \cdot i_\mathrm{fg}^{-1}\right)$, -
k	Thermal conductivity, W m^{-1} K^{-1}
L	Length, m
l	Length scale, m

$LMTD$	Log Mean Temperature Difference, °C
m	Mass flow rate, kg s^{-1}
Nu	Nusselt number, -
P	Pressure, kPa
Pr	Prandtl number, -
P_{r}	Reduced Pressure, -
$\dot{Q}$	Heat Duty, W
R	Thermal resistance, K W^{-1}
Re	Reynolds number, -
Sc	Schmidt number, -
Sh	Sherwood number, -
S_{r}	Slip ratio, -
T	Temperature, °C
U	Overall heat transfer rate, W m^{-2} K^{-1}
u	Phase velocity, m s^{-1}
X_{tt}	Martinelli parameter
z	Distance
y	Vapor quality, -
X	Concentration, kg kg^{-1}

Greek Symbols

δ	Film thickness, m
Δ	Change in variable, -
ε	Void fraction, -
η	Liquid fraction in upper film, -
θ	Stratified film angle, rad
κ	Heat transfer enhancement factor, -
λ	Mass transfer coefficient, m s^{-1}
μ	Viscosity, kg m^{-1} s^{-1}
ξ	Liquid fraction in upper film, -
ρ	Density, kg m^{-3}
σ	Surface tension, N m^{-1}
τ	Shear stress, Pa
ϕ	Two-phase friction pressure drop multiplier, -
χ	Temperature difference correction factor, -

Subscripts/Superscripts

amb	Ambient
annulus	Test section annulus, coolant water side
avg	Average
conv	Convective
coolant	Pre- and Post- condenser coolant water
critical	Critical value
deceleration	Pressure drop due to momentum changes
E	Entrainment
Equiv.	Equivalent thermal resistance of annulus and tee sections
Evap	Evaporator
f	Working fluid
FF	Falling film
fg	Vapor-to-liquid saturation states
film	Film temperature
fr	Friction
Glide	Zeotropic mixture temperature glide, (T_{dew} - T_{bubble})
h	Hydraulic
i	Inner
ins	Insulation
int	Interfacial roughness
interface	Vapor-liquid interface
inlet	Inlet to the test section

L	Liquid
LO	Liquid only
LM	Log Mean
loss	Ambient losses
measured	Measured value
nat	Natural convection
o	Outer
outlet	Outlet of the test section
OT	Outer tube
post	Post-condenser
pre	Pre-condenser
pri	Primary loop
pump	Primary loop pump
rad	Radiation
red	Reduced
ref	Working fluid
sat	Saturation
sec	Secondary loop
subcool	Subcooled state
superheated	Superheated state
Test	Test section
Tee	Tee section at inlet and outlet of test section
tt	turbulent-turbulent

tube	Main line tubing containing working fluid
TP	Two-phase
V	Vapor
w	Water
wall	Test section wall

SUMMARY

A study of the condensation of hydrocarbons and zeotropic hydrocarbon mixtures in smooth horizontal tubes was conducted. Measurements of condensation heat transfer coefficients and frictional pressure drop were taken over a range of mass fluxes (G = 150 – 450 kg m^{-2} s^{-1}), a range of reduced pressures (P_r = 0.25 - 0.95), for two tube diameters (D = 7.75 and 14.45 mm), several working fluid-to-coolant temperature differences (ΔT_{LM} = 3 – 14°C) and temperature glides (ΔT_{Glide}) between 7 - 14°C. The wide range of conditions investigated in this study provides considerable insight on the transport phenomena influencing condensation in pure fluids and their mixtures. The trends in heat transfer coefficient and frictional pressure gradient are discussed and compared with the predictions of correlations from the literature. The results of the experiments, combined with previous flow visualization studies on hydrocarbons, were used to develop physically consistent heat transfer and frictional pressure gradient models that are applicable to pure fluids and zeotropic mixtures. A framework was developed for zeotropic mixture condensation that recommends a specific modeling approach based on the observed trends in the heat transfer coefficient and the points of deviations from pure fluid trends.

The documentation of the condensation heat transfer and pressure drop behavior of environmentally friendly refrigerants, and the development of accurate correlations, will facilitate their widespread introduction as a working fluid for refrigeration cycles. Furthermore, the accurate pure fluid models, which serve as a baseline case for zeotropic mixture modeling, yield more effective predictions of zeotropic mixture condensation, which will lead to increased efficiencies of chemical processing plants.

CHAPTER 1 INTRODUCTION

As an integral component in power, refrigeration and separation cycles, the condenser demands a lot of attention and accurate modeling/correlations to ensure that optimum efficiencies are achieved. Conventional HVAC cycles have used synthetic refrigerants with relatively good heat transfer characteristics and low saturation boiling temperatures to avoid fluid freezing. However, synthetic refrigerants have deleterious side-effects on the environment, e.g., they contribute to global warming potential (GWP). Moreover, replacing synthetic refrigerants with alternative fluids that have similar boiling point characteristics, but larger phase-change enthalpies, can lead to increased system efficiencies. Increased system efficiencies can be accomplished with higher heat transfer rates, which are often associated with larger phase-change enthalpies. Systems using these fluids can therefore operate at lower mass flow rates to achieve similar heat duties. Operating at a lower mass flow rate is advantageous because it decreases the exergy destruction that occurs due to fluid friction Bejan (1980).

Hydrocarbons are natural fluids that can be used as a replacement for synthetic refrigerants in refrigeration cycles, and they fit the desired characteristics outlined above. However, hydrocarbons do not exist in the environment in a pure state. For example, natural gas that is extracted from the Earth contains varying concentrations of methane, ethane, propane and butane. The process industry refines and purifies such raw fluids into its constituent ingredients. One of the cycles used to separate miscible fluids is the continuous distillation process shown in Figure 1.1; a continuous gas separation process heats and boils a fluid mixture, condenses the vapor stream in the condenser, and delivers purified fluid streams. The design and performance of the condenser, which is highlighted, is a major consideration in the continuous distillation process. Effective

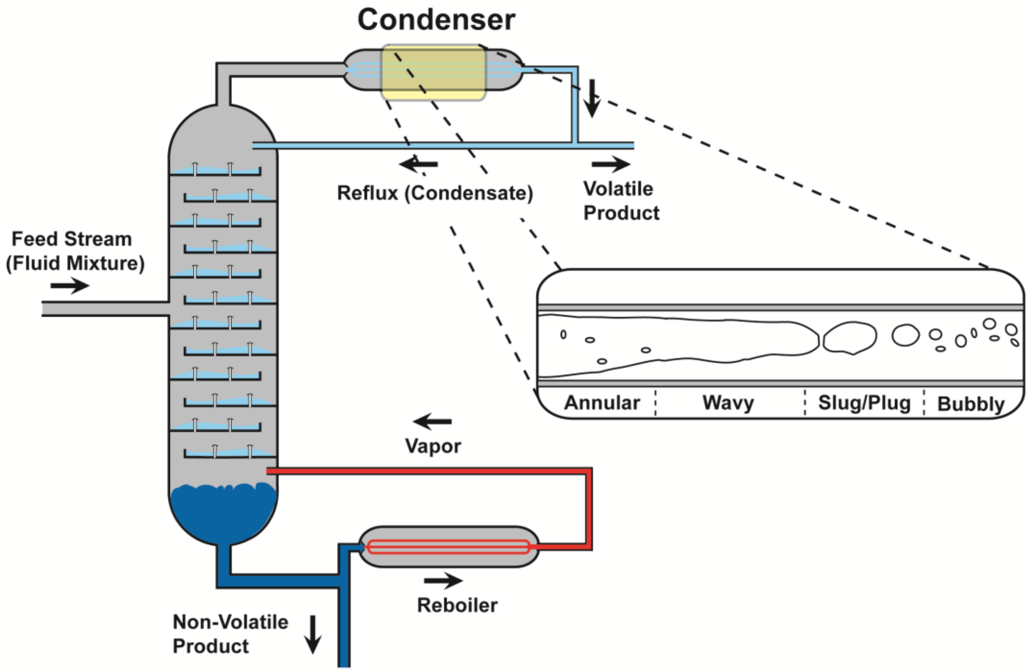

Figure 1.1: Distillation cycle with sample flow visualization in the condenser

design of the condenser and precise determination of the operating conditions increases cycle efficiencies. However, to optimize the cycle, a precise knowledge of the condensation heat transfer and fluid pumping characteristics is required. The following section describes in detail the important design considerations for condensers.

1.1 Condenser Design

Condenser design is a multivariate problem, and determining the optimum combination of dimensions and operating conditions requires comprehensive knowledge of the behavior of the heat transfer coefficient and pressure drop for a wide range of operating conditions. Some of the considerations for the design engineer are: a) condenser size (channel size and total surface area required to achieve complete condensation), b) condenser configuration (tube orientation and design, i.e., vertical/horizontal, shell-and-tube/tube-in-tube), c) operating conditions of the condensing fluid and d) required coolant temperatures and flow rates. The following section describes common considerations for the design of a condenser.

1.1.1 Channel Diameter

The distillation process described above is typically utilized in refineries or processing plants. These cycles operate on large scales where expensive setup costs can be offset by the large volumes of refined products. To achieve the required scaling, larger tube diameters are used in the heat exchangers. The condensation heat transfer coefficient and frictional pressure gradient typically decrease with increasing tube diameter, therefore reducing the pumping requirements and the amount of exergy destroyed. However, a decrease in the frictional pressure gradient corresponds to a decrease in the rate of condensation. Thus, there is a trade-off between the surface area and the pumping requirement based on the tube diameter choice. The present study examines the heat transfer and pressure drop characteristics of two commonly used tube diameters in the process industry.

Figure 1.2 shows that the predictions of four correlations, two for the heat transfer coefficient and two for the frictional pressure gradient. The frictional pressure gradient is a widely studied problem, in particular for air-water mixtures – and the predictions of the two correlations are similar. However, it is much more difficult to accurately measure the condensation heat transfer coefficient, and for similar conditions, can vary widely between investigators. Moreover, experiments with different tube diameters often require entirely new experimental setups; thus there are fewer studies showing comparisons in the heat transfer coefficient between tube diameters. Correlations developed to predict the experimental values of heat transfer coefficient could have very different scaling across

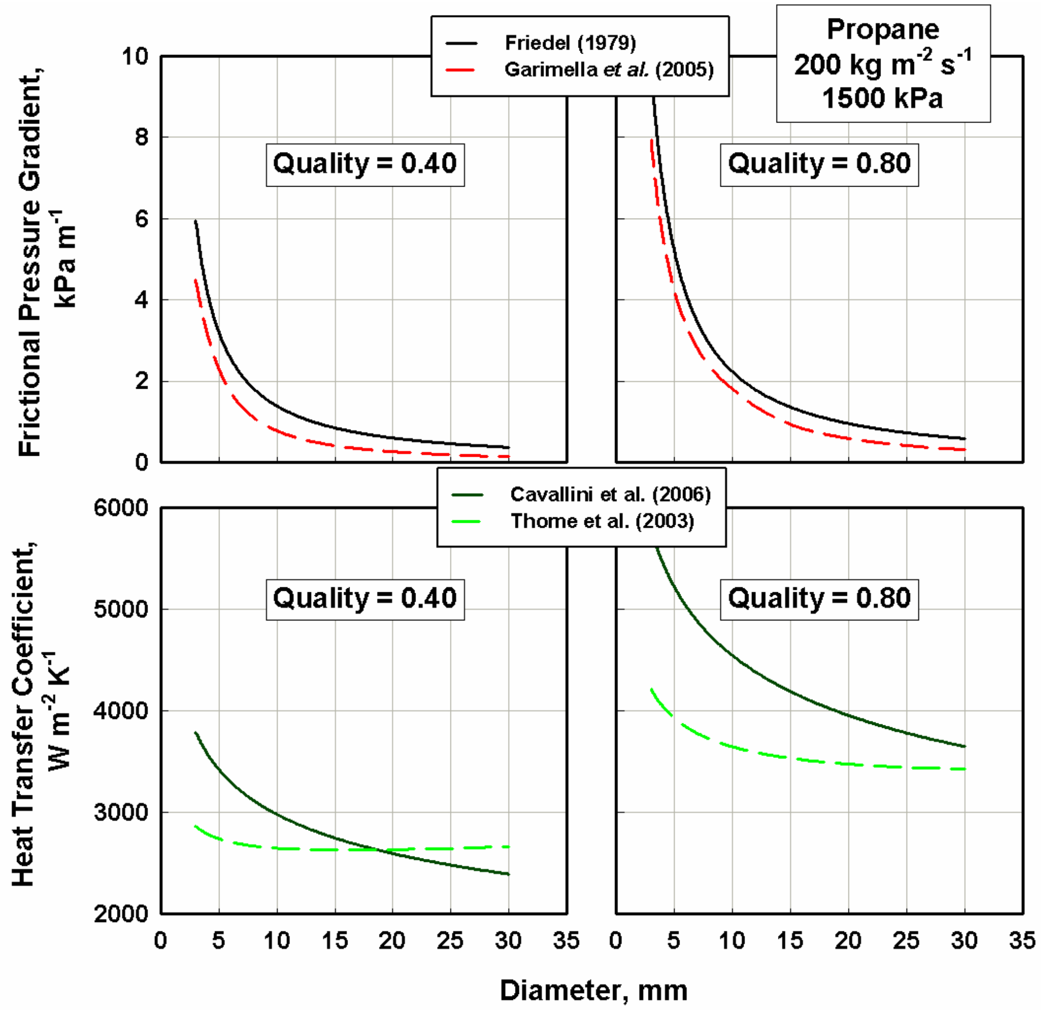

Figure 1.2: **Correlation predictions for the heat transfer coefficient and frictional pressure gradient**

diameters, and can result in conflicting predictions. For example, the Cavallini *et al.* (2006) model predicts a continual decrease in the heat transfer coefficient as the diameter increases for both vapor qualities. The Thome *et al.* (2003) correlation predicts a flat trend in the heat transfer coefficient at a high vapor quality for larger tube diameters, i.e., > 15 mm, and an increase in heat transfer coefficient with tube diameter at low vapor qualities.

1.1.2 Reduced Pressure

A relatively large body of work exists for the tube diameters of interest in the present study. However, the majority of these studies focuses on fluids such as air-water mixtures, which have very large liquid-to-vapor density ratios, or synthetic refrigerants with experiments conducted over a limited range of saturation conditions typically of interest to the HVAC industry. Often, heat transfer and flow visualization studies using glass test sections are conducted at relatively low saturation pressures. Therefore, the scaling of the condensation heat transfer coefficient and frictional pressure drop as pressures approach the critical point is not well understood.

Increasing saturation temperature leads to conditions that decrease heat transfer coefficients and frictional pressure gradients due to a decreasing liquid density and increasing vapor density, which reduces vapor-liquid shear and the heat transfer rate as well as the frictional losses. However, because few studies experimentally demonstrate this across a wide range of reduced pressures, the exact scaling of the heat transfer coefficient and frictional pressure gradients across a wide enough range of saturation conditions is not well known. As the saturation pressure approaches the critical point, the ratios of density and viscosity of the vapor and liquid phases, and the thermal conductivity change considerably from the corresponding values at lower pressures, as shown in Table 1.1. With such significant changes in fluid properties, it is unclear whether the same correlations at the lower saturation conditions can be directly extrapolated to higher saturation conditions. The present study addresses this issue by conducting heat transfer and pressure drop experiments across a wide range of reduced pressures, $0.25 < P_r < 0.95$.

Table 1.1. Thermodynamic and transport property changes up to the critical point

P_{sat}	P_{red}	T_{sat}	μ_L	μ_V	$\mu_L\ \mu_V^{-1}$	ρ_L	ρ_V	$\rho_L\ \rho_V^{-1}$	k_L	Pr_L
kPa	-	°C	$kg\ m^{-1}\ s^{-1}$		-	$kg\ m^{-3}$		-	$W\ m^{-1}\ K^{-1}$	-
1080	**0.25**	30	9.2×10^{-5}	8.5×10^{-6}	11	485	23	21	0.092	2.8
1520	**0.36**	45	7.9×10^{-5}	9.1×10^{-6}	9	459	34	14	0.085	2.8
2120	**0.50**	60	6.6×10^{-5}	1.0×10^{-5}	7	428	50	9	0.078	2.8
2850	**0.67**	75	5.3×10^{-5}	1.1×10^{-5}	5	389	73	5	0.072	3.0
3425	**0.81**	85	4.4×10^{-5}	1.3×10^{-5}	3	355	98	4	0.068	3.5
4035	**0.95**	94	3.4×10^{-5}	1.6×10^{-5}	2	300	144	2	0.070	7.1

$P_{critical}$	$T_{critical}$
4251 kPa	95°C

1.1.3 Working fluid-to-Coolant Temperature Difference

The temperature difference between the coolant stream and the condensing fluid directly affects the total rate of condensation. However, a very large temperature difference between the coolant and condensing fluids can lead to greater exergy destruction in the condenser, which decreases its thermodynamic efficiency. Additionally, the effect of coolant-to-working fluid temperature difference on the condensation heat transfer coefficient inside tubes has not been systematically investigated.

The fundamental theories for the drop-wise and film modes of condensation predict opposite trends with temperature difference. The consensus for drop-wise condensation is that the heat transfer coefficient is directly dependent on temperature difference, as illustrated by Le Fevre and Rose (1965) and Rose (2002), while the analytical study by Nusselt (1916) predicts an inverse temperature dependence on the heat transfer coefficient. The Nusselt (1916) film condensation model has been shown to be accurate for predicting the trends in heat transfer coefficient for low Reynolds number films on flat plates and the external surfaces of horizontal tubes. However, increasing vapor velocities and film Reynolds numbers produce surface waves in the condensate film, which increases the interfacial area of the film and induces large amounts of turbulent mixing. These factors significantly increase the heat and mass transfer through the film, but are not accounted for in the Nusselt (1916) model. Several authors (Fujita and Ueda, 1978; Ghiaasiaan, 2007; Gstöhl, 2004; Lee and Rose, 1984; Mudawwar and El-Masri, 1986) have shown that the heat transfer coefficient increases with increasing Reynolds number after a critical Reynolds number has been surpassed. Thus, for higher Reynolds numbers, the Nusselt film model incorrectly predicts both the trends with temperature difference and the magnitude of heat transfer coefficient. These trends in the heat transfer coefficient for falling films are shown in the schematic in Figure 1.3 for a range of Reynolds numbers.

The critical Reynolds number at which the departure from Nusselt film theory, and a reversal of the trend, happens is either a constant value of 30 (Ghiaasiaan, 2007) or a function of the Kapitza number, i.e., saturated fluid properties. The critical Reynolds number is only a function of fluid properties, which suggests that increasing reduced pressure will produce conditions where the Nusselt film theory is invalid. The liquid viscosity, liquid density and surface tension all decrease at higher reduced pressures, which dramatically increases the Kapitza number and decreases the critical Reynolds number where waviness is incipient. For example, propane at a 30°C saturation temperature has a critical Reynolds number of 33, while for a 94°C saturation temperature, the critical Reynolds number is 14. Additionally, the decrease in the liquid viscosity results in larger liquid film Reynolds numbers. Thus, as pressure is increased,

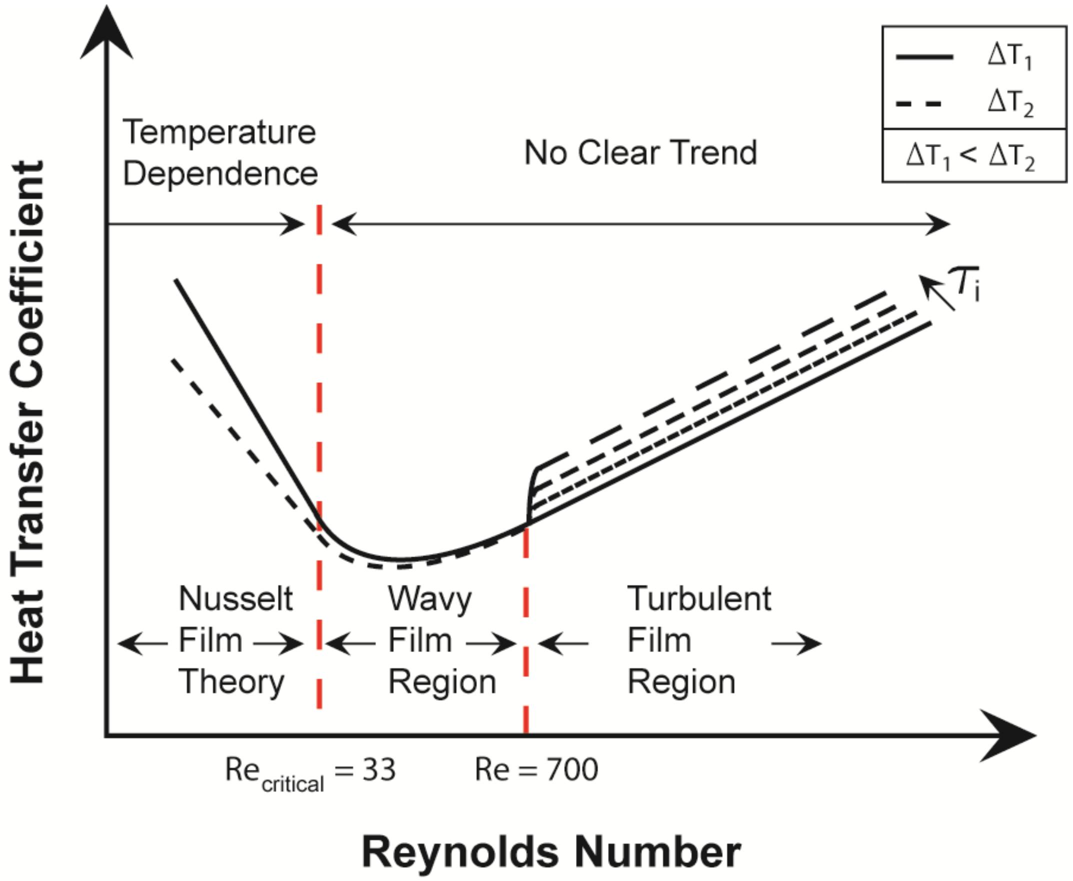

Figure 1.3: Trends in the falling film heat transfer coefficient with Reynolds number

the threshold for waviness decreases and the liquid Reynolds number increases, which suggests that waviness is an important consideration for all vapor qualities at higher reduced pressures. Moreover, thicker liquid films exist at higher reduced pressures, which increase the likelihood of liquid-phase subcooling being an important consideration during condensation.

The discussion above illustrates that models and correlations available in the literature may not predict condensation at high temperature differences or at high reduced pressures accurately. The present study addresses these issues by investigating the condensation heat transfer coefficient at various coolant-to-working fluid temperature differences, over a range of reduced pressures, $0.25 < P_r < 0.67$, and mass fluxes.

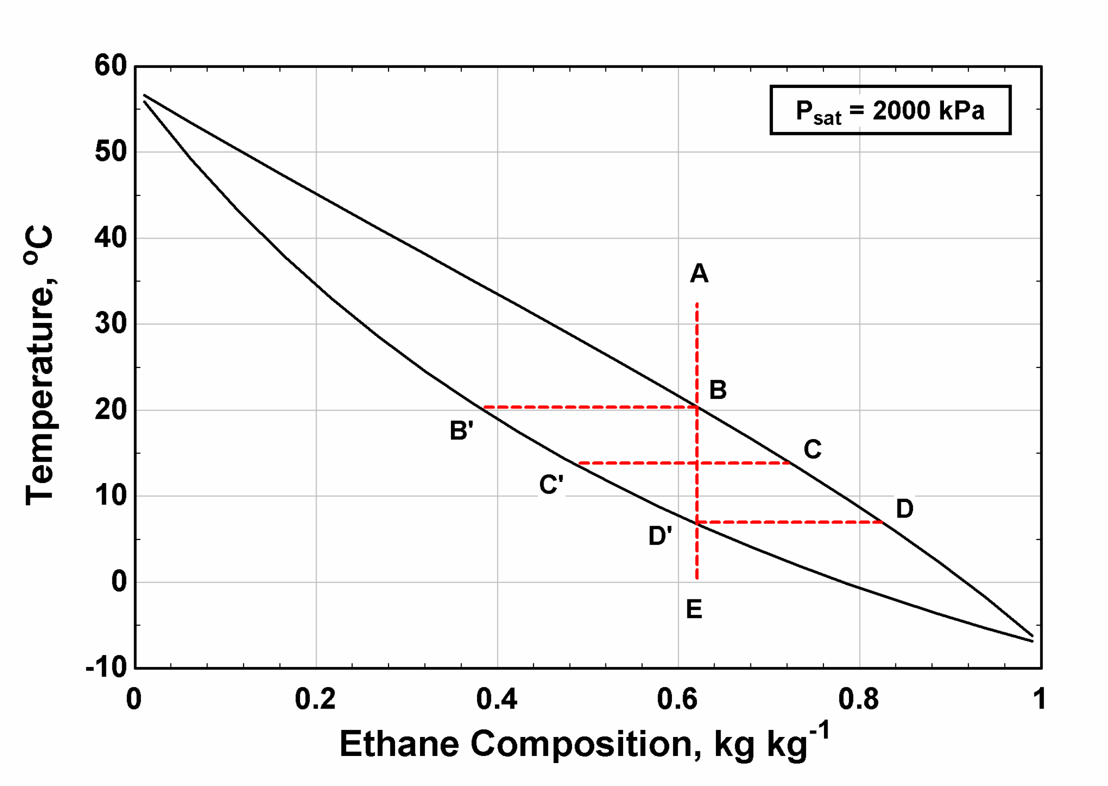

Figure 1.4: Equilibrium temperature and concentration diagram (T-x-y)

1.1.4 Mixture Effects

The equilibrium condensation process for a zeotropic mixture of ethane and propane follows the process shown in Figure 1.4. The concentration shown in Figure 1.4 is the mass fraction of ethane in an ethane-propane mixture. Heat is removed from the superheated vapor mixture at state A until it reaches the saturation point. The first drops of condensate have the equilibrium concentration shown at point B’, with the vapor concentration at point B. As more heat is removed, the liquid-phase composition follows the bubble point curve and progresses from B’ to C’ to D’. The equilibrium liquid-phase concentration shifts from a rich composition of propane to a liquid that is increasingly rich in ethane. The enriching of the liquid phase in ethane is produced by ethane rich-vapor condensing to the ethane-poor liquid. At point D’, the liquid is almost at the original vapor phase composition. Similarly, the vapor-phase concentration follows the dew point curve and the vapor-phase concentrations progress from B to C to D. If more heat is removed beyond state point D, the liquid begins to subcool; however, the concentration of the mixture remains constant. The bubble and dew point curves in Figure 1.4 are calculated using REFPROP Version 9.1 (Lemmon *et al.*, 2013). They are the vapor and liquid saturation phase temperatures for a specified bulk mixture concentration at a saturation pressure, shown in Eq (1.1).

$$\begin{aligned} T_{\text{bubble}} &= f\left(\text{fluid}, P_{\text{sat}}, X, y=0\right) \\ T_{\text{dew}} &= f\left(\text{fluid}, P_{\text{sat}}, X, y=1\right) \end{aligned} \tag{1.1}$$

Typically when zeotropic mixtures condense, the perceived heat transfer coefficient is complicated by the shifts in vapor- and liquid- phase concentrations and the

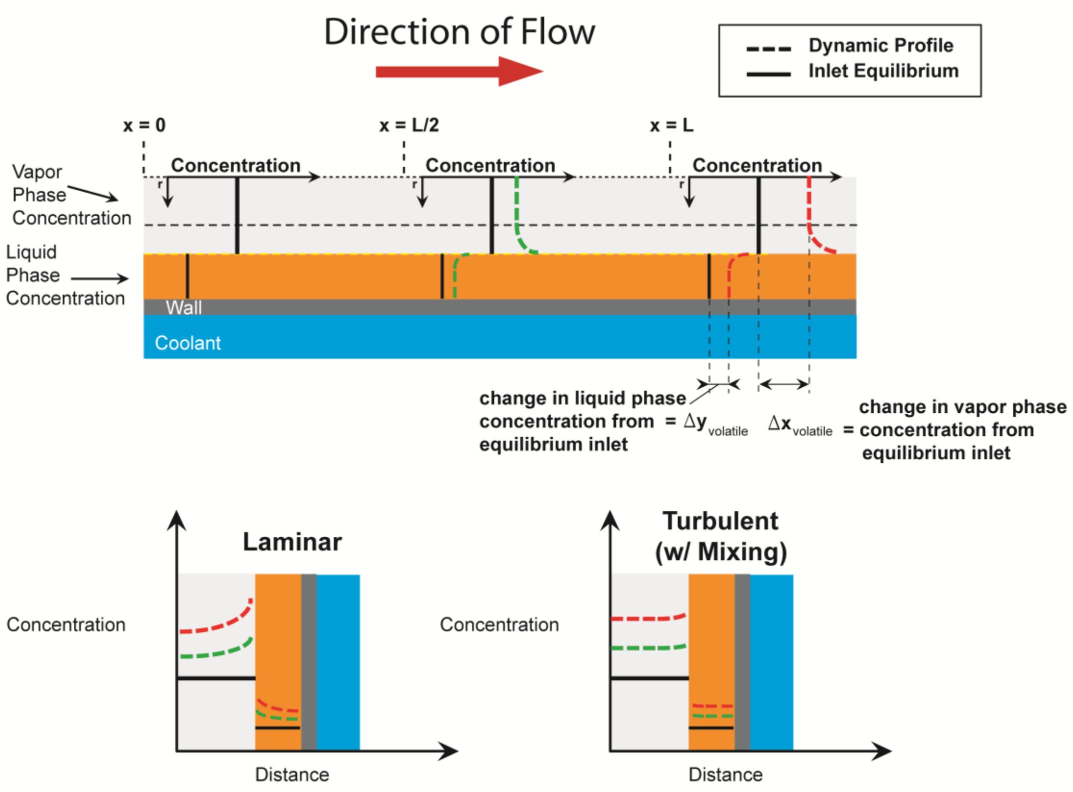

Figure 1.5: Concentration gradients during zeotropic mixture condensation

condensation process cannot be expected to exactly follow the equilibrium path shown in Figure 1.4. A more common representation of the condensation process of a zeotropic mixture is shown in Figure 1.5. This figure shows a non-equilibrium condition developing in the liquid and vapor phases as the two-phase fluid progresses along the condenser, and as heat is simultaneously removed. When heat is removed from a two-phase zeotropic mixture, the less volatile components of the mixture more readily condense from the vapor to the liquid phase. This occurs locally at the interface and produces a region on either side of the interface that is richer in the more volatile component. The vapor region close to the interface is richer in the more volatile component because the less volatile component has condensed to liquid. The liquid region close to the interface becomes richer in the more volatile component because the vapor phase, which was initially richer in the more volatile component, increases the concentration of the more volatile component locally at the interface of the liquid phase.

Along with the conceptual explanation of the concentration gradients for an arbitrary tube length, shown in Figure 1.5, is a more detailed description of the types of concentration gradients that can develop, specifically for either laminar flows or turbulent flows. For laminar flows, a smooth, almost linear concentration gradient can develop from the interface to the vapor bulk. For turbulent flows, the vapor and liquid phases have a more uniform concentration as a result of turbulent mixing. For the mixture shown in Figure 1.4, condensation results in an increase in the concentration of the more volatile fluid in both phases.

Furthermore, the concentration gradients illustrated in Figure 1.5 for the laminar and turbulent conditions have contrasting impacts on the rate of condensation. In laminar

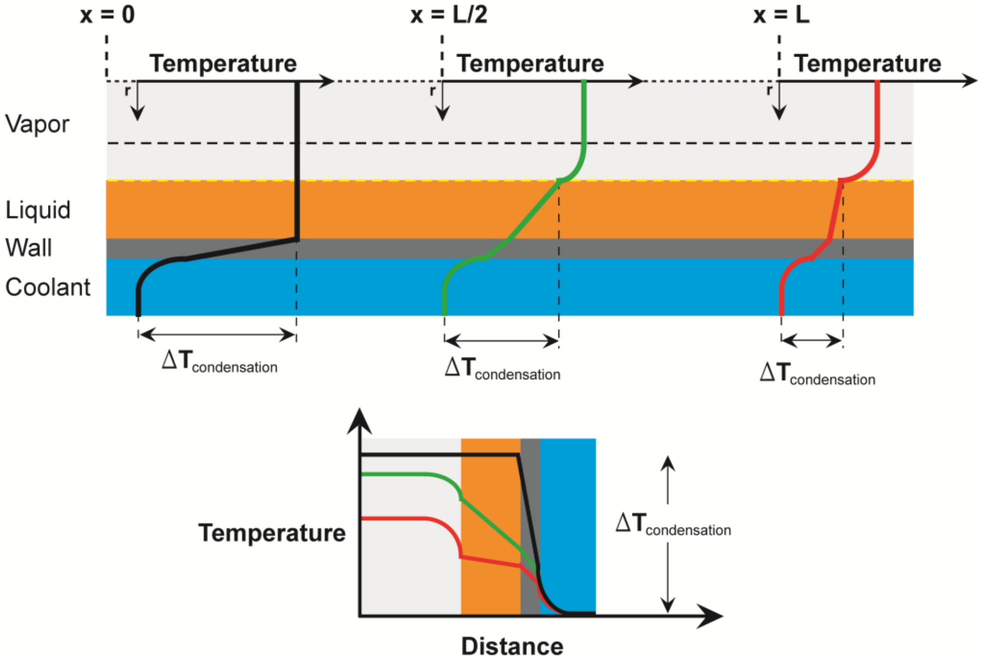

Figure 1.6: Temperature gradients during zeotropic mixture condensation

flow, the concentration gradient manifests as a mass transfer resistance in the vapor phase. This impedes the heat transfer rate and decreases the condensation rate. In some cases, the mass transfer resistance can be sufficiently restrictive that it causes sub-cooling of the liquid phase rather than further condensation. Therefore, the existence of a concentration gradient is commonly referred to as producing a lower "apparent" heat transfer coefficient than a pure fluid. In turbulent flow, the high rate of mass transfer in the vapor phase and turbulent mixing produces more uniform phases. This maintains the phase and interface temperatures closer to the equilibrium temperatures. As such, over an arbitrary length of condenser, the higher rate of mass transfer results in greater changes in the concentration of the two phases. Condensation more closely follows the equilibrium curves, and inspection of Figure 1.4 shows that an increase in the concentration of the more volatile fluid produces lower temperatures of both phases. Clearly the equilibrium condition is desirable, but it is not without complications in the design of condensers. For example, if the condenser is not divided into sufficient segments, then the driving temperature for condensation can be inaccurate, resulting in incorrect predictions of the required surface area for the condenser.

Figure 1.6 shows the temperature gradients that develop during zeotropic mixture condensation. In contrast to pure fluids, temperature gradients are expected to develop in both the liquid and the vapor phases. The key temperature difference that determines the condensation rate is the temperature difference between the interface and the coolant. Importantly, this temperature difference decreases as the concentration of the liquid phase increases in the more volatile component, i.e., from points B' to D'. Determining the temperatures of the phases and the interface is further complicated by the mass transfer resistance and the local concentrations of the species on either side of the interface.

It is clear from the discussion above that the presence of concentration and temperature gradients and the effects of laminar and turbulent conditions present various additional challenges in predicting the condensation rate of zeotropic mixtures. Specifically, the challenges relate to the following unknowns:

- vapor-phase mass transfer
- liquid-phase mass transfer
- interface temperature
- The heat transfer in the vapor and liquid phases

1.2 Need for Additional Work

The present study addresses the deficiencies in the understanding of condensation outlined above by:

1) Documenting the condensation heat transfer coefficient and frictional pressure drop of pure hydrocarbons for multiple mass fluxes, two tube diameters (7.75 and 14.45 mm), six saturation pressures from low reduced pressures ($P_r = 0.25$) to the near-critical point ($P_r = 0.95$), and four working fluid-to-coolant temperature differences ($3 < \Delta T < 13$ K.)
2) Developing a physically consistent condensation heat transfer coefficient and frictional pressure drop model for pure hydrocarbons that can be applied to a wide range of operating conditions.
3) Documenting the apparent condensation heat transfer coefficient across two concentrations of ethane and propane mixtures with three mass fluxes, two tube diameters and three saturation pressures.
4) Comparing the most commonly used modeling approaches for predicting heat transfer coefficient and frictional pressure drop for pure and zeotropic mixtures of hydrocarbons.
5) Developing a set of criteria to determine the conditions for which mass transfer effects significantly affect the condensation heat transfer coefficient, and recommending a modeling approach for defined sets of operating conditions.

1.2.1 Organization of Thesis

The thesis is organized as follows:

1. **Chapter 2** presents experimental results for pure fluid condensation. The results are accompanied by a detailed discussion of the trends and comparison with correlations from the literature.

2. **Chapter 3** presents a detailed exploration of the effect of temperature difference on the heat transfer coefficient, along with comparisons with correlations from the literature.
3. **Chapter 4** outlines three models: a) a pure-fluid condensation heat transfer coefficient model, b) a frictional pressure drop model and c) a coolant-to-working fluid temperature difference modification to the pure fluid model.
4. **Chapter 5** presents experimental results on the condensation of zeotropic mixtures of propane and ethane. This is accompanied by a detailed discussion of the trends and comparison with pure fluid correlations from the literature and the most commonly used techniques that are used to account for the effect of zeotropic mixtures.
5. **Chapter 6** outlines new design criteria that highlights conditions for which the mass transfer effects of zeotropic mixtures must be explicitly modeled.
6. **Chapter 7** presents the conclusions from this study and provides recommendations for future work.

CHAPTER 2 PURE FLUID HYDROCARBON MEASUREMENTS

2.1 Introduction

Synthetic refrigerants, such as hydrofluorocarbons (HFCs), are the most common working fluids used in refrigeration cycles. They have excellent thermophysical properties and boil and condense at temperatures well suited for HVAC&R systems. Propane, a natural refrigerant that has a Global Warming Potential (GWP) of 3, has superior thermodynamic and transport properties when compared to HFCs. Thus, at similar operating conditions, the heat transfer characteristics of propane are expected to be better than those of synthetic refrigerants. Therefore, propane is an excellent candidate as a replacement working fluid for HFCs that are being phased out. Because technical improvements have addressed to a large extent safety matters such as pressure sealing of systems, the remaining limiting factor hindering widespread use of propane is the limited knowledge of the boiling or condensation heat transfer and pressure drop behavior at the conditions typically of interest to the HVAC&R sector.

Furthermore, the process industry, which produces pure hydrocarbons from the separation of multi-component mixtures, relies on condensers as the final stage in the refining process for continuous distillation columns. Accurate knowledge of the condensation of pure fluids is the first step in understanding the behavior of multi-component mixtures. Thus, for appropriate condenser design and efficient cycle operation, knowledge of the heat transfer coefficient and frictional pressure drop across a wide range of operating conditions is necessary.

Previous experimental condensation studies on both synthetic and natural working fluids have focused largely on relatively narrow ranges of saturation conditions and reduced pressures. As a result, the available heat transfer and pressure drop models have not been validated against experimental data over the wide range of operating conditions of interest across the process and HVAC industries, even for synthetic refrigerants. Furthermore, no models have been developed specifically for natural refrigerants, while the available models have typically been applied to natural refrigerants with mixed results. This lack of available information and reliable correlations hampers the optimal design of condensers. The following is a review of the experimental studies in the literature relevant to the condensation of hydrocarbons.

2.2 Prior Work

Several studies in the literature have investigated the condensation of synthetic refrigerants. However, as noted by several researchers, e.g., Granryd (2001) and Miyara (2008), condensation of hydrocarbons has received only sparse attention. The studies on hydrocarbon condensation have been conducted using mostly propane, propylene and butane as the working fluid. Moreover, these experiments have been conducted across a narrow range of reduced pressures. The narrow range of reduced pressures does not provide a sufficiently large data set, with wide variations in fluid properties and vapor-to-liquid property ratios that would be necessary for the development of broadly applicable correlations.

Chang *et al.* (2000) investigated the performance of several pure hydrocarbons and their zeotropic mixtures in a heat pump, examining both evaporation and condensation processes in an 8-mm ID tube at a saturation temperature of 45°C. The performance is compared to the results for refrigerant R22, and some hydrocarbons are shown to have better performance characteristics than R22. Thome *et al.* (2003) noted that there appear to be significant errors in their experimental results, especially for high vapor quality and low mass flux conditions.

Lee *et al.* (2006) conducted complete condensation heat transfer and pressure drop studies in a long U-shaped tube-in-tube condenser on R22, iso-butane, propane and propylene flowing through 8-mm and 10.92-mm ID tubes at saturation temperatures between 35 – 45°C, which corresponds to a range of reduced pressures between 0.13 and 0.17 for iso-butane, and 0.29 – 0.40 for propane and propylene. They showed that for all mass fluxes and tube diameters considered, the heat transfer coefficient was greater, by at least 31%, for the hydrocarbons than for the synthetic refrigerant, while the pressure drop increased by at least 50%.

Park *et al.* (2008) investigated the condensation of R22, propylene, propane, iso-butane and DME in an 8-mm tube at 40°C. They showed that all of the hydrocarbons have greater heat transfer coefficients than the synthetic refrigerant. The highest heat transfer coefficients for the natural refrigerants occur at the lowest reduced pressures for that fluid. The synthetic refrigerant (R22) studied for comparison to the hydrocarbon data has a lower reduced pressure at 40°C than that of both propane and propylene, but also has a lower measured heat transfer coefficient, indicating that reduced pressure is not the only consideration affecting heat transfer rate. They note that the Jung *et al.* (2003) correlation most accurately predicts their experimental results.

Ağra and Teke (2008) conducted condensation studies on iso-butane in a 4-mm tube at low mass fluxes, between 47 and 116 kg m^{-2} s^{-1}, and for saturation temperatures between 30°C and 43°C. Their results showed that a change in the saturation temperature of the working fluid had almost no effect on the heat transfer coefficient. They conducted

Table 2.1. Experimental Testing Conditions

Mass Flux, kg m^{-2} s^{-1}	Saturation Temperature, ^{o}C (Reduced Pressure) 30 (*0.25*)	45 (*0.36*)	60 (*0.50*)	75 (*0.67*)	85 (*0.81*)	94 (*0.95*)	Internal Diameter
150	X	X	X	X	X	X	7.75 & 14.45 mm
300	X	X	X	X	X	X	
450			X	X	X	X	

experiments at different coolant-to-working fluid temperature differences and showed an inverse relationship between temperature difference and heat transfer coefficient.

The above discussion shows that hydrocarbon condensation has not been widely investigated. Furthermore, no studies have reported condensation heat transfer for either hydrocarbons or synthetic refrigerants across reduced pressure ranges spanning most of the vapor-liquid dome. Therefore, there has not been adequate validation of the widely used condensation heat transfer and pressure drop models across large ranges of transport and thermodynamic properties. A systematic documentation of the influence of typical parameters that affect the condensation process with wide variations in the thermodynamic and transport properties is therefore required to better understand the use of propane as a working fluid.

This study addresses this deficiency in the literature by providing experimental results documenting condensation heat transfer coefficients and frictional pressure gradients for a wide reduced pressure range, three mass fluxes, and two tube diameters, as shown in Table 2.1. This information is used to develop physically consistent heat transfer and frictional pressure gradient models in Chapter 4.

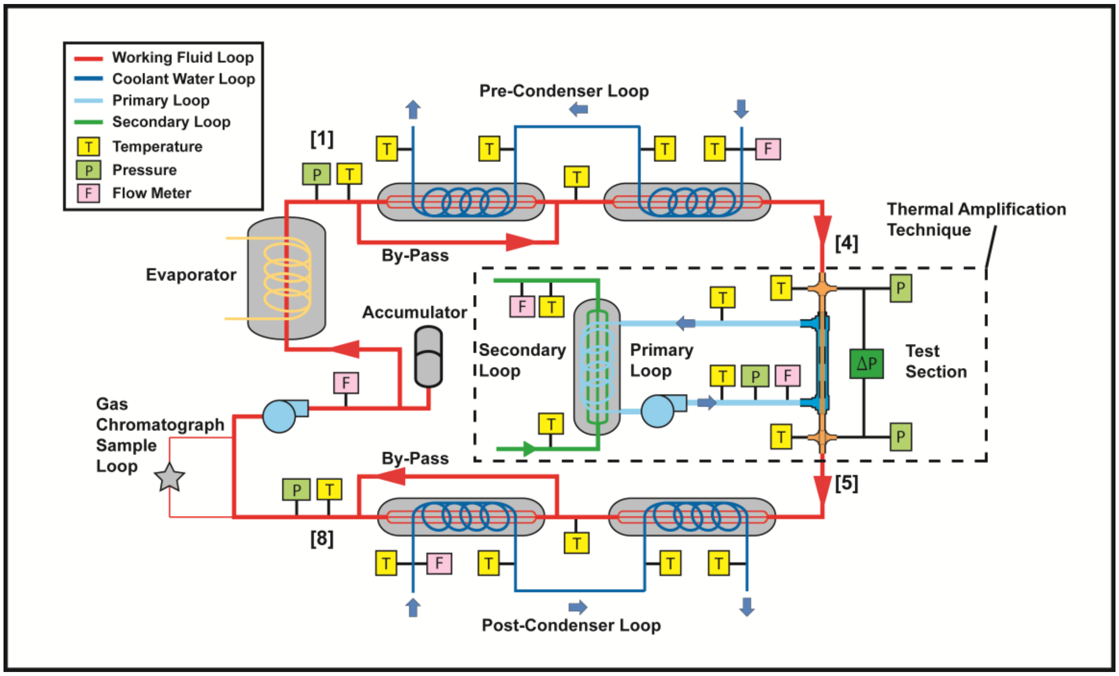

Figure 2.1: Facility schematic

2.3 Experimental Approach

The test facility used to conduct the heat transfer and pressure drop measurements was first developed for flow visualization studies in mini-channels by Coleman and Garimella (2000). It was subsequently updated to conduct pressure drop and heat transfer tests on condensing R134a by Garimella and Bandhauer (2001), and further modified by several researchers to enable testing over a wider range of diameters, mass fluxes, reduced pressures and fluids by Jiang and Garimella (2003), Mitra and Garimella (2003b), Andresen (2006), Keinath and Garimella (2011) and Milkie (2014). Minor adjustments and re-calibrations were made to this facility to enable the tests in the present study, including pressure sealing the facility for high operating pressures, adding liquid- and vapor-phase temperature measurements along the two-phase section of the loop, replacing pumping components to enable testing with a low viscosity fluid, i.e., propane, and installing safety and alarm components to address the flammable nature of the fluid.

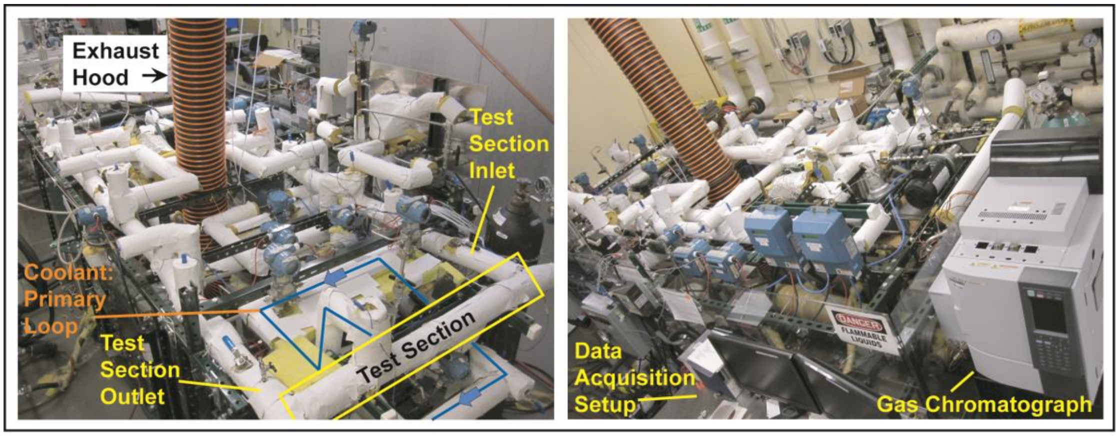

Figure 2.2: Front and rear photograph of the built facility

Details of the test facility, shown in a schematic in Figure 2.1 and with photographs of the built facility (Figure 2.2,) are provided in Appendix B; a brief overview is provided here. The primary feature of the test facility is a closed loop containing the working fluid, with four working fluid state points noted here to aid the discussion below. The working fluid is pumped from a sub-cooled state (state point **8**) through a steam-heated helical tube-in-tube evaporator where the working fluid is brought to a superheated state (state point **1**). The temperature and pressure are measured at this superheated point to completely determine the thermodynamic state. The superheated working fluid flows through either one or two shell-and-tube pre-condensers in series, depending on the mass flux and test tube diameter, where it is cooled by a countercurrent flow of coolant water. The fluid then enters the copper test section, consisting of a tube-in-tube condenser, where an additional change in quality is accomplished.

The test section inlet condition or inlet quality (state point **4**) is obtained by measuring the pressure at the test section inlet and conducting an energy balance between the superheated state and the heat gain of the coolant water to determine the test section inlet enthalpy. After flowing through the test section, the working fluid is condensed in either one or two shell-and-tube post-condensers in series to a sub-cooled state. At the sub-cooled state, the temperature and pressure are measured to establish the thermodynamic state of the working fluid. The test section outlet condition or outlet quality (state point **5**) is identified by measuring the pressure at the outlet of the test section and conducting an energy balance between the sub-cooled thermodynamic state and the heat gain of the coolant water to determine the test section outlet enthalpy. The equations shown in Eq. (2.1) are used to calculate the inlet, outlet and average test section enthalpies, and the corresponding qualities.

$$\left.\begin{aligned} i_{\text{TS,inlet}} &= i_{\text{superheat}} - \frac{\left(\dot{Q}_{\text{pre-condenser}} + \dot{Q}_{\text{ambient}}\right)}{\dot{m}_{\text{refrigerant}}} \\ i_{\text{TS,outlet}} &= i_{\text{subcool}} + \frac{\left(\dot{Q}_{\text{post-condenser}} + \dot{Q}_{\text{ambient}}\right)}{\dot{m}_{\text{refrigerant}}} \end{aligned}\right\} \rightarrow i_{\text{TS,average}} = \frac{i_{\text{TS,inlet}} + i_{\text{TS,outlet}}}{2} \qquad (2.1)$$

The heat duty of the test section is a critical quantity for deducing the condensation heat transfer coefficient. The thermal amplification technique outlined by Garimella and Bandhauer (2001) is used to obtain an accurate test section heat duty measurement. This process ensures a decoupling of the two competing parameters that typically limit accurate isolation of the condensing heat transfer coefficient—a large temperature rise in the test section coolant fluid and a low test section coolant thermal resistance.

To achieve these objectives, two coupled loops—a primary and a secondary loop—are used in combination. The primary loop is a closed loop containing pressurized water that removes heat from the test section and rejects it to the secondary loop through a shell-and-tube heat exchanger. The flow rate of water in the primary loop is high to ensure high heat transfer coefficients on the annulus side of the test section and therefore low coolant water thermal resistance contribution to the total conductance, *UA*. The secondary loop coolant water flows at a low rate. When the primary loop rejects its heat to this flow, it results in a large temperature rise in the coolant. The heat duty across the test section is determined by subtracting the primary loop pump heat addition from the secondary loop heat duty, see Eq. (2.2). The primary loop pump heat addition was determined based on pump curves and dedicated pump recirculation tests, which yielded curvefits for the heat dissipation as a function of volumetric flow rate.

$$\begin{aligned} \dot{Q}_{\mathrm{TS}} &= \dot{Q}_{\mathrm{secondary}} + \dot{Q}_{\mathrm{ambient}} - \dot{Q}_{\mathrm{pump\ heat\ addition}} \\ \dot{Q}_{\mathrm{secondary}} &= \dot{m}_{\mathrm{secondary}} \left(i_{\mathrm{secondary\text{-}outlet}} - i_{\mathrm{secondary\text{-}inlet}} \right) \end{aligned} \tag{2.2}$$

The test section heat transfer coefficient is calculated using the *UA-LMTD* method shown in Eq. (2.3). The overall *UA* is a function of the condensation resistance, the tube wall conduction resistance and the resistance of the coolant in the annulus, which is determined from a curve-fit by Garimella and Christensen (1995a) for laminar and turbulent Nusselt numbers for convective heat transfer in annuli.

$$\begin{aligned} \dot{Q}_{\mathrm{TS}} &= UA \cdot \Delta T_{\mathrm{LM}} \\ UA &= \left(R_{\mathrm{annulus}} + R_{\mathrm{conduction}} + \frac{1}{h_{\mathrm{condensation}} A_{\mathrm{in}}} \right)^{-1} \end{aligned} \tag{2.3}$$

The working fluid temperatures used in the *LMTD* calculation are based on equilibrium conditions using the measured pressure and derived test section enthalpy, while the coolant temperatures are measured quantities.

One of the major advantages of the thermal amplification technique is that it facilitates measurements of small test section heat duties or quality decrements (Δq ~ 0.1). Conducting measurements in small quality decrements ensures high resolution in heat transfer coefficients as a function of quality. Without such fine resolution, the measured heat transfer coefficients would represent larger quality ranges, thereby masking the variations across different flow regimes and the respective transport phenomena. The second major advantage of this method is that it results in significantly lower uncertainties in the measured heat transfer coefficients.

The frictional pressure drop is calculated by measuring the total pressure drop in the test section and accounting for the change in momentum, i.e., deceleration, of the condensing vapor. Equations (2.4) and (2.5) are used to calculate the total frictional pressure drop. For all data points in the present study, the correlation developed by Baroczy (1963) is used to calculate the vapor void fraction. The average deceleration pressure drop is approximately 18% of the total measured pressure drop, and 10% and 25% for the 7.75 mm and 14.45 mm tube diameter, respectively.

$$\Delta P_{\text{frictional}} = \Delta P_{\text{measured}} - \Delta P_{\text{deceleration}} \tag{2.4}$$

$$\Delta P_{\text{deceleration}} = G^2 \left\{ \left[\frac{q^2}{\rho_{\text{V}}\,\varepsilon} + \frac{(1-q)^2}{\rho_{\text{L}}\,(1-\varepsilon)} \right]_{\text{out}} - \left[\frac{q^2}{\rho_{\text{V}}\,\varepsilon} + \frac{(1-q)^2}{\rho_{\text{L}}\,(1-\varepsilon)} \right]_{\text{in}} \right\} \tag{2.5}$$

The calculations outlined above were performed using Engineering Equation Solver (EES) software (Klein, 2012). The thermodynamic and transport properties of the coolant water and working fluids were calculated using REFPROP Version 9.1 (Lemmon *et al.*, 2013), which uses the Helmholtz equation of state for propane from Lemmon *et al.* (2009).

2.4 Experimental Results

The measured frictional pressure drop for both tubes and all saturation and mass flux conditions is shown in Figure 2.3. A selection of these results is presented in Figure 2.4, where the experimental results are subdivided based on the parameters typically of interest for heat exchanger design. The frictional pressure drops follow the expected trends with quality, saturation temperature, mass flux and tube diameter.

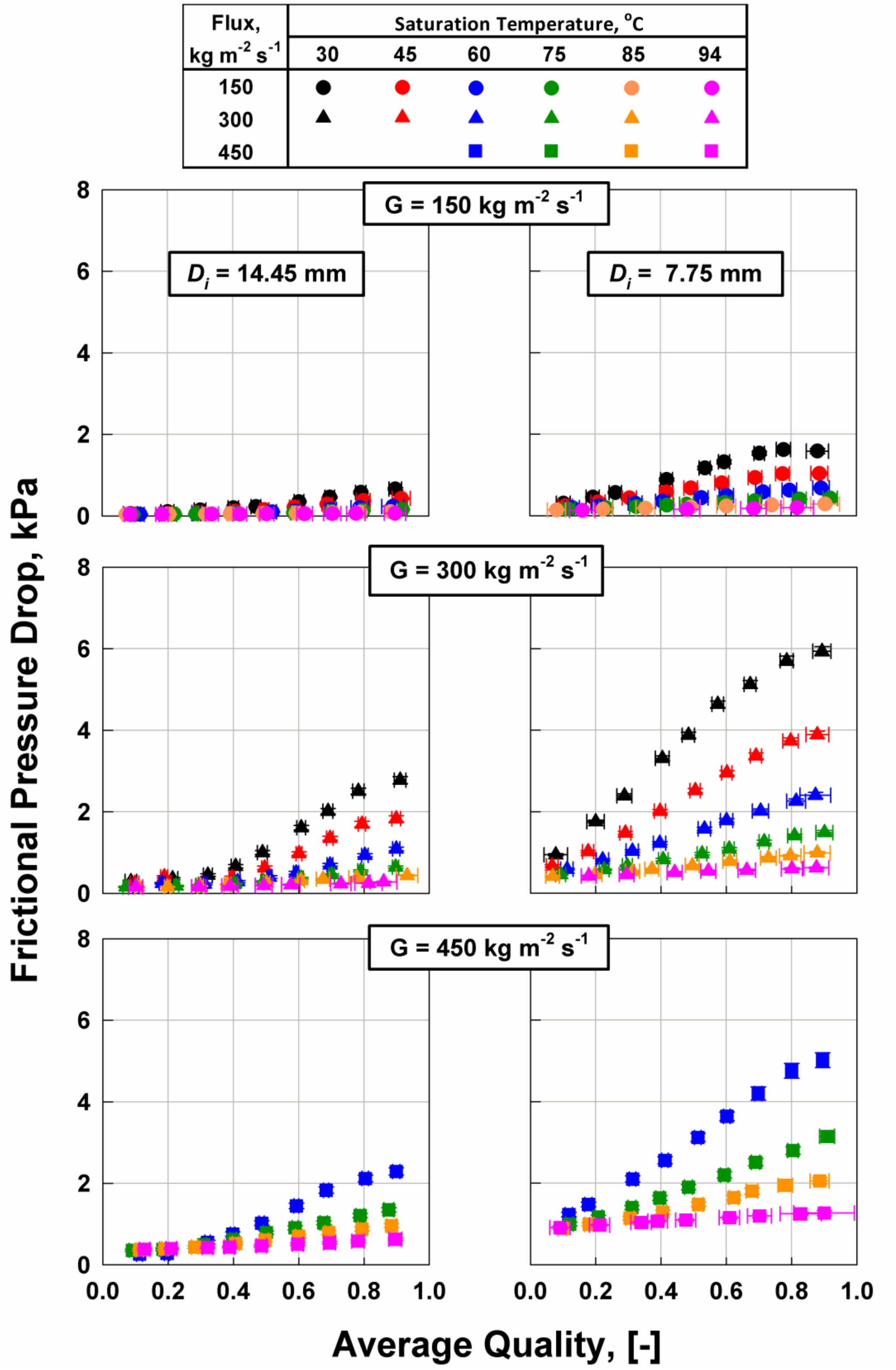

Figure 2.3: Experimental results - Frictional pressure drop

The total two-phase frictional pressure drop can be thought of as a summation of the

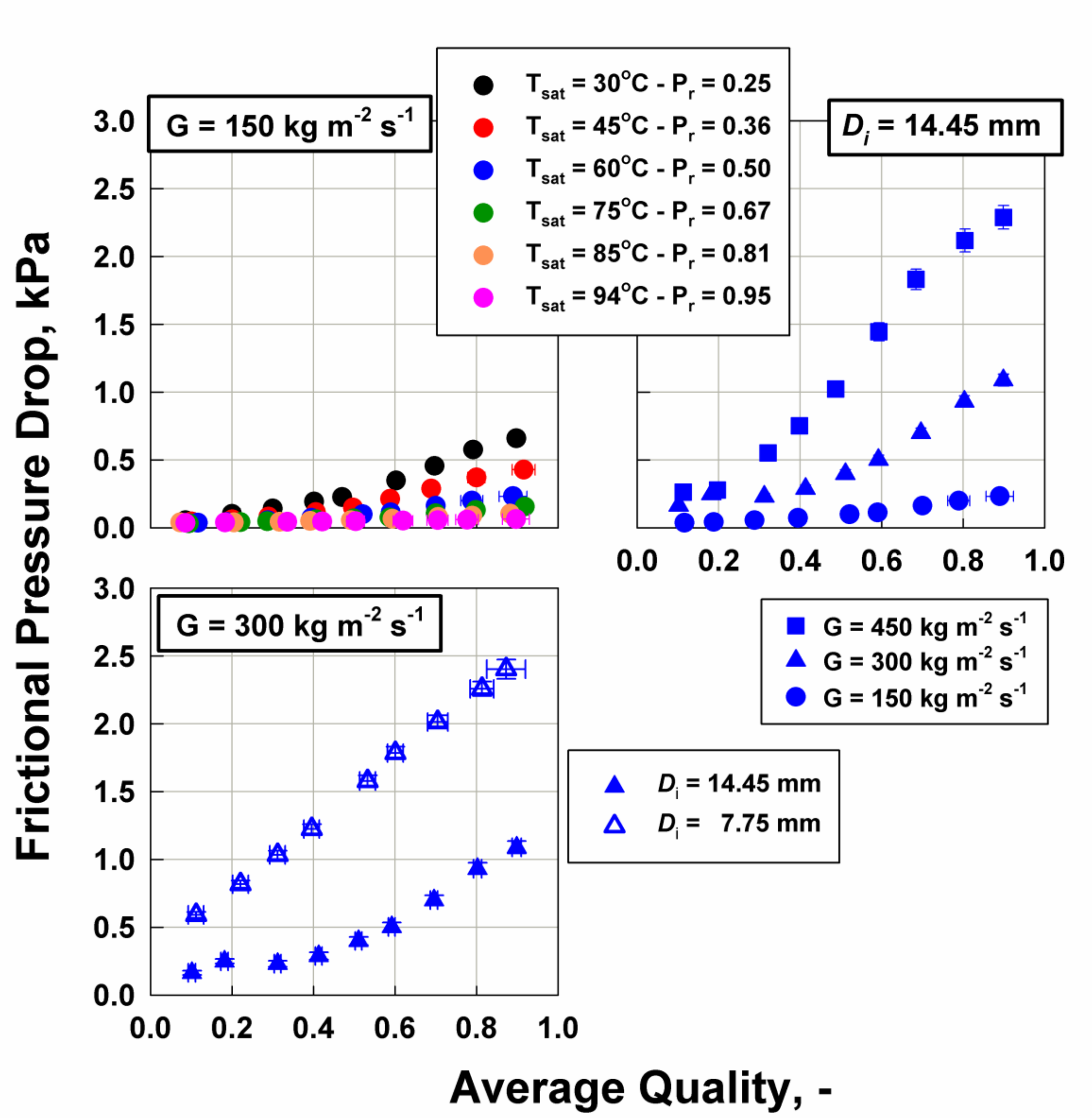

Figure 2.4: Summary of trends - Frictional pressure drop

liquid-phase and vapor-phase pressure drops and the pressure drop due to the interactions between the phases. The relative contribution of each of these terms determines the total frictional pressure drop for a given set of conditions.

The experimental results show that the frictional pressure drop decreases with increasing saturation temperature. An increasing saturation temperature results in a denser vapor phase and less dense liquid phase, which at similar mass flux and quality conditions, results in a lower vapor-phase velocity. The vapor-phase pressure drop often dominates the total two-phase frictional pressure drop; therefore, reduced vapor-phase velocities results in a decrease in the two-phase frictional pressure drop. Increases in mass flux and vapor quality result in an increase in the frictional pressure drop. This is mostly due to two factors: a) increasing fluid shear due to increasing overall phase velocities, and b) increasing vapor-liquid phase interactions. Higher mass fluxes have more rapidly moving vapor and liquid phases and greater velocity gradients, leading to greater frictional pressure drop. Larger vapor qualities result in higher void fractions and correspondingly larger frictional pressure drops.

The trends in frictional pressure drop with mass flux, quality, and saturation temperature are the same for both diameters. At a given mass flux, the homogenous velocities are similar for both tube diameters; however, the frictional pressure drop increases for smaller tube diameters because smaller tube diameters have greater velocity gradients at the tube wall. However, the increase in frictional pressure drop is greater than the decrease in diameter. For example, at a saturation temperature of 60°C, a q_{avg} of 0.593, and a mass flux of 149.5 kg m^{-2} s^{-1}, the frictional pressure drops for the 14.45-mm and 7.75-mm tube diameters are 0.111 kPa and 0.493 kPa, respectively.

All of the measured condensation heat transfer coefficients are shown in Figure 2.5, while the trends as a function of parameters typically of interest to heat exchanger design are shown in Figure 2.6. The trends in the heat transfer coefficient can be explained by reference to the liquid condensate film that forms on the inner tube wall. This liquid film represents the primary thermal resistance to heat transfer; therefore, knowledge of the changes in the film thickness and its dynamic characteristics can explain the observed trends.

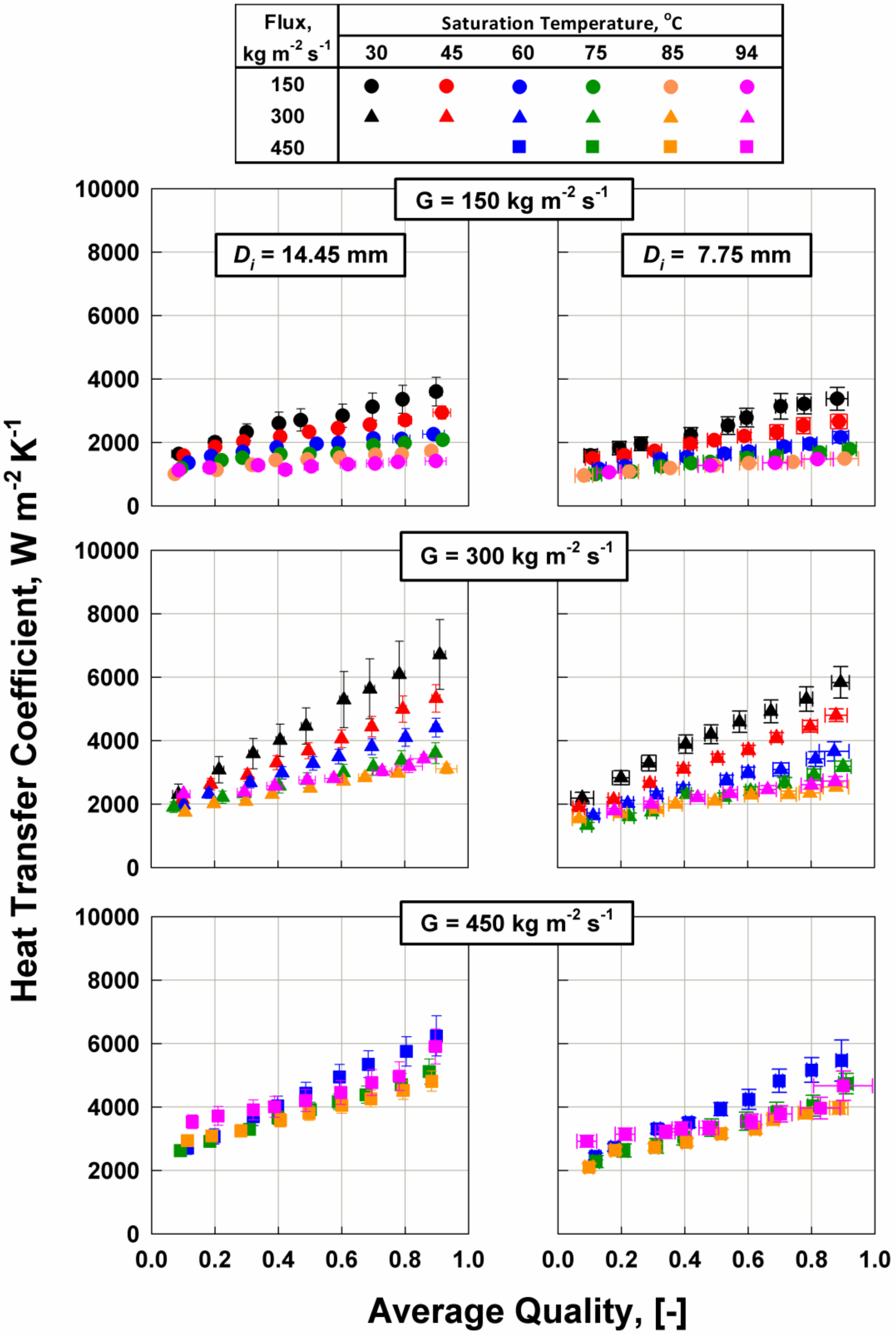

Figure 2.5: Experimental results – Heat transfer coefficient

According to the Breber *et al.* (1980) flow regime map (Figure 2.7,) the expected flow regimes in this study are stratified/wavy and annular. The stratified flow regime is

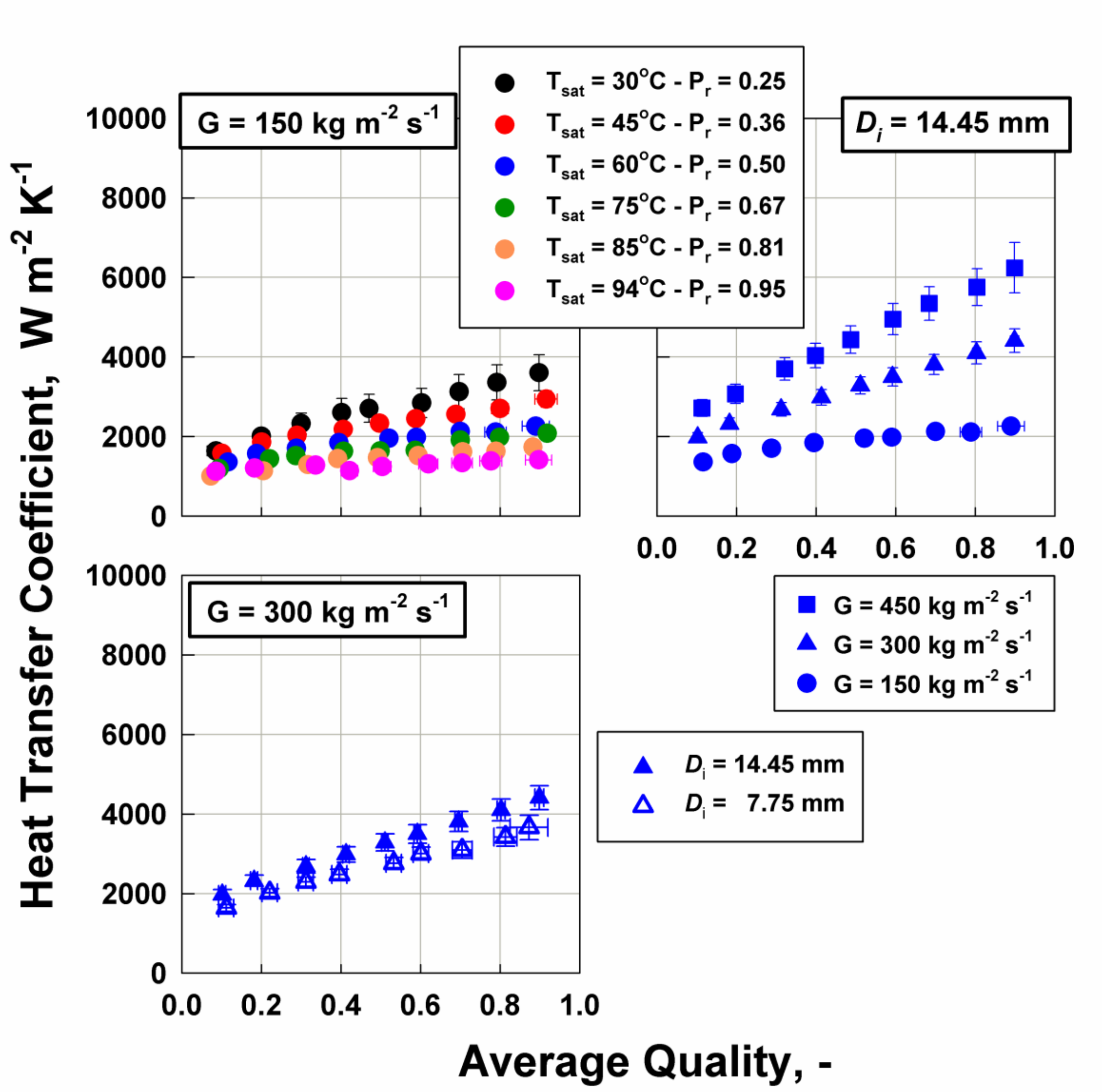

Figure 2.6: Summary of trends - Heat transfer coefficient

characterized by the dominance of gravity over shear forces, while in the annular regime, shear forces dominate. Stratified flow often has a falling film in the upper portion of the tube and a liquid pool at the base of the tube, while in annular flow, the liquid film is evenly distributed around the inner tube periphery. These two flow regimes are often modeled under idealizations of smooth liquid films; however, recent flow visualizations studies have shown that the liquid film is in fact in an agitated state (Milkie, 2014).

Figures 2.5 and 2.6 show that an increase in saturation temperature causes a decrease in the heat transfer coefficient. Increases in the saturation temperature result in an

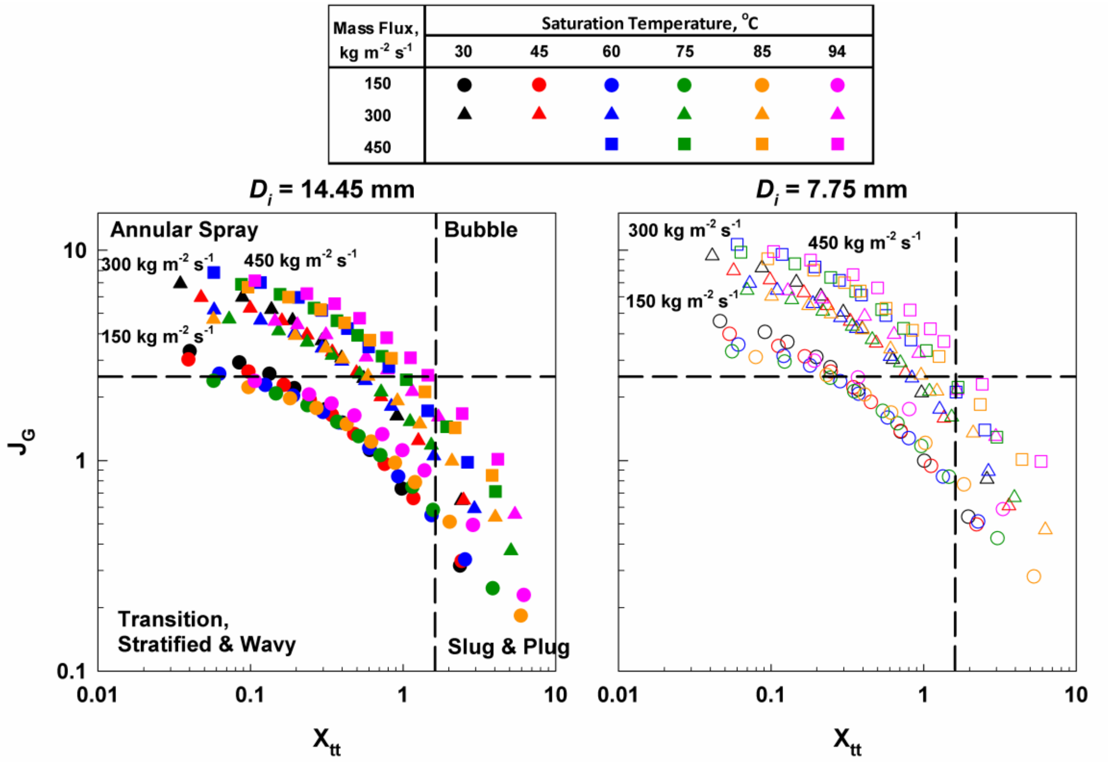

Figure 2.7: Predicted flow regimes – Breber *et al.* map

increase in vapor density and a decrease in liquid density; these changes in densities results in a decreased vapor void fraction. A decreased vapor void fraction also implies that a larger fraction of the cross section is occupied by liquid condensate, which presents a greater thermal resistance to heat transfer, and therefore leads to a lower heat transfer coefficient. It should be noted that increasing saturation temperature results in a reduction in liquid phase viscosity and an increase in liquid thermal conductivity. These latter effects would serve to increase the heat transfer coefficient; however, their augmenting effect on heat transfer is lower than the impeding effect of the increased film thickness, which leads to an overall decrease in heat transfer coefficient with increasing saturation temperature.

At high reduced pressures ($P_r > 0.85$) and low vapor qualities ($q < 0.3$), the trend outlined above for heat transfer coefficient with saturation temperature reverses. This is due to a trade-off between several competing factors promoting and inhibiting heat transfer: a) at these high reduced pressures, the vapor fraction decreases, with a corresponding increase in the liquid phase fraction, b) there is a dramatic decrease in liquid phase viscosity, and c) liquid thermal conductivity increases slightly. For example, with a change in saturation temperature from 85°C to 94°C, the liquid viscosity decreases from 44.3×10^{-6} kg m^{-1} s^{-1} to 33.3×10^{-6} kg m^{-1} s^{-1}, and the thermal conductivity increases from 68 mW m^{-1} K^{-1} to 70 mW m^{-1} K^{-1}, and at a quality of 0.2, the void fraction decreases from 0.42 to 0.33, respectively. Thus, the largest change among these parameters is in the liquid viscosity, which offsets the larger film thickness and therefore results in an overall increase in heat transfer coefficient from 1134 W m^{-2} K^{-1} to 1208 W m^{-2} K^{-1} between these two saturation temperatures.

At a given saturation temperature and mass flux, an increase in vapor quality results in a larger portion of the tube cross section being occupied by vapor and therefore a smaller liquid film thickness, which increases the heat transfer coefficient. Similarly, larger mass fluxes result in higher heat transfer coefficients. At a given vapor quality and saturation temperature, increasing the mass flux results in increasing phase velocities and greater shearing of the vapor-liquid interface by the vapor phase. The greater phase velocities increase the turbulence in the liquid film and the greater vapor shear increases interfacial disturbances, both of which result in increasing heat transfer coefficients.

The results of the present study show that the tube diameter is less important in determining the heat transfer coefficient than it is for frictional pressure drop for the diameters under consideration. Heat transfer coefficients often decrease with an increase in tube diameter. However, for the tube diameter of interest in the present study, it has been observed that there is greater entrainment of the liquid phase in the vapor core for the larger tube diameter (Milkie, 2014). Liquid entrainment occurs when the ratio of forces promoting liquid entrainment, i.e., shear forces, are greater than the forces inhibiting entrainment, i.e., surface tension/radius of curvature. The correlation of Govan *et al.* (1989), which provides closure equations for the rate of entrainment equations outlined by Carey (1992), predicts a finding similar to that of Milkie (2014), i.e., increased liquid entrainment in the larger tube. The increased entrainment in the larger tube leads to greater proportional reduction in the liquid film thickness, which, as noted above, increases the heat transfer coefficient. Furthermore, the larger radius of curvature of the larger diameter tube results in reduced influence of the stabilizing forces due to surface tension on the liquid-vapor interface, which leads to greater interfacial roughness in the larger tube diameter. The increased entrainment and greater interfacial roughness in the larger diameter tube can serve to increase the heat transfer coefficient, and therefore explain the observed trends.

It should be noted that the trend of increasing heat transfer coefficient with tube diameter is most significant at higher reduced pressures. The greater liquid inventory at higher reduced pressures results in the likelihood of the larger interfacial disturbances already observed in the larger tube diameter having greater importance, thereby increasing the heat transfer coefficient. Furthermore, Govan *et al.* (1989) predict that the rate of entrainment will initially slightly decrease as the reduced pressure is increased from 0.25 to 0.50, but will increase significantly for higher reduced pressures, which would lead to increases in heat transfer coefficient.

2.5 Comparison with Literature

The heat transfer coefficients and frictional pressure drops measured in this study were compared with the predictions of several correlations from the literature. To facilitate the comparison between experimental results and predictions, two parameters - the average deviation (AD) and the absolute average deviation (AAD) - are defined and shown in Eq. (2.6) and (2.7).

$$\mathrm{AD} = \frac{1}{n}\sum_{i=1}^{n}\frac{predicted - measured}{measured} \tag{2.6}$$

$$\mathrm{AAD} = \frac{1}{n}\sum_{i=1}^{n}\left|\frac{predicted - measured}{measured}\right| \tag{2.7}$$

Figure 2.8 shows the comparison between the measured frictional pressure drop and the predictions of correlations by Lockhart and Martinelli (1949), Chisholm (1973), Friedel (1979a), Müller-Steinhagen and Heck (1986), Souza *et al.* (1992), Cavallini *et al.* (2002a), Garimella *et al.* (2005), Andresen (2006) and the homogenous flow correlation. The deviation of the predictions from the measured frictional pressure drops is summarized in Table 2.2; no model accurately captures all of the trends in the data or provides good statistical agreement. The correlation that predicts the observed trends with quality, saturation temperature and mass flux the best is the Garimella *et al.* (2005) correlation. This correlation also has the best statistical agreement, which is probably due to the fact that it is a flow regime dependent correlation that models the pressure drop in the dominant flow regime of interest in the present study, i.e., annular flow. Other commonly used correlations, such as the Friedel (1979a) and Müller-Steinhagen and Heck (1986) correlations, have similar statistical agreement; however, they significantly over-predict the pressure drop in the 14.45 mm tube diameter.

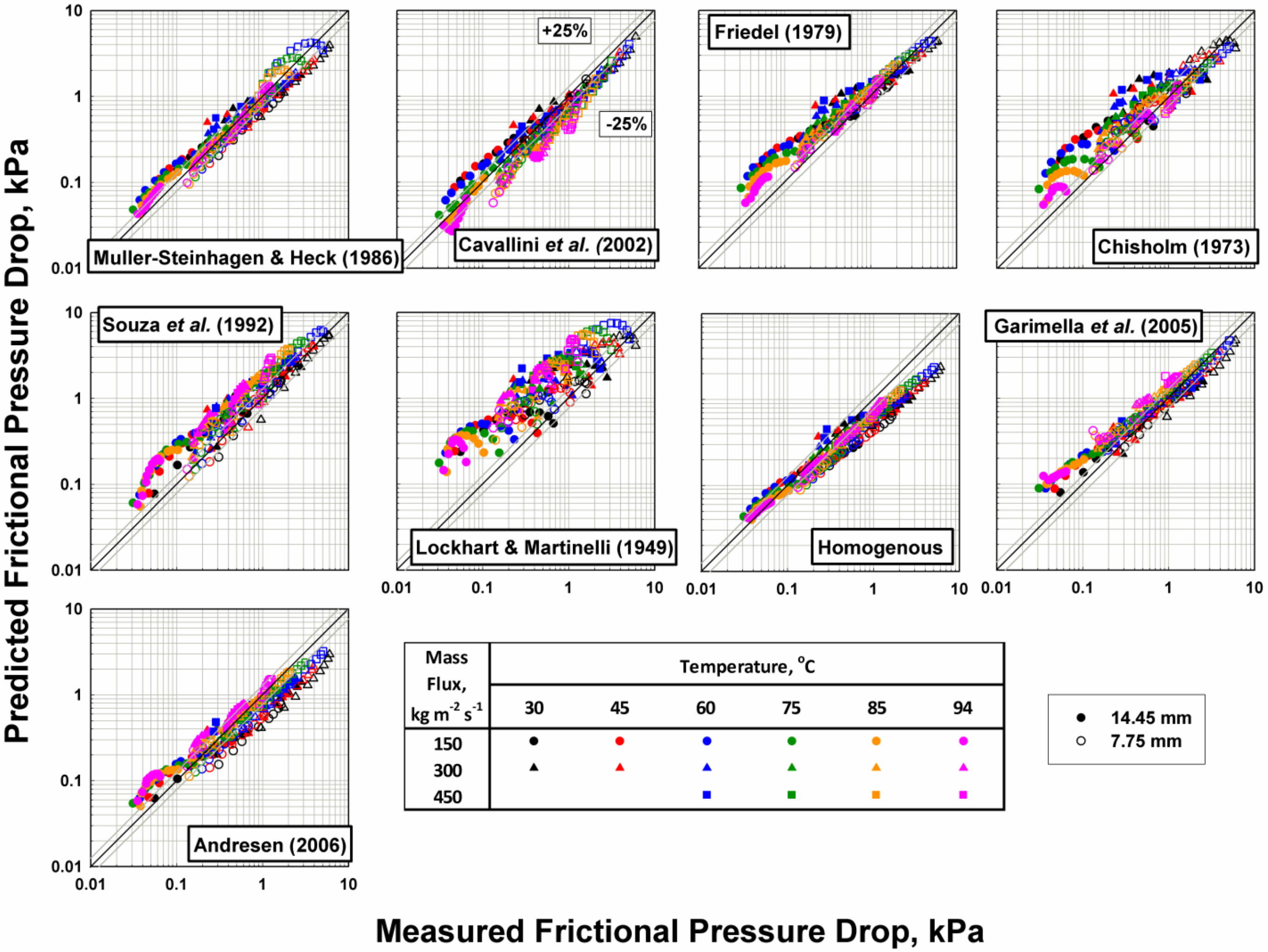

Figure 2.8: Comparison with literature predictions – Frictional pressure drop

Table 2.2. Comparison with Literature Correlations – Frictional Pressure Drop

Correlation	AAD, % 14.45 mm	AAD, % 7.75 mm	AD, % 14.45 mm	AD, % 7.75 mm	Overall AAD, %	Overall AD, %
Homogenous	24	43	-17	-43	33	-29
Lockhart and Martinelli (1949)	269	149	268	148	211	209
Chisholm (1973)	81	26	75	17	54	47
Friedel (1979)	67	18	65	12	43	39
Müller-Steinhagen and Heck (1986)	49	12	48	3	31	27
Souza *et al.* (1982)	94	37	81	4	69	47
Cavallini *et al.* (2002)	30	33	-8	-33	32	-20
Garimella *et al.* (2005)	30	22	7	-10	26	-1
Andresen (2006)	30	28	15	-24	29	-4

Figure 2.9 shows the comparison between the measured heat transfer coefficient and correlations by Traviss *et al.* (1973), Jaster and Kosky (1976), Shah (1979), Tandon *et al.* (1995), Dobson and Chato (1998), Moser *et al.* (1998), Cavallini *et al.* (2002a), Thome *et al.* (2003) and Cavallini *et al.* (2006). The deviation of the predictions from the measured heat transfer coefficients are summarized in Table 2.3. The models by Thome *et al.* (2003) and Cavallini *et al.* (2006) capture the low- and mid-range reduced pressure data well. It is likely that these correlations perform well in this range because they were developed with experimental data predominantly in this range, i.e., the exponents of the dimensionless numbers, which largely reflect the weighting given to the influence of turbulence on the heat transfer coefficient, have been determined from a best fit of data with a relatively narrow set of fluid property ratios. However, increased reduced pressures lead to significant changes in fluid property ratios, and for these conditions, the deviations between measured and predicted values increase significantly: both correlations have deviations greater than 40% for the reduced pressures greater than 0.8.

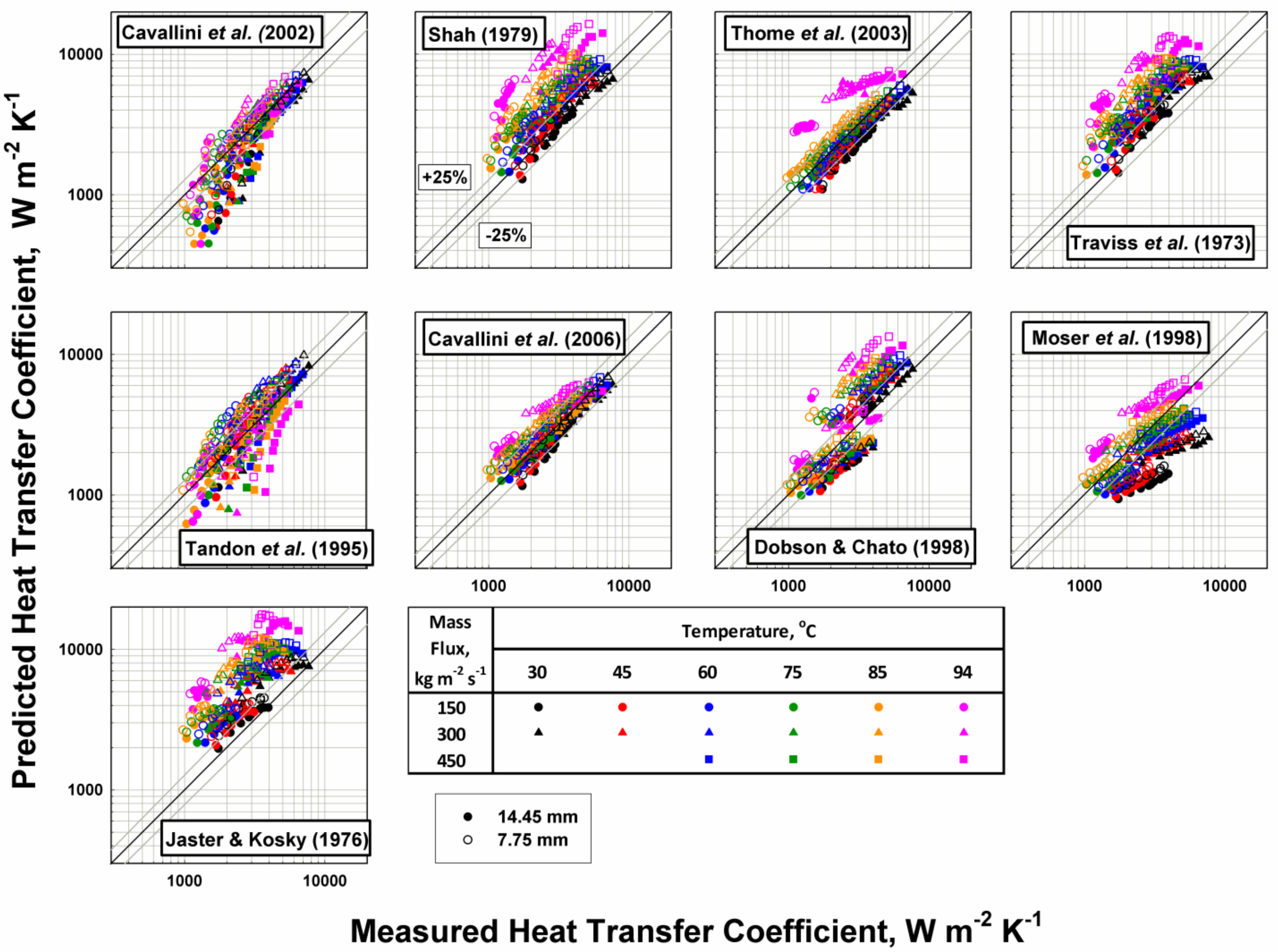

Figure 2.9: Comparison with literature predictions – Heat transfer coefficient

Table 2.3. Comparison with Literature Correlations – Heat Transfer Coefficient

Correlations	AAD, % 14.45 mm	AAD, % 7.75 mm	AD, % 14.45 mm	AD, % 7.75 mm	Overall AAD, %	Overall AD, %
Traviss *et al.* (1973)	79	122	79	122	100	100
Jaster and Kosky (1976)	126	187	127	187	156	156
Shah (1979)	74	121	75	121	97	97
Tandon *et al.* (1995)	22	42	-5	37	32	16
Dobson and Chato (1998)	40	71	18	66	55	42
Moser *et al.* (1998)	31	32	-14	6	31	-4
Cavallini *et al.* (2002)	24	25	-19	12	24	-4
Thome *et al.* (2003)	28	30	15	26	29	20
Cavallini *et al.* (2006)	13	38	7	38	25	22

The Thome *et al.* (2003) correlation predicts little change in heat transfer coefficient with diameter, which is the closest to the observed trend. The interfacial roughness factor introduced in this correlation increases with tube diameter, which increases the heat transfer coefficient and contributes towards the correct prediction of the measured trend in heat transfer coefficient.

Some correlations have very good average deviation statistics, for example the ADs for the Cavallini *et al.* (2002a) and Moser *et al.* (1998) correlations are both -4%, but this does not appropriately explain the very large scatter for both of these correlations. In particular, the Moser *et al.* (1998) correlation does not accurately capture the slope of the heat transfer coefficient with quality or the magnitude of the heat transfer coefficient with saturation temperature accurately. The Cavallini *et al.* (2002a) correlation captures the higher mass flux data well, but performs poorly at low mass fluxes, where it significantly under-predicts the heat transfer coefficients.

2.6 Conclusions

Condensation heat transfer and pressure drop data with propane as a working fluid are reported in this Chapter. The following are some of the conclusions drawn from this study:

- The heat transfer coefficient increases with mass flux and quality and decreases with saturation temperature.
- There is a slight increase in heat transfer coefficient with tube diameter within the range of diameters investigated.
- The frictional pressure drop increases with mass flux and quality, and decreases with increasing saturation temperature and tube diameter.
    - The Thome *et al.* (2003) correlation predicts the trends in heat transfer coefficient closest, while the Cavallini *et al.* (2006) correlation has the best statistical agreement, with an AD of 22% and AAD of 25%.
    - The Garimella *et al.* (2005) correlation predicts the trends in frictional pressure drop and has the best statistical agreement with the measured results.

These results are combined with physical considerations and analyses of the governing influences in Chapter 4, to yield heat transfer and pressure drop correlations with a wide range of applicability.

CHAPTER 3 EFFECT OF TEMPERATURE DIFFERENCE

3.1 Introduction

As an integral component in the power generation, refrigeration, and petrochemicals separations industries, the condenser demands attention and accurate predictive tools to ensure optimum efficiencies. The type of condenser chosen for the process depends on required heat transfer rates and the size, weight and economic constraints. Understanding the physical mechanisms of condensation is necessary for the development of accurate modeling. Despite the decades of research on condensation phenomena, the data, assumptions and simplifications used to develop condensation models have typically been applicable to narrow ranges of fluids, operating conditions and geometries. The discrepancies in prediction due to the narrow ranges of applicability get amplified in some instances when they are used as building blocks for more comprehensive, multi-regime models.

The various parameters typically of interest for the prediction of condensation heat transfer coefficient are shown in Eq. (3.1).

$$h = f\left(q, G, D, P_{\mathrm{sat}}, \Delta T\right) \tag{3.1}$$

One important aspect that has not received adequate attention in the literature on in-tube condensation is the effect of working fluid-to-wall temperature difference on the heat transfer coefficient. For reference, the fundamental theories for the drop-wise and film modes of condensation predict opposite trends with temperature difference. The Nusselt (1916) film theory predicts an inverse temperature dependence on heat transfer coefficient, whereas the consensus for drop-wise condensation is that heat transfer coefficient is directly dependent on temperature difference, as pointed out by Le Fevre and Rose (1965) and Rose (2002).

3.2 Prior work

The Nusselt (1916) film condensation model has been shown to be accurate at predicting the trends in heat transfer coefficient for low Reynolds number films on flat plates and the external surfaces of horizontal tubes (Fernando *et al.*, 2008; Gstöhl, 2004; Jung *et al.*, 2004; Park *et al.*, 2011). However, increasing vapor velocities and film Reynolds numbers induces surface waves in the condensate film, which increases the interfacial area of the film and induces additional mixing mechanisms. Both of these effects increase the heat and mass transfer through the film. The Nusselt (1916) model does not account for either of these effects, and thus, for higher Reynolds numbers the model incorrectly predicts both the trends and the magnitude of heat transfer coefficients, which has been illustrated by several authors (Fernando *et al.*, 2008; Fujita and Ueda, 1978; Ghiaasiaan, 2007; Gstöhl, 2004; Lee and Rose, 1984; Mudawwar and El-Masri, 1986; Park *et al.*, 2011). The critical Reynolds number where this departure and a reversal of the trend happens is either a constant value of 30 (Ghiaasiaan, 2007), or a function of the Kapitza number, i.e., saturated fluid properties. Importantly, this model is used as a building block in the majority of in-tube condensation models, even where turbulent flow conditions and significant interfacial roughness exist.

The fact that the critical Reynolds number is only a function of fluid properties suggests that increasing reduced pressure will correspond to conditions where the Nusselt film theory is not directly applicable. This is because increasing the reduced pressure decreases the liquid viscosity, density and surface tension, which dramatically increases the Kapitza number and decreases the critical Reynolds number where waviness is incipient. For example, at a saturation temperature of 30°C, propane has a critical

Reynolds number of 33, while for a 94°C saturation temperature, the critical Reynolds number is 14. Moreover, increasing the reduced pressure of a fluid dramatically decreases the liquid viscosity, which results in larger liquid film Reynolds numbers. Thus, as pressure is increased, the threshold for waviness decreases, while the liquid Reynolds number increases, which suggests that waviness is an important consideration at almost all vapor qualities at higher reduced pressures. Confirmation of these predictions has been provided by recent flow visualization studies by Milkie (2014) and Keinath (2012). They showed that the liquid film that develops in stratified flow is often not a smooth falling film, and can in fact be highly disturbed. Thus, the Nusselt film theory, and its predicted trend with temperature difference, need not be applicable for the majority of conditions for condensation inside tubes at elevated pressures.

Bromley (1952) and Rohsenow (1956) investigated the effect of condensate subcooling on the heat transfer coefficient. They noted that the effect of nonlinear temperature profiles is negligible for small Jakob numbers and thin films, i.e., low reduced pressures, but that subcooling is an important consideration at higher reduced pressures. Their analysis showed that subcooling the condensate would result in larger heat transfer coefficients compared to the value predicted by Nusselt (1916) film theory. They proposed a modified phase-change enthalpy including the Jakob number that accounted for the degree of subcooling. Both of these observations suggest that increasing reduced pressure leads to conditions where the trends predicted by the Nusselt film model are not valid, and the effect of a parameter such as ΔT could be opposite of the typically expected dependence.

Correlations based on a falling-film idealization have not suggested a definitive effect of the temperature dependence on the heat transfer coefficient. Chen *et al.* (1987) proposed a correlation that is a function of only the Reynolds number and Prandtl number for Reynolds numbers > 30, i.e., without any dependence on the temperature difference. Uehara and Kinoshita (1994) proposed a multi-regime model for dominant body-force condensation (gravity driven condensation). They recommended an inverse dependence of the heat transfer coefficient on the temperature difference in the laminar regime, sine wave regime and harmonic wave regime, and a proportional dependence of the heat transfer coefficient on the temperature difference in the turbulent regime.

Experimental verification of the effect of temperature difference on the heat transfer coefficient has been largely confined to low-reduced-pressure studies and for falling-film condensation. Recently, Jung *et al.* (2004) demonstrated the inverse trend in condensation heat transfer coefficient with temperature difference for low pressure hydrocarbons. However, Gstöhl (2004), who conducted experiments with R134a, demonstrated that the impact of heat flux is most pronounced at low Reynolds numbers (Nusselt film condensation) and decreases with increasing Reynolds number, or film thickness. Both of these experiments were conducted on the outside of tubes with an OD of 19 mm.

While most experimental investigations of in-tube condensation do not consider the impact of temperature difference, a few studies have mentioned the impact of temperature difference or heat flux on the condensation rate. Unfortunately, a consensus has not been reached on the exact trend in heat transfer coefficient with temperature difference. For example, investigators have reported that the condensation heat transfer coefficients:

a) increase with increasing temperature difference (Agarwal and Hrnjak, 2015; Chamra and Webb, 1995; Dobson and Chato, 1998; Yang and Webb, 1996)

b) increase with decreasing temperature difference (Cavallini *et al.*, 2001; Del Col *et al.*, 2010; Dobson and Chato, 1998; Soliman, 1986)

Soliman (1986) conducted condensation studies in the mist flow regime, although he did not conduct experiments with independent variation in the temperature difference. He demonstrated a slight increase in the heat transfer coefficient as the Jakob number decreased. He noted that Akers and Rosson (1960) and Altman *et al.* (1960) reported similar trends in their experimental results, at similarly high quality points.

Chamra and Webb (1995) reported the results of condensation experiments on R-22 in micro-finned 14.66 mm diameter tubes, and Yang and Webb (1996) reported condensation heat transfer coefficients of R-12 in 2.64 mm plain and micro-finned tubes. Both Chamra and Webb (1995) and Yang and Webb (1996) note that the heat transfer coefficient increases with heat duty. Their experiments covered mass fluxes from 150 – 327 kg m^{-2} s^{-1} and 400 – 1000 kg m^{-2} s^{-1}, respectively. Both papers reported that the heat transfer coefficient is proportional to heat flux to the power of 0.22 and 0.20, respectively.

Dobson and Chato (1998) conducted an extensive set of experiments using different fluids, tube diameters and saturation temperatures (reduced pressures). Three fluids and two saturation temperatures, i.e., 35 and 45°C, were investigated, corresponding to the following reduced pressures: R134a (P_r = 0.21 – 0.32), R22 (P_r = 0.27 – 0.39), and R32-R125 mixture (P_r = 0.43 – 0.55). The experiments were conducted for small temperature differences (1, 2, 3 and 4°C). In the stratified flow regime, they noted an inverse relationship between heat transfer coefficient and temperature difference at low mass fluxes, approximately 75 kg m^{-2} s^{-1}. For larger mass fluxes, > 300 kg m^{-2} s^{-1}, they noted the opposite trend with temperature difference, i.e., increasing temperature difference resulted in greater heat transfer coefficients. They attributed this trend to increased heat transfer occurring due to forced convection in the liquid pool at the base of the tube. They noted no dependence on temperature difference in the mist flow regime, > 650 kg m^{-2} s^{-1}, or in the annular flow regime.

Cavallini *et al.* (2001) conducted experiments on an 8-mm test section using R22, R134a, R236ea, R125, R32, R410A and for several refrigerant-to-wall temperature differences, i.e., 2.5-17°C. They state that for mass fluxes greater than 400 kg m^{-2} s^{-1}, there is no dependence on temperature difference, while for mass fluxes below 100 kg m^{-2} s^{-1}, they noted that the heat transfer coefficient increases with a decrease in temperature difference. They suggest that at the lower mass fluxes, Nusselt (1916) laminar film condensation prevails, resulting in an inverse dependence on temperature difference.

Del Col *et al.* (2010) conducted experiments on a 0.96 mm minichannel using R1234yf at a single saturation temperature of 40°C, which corresponds to a reduced pressure of 0.30 and a mass flux of 400 kg m^{-2} s^{-1}. They measured the heat transfer coefficient at refrigerant-to-coolant temperature differences of 11°C, 12°C, 14°C, 16°C, and 18°C. They did not note any dependence of heat transfer coefficient on the temperature dependence, and attributed this to the annular flow regime that is expected at these conditions throughout the vapor quality range.

Agarwal and Hrnjak (2015) observed an increase in the heat transfer coefficient with an increase in heat flux in the condensation region for heat fluxes between 5 and 10 kw

m^{-2} and a decrease in heat transfer coefficient for heat fluxes between 15 and 20 kw m^{-2}. They showed the heat transfer coefficient in the de-superheating stage increased with heat flux.

The present work addresses the conflicting results in the literature discussed above by specifically focusing on the influence of temperature difference on the condensation heat transfer coefficient with changes in typical design parameters, e.g., vapor quality, mass flux, and saturation pressure. This systematic study of the impact of temperature difference on the heat transfer coefficient identifies the trends and provides guidance on the modeling of this influence in heat transfer correlations

3.3 Experimental Procedure

The experimental setup, procedures and the data analysis methods used in this study of the condensation of propane across varying temperature differences are identical to the methods previously described in Chapter 2. The thermal amplification technique was used to deduce the condensing heat transfer coefficients. This technique ensures that the condensation resistance is the dominant thermal resistance to condensation, which minimizes the uncertainty in the condensation heat transfer coefficient introduced by the estimation of the coolant and wall resistances. The temperature difference between the coolant and working fluid also contributes to the measurement uncertainty, with small temperature differences leading to larger uncertainties. The temperature difference is a controlled and varied parameter in the present study, which makes minimizing this element of the heat transfer coefficient uncertainty difficult. Thus, using the thermal amplification technique to minimize the resistance network uncertainty is essential for minimizing the overall uncertainty in the measured condensation heat transfer coefficient.

Table 3.1. Experimental Test Conditions

Mass Flux, kg m^{-2} s^{-1}	**Saturation Temperature, ^{o}C (Reduced Pressure)**				**Internal Diameter**	**ΔT_{LM}**
	30 (0.25)	**45 (0.36)**	**60 (0.50)**	**75 (0.67)**		
150	X	X	X		**7.75 mm**	**4, 7, 11 and 13^{o}C**
300	X	X	X	X		
450			X	X		

The average uncertainty in the measured heat transfer coefficient for the present study was 6.3%, with a range of 2.1% to 19.2 %. The largest uncertainties were observed at the lowest working fluid-to-coolant temperature difference, with the average uncertainty of 9.7% at a ΔT_{LM} of 3°C, while the lowest uncertainties were observed at a ΔT_{LM} of 13°C, where the average uncertainty is 4.6%.

The test conditions investigated in the present study are outlined in Table 3.1. A single tube diameter (7.75 mm), three mass fluxes (150, 300 and 450 kg m^{-2} s^{-1}), and four saturation temperatures were studied. For each condition, the heat transfer coefficient is measured using four nominal temperature differences between propane and the coolant (4°C, 7°C, 10°C and 13°C). The test matrix consists of 306 data points. Thirty six data points were taken at all saturation temperatures greater than 30°C, while 27 data points were taken at each mass flux case at a saturation temperature of 30°C. Of the 306 data points, 99 were taken at a mass flux of 150 kg m^{-2} s^{-1}, 135 at a mass flux of 300 kg m^{-2} s^{-1}, and 72 at a mass flux of 450 kg m^{-2} s^{-1}. These controlled variations over the entire test matrix provide adequate representation of the influence of each relevant parameter in the data set.

3.4 Results and Discussion

3.4.1 Experimental Trends

Figure 3.1 shows all the measured heat transfer coefficients from the present study. It is clear that increasing the temperature difference between the working fluid and the coolant results in a larger measured condensation heat transfer coefficient. The same trends were observed across all of the mass fluxes in the test matrix. However, two key observations should be noted: first, the impact of ΔT_{LM} on the measured heat transfer coefficient diminishes with increasing ΔT_{LM}, and second, the effect of a changing ΔT_{LM} on the measured heat transfer coefficient is not the same for all saturation temperatures.

The diminishing effect of increasing the ΔT_{LM} can be seen by examining the 75°C saturation temperature results in Figure 3.1. In this case, the measured heat transfer coefficient reaches an approximate maximum as the ΔT_{LM} approaches 14°C. For discussion purposes, the measured heat transfer coefficient at 14°C is considered the "limiting" case for comparison with the other ΔT_{LM} results. The decrease in the heat transfer coefficient from the 14°C "limiting" case to the 4°C ΔT_{LM} case was approximately 24%, while the decrease in heat transfer coefficient from the 14°C "limiting" case to the 8°C ΔT_{LM} case was approximately 10%, and for the 11°C ΔT_{LM} case, it was approximately 4%. Thus, the influence of ΔT_{LM} on the heat transfer coefficient is not linear. This can be seen more clearly in Figure 3.2, where the heat transfer coefficients for the 150 kg m^{-2} s^{-1} mass flux and for a single quality of 0.30 are plotted as a function of temperature difference.

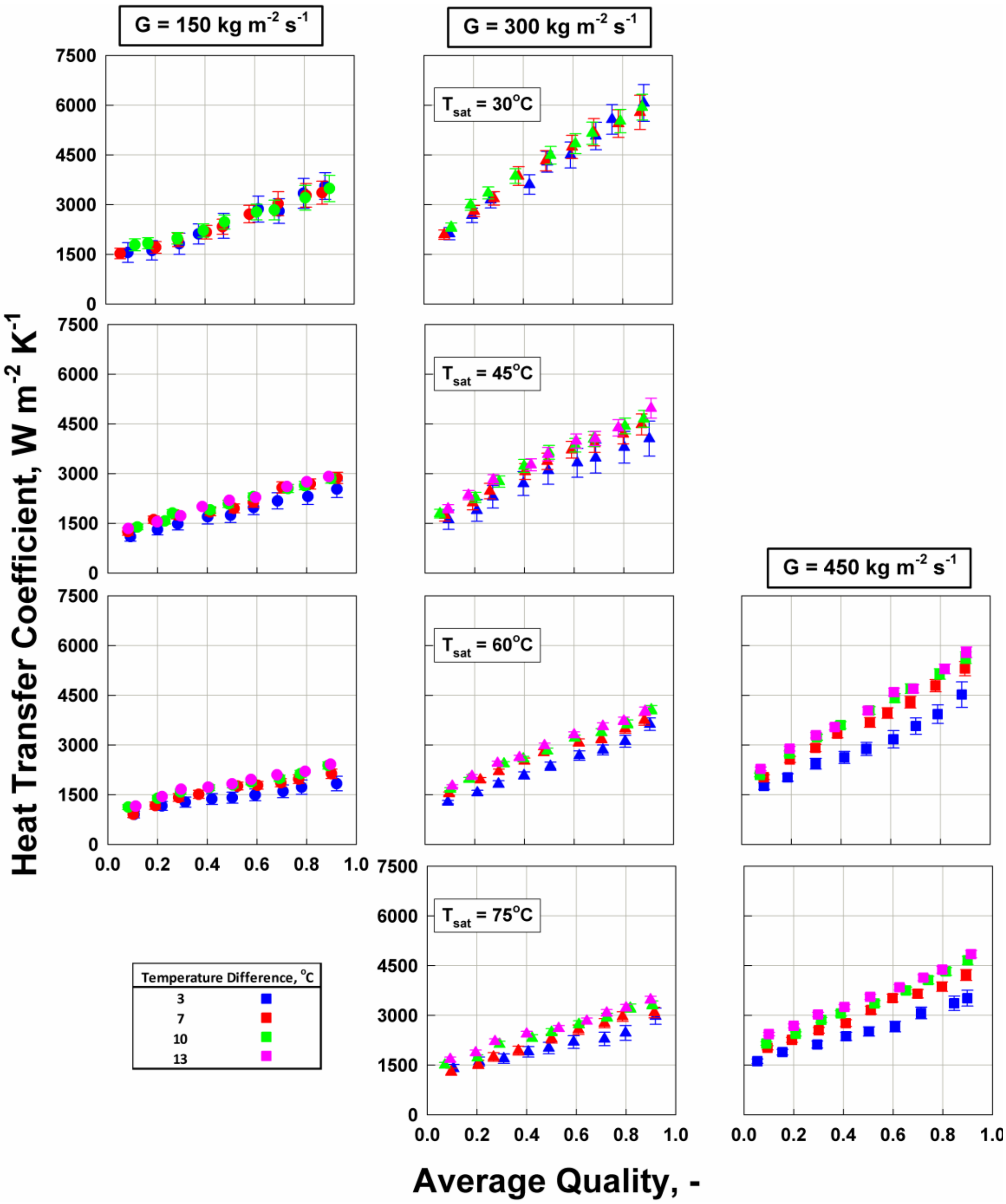

Figure 3.1: Measured heat transfer coefficients for all of the test conditions

Figures 3.1 and 3.2 also show that the effect of increasing ΔT_{LM} on the measured heat transfer coefficient scales with saturation temperature. The results show that there is a greater effect of ΔT_{LM} on the heat transfer coefficient at higher saturation temperatures than at lower saturation temperatures. This effect can be observed by noting that there is a

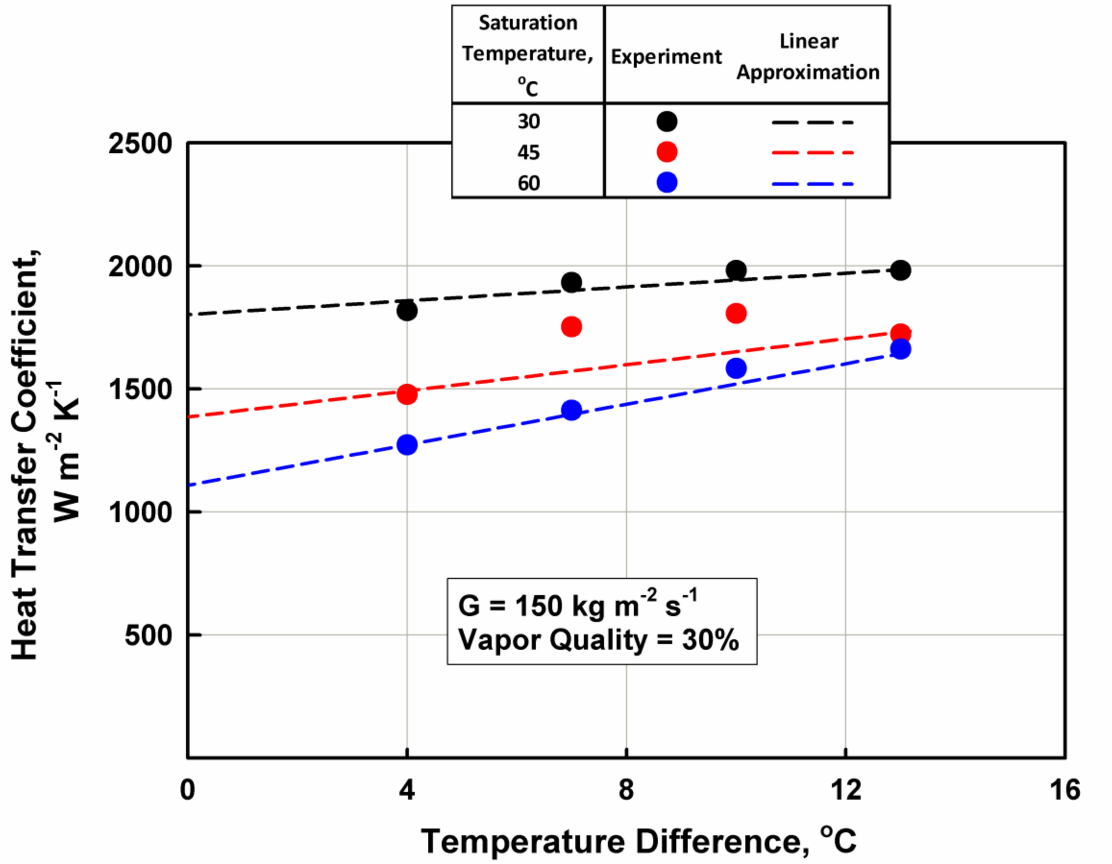

Figure 3.2: **Slope of heat transfer coefficients with increasing working fluid-to-coolant temperature difference**

greater spread in the heat transfer coefficients in Figure 3.1 and that the slopes of the linear curve-fits in Figure 3.2 increase with saturation temperature. For example, the 30°C saturation temperature has a narrow spread and an almost horizontal linear curve-fit in Figure 3.2, while the 60°C saturation temperature has a wide spread and large slope for the linear curve-fit. These trends can be explained by examining the effects of subcooling at the w all where the degree of liquid subcooling is dependent on the available liquid inventory at the wall.

3.4.2 Subcooled Condensate

Figure 3.3 shows the initial subcooling of a two-phase flow initially in equilibrium between the vapor and liquid phases, upon entering a section with a wall temperature

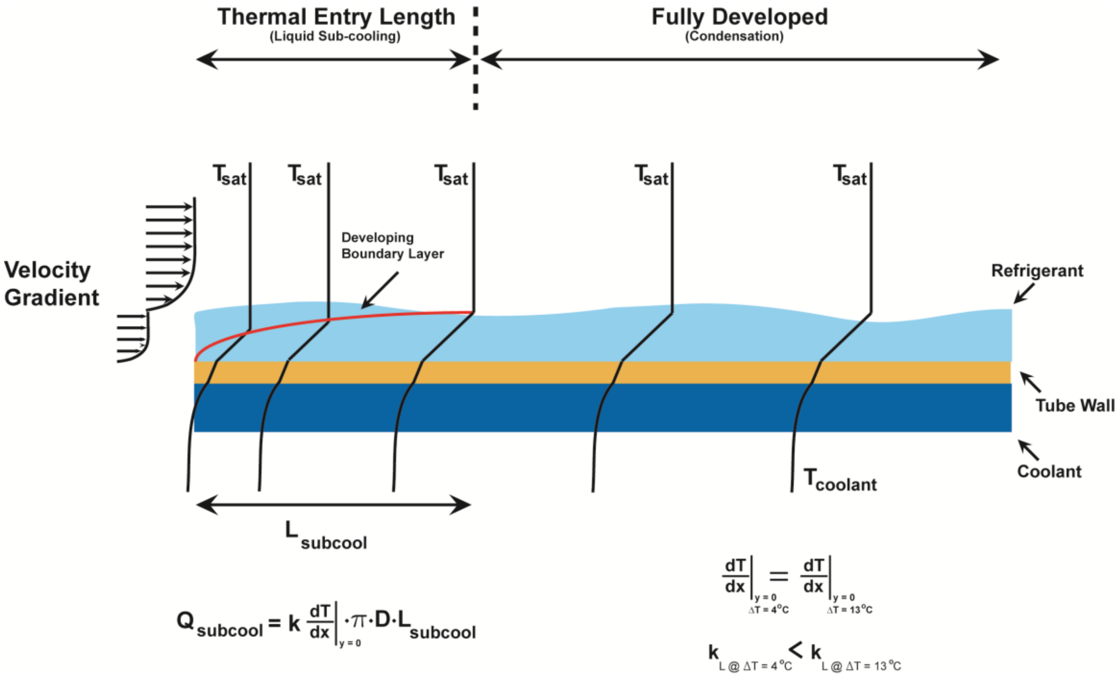

Figure 3.3: Developing temperature profiles and subcooled and phase-change regions

below the saturation temperature over a given thermal entry length, followed by condensation after the temperature wave penetrates through the liquid film and reaches the vapor-liquid interface. Analytically assessing the degree of liquid subcooling during these conditions is difficult due to a lack of available correlations for thermally developing two-phase flows inside tubes. Determining thermal entry lengths for two-phase flow is further complicated by the changing flow regimes and combinations of flow structures that typically occur for a condensing fluid. However, the temperature profiles shown in Figure 3.3 can be used to conceptually explain the trends shown in Figures 3.1 and 3.2. If the heat duty required to subcool the liquid is neglected (during condensation, this quantity is typically small in comparison to the phase change enthalpy), examination of Eq. (3.2) shows that the total heat duty in a given length of tube can be represented using either Newton's Law of Cooling or Fourier's Law. The local heat transfer coefficient is therefore a function of: a) the temperature gradient at the wall, b) the fluid properties at the wall and c) the temperature difference between the bulk fluid and the wall.

$$
\begin{aligned}
q'' &= h \cdot \left(T_{\text{bulk}} - T_{\text{wall}}\right) = k \left.\frac{dT}{dr}\right|_{\text{r}=\text{D}/2} \\
h &= k \left.\frac{dT}{dr}\right|_{\text{r}=\text{D}/2} \Big/ \Delta T
\end{aligned}
\tag{3.2}
$$

The exact profile of temperature gradient will change significantly with changes in quality, mass flux and flow regime; however, the temperature gradient and temperature difference between the bulk fluid and the wall should scale similarly. The thermal conductivity of interest is the liquid thermal conductivity of the fluid, which will be greatest closest to the wall. This can be demonstrated clearly by examination of Figure 3.4, which shows that the liquid thermal conductivity decreases as the saturation temperature increases. Therefore, as the temperature difference between the wall and bulk fluid increases, the liquid film thermal conductivity increases, which promotes heat transfer and leads to the higher measured heat transfer coefficients. A greater temperature difference causes larger decreases in the temperature of the fluid at the wall and therefore greater increases in the liquid thermal conductivity.

Additionally, at higher reduced pressures, the liquid-to-vapor density ratio decreases, which results in larger liquid film thicknesses at a given quality. This is accompanied by greater decreases in the liquid thermal conductivity. Therefore because thicker liquid films of lower thermal conductivity exist at higher saturation temperatures, they are more likely to be affected by the effects of subcooling discussed above. This result can be observed by examining the difference in the measured heat transfer coefficient from the “limiting” case of 14°C for two saturation temperatures. The percent difference in heat

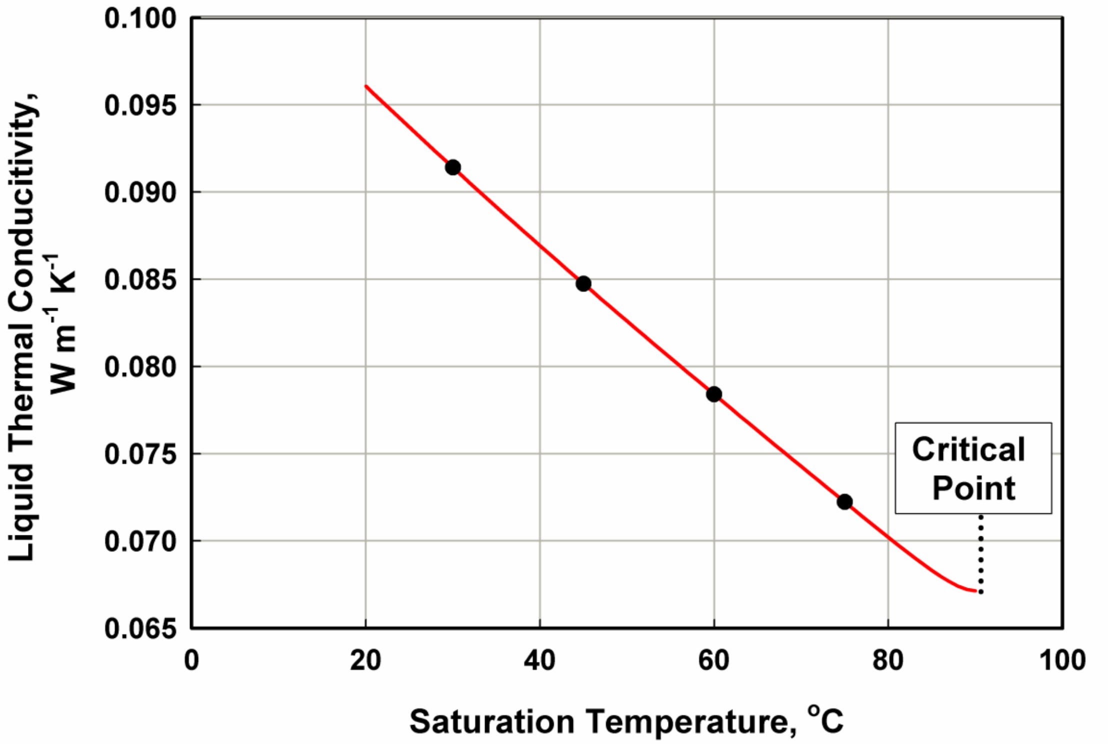

Figure 3.4: Thermal conductivity changes with temperature

transfer coefficient between the 14°C case and the 4°C at 75°C was 24%, while at 45°C it was 16%. This is further confirmed by the absence of changes in the measured heat transfer coefficient at the lowest saturation temperature 30°C for any ΔT_{LM}. It is likely that for the lowest saturation temperature case, the liquid film is too thin and the liquid-phase thermal conductivity is high enough to minimize the condensate film temperature gradients.

It is possible that liquid subcooling causes additional changes to properties of the liquid film that further promote heat transfer, e.g., the viscosity and density. However, the effect of changes in these properties is more difficult to isolate than the effect of the liquid thermal conductivity. Figure 3.1 also shows that mass flux and vapor quality have negligible impact on the trend in heat transfer coefficient with temperature difference, i.e., the same trend exists for all cases shown. Examination of Figure 3.2 shows that the

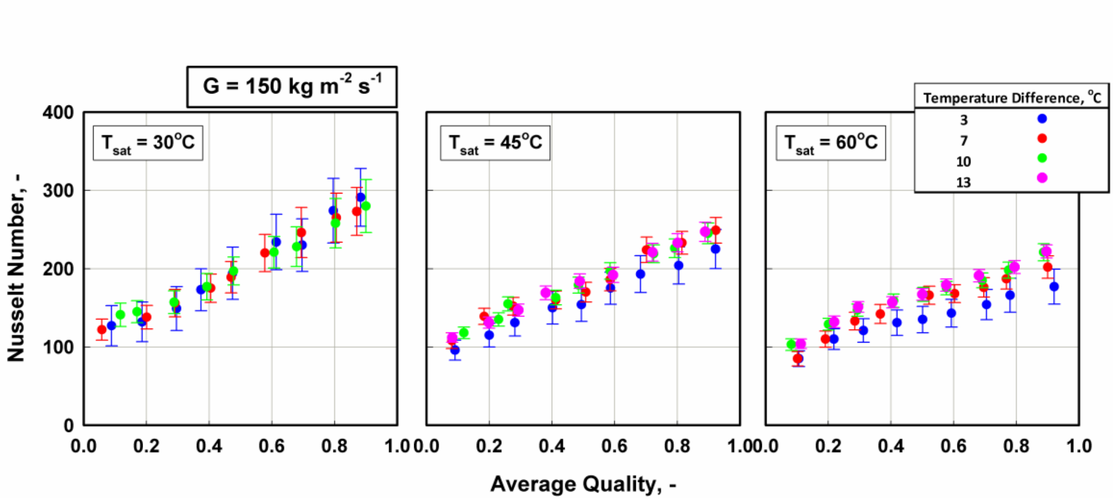

Figure 3.5: Nusselt number based on liquid thermal conductivity at wall temperature

heat transfer coefficient approaches a constant value, the *y*-axis intercept, for a temperature difference very close to 0°C. This represents the case for condensation in the absence of liquid subcooling.

The measured heat transfer coefficients for the 150 kg m^{-2} s^{-1} mass flux and all saturation temperatures from the present study were converted to Nusselt numbers using Eq. (3.3).

$$\mathrm{Nu} = \frac{hD}{k_\mathrm{l}} \quad \rightarrow \quad k_\mathrm{l} = k_\mathrm{l,sat} \quad \text{or} \quad k_\mathrm{l,wall} \tag{3.3}$$

The liquid thermal conductivity used in Eq. (3.3) is the subcooled liquid thermal conductivity determined from the wall temperature at the pressure of the working fluid, and not the saturated liquid thermal conductivity. Therefore, the liquid thermal conductivity used in Eq. (3.3) is different for each experimental ΔT_{LM}. Dividing the measured heat transfer coefficient by the higher (subcooled) thermal conductivity that exists at the wall reduces the Nusselt number more than if the saturated liquid thermal conductivity was used. The results of this operation are shown in Figure 3.5. By conducting this analysis, all of the Nusselt numbers coincide for the 30°C, 45°C and

60°C saturation temperatures, which supports the hypothesis that the changes in the measured heat transfer coefficient are due to changes in the condensate fluid properties. The one discrepancy with this argument is at a ΔT_{LM} of 4°C at the 60°C saturation temperature. These Nusselt numbers are slightly lower than the other LMTDs. However, at these experimental conditions (small temperature differences) the uncertainty in the measured heat transfer coefficient is consistently higher, which is due to the uncertainty of the thermocouples becoming a dominant portion of the uncertainty propagation calculation. For these temperature differences, differences in Nusselt numbers for the different temperature difference cases are within the uncertainty bands, which could be the cause of the slightly larger disagreement at the low temperature difference conditions.

3.4.3 Flow-Regime-Based Interpretation

As noted above, the effect of temperature difference on the rate of heat transfer is similar for all vapor qualities. However, the liquid film characteristics typically change significantly with vapor quality. At higher vapor qualities, there is a lower liquid inventory and a fast moving vapor phase, which typically results in a thin liquid film that is distributed circumferentially, as in annular flow. At lower vapor qualities, the liquid inventory is larger, but the vapor phase velocity is low, with correspondingly smaller shearing forces. At these conditions, a liquid film forms on the upper surface of the tube and flows downwards into a liquid pool. Samples of the high speed flow visualization studies by Milkie (2014) are shown in Figure 3.6a, b & c. They demonstrate that, for the 7 mm tube diameter, the liquid film is highly agitated by the faster moving vapor phase at all vapor qualities. Additionally, in the 7 mm tube, the pressure gradient is sufficient to force the liquid film in the upper section of the tube to move horizontally, similar to

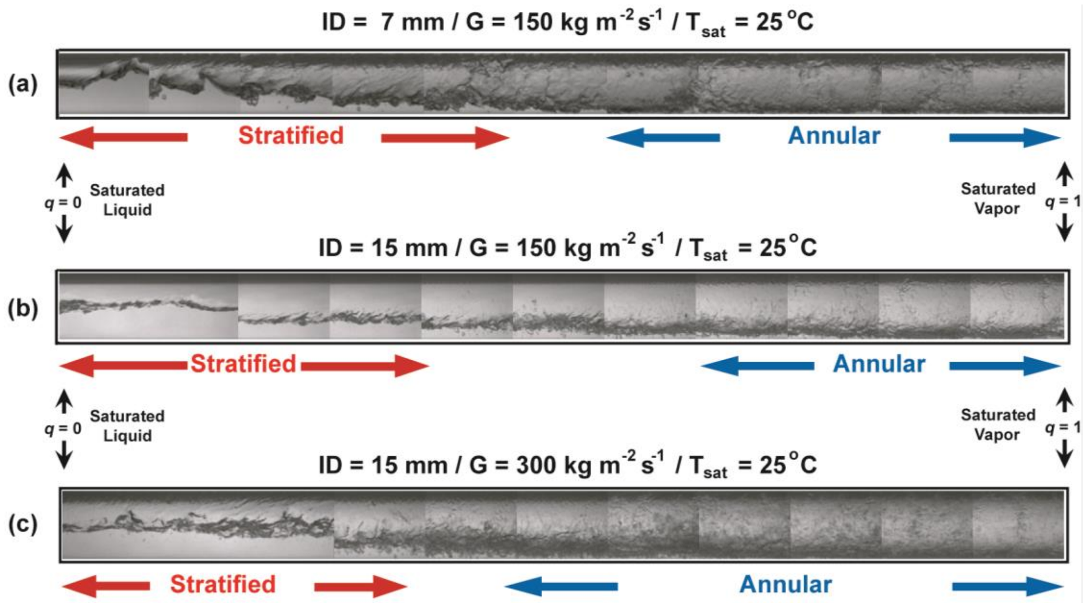

Figure 3.6: Flow visualization of the two-phase flow inside the 7.75 mm diameter tube

annular flow, and not vertically down as is typically idealized for a wavy flow regime. Therefore, these results suggests that smooth laminar Nusselt film condensation is not present at any stage of the condensation process for the conditions investigated in the present study, and the corresponding trends predicted by a Nusselt film model are not applicable. Moreover, the conditions in Figure 3.6a represent a lower bound of the experimental conditions investigated in the present study, i.e., they are at the lowest mass flux and a lower saturation temperature than investigated here. Thus, those cases have a lower liquid inventory at all vapor qualities. Therefore, the flow conditions displayed in this set of images are expected to be closer to the Nusselt film conditions than any of the conditions investigated in the present study; and if Nusselt (1916) film condensation does not occur for these conditions, it is unlikely to exist for any of the conditions in the present study.

Two categories of flow regimes are typically considered for horizontal flow condensation, e.g., stratified and annular. However, the axial motion of the liquid film in both flow regimes for this tube diameter causes the heat transfer mechanism to be most similar to the annular flow condition. In both the stratified and annular flow regimes, the major portion of the heat transfer takes place through the liquid films, i.e., the upper liquid film in the stratified regime and circumferential liquid film in annular regime. Thus, if the structural characteristics of the film are similar for low and high vapor qualities, the trend with temperature difference should be the same at all qualities. Milkie (2014) also conducted flow visualization studies for a larger tube diameter, 15 mm, shown in Figure 3.6b and c. At the low mass flux, 150 kg m^{-2} s^{-1}, the frictional pressure gradient in the 15 mm diameter tube is not large enough to cause distinct disturbances in the upper film, or to induce significant axial motion. Thus, these conditions more closely resemble smooth laminar condensation, i.e., the liquid film is smooth and falls vertically. Higher mass fluxes have a much larger pressure gradient, which produces similar flow characteristics as the 7 mm tube. Therefore, it is expected that the trends observed in the present study could exist for some of the conditions in the larger diameter tube. Additionally, smaller diameter tubes have greater pressure gradients, which should cause a higher fraction of liquid to be pushed into the upper film and induce axial motion. In this case, the conditions will even more closely resemble intermittent/annular flow. However, the larger curvature in small tubes dampens the interfacial waves and could produce a smoother film. The discussion above illustrates that applying the results of the present study to conditions beyond the experimental database should be accompanied by an understanding of the expected flow characteristics of the liquid film inside the tube.

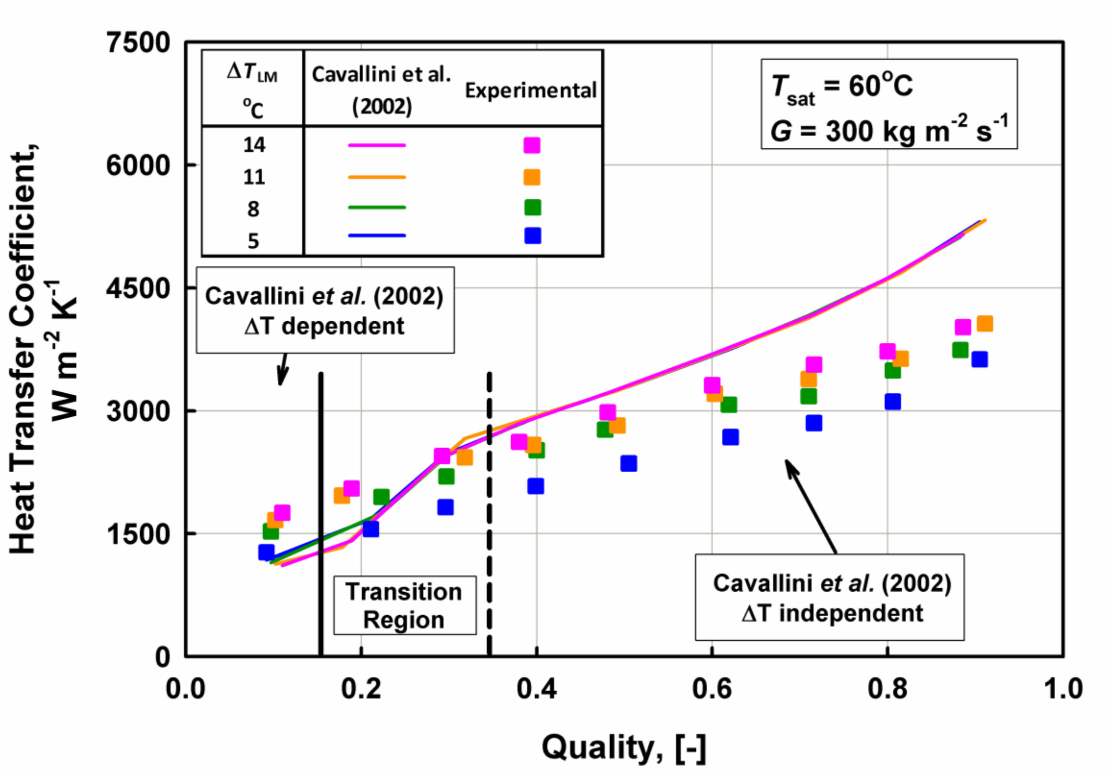

Figure 3.7: **Cavallini *et al.* (2002) correlation compared to the measured heat transfer coefficients**

3.4.4 Modeling the Effect of Temperature Difference

The most widely used correlations for predicting the condensation heat transfer coefficient propose using the Nusselt film theory in the stratified regime (Cavallini *et al.*, 2002a), or use a purely empirical approach (Shah, 1979). These correlations either predict a trend with temperature difference opposite to the results of the present study, or do not predict any influence of temperature difference. Figure 3.7 shows the measured heat transfer coefficients and the predictions using the Cavallini *et al.* (2002a) correlation. This correlation divides the flow into two regimes: stratified (temperature dependent) and annular (temperature independent). In the temperature dependent region, the correlation uses the Nusselt film theory to model the heat transferred through the upper film. Thus, it predicts an inverse dependence on heat transfer coefficient with temperature difference.

This can be observed at the lower vapor quality points in Figure 3.7, where the highest temperature difference cases are predicted to have a slightly lower heat transfer coefficient. This trend is contrary to the heat transfer coefficient measurements from the present study. Moreover, the magnitude of change in heat transfer coefficient with temperature difference predicted by their correlation does not agree with the results from this investigation. Their correlation predicts that an increase in the temperature difference from 3°C to 14°C will decrease the heat transfer coefficient from 1178 W m^{-2} K^{-1} to 1172 W m^{-2} K^{-1}, i.e., a change of -0.5%. The present study shows that at these same conditions, the heat transfer coefficient increases from 1271 W m^{-2} K^{-1} to 1755 W m^{-2} K^{-1}, a change of +27%.

Additionally, the results of the present study demonstrate that the temperature difference has an effect at all vapor qualities, while the Cavallini *et al.* (2002a) correlation predicts a convergence of the heat transfer coefficient at different temperature differences at higher vapor qualities. This trend is also seen in other commonly used correlations (Cavallini *et al.*, 2006; Dobson and Chato, 1998; Thome *et al.*, 2003).

Based on the above discussion of the results from the present study as well as the lack of agreement with the predictions of the correlations in the literature, a correlation is developed here that can be applied as a correction to the available heat transfer coefficient models. The general form of the equation is shown in Eq.(3.4); it is a ratio of the liquid thermal conductivities at the saturation temperature of the two-phase fluid and at the subcooled wall temperature, and the reduced pressure. The reduced pressure is included to adjust the scaling slightly at higher pressures where the effect of the temperature difference was most extreme. A regression analysis was conducted to

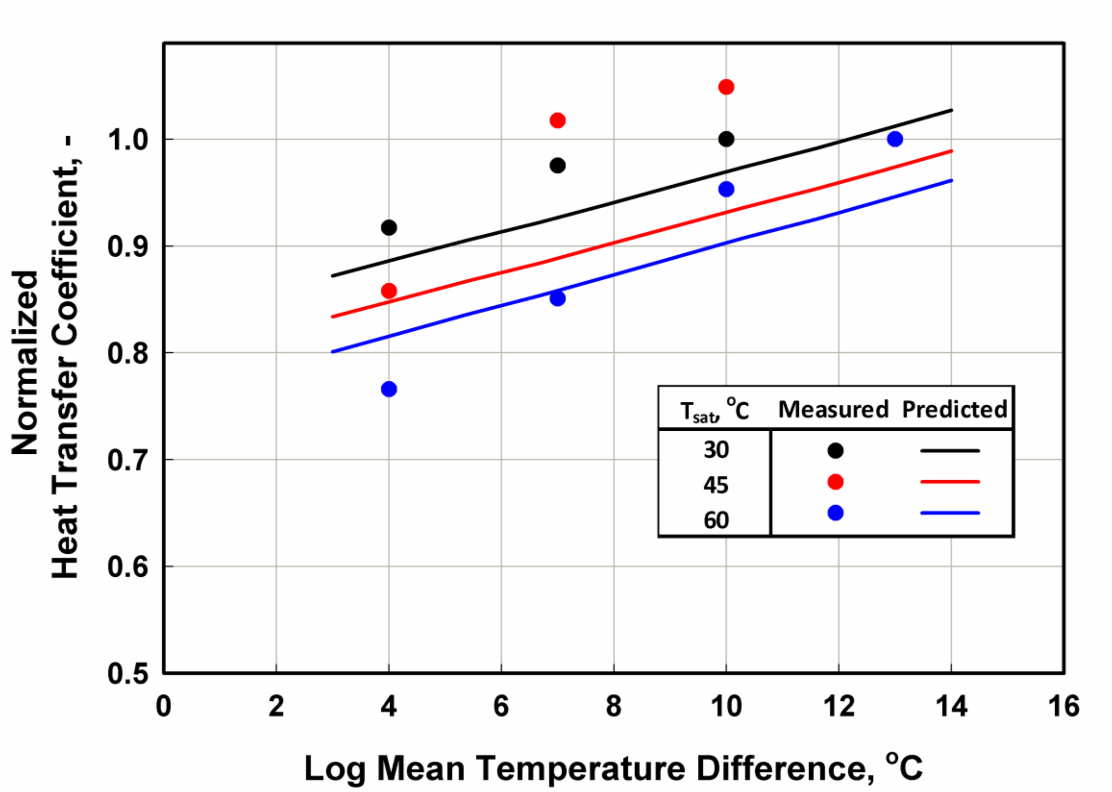

Figure 3.8: Comparison of the proposed correlation and the observed trends

determine the values for the exponents in Eq. (3.4), i.e., 2, 0.3 and 0.1. The correlation correctly predicts the trends observed in the present study. The model assumes that the predicted heat transfer coefficient is a maximum value, with the correction decreasing the heat transfer coefficient to the appropriate value for smaller temperature differences.

$$\chi_{\mathrm{LM}} = \left(\left(\frac{k_{\mathrm{l,wall\text{ - }subcool}}}{k_{\mathrm{l,sat}}} \right)^{2} - 0.3 \right) \cdot \frac{1}{P_{\mathrm{red}}^{\;0.1}} \tag{3.4}$$

Figure 3.8 shows some representative predictions of the model for propane at three saturation temperatures. To facilitate an appropriate comparison between the trends of the correlation and the experimental results, the measured heat transfer coefficients are normalized with the measured heat transfer coefficient at the maximum temperature difference, i.e., ΔT_{LM} = 14°C. The correlation correctly predicts a decrease in heat transfer coefficient at smaller temperature differences, and for higher saturation

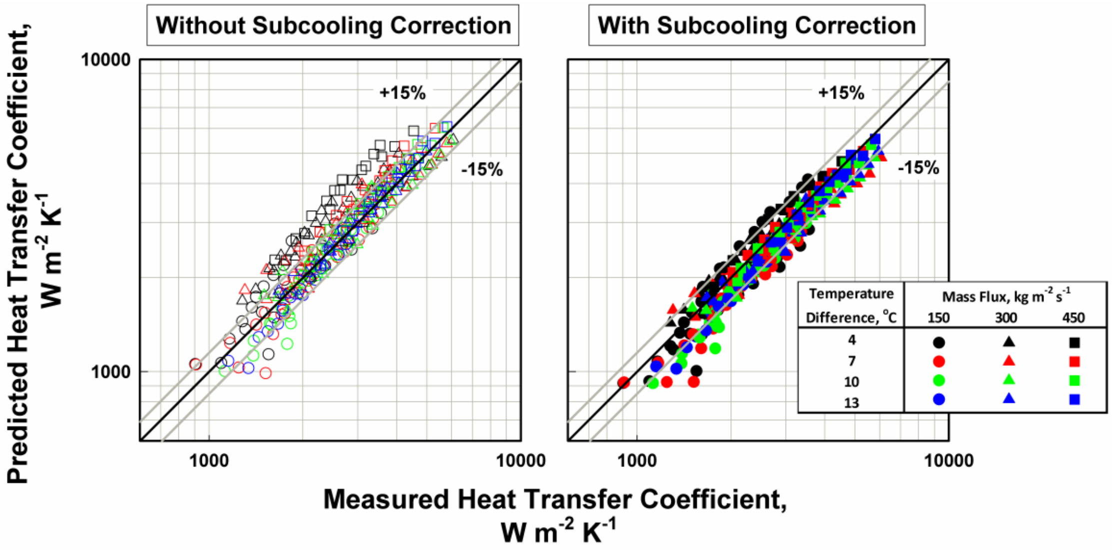

Figure 3.9: Demonstration of improved predictions possible using the subcooling correlation with Thome *et al.* (2003) correlation

pressures. The subcooling correction factor correlation does not approach a maximum value at the higher temperature differences, as was observed in the experiments; instead it continually increases with temperature difference. Refrigeration cycles and several chemical processing operations typically operate at low temperature differences (below 10°C). Therefore, this correlation is developed to adjust existing correlations for smaller temperature differences. As such, it is recommended that the correlation only be applied to temperature differences below 14°C to avoid predictions of unrealistic increases in the condensation heat transfer coefficient with temperatures above 14°C.

The correlation presented in Eq. (3.4) is used with the correlation for condensation heat transfer coefficient developed by Thome *et al.* (2003) to determine the improvements due to the proposed model. Figure 3.9 shows the average deviations with and without Eq. (3.4) applied. The correlation predicts the measured data well at the largest temperature difference, while the smaller temperature differences have greater deviations and are generally over predicted by the correlation.

Table 3.2. Proposed models improvements in predicted heat transfer coefficient

	Thome *et al.*	
ΔT_{LM}	**Unadjusted**	**Adjusted**
	AAD	
4°C	23.5	11.3
7°C	12.0	10.2
10°C	8.5	10.3
13°C	4.4	5.8

Table 3.2 shows the absolute average deviations (AADs) between the adjusted and unadjusted heat transfer coefficients for the Thome *et al.* (2003) correlation and all of the temperature differences investigated in the present study. The definition of absolute average deviation is shown in Eq. (2.7). Applying the proposed correlation can reduce the error for the Thome *et al.* (2003) correlation from 12.1% to 9.3%. Examination of the breakdown of the deviations at each temperature difference demonstrates that the higher temperature differences are well predicted by the underlying correlation alone. However, at the lower temperature difference, the Thome *et al.* (2003) correlation has average errors of up to 50%. At a temperature difference of 4°C, the Thome *et al.* (2003) correlation has an AAD of 23.5%. The errors can be reduced to 11.3% by applying the proposed subcooling correction correlation. Thus, the error in predicting the heat transfer coefficient can be more than halved.

3.5 Conclusions

The results of this study highlight the importance of considering the condensing fluid-to-coolant temperature difference during condensation of fluids inside tubes at high reduced pressures. A physical explanation considering temperature gradients in the condensate film was presented. This analysis demonstrated that subcooling of the condensate produces an increase in the thermal conductivity of the condensate that is large enough to account for the increases in heat transfer coefficient shown in the present study. The increase in the heat transfer coefficient with temperature difference is most significant at higher saturation temperatures and is largely unaffected by vapor quality and mass flux.

The Nusselt film theory, which is applicable only to laminar smooth falling-film condensation and often used as a building block for condensing flow heat transfer correlations, incorrectly predicts the trend with temperature difference for the conditions investigated. A comparison with the literature demonstrated that no correlations combine a high degree of accuracy in predicting the heat transfer coefficients for mid-/high reduced pressure conditions with the correct trend with temperature difference. A correlation that can be applied to existing correlations to correct for the effect of temperature difference on the condensation heat transfer coefficients is proposed here. Application of this model to the Thome *et al.* (2003) correlation for condensation heat transfer coefficients demonstrated that the deviations between the measured and predicted values could be significantly improved. The largest improvement occurred at the smallest temperature difference, where the error was halved. Further investigations of the temperature difference effect on tube diameter should be conducted to clarify whether a similar trend exists for other tube diameters and flow regimes.

CHAPTER 4 PURE FLUID MODEL DEVELOPMENT

4.1 Introduction

In this chapter attention turns to the development of heat transfer and pressure drop models based on the data reported and discussed in Chapter 2. In the past fifty years, many correlations for frictional pressure drop and condensation heat transfer coefficients have been proposed by investigators for flow inside tubes. Typically, the starting point for the most successful models is a study of the governing flow regimes, which guide the development of the respective models. Flow regime studies from the literature that are relevant to the present model development are discussed below.

4.2 Prior Work

4.2.1 Flow Regime Studies

Several flow regime studies have been conducted for a variety of fluids, saturation conditions, tube diameters and mass fluxes, e.g., Breber *et al.* (1980), Soliman (1982), Tandon *et al.* (1982), Dobson (1994), Dobson and Chato (1998), Coleman and Garimella (2003) and Milkie (2014). For a horizontal tube, depending on the mass flux, condensation could start as mist flow, which is characterized by liquid droplets entrained throughout the flow by fast moving vapor. As heat is removed and the quality decreases, the vapor fraction decreases, leading to decelerating vapor phase velocities. A circumferential liquid film is formed on the inside of the tube resulting in an annular flow regime, wherein the fast moving vapor is at the center of the tube, and pushes the surrounding liquid film horizontally. As further heat is removed and the quality decreases, the vapor velocity decreases further, thereby reducing the vapor shear on the liquid film. The axially moving circumferential liquid film therefore begins to fall downwards into a liquid pool at the bottom of the tube, resulting in a stratified flow. As quality decreases further, the liquid inventory increases and surface tension forces form vapor bubbles that are surrounded by a liquid film and liquid slugs accumulate on either side of the vapor bubbles, causing intermittent flow. For small tube diameters, sometimes stratified flow is bypassed entirely and a transition from annular flow to intermittent flow occurs.

Flow regime maps developed by Taitel and Dukler (1976), Breber *et al.* (1980), Tandon *et al.* (1982), El Hajal *et al.* (2003) and Nema *et al.* (2014) identify regions where each flow regime exists based on dimensionless numbers. However, some of these maps are complicated to integrate into heat transfer correlations, and would require models to be interpolated across various flow transition criteria. More simplified criteria that identify transition points for the mist, annular, stratified, and intermittent flow regimes have been developed. Soliman (1982) studied the mist-to-annular flow transition, and defined a modified Weber number that models the force balance between the destructive shear forces and the stabilizing surface tension and liquid viscous forces. Several authors have used the modified Froude number by Soliman (1982), which estimates the relative magnitudes of the vapor shear and gravity forces, to define the end of the annular regime and the beginning of the stratified regime. Jaster and Kosky (1976) proposed a constant value for the end of the stratified regime ($Fr = 5$) and the beginning of the annular regime ($Fr = 29$). Soliman (1982) and Dobson (1994) proposed a constant value of seven for the transition from wavy to annular flow. Dobson and Chato (1998) proposed a constant modified Froude number of 20 to be the transition between the wavy and annular flow regimes. Milkie (2014) identified modified Froude numbers of 10 and 20 as the stratified and annular flow regime boundaries, respectively. Tandon *et al.* (1982) and Cavallini *et al.* (2006) proposed using the dimensionless gas velocity defined by Wallis (1969), J_G, to define the boundaries for the stratified ($J_G = 2.0$) and annular ($J_G = 2.5$) regimes.

4.2.2 Pressure Drop Modeling Techniques

The most widely used correlations for two-phase frictional pressure drop use a form of Eq. (4.1) to predict the two-phase pressure drop. The two-phase frictional pressure drop is defined as a multiple, or a fraction, of the single phase pressure drops of the liquid, or vapor, respectively.

$$\left(\frac{dP}{dz}\right)_{\mathrm{TP}} = \phi_{\mathrm{V}}^{2}\left(\frac{dP}{dz}\right)_{\mathrm{V}} = \phi_{\mathrm{L}}^{2}\left(\frac{dP}{dz}\right)_{\mathrm{L}} = \phi_{\mathrm{LO}}^{2}\left(\frac{dP}{dz}\right)_{\mathrm{LO}} \tag{4.1}$$

The equation for the two-phase multiplier, ϕ_{L}, in Eq. (4.2) was first outlined by Chisholm (1967). Equation (4.2) can be used with the definition of the Martinelli parameter to produce the pressure gradient equation shown in Eq. (4.3). Thus, using the Chisholm (1967) two-phase multiplier approach, the individual contributions of the vapor, liquid and vapor-liquid interactions to the total frictional pressure drop can be modeled.

$$\begin{gathered}\phi_{\mathrm{L}}^{2} = 1 + \frac{C}{\mathrm{X}} + \frac{1}{\mathrm{X}^{2}} \\ X = \sqrt{\frac{\left({dP}/{dz}\right)_{\mathrm{L}}}{\left({dP}/{dz}\right)_{\mathrm{V}}}}\end{gathered} \tag{4.2}$$

$$\frac{dP}{dz} = \left(\frac{dP}{dz}\right)_{\mathrm{L}} + C\left[\left(\frac{dP}{dz}\right)_{\mathrm{L}}\left(\frac{dP}{dz}\right)_{\mathrm{V}}\right]^{0.5} + \left(\frac{dP}{dz}\right)_{\mathrm{V}} \tag{4.3}$$

Chisholm and Sutherland (1969) proposed different values for the constant C depending on whether laminar or turbulent flow existed in the liquid and vapor phases. Chisholm (1973) and Friedel (1979a) developed curve-fits for the two-phase multiplier,

ϕ_{LO}^2, in Eq. (4.1). Cavallini *et al.* (2002a) proposed adjustments to the exponents of the Friedel (1979a) model for the annular regime. Müller-Steinhagen and Heck (1986) proposed a correlation that linearly interpolates between the all-vapor and all-liquid frictional pressure drops. Garimella *et al.* (2005) developed a two-regime model for frictional pressure drop in the intermittent and annular flow regimes. Pressure drop in the annular regime is modeled using an interfacial friction factor for the vapor phase, which is a function of the Martinelli parameter, the liquid phase Reynolds number and a dimensionless surface tension parameter. These more physically consistent models have been shown to be accurate at predicting frictional pressure gradients as conditions change; however they could present difficulties in incorporation into design codes.

The early two-phase multiplier correlations are purely empirical, without adequate consideration of the specific flow characteristics during condensation. They therefore perform poorly when applied to conditions outside the conditions for which they were developed. Recent adjustments to the two-phase multiplier models incorporate some flow characteristics inside the tube by proposing a correlation for the constant, *C*, in Eq. (3), that is a function of dimensionless force balances. For example, Mishima and Hibiki (1996), Lee and Lee (2001) and Andresen (2006) all proposed correlations for the constant, *C*, in Eq. (3), that incorporated that relevant forces for their tube diameter range and saturation conditions. These correlations typically capture the magnitudes and trends in the frictional pressure gradient better than the original two-phase multiplier models.

4.2.3 Heat Transfer Modeling Techniques

As noted above, the characteristics of two-phase flow change significantly with changes in conditions, as does the heat transfer coefficient. Heat transfer coefficient models in the literature can be generally classified into two categories: a) single-regime and b) multi-regime models. The single-regime models are typically less accurate when applied across wide ranges of conditions, while the multi-regime models are complex but achieve better accuracy and tend to apply to a wider range of conditions.

Kosky and Staub (1971) proposed calculating the heat transfer coefficient using a shear velocity term that was calculated from the frictional pressure drop and the Martinelli analogy for turbulent momentum and heat transfer. Traviss *et al.* (1973) presented a single regime model that assumed a continuous annular flow regime and used the von Karman universal velocity profile and a momentum and heat transfer analogy to link increases in the frictional pressure drop to increases in the local heat transfer coefficient. Shah (1979) developed a single-regime curve fit correlation applying a two-phase multiplier based on the reduced pressure to the Dittus and Boelter (1930) single-phase liquid correlation. Moser *et al.* (1998) proposed using a heat and momentum analogy to define an equivalent Reynolds number. They suggested that if a condensing flow were replaced with an all-liquid flow with the same wall shear stress, the heat and momentum analogy should predict comparable heat transfer coefficients.

Jaster and Kosky (1976) developed one of the first flow regime dependent models. In the annular regime, they used a turbulent velocity profile approach and the heat and momentum analogy to model the heat transfer coefficient. In the stratified regime, they used a modified Nusselt (1916) falling-film model. Dobson and Chato (1998) divided the flow into either stratified or annular flow; they applied a modified Nusselt falling-film condensation model in the upper portion of the tube and a convective heat transfer model in the liquid pool at the base of the tube, the relative contributions of each mechanism were determined from the stratified film angle. Their annular regime model uses a two-phase multiplier term applied to a single-phase vapor correlation. Guo and Anand (2000) proposed a model that accounted for individual heat transfer mechanisms occurring along each of the walls of a horizontal square channel separately, with the total heat transfer coefficient calculated from an area-averaged summation of the four sides. Cavallini *et al.* (2002a) proposed a combined flow model that incorporated a modified Nusselt falling-film heat transfer correlation with a modified Dittus-Boelter liquid pool convective correlation in the stratified regime and the Kosky and Staub (1971) correlation in the annular regime. Thome *et al.* (2003) developed a regime specific correlation. The stratified regime model was similar to the Dobson and Chato (1998) model, however instead of using the Dittus and Boelter (1930) correlation for the base of the tube, they used their annular flow correlation. The annular flow correlation that they developed modeled heat transfer through an axially moving liquid film using a Dittus and Boelter (1930) type equation. They defined a film Reynolds number using a film thickness that was determined from an ideal annular liquid ring assumption. They proposed additional terms to account for the higher heat transfer rate attributable to interfacial disturbances.

In summary, correlations in the literature account for heat transfer in different flow regimes as follows:

a) Stratified flow: modeled as a vertical falling film with an axially moving liquid pool

b) Annular flow: modeled as a circumferential liquid ring, often correlated by dimensionless numbers

c) Transition region: modeled through interpolation between the stratified and annular flow regime models

The objective of incorporating physical sub-models that reflect the flow characteristics inside the tube during condensation is to ensure the models are broadly applicable. However, the method of using only vertical falling film models in the stratified regime may not be representative of the actual flow phenomena, as demonstrated by the recent flow visualization studies by Milkie (2014). He showed that the flow in the upper regions in the stratified regime is not always a vertical falling film, and that there is a significant axial motion imparted to the upper film that is caused by large pressure gradients that shear the vapor-liquid interface, which becomes increasingly important in smaller tube diameters (if stratified flow prevails), where the pressure gradients increase. Moreover, the vapor shear causes significant agitation and waviness of the liquid film in the upper section of the tube; thus, the film is not always smooth, which is a major assumption of the Nusselt film theory that is often used for the upper film region of the stratified flow models. Furthermore, the basic components of the complex in-tube condensation models are predominantly turbulent flow correlations. The exponents for the Reynolds and Prandtl number in the basic equations are typically curve-fit using a regression analysis to achieve an optimum fit to the experimental database. Therefore, the success of these correlations is closely tied to the range of experimental conditions at which they were developed and validated. Finally, interpolation between flow regimes results in large-scale averaging between flow-regime-specific correlations. This process detracts from the consideration of the underlying phenomena in the transition region and can be a source of error.

The present study addresses the deficiencies in the literature by presenting physically consistent heat transfer and pressure drop correlations that apply continuously across the vapor-liquid dome during condensation; i.e., the correlations do not rely on interpolation between flow regimes. Moreover, these models are validated against the experimental studies from Chapter 2. Additionally, experimental studies with pentane as the working fluid, conducted by Milkie (2014), are used to compare the predictions of the models for low-reduced-pressure hydrocarbon condensation. This expands to range of conditions from which the models are validated from 0.95 to 0.25 (propane alone) to 0.95 to 0.04 (propane and pentane). In these studies, a systematic investigation of the effect of mass fluxes, tube diameters, temperature difference, quality and reduced pressures on the condensation of propane was conducted. Therefore, this database provides equal weight to each operating condition, and the predictions of the proposed models are expected to be equally applicable to all operating conditions.

4.3 Pressure Drop Model

It can be seen from Eq. (4.3) that the total frictional pressure drop of a two-phase fluid may be viewed as a combination of the individual pressure drop contributions of the liquid-phase frictional pressure drop, the vapor-phase frictional pressure drop, and the frictional pressure drop due to the liquid-vapor interactions. Increasing phase interactions that occur at higher mass fluxes and qualities cause greater frictional losses. Decreasing the saturation pressure reduces the vapor density and results in higher vapor-phase velocities, which increase vapor-liquid shearing, and therefore causes greater frictional losses. Thus, the pressure drop increases with increasing mass flux and quality, and for a given fluid, with decreasing saturation pressure. The proposed pressure drop model uses the form of the equation shown in Eq. (4.3); the pressure drops in the liquid and vapor phases are calculated using the equations in Eq. (4.4) and (4.5). The friction factor is calculated from the Churchill (1977 (a)) curve-fit for laminar and turbulent flows using either the vapor or liquid velocities defined in Eq. (4.4) and (4.5) in the calculation of the Reynolds number.

$$\left.\frac{dP}{dz}\right|_{\mathrm{L}} = \frac{1}{2}\frac{f_{\mathrm{L}}\rho_{\mathrm{L}}v_{\mathrm{L}}^{2}}{D_{\mathrm{h}}} \quad \text{where: } v_{\mathrm{L}} = \frac{G\left(1-q\right)}{\rho_{L}} \tag{4.4}$$

$$\left.\frac{dP}{dz}\right|_{\mathrm{V}} = \frac{1}{2}\frac{f_{\mathrm{V}}\rho_{\mathrm{V}}v_{\mathrm{V}}^{2}}{D_{\mathrm{h}}} \quad \text{where: } v_{\mathrm{V}} = \frac{Gq}{\rho_{\mathrm{V}}} \tag{4.5}$$

The constant, *C*, in Eq. (4.3), is correlated as a function of the liquid Reynolds number, the slip ratio between the two phases, and the Bond number, shown in Eq. (4.6). The equations for each variable in Eq. (4.6) are shown in Eq. (4.7). These variables are chosen such that the relative importance of the phase interactions and the ratio of inertial, viscous and surface tension forces on the frictional pressure drop are effectively captured. The values for the constants a, b, c and d are determined using a regression analysis on the propane database and are found to be 20, -0.15, 1.15 and -0.2, respectively. The phase interactions are expected to increase with:

a) lower liquid Reynolds numbers, which occurs at lower saturation pressures and higher quality

b) higher slip ratios, which occur at the extremes of vapor and liquid velocities, e.g. higher qualities and lower saturation pressures

c) lower Bond numbers, lower saturation pressures where surface tension is an important force

$$C = a\,\mathrm{Re}^{b}\,S_{\mathrm{r}}^{\,c}\mathrm{Bo}^{d} \tag{4.6}$$

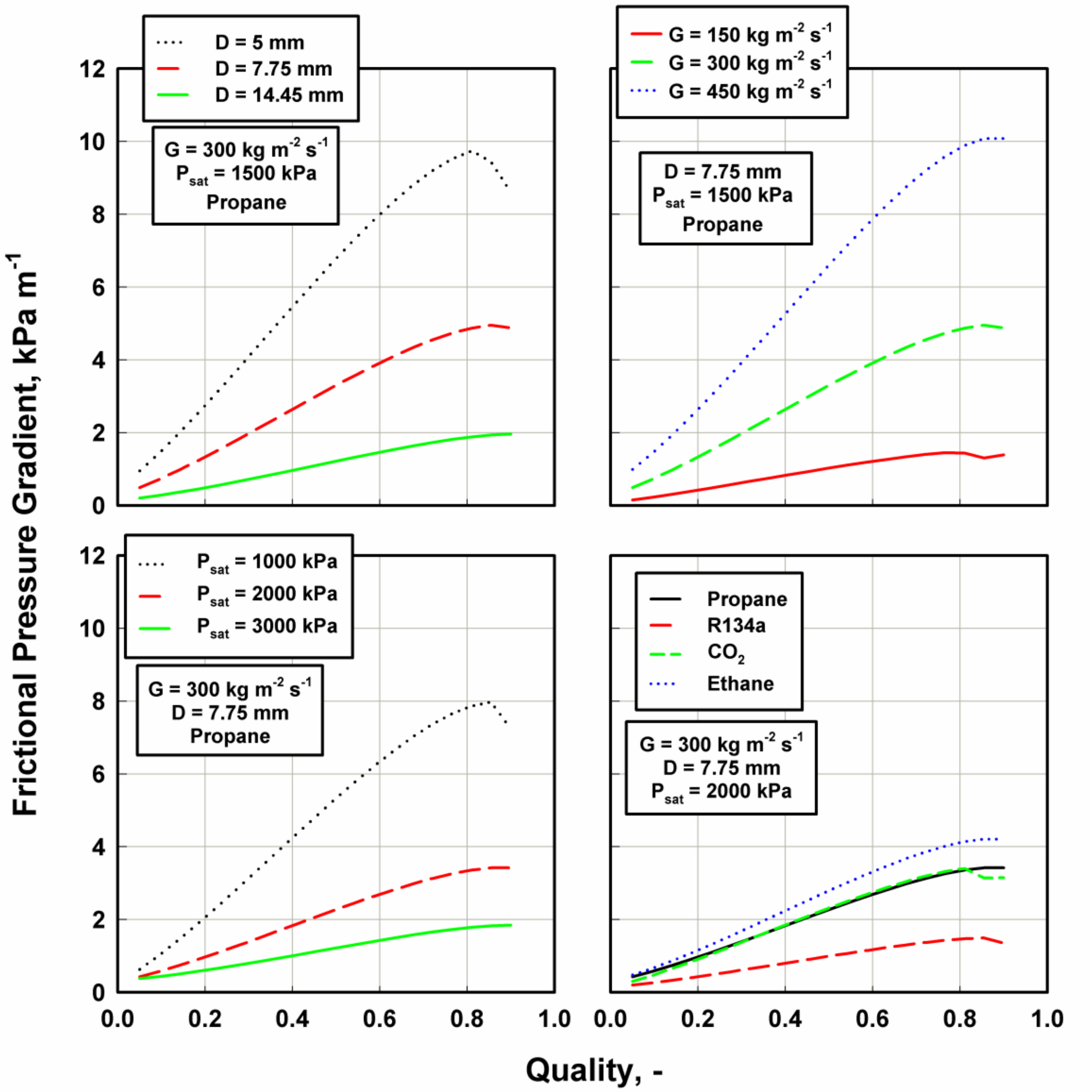

Figure 4.1: Frictional pressure drop model predictions

$$\mathrm{Re}_{\mathrm{L}} = \frac{G(1-q)D_{\mathrm{h}}}{\mu_{\mathrm{L}}}$$

$$S_{\mathrm{r}} = \frac{\rho_{\mathrm{L}}}{\rho_{\mathrm{V}}} \cdot \frac{q}{1-q} \cdot \frac{1-\varepsilon}{\varepsilon} \equiv \frac{u_{\mathrm{V}}}{u_{\mathrm{L}}} \tag{4.7}$$

$$\mathrm{Bo} = \frac{(\rho_{\mathrm{L}} - \rho_{\mathrm{V}}) g D_{\mathrm{h}}^{2}}{\sigma}$$

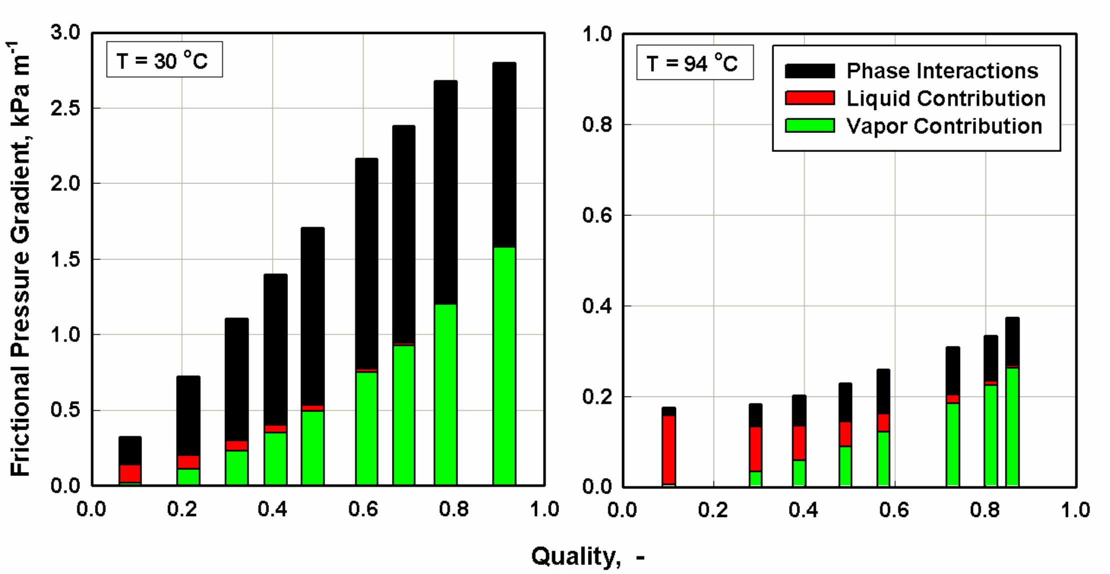

Figure 4.2: **Liquid, vapor and phase interaction contributions to total pressure drop at two saturation temperature**

4.3.1 Pressure Drop Model Predictions

The predictions of the proposed pressure drop correlation are shown in Figure 4.1 for different saturation temperatures, mass fluxes, tube diameters and fluids. The model predictions such as the pressure drop increasing with increasing mass flux and quality, and decreasing with increasing saturation pressure and tube diameter are in agreement with the observed trends. Figure 4.2 demonstrates the individual contributions to the total pressure drop due to the liquid phase, the vapor phase, and the liquid and vapor phase interactions. At low saturation pressures, the liquid occupies a small fraction of the tube cross sectional area due to high liquid densities. This results in a low liquid phase velocity, and therefore minimal pressure drop contributions. Also, the vapor phase has a very high velocity, which results in high slip ratios and large frictional losses. Thus, for these conditions, the contribution of pressure drop in the liquid phase to the total frictional pressure drop is small. Conversely, at high saturation pressures, liquid occupies significant fractions of the cross sectional area due to a significant decrease in density.

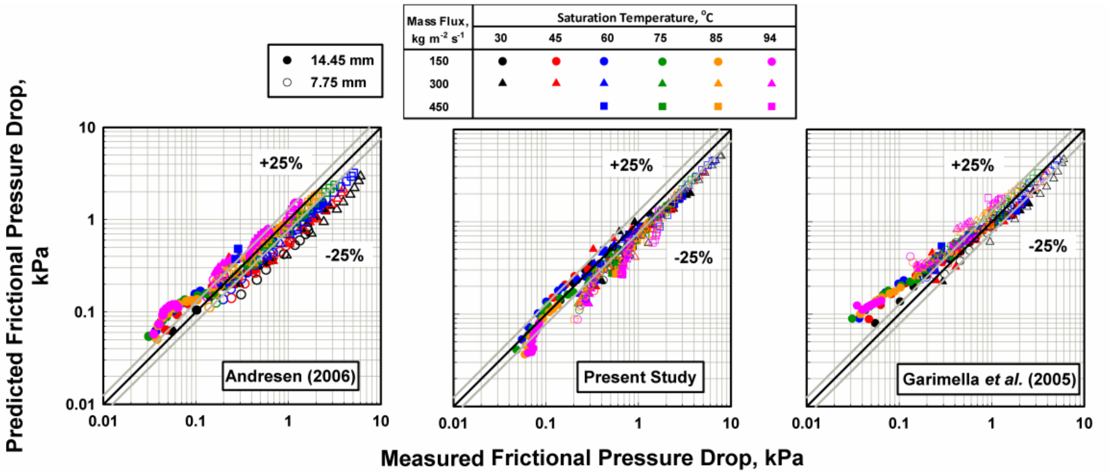

Figure 4.3: Comparison with model predictions – Frictional pressure drop

Moreover, the vapor-phase density increases, which results in a low vapor-phase velocity. At these conditions the frictional losses in the liquid phase contribute significantly to the total frictional pressure drop and the vapor phase contributions decrease. Moreover, the phase interaction contribution to the total frictional pressure drop is greater at lower saturation pressures. The ratio of vapor phase velocity to liquid phase velocity is greater at lower saturation pressures, which causes greater disturbances in the liquid vapor interface and greater frictional losses.

A comparison between the measured frictional pressure drop and existing correlations was reported in Chapter 2. The correlations that predicted the trends closest were the Garimella *et al.* (2005) and the Andresen (2006) correlation, and in Figure 4.3, the predictions of these correlations are shown in comparison to the predictions of the proposed model. These correlations demonstrate the trend that was observed for most correlations from the literature, which is that the frictional pressure drop at high saturation pressures and in the larger tube diameter (*ID* = 14.45 mm) is typically over-predicted. This suggests that conditions where lower pressure drop is expected are

Table 4.1. Proposed Model Predictions Compared to Database – Pressure Drop

		AD	AAD	within ±25%	
Mass Flux, kg m^{-2} s^{-1}	**150**	16.1%	24.0%	63%	**Propane**
	300	-1.5%	16.0%	81%	
	450	-9.6%	14.6%	78%	
Diameter, mm	**7.75**	-8.8%	10.9%	85%	
	14.45	13.7%	25.8%	63%	
Totals		3%	18%	74%	**Propane**
		-11%	14%	85%	**Mixtures**
		-13%	26%	59%	**R410A**
		-21%	22%	57%	**R404A**
		2%	16%	78%	**Pentane**
		3%	16%	84%	**R245fa**

typically over-predicted. With the model proposed here, pressure drops at these conditions are no longer over-predicted.

The average deviations and absolute average deviations, Eq. (2.6) and Eq. (2.7), between the proposed correlation and the condensation database are provided in Table 1. The proposed correlation has an overall AD of 3% and an overall AAD of 18% for the propane data, while the correlations by Andresen (2006) and Garimella *et al.* (2005) have AADs of 29% and 26%, respectively. Thus, the proposed model provides a significant improvement in accuracy over existing correlations; moreover, it more accurately scales the predicted frictional pressure drop with increasing saturation pressure and tube diameter than the existing correlations. Table 4.1 also shows the comparison the proposed model has with previous investigators' condensation data for similar tube diameters, e.g., 6 mm – 19 mm, and a variety of pure fluids and zeotropic mixtures, e.g., pure n-pentane and synthetic refrigerants (R404A, R410A and R245fa) and zeotropic mixtures of ethane and propane. The correlation slightly under-predicts the high pressure refrigerants

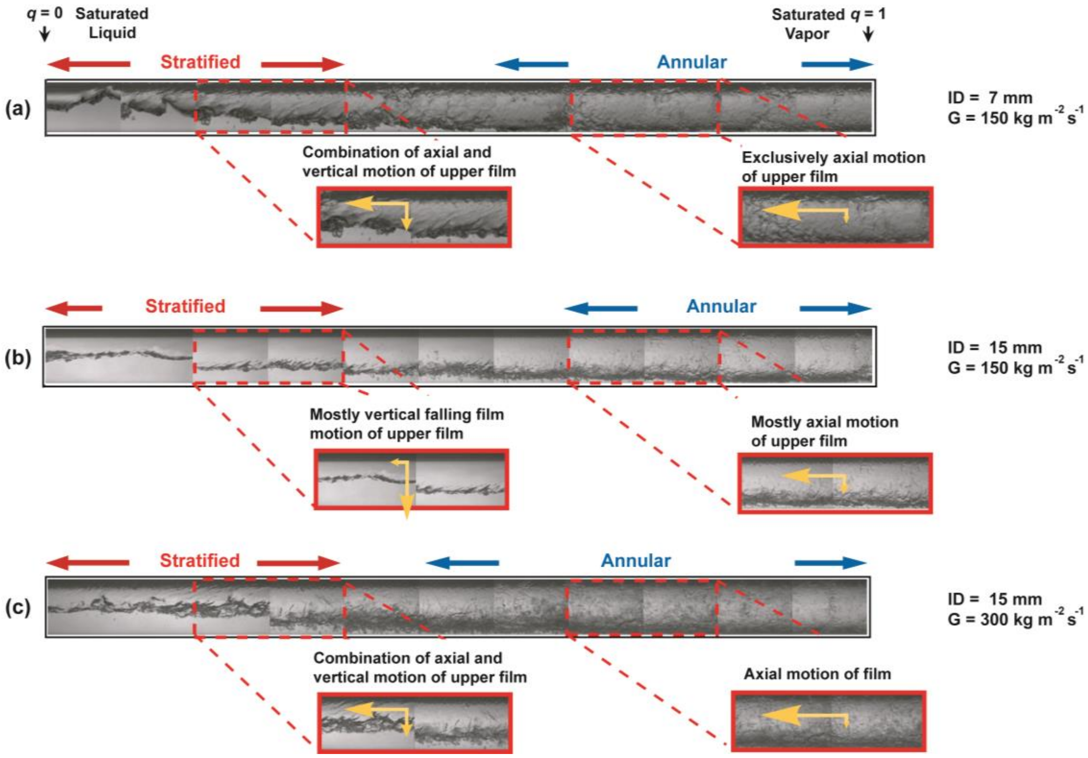

Figure 4.4: **Flow visualization of the two-phase flow showing changes in upper liquid film characteristics with changing tube diameter**

(R410A and R404A), and predicts the lower pressure refrigerants (n-pentane and R245fa) well. Thus, the proposed correlation predicts both high and low reduced pressure data well, with an overall AD of 7% and AAD of 19%.

4.4 Heat Transfer Coefficient Model

The basis for the development of the heat transfer coefficient correlation is the high-speed flow visualization experiments conducted by Milkie (2014) with propane as the working fluid at operating pressures, mass fluxes, and tube diameters similar to the conditions of the heat transfer database. Figure 4.4 shows a selection of the flow visualization images in 10% quality increments. A key focus of the heat transfer model proposed in the present study is to accurately reflect the evolution of the upper liquid film of the tube with changing quality. Therefore, qualitative and quantitative information is extracted from the flow visualization studies and used in the development of the heat transfer coefficient model.

4.4.1 Flow Regime Characteristics

Figure 4.4 shows the flow characteristics of the 7 mm and 15 mm tube diameters for a low saturation temperature (25°C) and two mass fluxes. Two boxes are highlighted, one at a low quality and one at a high quality; the size of the yellow arrows indicates whether the upper condensate film is moving horizontally or vertically. Thus, if a large horizontal arrow and a small vertical arrow are shown, the upper condensate film is moving mostly horizontally. Conversely, if the arrows are of equal size in the horizontal and vertical directions, then the upper film moves with a combination of horizontal (axial) motion and vertical (falling film) motion. The purely horizontal motion and purely vertical motion conditions can be compared to the idealized regime conditions for annular film condensation or for vertical falling-film condensation, respectively.

A series of the images shown in Figure 4.4 is reproduced in Figure 4.5a, while in Figure 4.5b, a graphical explanation of the evolution of the flow of the upper film with increasing quality is shown. The angle of the waves indicates the same phenomena as the yellow arrows in Figure 4.4, i.e., whether the upper film is moving predominantly horizontally or vertically. Figures 4.5c and 4.5d explain the evolution of the vapor and liquid velocities and the corresponding shear stresses each phase exerts on the interface, with changing quality. Condensation begins when liquid forms on the inside surfaces of the tube. At qualities close to saturated vapor, the vapor velocity is high, Figure 4.5c. The high vapor velocity exerts large vapor shear forces on the condensate, Figure 4.5d, which evenly distributes the liquid film around the tube inside surface. Figure 4.5b shows that at

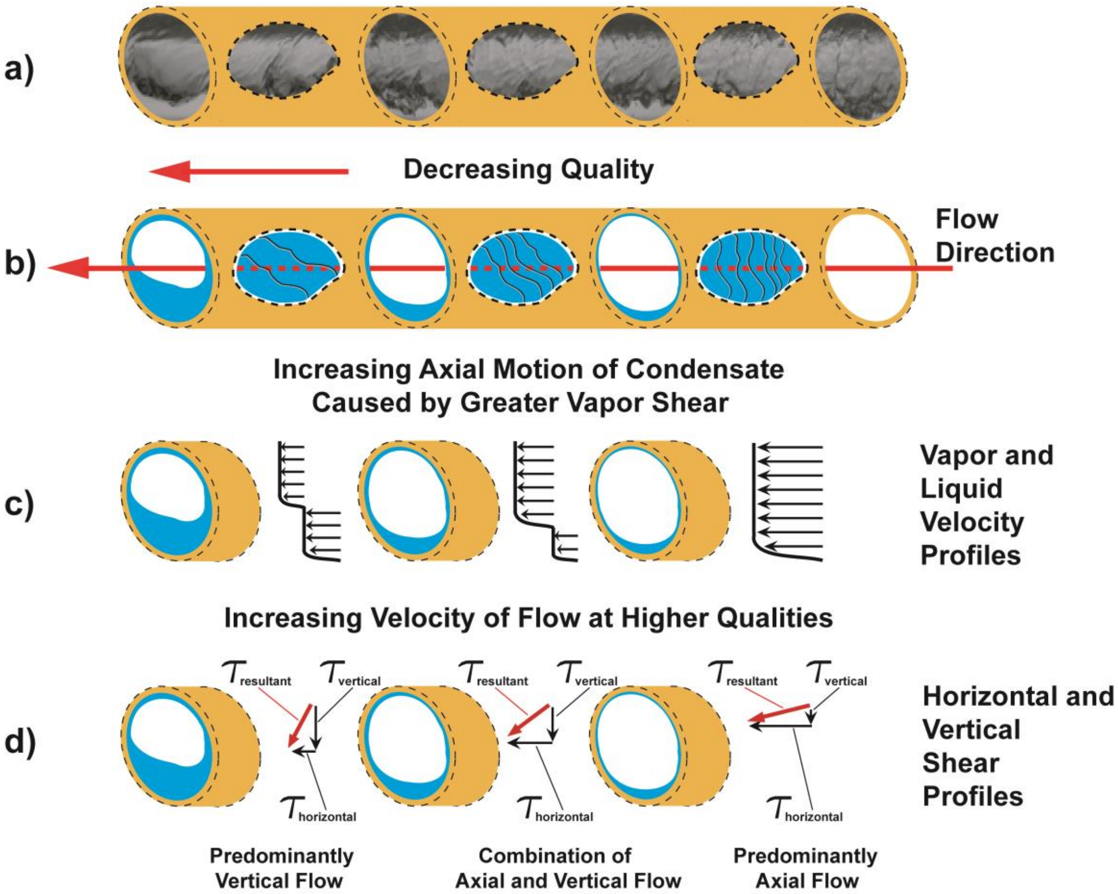

Figure 4.5: Evolution of liquid film direction of motion

these conditions, the motion of the waves is predominantly horizontal, as is the direction of flow of the upper film. As condensation progresses, the vapor velocity decreases and the liquid inventory increases. The reduction in vapor velocity causes a corresponding decrease in vapor shear forces exerted by the vapor on the liquid condensate, which results in the gravitational (vertical) forces becoming increasingly important in dictating the direction of the liquid film, Figure 4.5d. At these conditions, the vertical and horizontal forces are approximately equal and a combination of horizontal and vertical flow ensues. It is clear from the explanation above that the motion of the upper film evolves from purely horizontal to a combination of horizontal and vertical. For the conditions studied by Milkie (2014), the flow was never in a purely vertical falling-film mode.

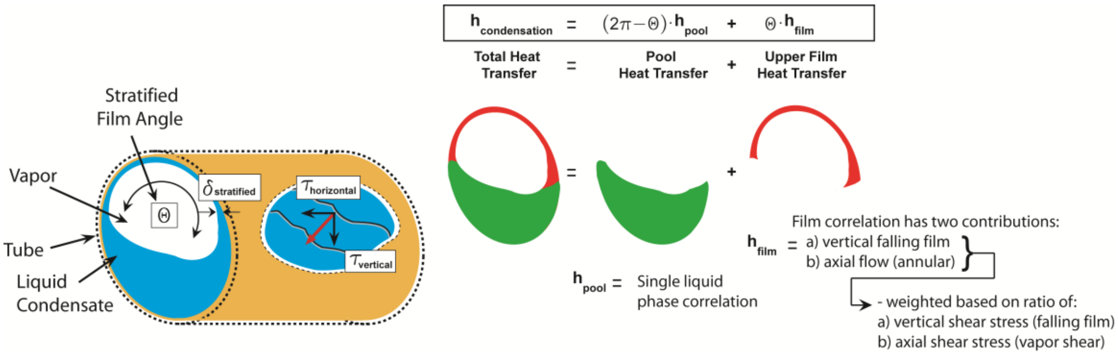

Figure 4.6: Condensation heat transfer model description

4.4.2 Heat Transfer Model

The proposed correlation incorporates these observations by modeling the total condensation heat transfer coefficient as a combination of heat transfer in the upper film, which is a combination of vertical falling film and annular film condensation, and heat transfer in the liquid pool, shown schematically in Figure 4.6. The correlation weighs the falling film and annular film heat transfer contributions to the total film heat transfer based on whether the flow of the upper film is predominantly vertical or horizontal, respectively. The frictional pressure gradient and film thickness are used to determine the contributing horizontal and vertical shear forces, respectively.

The contributions of the upper film heat transfer coefficient and the heat transfer coefficient in the liquid pool to the total condensation heat transfer coefficient are calculated using Eq. (4.8). The exposed tube surface area that is in contact with the upper film and the exposed tube surface area that is in contact with the liquid pool at the base of the tube determine the relative contributions of the two models to the total condensation heat transfer coefficient.

$$h_{\text{condensation}} = \frac{h_{\text{film}}\theta + h_{\text{pool}}\left(2\pi - \theta\right)}{2\pi} \tag{4.8}$$

4.4.3 Liquid Film Heat Transfer Model

The total film heat transfer coefficient is calculated using Eq. (4.9). The contributions of the vertical falling film or the horizontal annular film to the total film heat transfer coefficient are determined using coefficients *A* and *B* in Eq. (4.10).

$$h_{\text{upper film}} = A \cdot h_{\text{falling film}} + B \cdot h_{\text{annular}} \tag{4.9}$$

4.4.3.1Vertical and Horizontal Contributions

Coefficients *A* and *B* are determined from the relative shear stresses of a freely falling liquid film and the frictional pressure gradient. A resultant shear stress term is defined that characterizes the total shear stress of the two-phase fluid; from this, the relative contributions of the vertical or horizontal shear terms to the resultant shear stress can be calculated: the ratios are the coefficients *A* and *B*. Therefore, coefficients *A* and *B* vary between zero and one; if *A* is one, purely vertical falling film flow prevails, while if *B* is one, purely horizontal annular flow prevails. The coefficients *A* and *B* have a direct relationship with measured values. Coefficient *B* is determined directly from the correlated frictional pressure gradient, which was developed specifically for the conditions investigated in Chapter 2. Coefficient *A* is determined directly from the film thickness correlation outlined in Eq. (4.15) below.

$$\begin{aligned}
\tau_{\text{vertical}} &= \Delta\rho g \delta_{\text{stratified}} \\
\tau_{\text{horizontal}} &= \left.\frac{dP}{dz}\right|_{\text{frictional}} \frac{\pi D^2/4}{\pi D} \\
\tau_{\text{resultant}} &= \sqrt{\tau_{\text{vertical}}^2 + \tau_{\text{horizontal}}^2} \\
A = \frac{\tau_{\text{vertical}}}{\tau_{\text{resultant}}} \quad &\& \quad B = \frac{\tau_{\text{horizontal}}}{\tau_{\text{resultant}}}
\end{aligned} \tag{4.10}$$

In a small tube diameter, the frictional pressure gradient is typically large and the liquid inventory is typically low. A large frictional pressure gradient results in a large horizontal shear stress in Eq. (4.10). The vertical and horizontal shear terms are calculated independently; the vertical shear is calculated directly from the liquid film thickness assuming it is a free falling laminar film. Therefore a low liquid inventory, which typically leads to a thin liquid film inside the tube, results in a small vertical shear stress in Eq. (4.10). Thus, the large horizontal shear stress due to the frictional pressure gradient dominates the resultant shear term, which results in the coefficient *B* being close to one and the coefficient *A* being close to zero, i.e., mostly horizontal annular-*type* flow. Conversely, larger tube diameters typically have smaller frictional pressure gradients and thicker liquid films; therefore for a similar set of operating conditions to the smaller tube diameter, i.e., similar quality, mass flux and saturation pressure, coefficient *A* will be closer to one and coefficient *B* will be closer to zero, for the larger tube diameter. These latter coefficients mean that the flow will be closer to typical stratified flow conditions in a larger diameter tube than in a smaller diameter tube.

It should be noted that the modeling technique developed here facilitates a continual adjustment of the contributions of the falling film and annular flow models to the total film heat transfer model throughout the condensation process. Therefore it inherently models the evolution of the flow inside tubes from stratified to annular flow, without the need for interpolation between regime-specific sub-models.

4.4.3.2Vertical and Axial Film Nusselt Number Correlations

The Nusselt number correlations used to determine the annular and falling-film heat transfer coefficients are shown in Eq. (4.11) and (4.12), respectively. The annular correlation used is similar to the Thome *et al.* (2003) correlation, where the heat transfer coefficient due to a horizontal annular film is modeled. Thome *et al.* (2003) used an additional term to account for increased heat transfer rates due to wave disturbances in the liquid film and interfacial roughness, κ_i. The correlation proposed here includes this original term but incorporates an additional term that accounts for an effective reduction in the film thickness due to condensate entrainment, κ_E, which is not accounted for in the Thome *et al.* (2003) equation. This factor is included in the proposed model because the flow visualization studies noted considerable entrainment in the vapor core. The correlation for the falling-film heat transfer coefficient is adapted from a correlation by Edwards *et al.* (1978) for turbulent film heat transfer. The same interfacial roughness term, κ_i, that is used in the annular heat transfer coefficient model is used in the falling film correlation. This term accounts for the same heat transfer enhancements as in the annular model due to film disturbances at the interface between the vapor and liquid condensate. The values of the coefficients in the falling film and annular correlations differ from both of the equations by Thome *et al.* (2003) and Edwards *et al.* (1978); the constants are based on regression fits to the heat transfer database reported in Chapter 2.

$$\begin{aligned}
\mathrm{Nu} &= \frac{\delta_{\mathrm{film}} h_{\mathrm{annular}}}{k_{\mathrm{L}}} = 0.0039 \cdot \mathrm{Re}^{0.775}\, \mathrm{Pr}_{\mathrm{L}}^{0.3} \cdot \kappa_i \cdot \kappa_E \\
\kappa_i &= 1 + \left(\frac{\Delta \rho g \delta_{\mathrm{film}}^2}{\sigma} \right)^{0.1} \left(\frac{u_{\mathrm{V}}}{u_{\mathrm{L}}} \right)^{0.5} \\
\kappa_E &= \left(\frac{\delta_{\mathrm{film}}}{\delta_{\mathrm{effective}}} \right)
\end{aligned} \tag{4.11}$$

$$\begin{aligned}
\mathrm{Nu} &= \frac{l_{\mathrm{FF}} h_{\mathrm{falling\ film}}}{k_{\mathrm{L}}} = 0.2 \cdot \mathrm{Re}^{-0.08}\, \kappa_i \\
l_{\mathrm{FF}} &= \left[\frac{\left(\mu_{\mathrm{L}} / \rho_{\mathrm{L}} \right)^2}{g} \right]^{1/3}
\end{aligned} \tag{4.12}$$

The characteristic length used in the Nusselt number correlation for annular flow, Eq. (4.11), is the thickness of the upper liquid film. The Reynolds number, Eq. (4.13), is based on the upper film thickness, which is also the case in Eq. (4.11) and Eq. (4.12).

$$\mathrm{Re} = \frac{4G(1-q)\delta_{\mathrm{film}}}{(1-\varepsilon)\mu_{\mathrm{L}}} \cdot \xi \tag{4.13}$$

4.4.3.3Liquid Film Thickness

The thickness of the liquid film is an important indicator for predicting heat transfer coefficient trends. Thinner liquid films are expected to present a smaller thermal resistance to heat transfer, and with a pure conduction idealization, greater heat transfer coefficients. For in-tube condensation, interfacial roughness must also be considered in understanding and modeling the heat transfer coefficients.

An ideal film thickness can be determined in the annular flow regime assuming the liquid forms an annular liquid ring that uniformly coats inner surface of the tube, and a correlation for the void fraction, Eq. (4.14). The correlation by Baroczy (1963) for void fraction with the coefficients proposed in Eq. (4.11) and (4.12) is recommended here, and has been shown to be accurate for reduced pressures between 0.38 and 0.77 by Keinath (2012).

$$\delta_{\mathrm{annular}} = \frac{D}{2}\left(1-\sqrt{\varepsilon}\right) \tag{4.14}$$

Determining the film thickness in the stratified regime can be complicated by the poorly understood effects of the frictional pressure gradient on the state of the liquid film. Figure 4.7 shows a schematic explaining the variation in upper film characteristics for the small and large tube diameters considered in the development of this model. The schematics and graphs beside each image show that the quantity of liquid in the pool at the base of the tube is greater in the 15 mm tube diameter. The conditions in the 7.75 mm

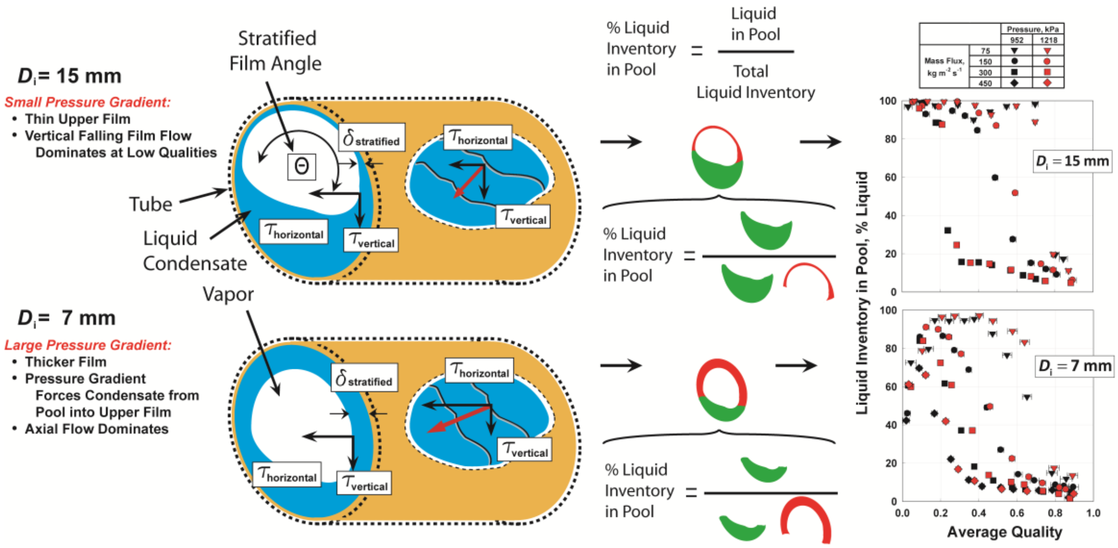

Figure 4.7: Upper liquid film thickness changes with tube diameter

tube are a combination of annular and stratified flows, while in the 14.45 mm tube, the conditions are similar to what is expected in typical stratified flow. Milkie (2014) measured the height of the condensate in the pool at the bottom of the tube for both tube diameters, and demonstrated that the 7.75 mm diameter tube has a greater film thickness-to-diameter ratio than the 14.45 mm diameter tube, which means more liquid inventory exists in the upper film in the 7.75 mm diameter tube than in the 14.45 mm diameter tube. The larger frictional pressure gradients in the smaller tube diameter (7.75 mm) force the liquid that typically pools at the base of the tube along the tube walls and into the upper liquid film. The smaller frictional pressure gradients in the 14.45 mm tube are not strong enough to force liquid from the pool into the upper film; therefore, the major portion of the condensate is contained in the pool in the larger diameter tube, and a thin film forms on the inside of the larger tube that falls vertically down into the pool at the base.

The correlation shown in Eq. (4.15) is proposed for the calculation of the fraction of the total liquid inventory contained in the upper film; therefore η represents the fraction of the total liquid inventory that is contained in the upper liquid film. The correlation is developed using the results of Milkie (2014), shown on the right of Figure 4.7. Examination of Eq. (4.15) shows that, at a nominal mass flux condition of 150 kg m^{-2} s^{-1}, a 7 mm diameter tube has a greater fraction of liquid in the upper film than a 15 mm tube diameter, which reflects the observations noted above.

$$\eta = 1 - \left(1 + \left(\mathrm{Fr}_{So}\right)^{2.5}\right)^{-0.05} \tag{4.15}$$

It should be noted that Eq. (4.15) predicts that the fraction of liquid in the upper film is independent of vapor quality, which suggests that the increase in liquid inventory that occurs with decreasing quality is added mostly to the pool at the base of the tube, and that the upper film remains largely unchanged within the stratified regime. Therefore Eq. (4.15) is applied only to the stratified regime; beyond (upstream of) the stratified regime, the fraction of liquid in the pool drops rapidly to annular flow conditions.

The fraction of liquid calculated using Eq. (4.15) is shown as the red area of liquid condensate in the upper film in Figure 4.7. This fraction/area can be used to calculate the upper liquid film thickness using Eq. (4.16) where it is assumed that the liquid condensate is evenly distributed across the upper film surface area. Similar to Eq. (4.8), the upper film surface area is determined using the stratified film angle. For the remainder of this discussion, the film thickness determined from Eq. (4.15) and (4.16) is termed the “stratified film thickness.” Using the stratified film thickness and the film thickness calculated from the ideal annular flow assumption, i.e., the “annular film thickness,” two film thicknesses can be defined for use in Eqs. (4.11) and (4.13).

The film thickness, δ_{film}, uses the stratified film thickness when the Froude number is less than seven and the annular film thickness when the Froude number is greater than seven. The calculation of the vertical shear stress, Eq. (4.8), uses the stratified film thickness at every point. This does not affect the calculations of coefficients *A* and *B* significantly. For Froude numbers greater than seven, the frictional pressure gradients are the dominant shear stress terms in the calculation of the resultant shear stress; therefore, the flow is predominantly horizontal at this point and a decrease in film thickness to the annular film thickness has minimal impact on either the resultant shear stress or the values of coefficients *A* and *B*.

$$\eta\left(1-\varepsilon\right)\frac{\pi D^2}{4}=\frac{\theta}{2\pi}\pi\left(\frac{D^2}{4}-\left[\frac{D}{2}-\delta_{\text{stratified}}\right]^2\right) \tag{4.16}$$

The film Reynolds number in Eq. (4.13) must be defined using the fraction of liquid mass flux that is actually contained in the upper film. Thus, the film Reynolds number must be corrected for the actual fraction of liquid in the upper film using the variable, ξ, which is equal to the fraction of liquid in the upper film, η, for Froude numbers less than seven, or equal to one for all other cases. Finally, to complete the definition of the Reynolds number, an effective void fraction must be defined in the stratified region that represents the void space corresponding to the stratified film thickness. Figure 4.8 shows the void fraction being calculated schematically, as also shown in Eq. (4.17). The stratified void fraction is the void fraction that would exist if the pool at the base of the tube was neglected and the stratified film thickness that coats the upper surface of the tube was extended circumferentially. This is equivalent to defining a void fraction that corresponds to annular flow conditions with a film thickness equal to the stratified film thickness. It is necessary to define this void fraction because the film velocity and Reynolds number here are specific to the liquid film thickness coating the upper surface of the tube. If the original void fraction that is calculated directly from the Baroczy

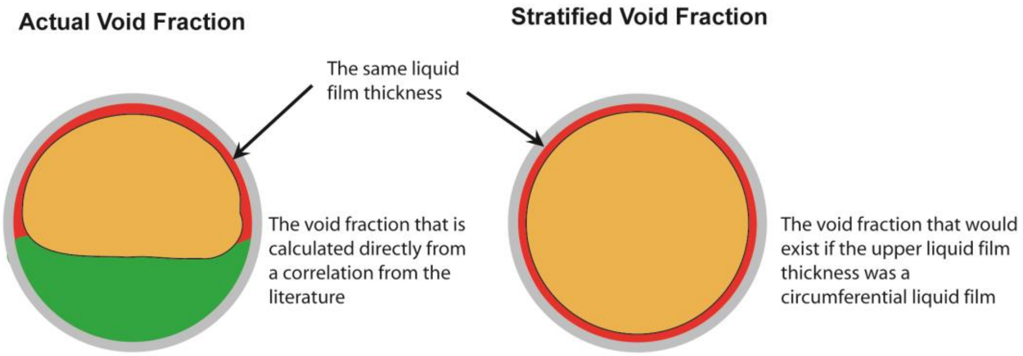

Figure 4.8: Effective void fraction

(1963) correlation was used in each of these calculations, the liquid film velocity and Reynolds number would be under predicted.

$$\varepsilon_{\text{stratified}} = \left(\frac{D/2 - \delta_{\text{stratified}}}{D/2} \right)^2 \tag{4.17}$$

4.4.3.4Vapor and Liquid Phase Velocities

A correction to the liquid film velocity in Eq. (4.18) is made similar to the correction made to the film Reynolds number in Eq. (4.13). The liquid film velocity uses the actual fraction of liquid in the upper film, ξ, and the stratified film void fraction for Froude numbers less than seven. A summary of the conditions for assigning the film thickness, actual liquid fraction and effective void fraction is provided in Table 4.2.

[Insert Table 2 approximately here.]

$$\begin{aligned} u_{\text{L}} &= \frac{G(1-q)}{\rho_{\text{L}}(1-\varepsilon)} \cdot \xi \\ u_{\text{V}} &= \frac{Gq}{\rho_{\text{V}} \varepsilon_{\text{Baroczy}}} \end{aligned} \tag{4.18}$$

4.4.3.5Liquid Entrainment

The factors that determine the quantity of entrained liquid in the vapor core are a result of a force balance between the constraining forces due to surface tension and the radius of curvature of the tube, which impede entrainment, and the frictional pressure

Table 4.2. Summary of conditions in stratified and annular regimes

IF: $\mathrm{Fr}_{\mathrm{So}} \le 7$	IF: $\mathrm{Fr}_{\mathrm{So}} > 7$
$\delta_{\text{film}} = \delta_{\text{stratified}}$	$\delta_{\text{film}} = \delta_{\text{annular}}$
$\delta_{\text{effective}} = \delta_{\text{stratified}}$	$\delta_{\text{effective}} = \delta_{\text{entrain}}$
$\xi = \eta$	$\xi = 1$
$\varepsilon = \varepsilon_{\text{stratified}}$	$\varepsilon = \varepsilon_{\text{Baroczy}}$

gradient, which can shear liquid droplets and promote entrainment. As noted previously, the high-speed flow visualization studies demonstrated that liquid entrainment was greater in the 14.45 mm diameter tube compared to the entrainment in the 7.75 mm diameter tube. The correlation by Govan *et al.* (1989) that provides closure to the rate of entrainment equations outlined in Carey (1992) predicts a similar result. Therefore, droplets are more easily sheared from the condensate film in the larger tube diameter, which leads to a greater effective reduction in liquid inventory on the walls.

The reduction in liquid inventory results in a decrease in the condensate film thickness. As previously noted, a decreasing film thickness can result in a smaller thermal resistance, which results in higher condensation heat transfer coefficients. The model proposed here addresses entrainment by adding a correction factor to account for a reduced effective film thickness of the condensate film, as shown in Eq. (4.19). It should be noted that the rate of entrainment is only significant in the annular regime, where frictional pressure gradients and vapor velocities increase significantly, i.e., Froude numbers greater than seven. Therefore, the effective film thickness used in Eq. (4.11) is equal to the stratified film thickness for Froude numbers less than seven, and equal to the entrained film thickness from Eq. (4.19) for all other conditions.

$$\delta_{\text{entrain}} = \frac{D}{2}\left(1-\sqrt{E\left(1-\varepsilon\right)+\varepsilon}\right) \tag{4.19}$$

The Govan *et al.* (1989) closure equations are coupled and require an iterative solution. Therefore a new entrainment model to simplify the implementation of the heat transfer coefficient model, is proposed here, as shown in Eq. (4.20). This model predicts the trends of the Govan *et al.* (1989) closure equations and allows a direct calculation of the fraction of entrained liquid, *E*.

$$E = 0.0003\left(\frac{u_{\mathrm{V}}}{\sqrt{gD}}\right)^{0.5}\left(\frac{\Delta\rho g D^2}{\sigma}\right)^{0.75} \tag{4.20}$$

4.4.4 Liquid Pool Heat Transfer Model

The Nusselt number correlation for the pool heat transfer coefficient is the Dittus and Boelter (1930) correlation shown in Eq. (4.21).

$$\begin{aligned} Nu &= \frac{h_{\mathrm{pool}}D}{k_{\mathrm{L}}} = 0.023\,\mathrm{Re}_{\mathrm{L}}^{0.8}\,\mathrm{Pr}_{\mathrm{L}}^{0.3} \\ \mathrm{Re}_{\mathrm{L}} &= \frac{G(1-q)D}{\mu_{\mathrm{L}}} \end{aligned} \tag{4.21}$$

4.4.5 Stratified Film Angle

The stratified film angle, θ, used in Eq. (4.8) and (4.16) is calculated using Eq. (4.22) . This equation was originally proposed by Thome *et al.* (2003) and provides a good approximation of the stratified film angle. Moreover, because it is only a function of void fraction, it also eliminates the final series of iterative equations that are typical of the earlier models by Cavallini *et al.* (2002a) and Dobson and Chato (1998).

$$\theta = 2\pi - 2\left[\begin{aligned} &\pi(1-\varepsilon) + \frac{3\pi}{2}\left(1 - 2(1-\varepsilon) + (1-\varepsilon)^{1/3} - \varepsilon^{1/3}\right) \\ &-\frac{1}{200}(1-\varepsilon)\varepsilon\left(1-2(1-\varepsilon)\right)\left(1+4\left((1-\varepsilon)^2+\varepsilon^2\right)\right) \end{aligned}\right] \tag{4.22}$$

Figure 4.9 shows four representative quality points with the corresponding stratified film angles and the upper film thicknesses. The conditions shown in Figure 4.9 show two

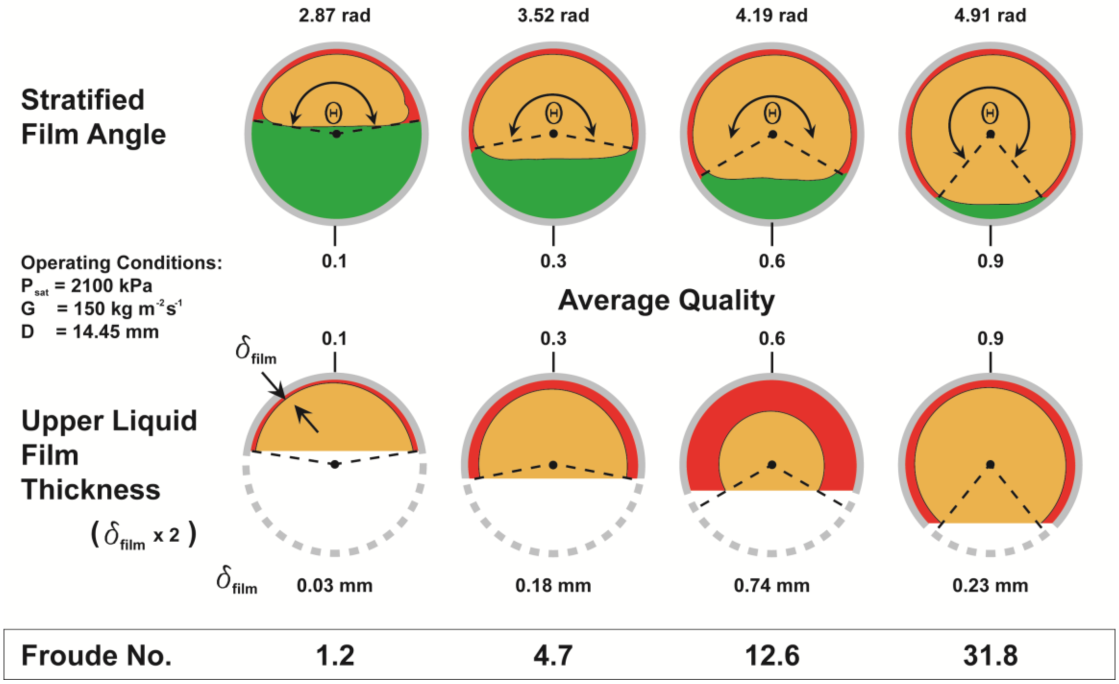

Figure 4.9: Evolution of stratified film angle and liquid film thickness

cases where the Froude number is below seven and two cases where the Froude number is above seven. The angles and film thicknesses shown in Figure 4.9 are the stratified film angles and film thicknesses predicted using the present model. (Film thicknesses shown in Figure 4.9 are amplified to twice their actual values to more clearly demonstrate the changes in the film thickness with increasing quality.) At low quality, a thin liquid film forms on the upper tube wall and the major portion of the liquid is pooled at the base of the tube. At these conditions, the upper liquid film is equally influenced by the vertical and horizontal shear stresses. However, higher qualities have lower liquid inventory, lower vertical shear stresses, and a higher vapor-phase velocity, which results in a corresponding increase in the horizontal vapor shear. At these conditions, the liquid that would be pooled at the base of the tube in stratified flow is forced into a more circumferential annular flow pattern. At upstream locations, where the flow is in more annular-like conditions, the greater horizontal shear forces push the liquid circumferentially, which yields a slightly thicker liquid film. However, further upstream, as the quality increases further towards the saturated vapor state near the inlet, the liquid inventory decreases and film thickness decreases further.

Figure 4.9 shows that the values of the upper liquid film thickness change at each quality throughout the vapor-liquid dome, which should be expected. This is in contrast to the typical method of modeling the evolution of the liquid film using the Nusselt (1916) film model where a constant upper liquid film thickness used in the Nusselt number calculation, with the overall correlation adjusted by an empirical correlation that is a function of void fraction or quality until transition to annular flow occurs.

4.4.6 Temperature Difference Correction Factor

Finally, the heat transfer coefficient was shown to be a function of the temperature difference between the working fluid and the coolant in Chapter 3, where a correction factor that accounts for the increase in heat transfer coefficients that occurs due to liquid sub-cooling at higher reduced pressures was also presented. This factor is shown in Eq. (4.23), and should be applied to the total condensation heat transfer coefficient calculated in Eq. (4.8).

$$\begin{aligned} h_{\text{adjusted}} &= h_{\text{condensation}} \cdot \chi_{\text{LM}} \\ \chi_{\text{LM}} &= \left(\left(\frac{k_{\text{l,wall - subcool}}}{k_{\text{l,sat}}} \right)^2 - 0.3 \right) \cdot \frac{1}{P_{\text{red}}^{\ 0.1}} \end{aligned} \tag{4.23}$$

4.4.7 Heat Transfer Model Predictions

Figure 4.10 shows the predictions of the proposed heat transfer coefficient model for typical operating conditions and different working fluids. The heat transfer coefficient increases at higher mass fluxes and qualities, and decreases at higher saturation pressure,

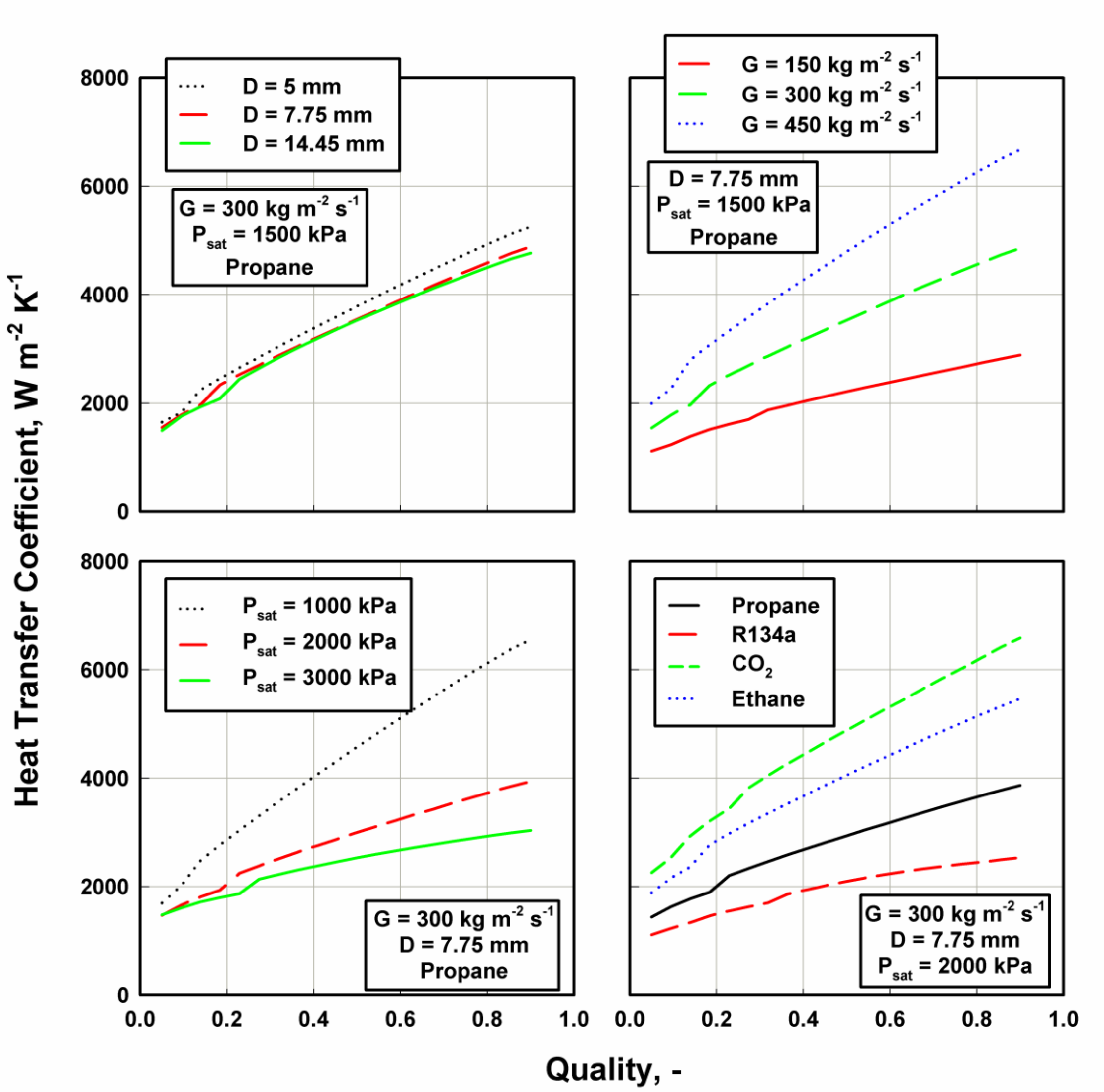

Figure 4.10: Heat transfer coefficient model predictions

as expected. The heat transfer coefficient increases smoothly with quality as it transitions between the stratified and annular flow regimes. There is a slight change in slope for each curve that occurs when the Froude number transitions from below to above seven. As noted above, the present model uses two methods to calculate the upper liquid film thickness, the transition between these two methods causes the slight change in slope shown in Figure 4.10. However, because the upper liquid film thickness is used to calculate the weighting factors, A and B, for the axial and vertical heat transfer coefficients, the change in methodology for calculating the film thickness does not result

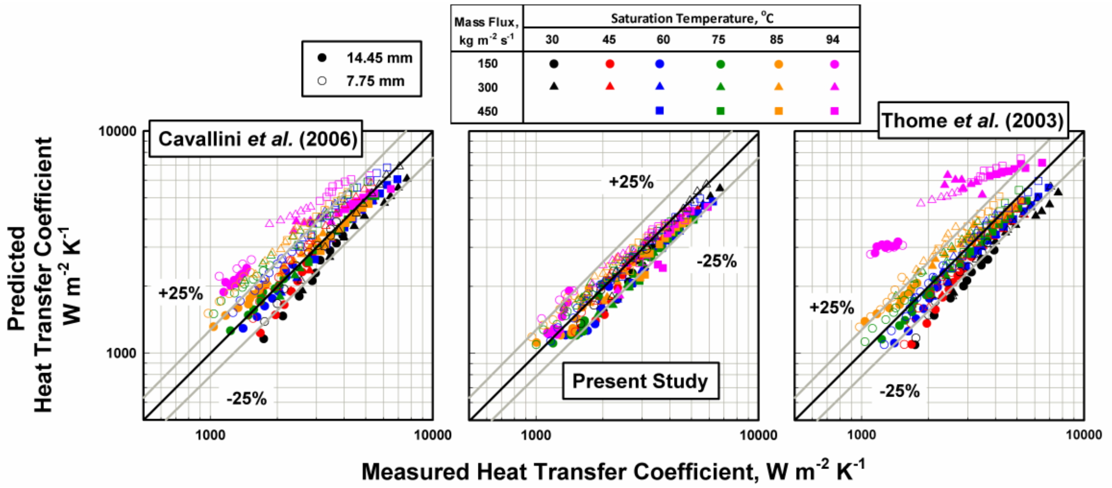

Figure 4.11: Comparison with model predictions – Heat transfer coefficient

in any appreciable changes in the magnitudes of the predictions of the present model. No interpolation was necessary between flow regimes; therefore, the predictions reflect a better representation of the actual variations in flow phenomena with increasing quality.

The interfacial roughness term is greater for the 14.45 mm tube diameter than the 7.75 mm tube diameter; this is due to a greater liquid inventory and reduced influence of surface tension that acts to stabilize the vapor-liquid interface. Additionally, it typically increases with quality as the slip ratio increases, and then subsequently decreases slightly as the film thickness decreases rapidly close to the saturated vapor state. For example, the interfacial roughness increases from a magnitude of 2.46 to 2.65 at a mass flux of 300 kg m^{-2} s^{-1}, an average quality of 0.50 and at a saturation temperature of 60°C for the 7.75 mm and 14.45 mm diameter tubes, respectively. Additionally, the interfacial roughness typically has a maximum close to the 0.50 quality, and decreases with increasing and decreasing quality. For example, at a 300 kg m^{-2} s^{-1} mass flux and 60°C saturation temperature the 7.75 mm tube diameter has a maximum of 2.46 at a quality of 0.66. For the same conditions the interfacial roughness does not change much as the quality increases to a high quality of 0.95 where the interfacial roughness term is 2.40.

Table 4.3. Proposed Model Predictions Compared to Database – Heat Transfer Coefficient

		AD	AAD	within 25%	
Mass Flux, kg m^{-2} s^{-1}	**150**	-0.3%	11.4%	91%	**Propane**
	300	-4.7%	10.6%	99%	
	450	-9.4%	11.3%	93%	
Diameter, mm	**7.75**	4.2%	7.6%	96%	
	14.45	-12.3%	14.3%	93%	
Totals		-4%	11%	95%	**Propane**
		7%	15%	85%	**R410A**
		18%	20%	70%	**R404A**
		42%	43%	32%	**Pentane**
		30%	31%	45%	**R245fa**

Additionally, the interfacial roughness term decreases significantly as quality decreases to reach a minimum of 1.99 at the lowest quality, ~0.05, for the same set of operating conditions.

Figure 4.11 shows the predictions of the present model with the measured heat transfer coefficient from Chapter 2. The clustering close to the 45° line for the majority of the database conditions indicates very good agreement. Slightly larger deviations are observed for reduced pressures greater than 0.95, in particular for the smaller diameter tube results. The measured heat transfer coefficient for these points were taken at much larger test section quality changes, ~40%, compared to other conditions in the database, quality changes ~10%. These conditions may be poorly predicted because the measured heat transfer coefficients have been averaged over too large of a quality range. Thus, the measured heat transfer coefficient for these points may not represent the best resolved

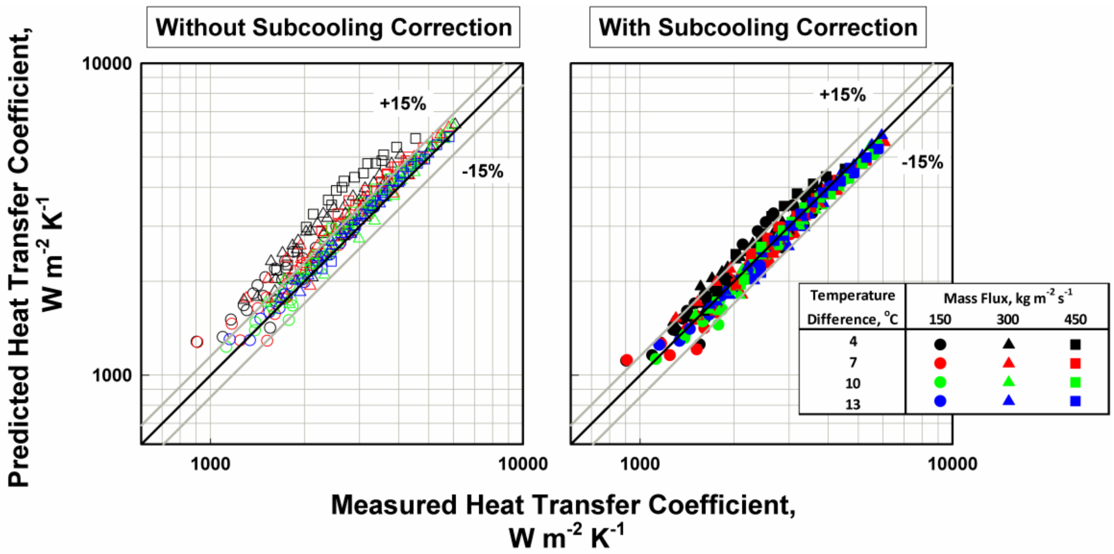

Figure 4.12: Heat transfer coefficient model predictions with subcooling factor

actual heat transfer coefficients. The statistical comparison for the entire database is summarized in Table 4.3.

Because approximately the same amount of data was collected at each operating condition, the accuracy of the proposed correlation across the range of database conditions, e.g., the average absolute deviation (AAD), is equal for all mass fluxes.

In Chapter 2, predictions from the most widely used correlations in the literature were compared to the propane database. The correlations by Cavallini *et al.* (2006) and Thome *et al.* (2003) had the best agreement, with ADs and AADs of 22% and 25% and 20% and 29%, respectively. A comparison of these correlations and the present model is shown in Figure 4.11. The present correlation provides significantly better overall agreement with the measured data and considerably less scatter between operating conditions. Table 4.3 shows that the ADs and AADs are -1% and 12%, respectively. Moreover, the present correlation predicts the higher reduced pressure conditions well, whereas no correlations in the literature consistently predict reduced pressure conditions from 0.25 to 0.95 well. Table 3 shows that the pentane data of Milkie (2014) have slightly poorer predictions; however, the 14.45 mm data are predicted well with an AD of 14%. The pressure drop for pentane in the smaller tube diameter (7.75 mm) is very large, in some cases 50 kPa m^{-1}, while the data for these points are at saturation pressures between 100 kPa and 300 kPa. At these saturation pressures, the change in saturation temperature with pressure is between 0.3°C kPa^{-1} and 0.15°C kPa^{-1}. Therefore with a change in saturation pressure inside the test section of ~50 kPa, the change in saturation pressure is between 15°C and 6.5°C. Thus, there are significant changes in the saturation conditions for these points, which can result in errors when comparing the predictions of the model to the measured data. Moreover, the annular film thickness is sensitive to the void fraction correlation used; the Baroczy (1963) might not be applicable to these low saturation pressure conditions (P_r ~ 0.03).

Applying the subcooling correlation to the propane database developed to investigate the effect of temperature difference can reduce the error of the unadjusted correlation from 13.3% to 5.4%; as shown graphically in Figure 4.12. Examination of the breakdown of the deviations at each temperature difference (shown in Table 4.4) demonstrates that the higher temperature differences are well predicted by the underlying correlations alone. However, at the lower temperature difference, the average errors can be up to 50%. At a temperature difference of 4°C, the unadjusted correlation has an AAD of 27.5%. This error can be reduced to 9.8% by applying the proposed subcooling correction correlation.

4.5 Conclusion

The heat transfer coefficients and pressure drops measured during condensation of propane in smooth horizontal tubes as reported in Chapter 2 and 3 were combined with physical insights from prior flow visualization studies to develop frictional pressure drop and condensing heat transfer coefficient correlations that are valid for tubes with internal diameters between 6 and 19 mm. The pressure drop model accounts for the frictional pressure drops due to vapor and liquid flows as well as the additional frictional pressure drop due to liquid- and vapor- phase interactions. The model scales the individual contributions to the total pressure drop accurately based on changes in the velocities of the phases and the liquid inventory at given conditions inside the tube. A new technique that accurately models the evolution of the direction of flow of the upper liquid film with changes in quality for the prediction of heat transfer coefficients was introduced. The technique ensures a consistent physical representation of the conditions inside the tube throughout the condensation process, without the interpolations between flow regimes typically used by other correlations.

The models were developed for a very wide range of operating conditions for pure natural fluids (propane and pentane), but were also validated with synthetic refrigerant heat transfer and pressure drop data. The models show improved agreement with the frictional pressure drop and heat transfer coefficient measurements in the database when compared to the predictions of the correlations available in the literature.

CHAPTER 5 ZEOTROPIC MIXTURE MEASUREMENTS

5.1 Introduction

Condensation of binary or higher order zeotropic mixtures is affected by two factors that effectively reduce the heat transfer rate in condensers. Firstly, as vapor is converted to liquid, there is a nonlinear shift in the equilibrium phase concentrations. This change in equilibrium phase concentrations causes a change in the equilibrium temperature, which results in a non-constant condensation temperature (temperature glide, i.e., the difference between the bubble point and dew point temperatures.) Thus, the driving temperature ($T_{\text{interface}} - T_{\text{wall}}$) for condensation decreases throughout the condensation process, which reduces the heat transfer rate. Secondly, the components of a zeotropic mixture have different saturation temperatures and mass transfer rates from the vapor phase to the liquid phase. Moreover, the condensation process is a local interfacial phenomenon with the less volatile component condensing more readily than the more volatile component, which results in a concentration gradient in the vapor phase. The concentration gradients in the vapor and liquid phases are often referred to as a non-equilibrium condition. This mass transfer resistance limits the condensation process. Thus, the change in equilibrium condition reduces the overall heat transfer rate and the non-equilibrium condition limits the rate of condensation possible.

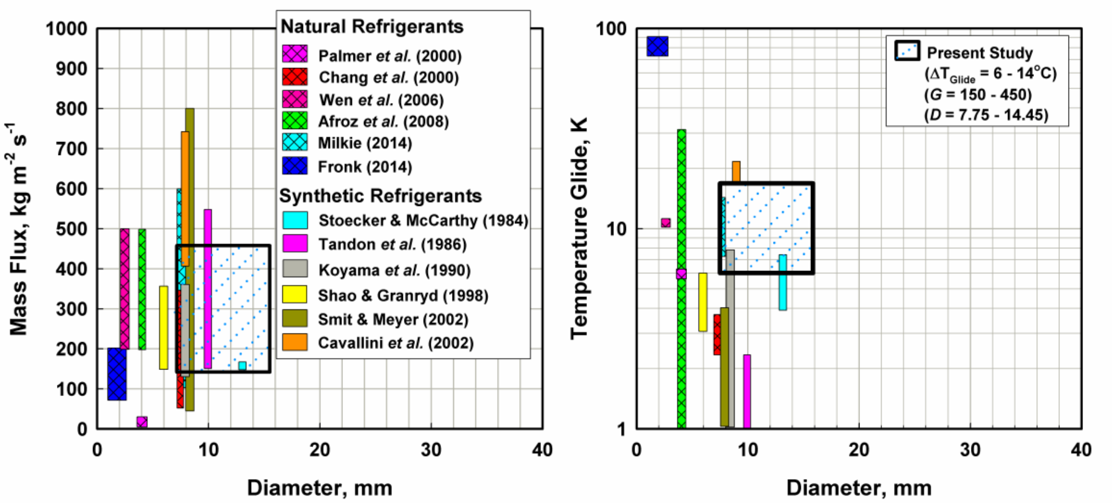

Figure 5.1: Summary of studies in the literature on zeotropic mixtures

The condenser size is highly sensitive to both the temperature difference between the working fluid and the coolant and the heat transfer coefficient. A decrease in either of these parameters results in a greater surface area requirement to achieve condensation of the zeotropic mixture. Thus, knowledge of the development of the equilibrium and non-equilibrium conditions, and whether they are significant considerations during the modeling process is critical in correctly determining the required condenser surface area.

5.2 Prior Work

The non-equilibrium conditions that develop across the tube cross section during condensation experiments can result in inaccuracies in measured heat transfer coefficients. There are few studies on the condensation of zeotropic mixtures in the literature, and fewer still of condensation studies of zeotropic mixtures of hydrocarbons. Figure 5.1 shows a map of the published condensation studies conducted using zeotropic mixtures of synthetic and natural working fluids; they are mapped as a function of tube diameter, mass flux and temperature glide. It is clear from the figure that the majority of these studies are for low temperature glides and are generally conducted using a single tube diameter.

The trends in condensation heat transfer coefficient for zeotropic mixtures generally follow the same trends with mass flux, tube diameter, and vapor quality and saturation pressure as pure fluids. The key difference between zeotropic mixtures and pure fluids is the degree by which the equilibrium and non-equilibrium condition decrease the heat transfer rate. The trends that have been reported by previous investigators are outlined below.

Several authors (Cavallini *et al.*, 2000; Fronk, 2014; Milkie, 2014; Shao and Granryd, 1998; Smit and Meyer, 2002; Wen *et al.*, 2006) have studied the effect of mass flux on heat transfer coefficient. Shao and Granryd (1998) and Smit and Meyer (2002) noted that the condensation rate is affected mostly at low mass fluxes and in the stratified regime. Milkie (2014) noted that similar trends in the heat transfer coefficient are observed for mixtures as for pure fluids with mass flux; however, the overall magnitude of the heat transfer coefficient was appreciably lower. Fronk (2014) conducted condensation experiments on ammonia-water mixtures flowing through small diameter (D_h < 3 mm) channels and at low mass fluxes where laminar flow is expected to dominate. He noted that the heat transfer coefficient can be degraded throughout the condensation process for any design conditions.

The effect of concentration on zeotropic mixture condensation is the most widely investigated parameter by researchers (Afroz *et al.*, 2008; Cavallini *et al.*, 2000; Chang *et al.*, 2000; Fronk, 2014; Koyama *et al.*, 1998; Shao and Granryd, 1998; Stoecker and McCarthy, 1984; Tandon *et al.*, 1986). Koyama *et al.* (1990), Shao and Granryd (1998), Chang *et al.* (2000) and Afroz *et al.* (2008), who have conducted experiments with relatively low temperature glides, e.g., less than 6°C, report that the heat transfer coefficient varies nonlinearly with concentration between the corresponding two pure fluids. The mixture heat transfer coefficient decreases with increasing concentration of one component, reaches a minimum, and then reverses trend with further increases in concentration. Koyama *et al.* (1990) provided an experimental polytropic correlation that models this behavior for mixtures of R22 and R114. Stoecker and McCarthy (1984), Tandon *et al.* (1986), Wen *et al.* (2006), Afroz *et al.* (2008), and Milkie (2014) noted that the heat transfer coefficient for the mixture generally fell between the values for the two pure fluids. Fronk (2014) observed that increasing the concentration of ammonia in water above 0.8 caused degradation in the heat transfer coefficient that was significant enough to cause the heat transfer coefficient to decrease with vapor quality by more than 50%.

While zeotropic mixture concentration can be related to the temperature glide, investigators have typically used fluid concentration as the relevant parameter for assessing the trends in heat transfer coefficient for their chosen fluid combinations. However, the temperature glide is a more informative parameter than concentration for predicting the degree of degradation of the heat transfer coefficient in fluid mixtures, when compared to pure fluid studies. The temperature glide is a more general metric that allows different fluids pairs to be compared. Moreover, the equilibrium modeling technique proposed by Silver (1947) and Bell and Ghaly (1973) predicts that increasing the temperature glide would result in greater mass transfer resistances and therefore a greater degradation in heat transfer coefficient. Inspection of Figure 5.1 shows that the majority of studies have been conducted for relatively low temperature glides, i.e., less than 8°C, with few studies conducted in the mid-temperature glide range (ΔT_{Glide} = 6 - 15°C). Even for low-temperature glides such as those conducted by Stoecker and

McCarthy (1984) ($\Delta T_{\mathrm{Glide}}$ = 3.4 - 7.3°C), Tandon *et al.* (1986) ($\Delta T_{\mathrm{Glide}}$ = 0.4 - 2.6°C), Koyama *et al.* (1990) ($\Delta T_{\mathrm{Glide}}$ = 0 - 8.5°C), Shao and Granryd (1998) ($\Delta T_{\mathrm{Glide}}$ = 3 - 5.8°C) and Smit and Meyer (2002) ($\Delta T_{\mathrm{Glide}}$ 0 - 6.5°C), the heat transfer coefficient degraded when compared to the highest pure component heat transfer coefficient. Some mixture concentrations exhibit local heat transfer coefficients lower than both the corresponding pure fluid values, (Koyama *et al.*, 1990). In the mid-temperature glide range, the studies by Afroz *et al.* (2008) and Milkie (2014) noted that the heat transfer coefficient decreased with increasing temperature glide. Fronk (2014) is the sole investigator in the literature to have studied condensation of high-temperature-glide mixtures ($\Delta T_{\mathrm{Glide}}$ = 78 - 93°C). He noted that for high-temperature-glide mixtures, the heat transfer coefficient can decrease sharply with increasing quality, creating a local maximum value midway between the vapor and liquid saturation points. For these fluid concentrations, the local maximum corresponded to the point where the slope of the equilibrium temperature as a function of vapor quality changes dramatically. In this region, there is a significant change in temperature glide for a specific change in quality, which indicates a large change in phase concentrations, which acts similar to a de-superheating process on the vapor. This study highlighted the large impact of changes in phase concentrations on the condensation process, leading to significant mass transfer resistances that in turn can cause significant liquid subcooling.

As noted above, the majority of condensation experiments have been conducted using a single tube diameter. Thus the effect tube diameter has on the mixture effects during condensation are unclear. Fronk (2014) conducted experiments on tube diameters between 0.98 and 2.16 mm, but did not report any dominant trends in heat transfer coefficient with tube diameter. Furthermore, aside from Milkie (2014), who conducted experiments for reduced pressures between 0.05 and 0.21 for one tube diameter and one mixture concentration, the effect of saturation pressure on zeotropic mixture condensation has not received attention thus far.

There are three commonly used techniques for predicting the mixture heat transfer coefficient,: a) the approximate/equilibrium method, proposed by Silver (1947) and Bell and Ghaly (1973), b) the fundamental framework/non-equilibrium film method outlined by Colburn and Drew (1937), and c) empirical correlation adjustments to a pure fluid model. No consensus exists in the literature about the most applicable method for a particular set of conditions. Several investigators (Koyama *et al.*, 1990; Shao and Granryd, 1998; Tandon *et al.*, 1986) have developed empirical adjustments to the pure fluid heat transfer coefficient for their low-temperature-glide mixtures, where only slight departures from the pure fluid model predictions are expected. Cavallini *et al.* (2002b) proposed using the equilibrium method (Bell and Ghaly, 1973; Silver, 1947) for their mid-temperature-glide studies. For mixtures with a similar temperature glide, Milkie (2014) neglected sub-cooling of the liquid condensate and proposed using the non-equilibrium method outlined by Colburn and Drew (1937). Fronk (2014) proposed using the Colburn and Drew (1937) framework for the high-temperature-glide mixtures he investigated, and suggested accounting for liquid subcooling and proposed calculating the sub-cooled liquid temperature using the following equation: $T_{\mathrm{L,out}} = T_{\mathrm{wall}} + 1/3\left(T_{\mathrm{interface}} - T_{\mathrm{wall}}\right)$.

The above discussion of the literature on the condensation of zeotropic mixtures points out some gaps and deficiencies in the understanding of the effects of mixture compositions and temperature glides on heat transfer rates. Specifically, an understanding of the effect of saturation pressure, tube diameter and mid-range temperature glides on zeotropic mixture condensation is missing. Moreover, a consensus has not been established about the modeling technique that applies best to the mid-temperature glide range. The present work addresses these limitations by providing measurements of the heat transfer coefficients of condensing zeotropic mixtures of hydrocarbons, i.e., mixtures of ethane and propane, across a wide range of conditions. The specific parameters investigated are: temperature glides (6 - 14°C), mass fluxes (150 – 450 kg m^{-2} s^{-1}), tube diameters (7.75 – 14.45 mm) and reduced pressures (0.46 – 0.87). The range of conditions investigated in this study, much wider than those seen in the literature, and the systematic study of the influence of each of these parameters, will provide considerable insight on the transport phenomena influencing the zeotropic mixture condensation process.

5.3 Experimental Setup, Data Analysis and Test Conditions

The experimental setup used to measure the condensing heat transfer coefficients of the zeotropic mixtures is identical to the setup used to measure pure fluid, i.e., propane, heat transfer coefficients presented in Chapter 2. To further enable measurements of concentrations of the binary mixture, a gas chromatograph (GC), Shimadzu GC-2014 was added to the subcooled section of the loop, downstream of the post condenser at state point **(8)** in Figure 2.1. A small 100 µL liquid sample of the condensed mixture is removed from the loop, which is evaporated in the GC and the concentration is measured using a thermal conductivity detector. A comprehensive description of this setup and its operation is provided in Appendix B. The bulk concentration was used with the measured temperatures and pressures to determine the enthalpies of the superheated and subcooled points, state points **(1)** and **(8)**. Using these state points, an energy balance on the pre- and post- condensers is conducted to determine the inlet and outlet enthalpies and qualities of the test section, state points **(4)** and **(5)**.

A piston accumulator, located downstream of the pump, facilitates precise control of the system pressure. The piston accumulator has two chambers, the void space and the working fluid space. Initially the piston starts close to the bottom dead center position and a large void space exists. The void space is attached to a line that connects to both a nitrogen tank and the ambient. To maintain the system pressure at the desired condition, subcooled liquid is released into the accumulator by depressurizing the void space. The high pressure of the working fluid loop causes the piston inside the accumulator to shift upwards, allowing more liquid to occupy the working fluid space at the bottom of the accumulator. A comprehensive description of this setup and its operation is outlined in Appendix B.

Charging was accomplished by first introducing the propane and then the ethane. The mass of propane that was introduced corresponded to the desired mass fraction of mixture, which was calculated from the known volume of the working fluid loop. The ethane was introduced slowly to ensure the targeted concentration was approached and not overshot. The concentration of the mixture was checked by pressurizing the working fluid loop and circulating the working fluid in a liquid state and taking a sample measurements with the gas chromatograph. Both the propane and ethane fluids used throughout the present study are of instrument-grade purity. A comprehensive description of this setup and its operation is outlined in Appendix B.

Table 5.1 Summary of Experimental Conditions

Mass Flux, kg m^{-2} s^{-1}	**33% Ethane**			**67% Ethane**			**Internal Diameter**
	Saturation Temperature, °C (Reduced Pressure)						
	30 (*0.46*)	**45 (*0.61*)**	**60 (*0.80*)**	**25 (*0.60*)**	**35 (*0.73*)**	**45 (*0.87*)**	
ΔT_{Glide}	**13°C**	**11°C**	**8°C**	**10°C**	**8°C**	**6°C**	
150	X	X	X	X	X	X	**7.75**
300	X	X	X	X	X	X	
450	X	X	X	X	X	X	
150	X	X	X	X	X	X	**14.45**
300	X	X	X	X	X	X	
450	X	X	X	O	X	X	

O G = 375 kg m^{-2} s^{-1} & T_{sat} = 30°C

The test conditions investigated in the present study are outlined in Table 5.1. Two tube diameters (7.75 mm and 14.45 mm), three mass fluxes (150, 300 and 450 kg m^{-2} s^{-1}), two mixture concentrations (33% ethane/67% propane and 67% ethane/33% propane) and three saturation pressures (corresponding to reduced pressures between 0.46 – 0.87) for each mixture concentration are studied. The previous investigation on propane condensation across a very wide range of saturation conditions is used as the baseline pure fluid case for the zeotropic mixture studies presented here.

Figure 5.2 illustrates, using a resistance network, the thermal and mass transfer resistances that develop during zeotropic mixture condensation. For a condensing zeotropic mixture, two condensation heat transfer coefficients can be defined: a) an equilibrium heat transfer coefficient, and b) a film heat transfer coefficient. The equilibrium heat transfer coefficient assumes equilibrium throughout the condensation process; therefore, in the data reduction procedure, it uses equilibrium temperatures in the ΔT_{LM} calculation, which are calculated using the measured bulk concentration (assumed

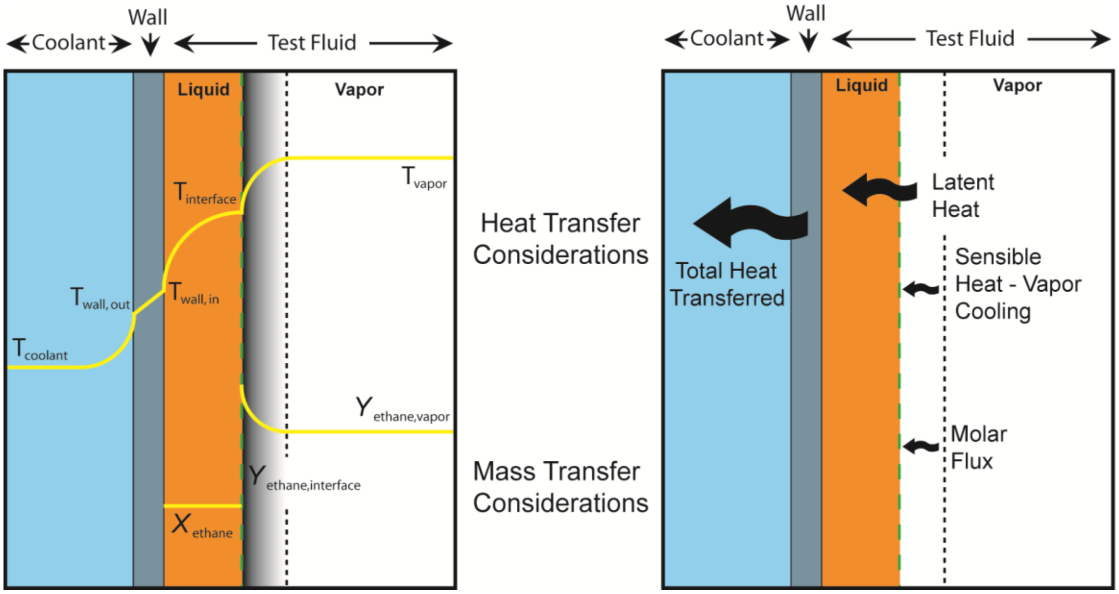

Figure 5.2: Schematic demonstrating concentration and temperature gradients

constant), measured saturation pressures, and an equilibrium enthalpy at the inlet and outlet of the test section. The film heat transfer coefficient is derived from the equilibrium inlet temperature and interface temperature at the outlet of the test section, which are subsequently used in the ΔT_{LM} calculation. The interface temperature is not measured during the experiments; thus, it must be calculated using the Colburn and Drew (1937) framework. However, closure of the equations depends on several assumptions about the flow, including a correlation for the mass transfer coefficient, which is not necessarily known or accurate. The heat transfer coefficients presented throughout the present study are calculated using the equilibrium temperatures in the ΔT_{LM} calculation; therefore they are equilibrium/apparent heat transfer coefficients.

5.4 Results and Discussion

Figure 5.3 shows the measured equilibrium heat transfer coefficients for the two fluid concentrations across all of the mass flux and saturation conditions for the 7.75 mm tube diameter. The general trends in heat transfer coefficient with the mass flux,

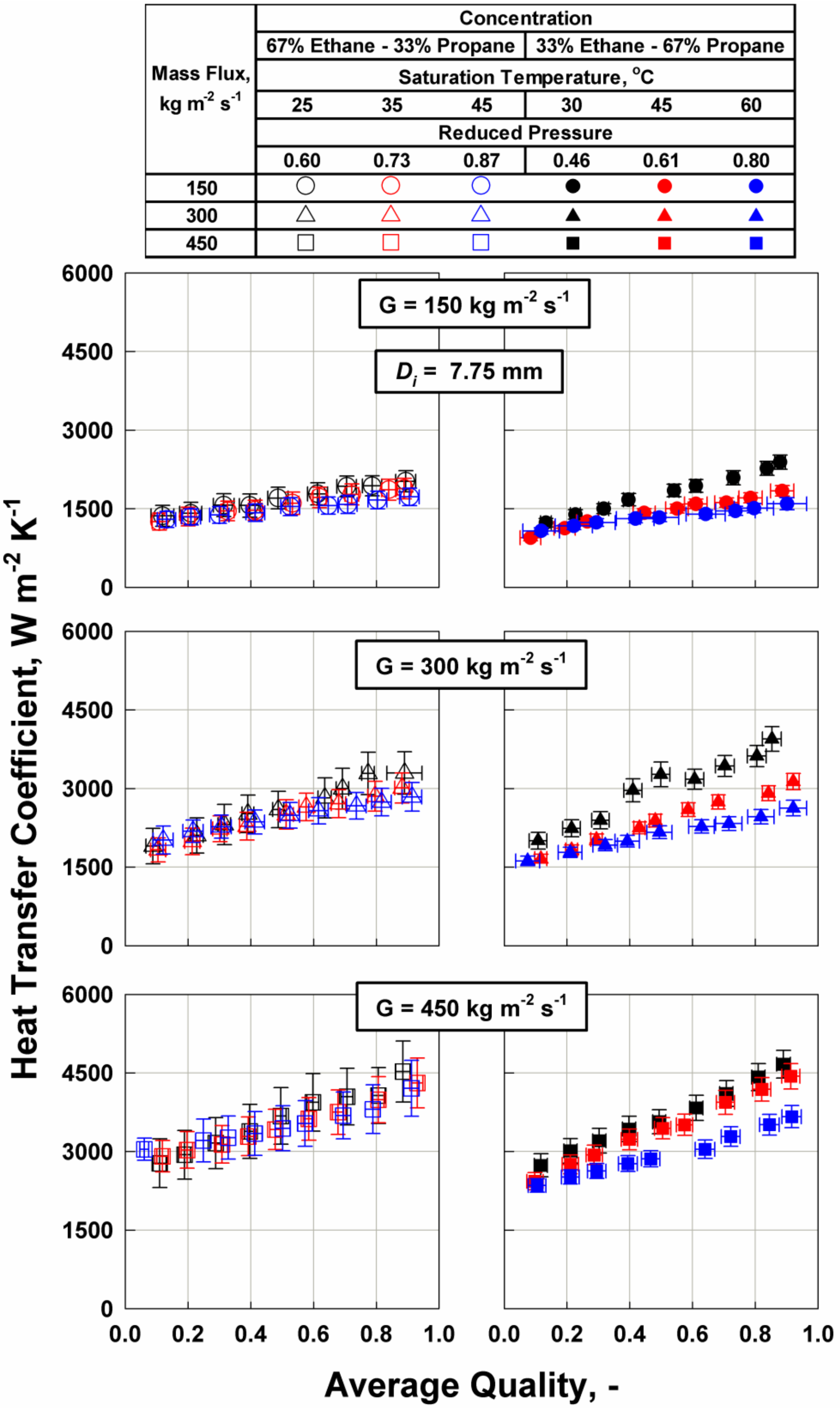

Figure 5.3: **Experimental results – Heat transfer coefficient for the 7.75 mm diameter tube**

saturation temperature and quality are the same as those reported in Chapter 2 for the

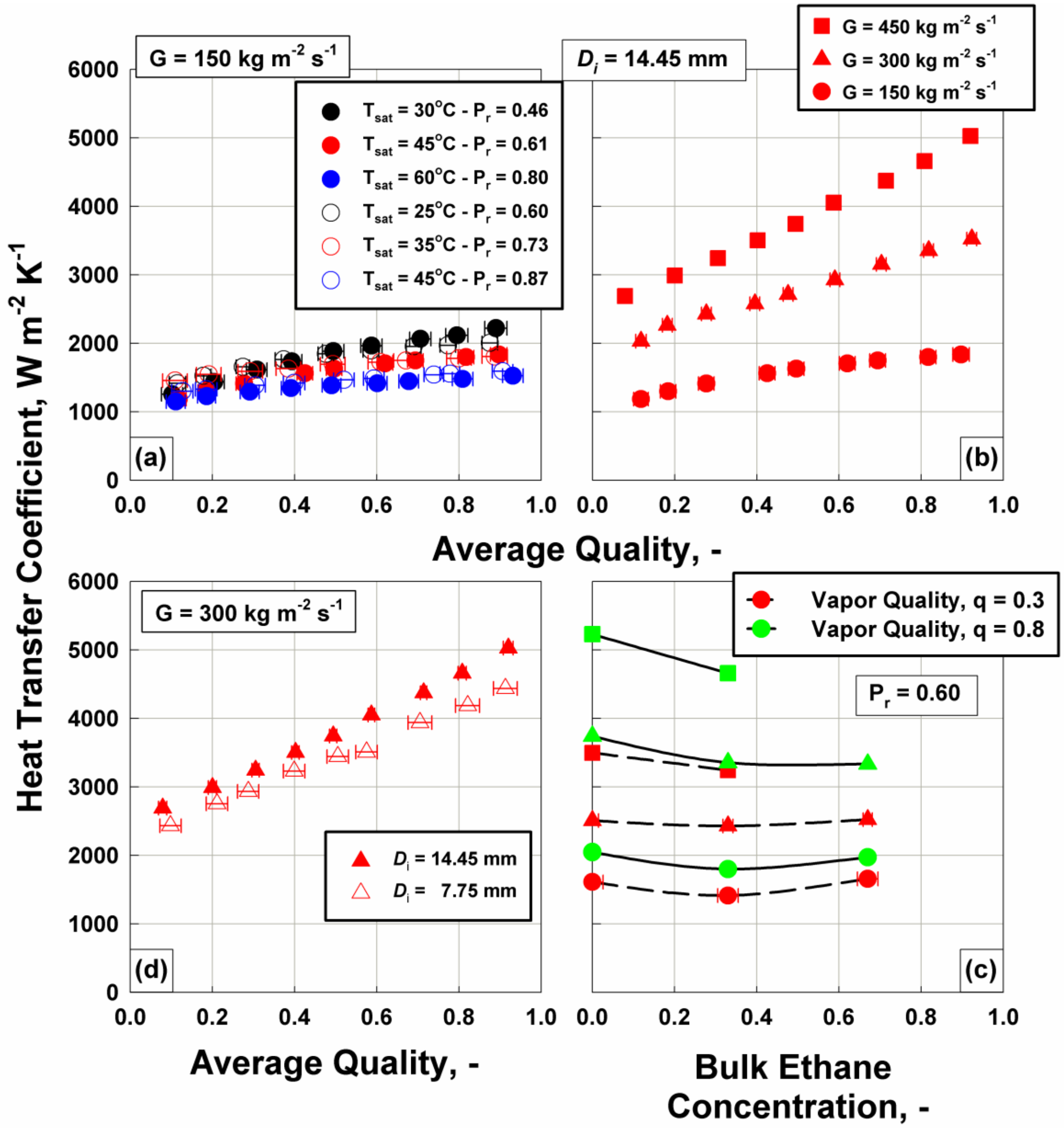

Figure 5.4: Summary of trends - Heat transfer coefficient

pure fluids. However, at the lowest mass flux (150 kg m^{-2} s^{-1}) and across all saturation conditions, there is noticeable flattening of the slope of the heat transfer coefficient with increasing vapor quality. This is due to lower vapor-phase heat transfer coefficients, decreased turbulence and therefore less mixing in the vapor phase at such low mass fluxes, which results in the increasing importance of mass transfer effects. Therefore, it is expected that there is a significant mass transfer resistance in the vapor phase, which degrades the condensation heat transfer coefficient at the lower mass fluxes. At higher mass fluxes, there is no flattening, which is due to the larger heat transfer coefficients in the vapor phase, increased turbulence and increased mixing of the vapor phase, which results in minimal concentration gradients. Thus, the increased mixing results in a more uniform vapor phase, which is expected to be close to equilibrium conditions.

Figure 5.4 shows the trends in heat transfer coefficient with changes in each of the design parameters investigated in the present study. Similar to the results from the pure propane experiments, the reduced pressure of the mixture was the best predictor of the comparable magnitudes of the heat transfer coefficients, with increasing reduced pressures resulting in lower heat transfer coefficients.

For comparative purposes, none of the experimental conditions for the two mixtures were identical; however, the 45°C saturation condition for 33% ethane/67% propane and the 25°C saturation condition for 67% ethane/33% propane have reduced pressures of 0.61 and 0.60, respectively. Comparison between these two conditions shows that the heat transfer coefficients are almost, but not quite, identical. For example, at a mass flux of 300 kg m^{-2} s^{-1} in the 7.75 mm tube and a vapor quality of 0.5, the measured heat transfer coefficients are 2388 W m^{-2} K^{-1} and 2598 W m^{-2} K^{-1} for the 33% and 67% ethane concentrations, respectively. Moreover, Figure 5.4c shows the heat transfer coefficients for a 30% and 80% quality for the two mixtures and the pure propane results at approximately similar reduced pressure. Compared to the pure propane case, adding ethane causes a slight decrease in the measured heat transfer coefficient for the 33% ethane/67% propane mixture concentration. Increasing the bulk ethane concentration further from 33% to 67% ethane results in an increase in the heat transfer coefficient. The result is similar for both vapor qualities shown in Figure 5.4c. At a reduced pressure of

0.6, the temperature glide for the 33% ethane/67% propane concentration is 11°C, while for the 67% ethane/33% propane case, it is 10°C. Therefore the lower heat transfer coefficients observed for the 33% ethane mixture correspond to the mixture with the higher temperature glide, which is a trend that has been highlighted by other investigators (Koyama *et al.*, 1990; Shao and Granryd, 1998).

Similar to the results for pure propane, the heat transfer coefficients for the 14.45 mm diameter tube were slightly higher than those for the 7.75 mm diameter tube. Furthermore, increasing the reduced pressure increased the impact of mass transfer effects on the heat transfer coefficient. This is evidenced by the flatter slopes of the heat transfer coefficients at higher reduced pressures. Vapor-phase heat transfer coefficients are lower at higher reduced pressures, which causes the mass transfer effects to become an increasingly important transfer resistance and causes greater degradation in the condensation heat transfer coefficient.

The mixture heat transfer coefficients measured in the present study were compared with the pure fluid heat transfer coefficient model developed in Chapter 4 that was calculated at equilibrium mixture conditions and implemented in the equilibrium method of Silver (1947), Bell and Ghaly (1973). The model predictions are overlaid with the experimental results in Figure 5.5 for the 14.45 mm tube diameter. The combination of the correlation developed for pure hydrocarbons used with the equilibrium method of Silver (1947), Bell and Ghaly (1973) performs very well for the 14.45 mm tube. Figure 5.6 shows that 100% of the data for both tube diameters are predicted within ±25%, with an absolute average deviation of 8.5%. The 7.75 mm tube has an average deviation of

9.7%, while the 14.45 mm tube has an average deviation of -2%. Table 5.2 shows a summary of this comparison.

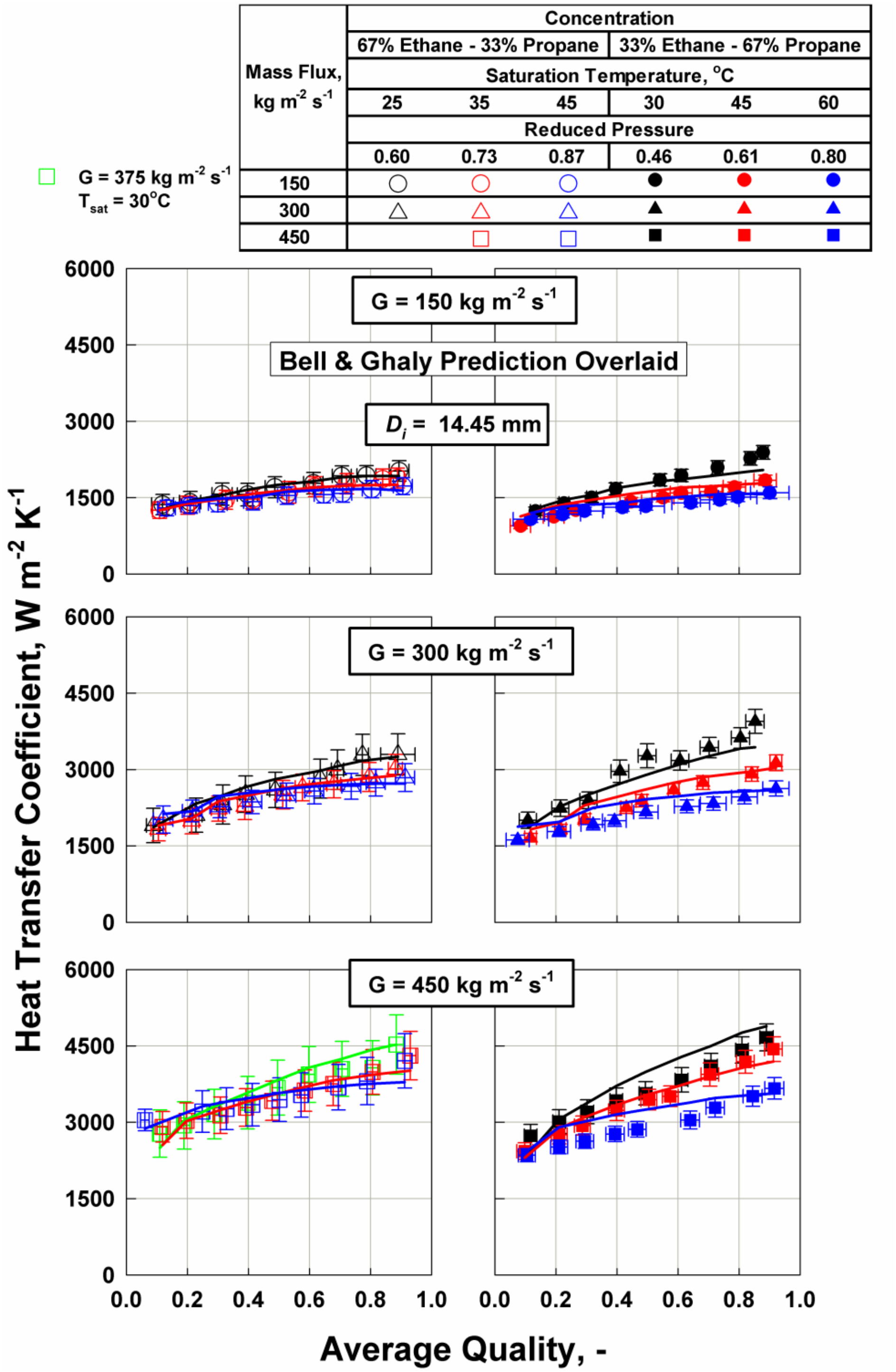

Figure 5.5: **Experimental results – Heat transfer coefficient for the 14.45 mm diameter tube with predictions of Bell and Ghaly (1973) model overlaid**

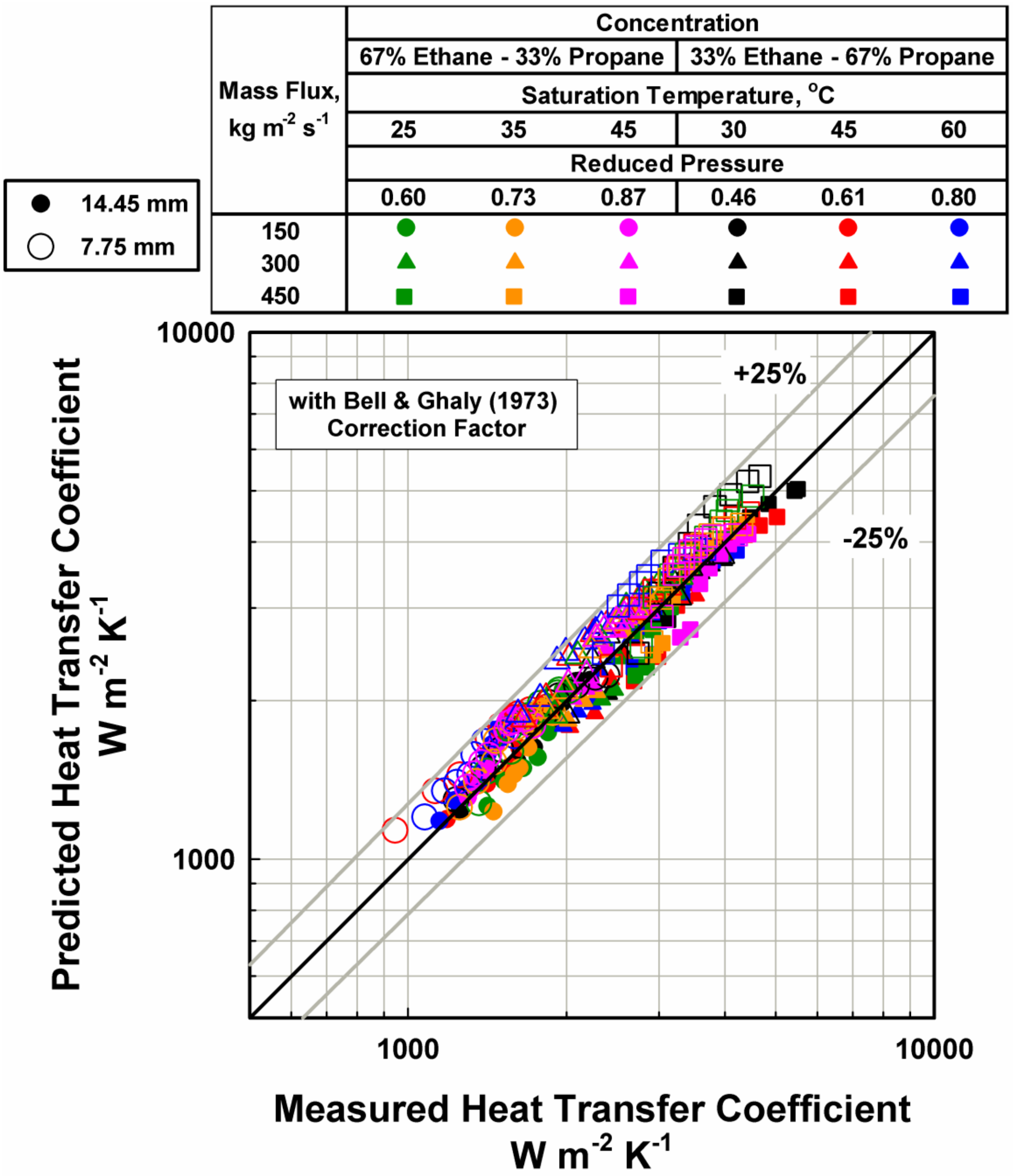

Figure 5.6: Comparison with proposed model predictions – Heat transfer coefficient

The (Bell and Ghaly, 1973) correction factor can range between zero and unity; however, for the conditions in the present study the mass transfer correction factors ranges, for the 33% ethane/67% propane mixture, from 0.11 to 0.24 for a reduced pressures of 0.60 and 0.87, respectively and from 0.12 to 0.22 for the 67% ethane/33% propane mixture for reduced pressures of 0.46 and 0.80, respectively. As noted

Table 5.2 Comparison with Proposed Model

		AD	AAD	% within 25%
Mass Flux, kg m^{-2} s^{-1}	**150**	6.0%	8.4%	100%
	300	3.8%	8.4%	100%
	450	1.7%	8.7%	100%
Diameter, mm	**7.75**	9.7%	10.6%	100%
	14.45	-2.0%	6.4%	100%
Total		3.9%	8.5%	100%

previously, the thermal and transport properties of the fluids are calculated using REFPROP version 9.1. The phase change enthalpy derived from REFPROP is the total phase change enthalpy that incorporates the enthalpy of mixing, which is typically small in comparison to the total latent heat of phase change..

5.5 Colburn and Drew (1937) Analysis

The average changes in vapor quality within the test section for all of the data points in the present study are 11.2% and 6.4% for the 7.75 mm and 14.45 mm tube diameters, respectively. Because condensation causes the development of concentration gradients and concentration shifts, it should be expected that larger heat duties in the test section can result in greater concentration changes in the vapor and liquid phases from the test section inlet to the outlet. This causes an additional complication when comparing experimental results across tube diameters for conditions with large changes across the test section.

A design analysis using the Colburn and Drew (1937) framework for non-equilibrium mixture condensation is conducted here to determine whether the outlet conditions of the vapor and liquid phases for the two tube diameters change significantly with heat duty, and whether the equilibrium heat transfer coefficients for two tube diameters are directly comparable. This analysis does not use the results from the experimental portion of this study; rather it provides the phase concentration and phase temperature changes for the two tube diameters for two specified quality changes, i.e., Δy = 0.05 or 0.10. To derive clear trends from this analysis, it is imperative to keep as many variables constant between the two tube diameters. The procedure followed and the assumptions implemented to provide closure to the design procedure are outlined here. The results of this analysis can be used as a guide in the design of condensers.

5.5.1 Design Procedure

The iterative procedure of Price and Bell (1973) is used to solve the coupled heat, mass and species balance equations provided by Colburn and Drew (1937). Equations (5.1) and (5.2) show the calculation of the sensible heat duty of the vapor.

$$\dot{Q}_{sensible,vapor} = \kappa \cdot h_{vapor} \cdot \pi D_{\text{int}} L_{test} \cdot \frac{\left(T_{vapor,in} - T_{\text{int},in}\right) - \left(T_{vapor,out} - T_{\text{int},out}\right)}{\ln\left(\dfrac{\left(T_{vapor,in} - T_{\text{int},in}\right)}{\left(T_{vapor,out} - T_{\text{int},out}\right)}\right)} \tag{5.1}$$

$$\dot{Q}_{sensible,vapor} = \dot{m}_{vapor} C_{p,v} \left(T_{vapor,in} - T_{vapor,out}\right) \tag{5.2}$$

The Churchill (1977 (b)) equation was used to determine the vapor-phase heat transfer coefficient. The Ackermann (1937) correction factor is used to account for the effect of non-zero mass flux on the transport of thermal energy in the vapor phase.

$$\begin{aligned} \kappa &= \frac{a}{1 - \exp\left(-a\right)} \\ a &= \frac{m'' C_{p,v}}{h_{vapor}} \\ m'' &= \dot{N}_{ethane} MW_{ethane} + \dot{N}_{propane} MW_{propane} \end{aligned} \tag{5.3}$$

The Chilton and Colburn (1934) heat and mass transfer analogy, Eq. (5.4), is used to determine the mass transfer coefficient in the vapor phase based on the vapor-phase heat transfer coefficient.

$$\begin{aligned}\mathrm{Sh}_{vapor} &= \mathrm{Nu}_{vapor}\left(\frac{\mathrm{Sc}_{vapor}}{\mathrm{Pr}_{vapor}}\right)^{1/3}\\ \beta_{vapor} &= \frac{\mathrm{Sh}_{vapor}D_{ethane-propane}}{D_{in}}\end{aligned} \tag{5.4}$$

The condensing fluxes, mass flow rates, and concentrations of each phase are calculated using Equations (5.5) and (5.6). The outlet phase concentrations are coupled to the heat duty in the test section using Eq. (5.7).

$$\begin{aligned}\dot{N}_{total} &= \dot{N}_{ethane} + \dot{N}_{propane} = \beta_{vapor}C_{T,V}\ln\left(\frac{z-\tilde{y}_{ethane,\mathrm{int},avg}}{z-\tilde{y}_{ethane,avg}}\right)\\ z &= \frac{\dot{N}_{ethane}}{\dot{N}_{total}}\end{aligned} \tag{5.5}$$

$$\begin{aligned}\dot{m}_{L,out} &= \dot{m}_{L,in} + \dot{N}_{ethane}MW_{ethane}A_{\mathrm{int}} + \dot{N}_{propane}MW_{propane}A_{\mathrm{int}}\\ \dot{m}_{V,out} &= \dot{m}_{V,in} - \dot{N}_{ethane}MW_{ethane}A_{\mathrm{int}} - \dot{N}_{propane}MW_{propane}A_{\mathrm{int}}\\ x_{ethane,out}\dot{m}_{L,out} &= x_{ethane,in}\dot{m}_{L,in} + \dot{N}_{ethane}MW_{ethane}A_{\mathrm{int}}\\ y_{ethane,out}\dot{m}_{L,out} &= y_{ethane,in}\dot{m}_{L,in} - \dot{N}_{ethane}MW_{ethane}A_{\mathrm{int}}\end{aligned} \tag{5.6}$$

$$\begin{aligned}\dot{m}_{total}i_{out} &= \dot{m}_{vapor,out}i_{vapor,out} + \dot{m}_{liquid,out}i_{liquid,out}\\ i_{out} &= i_{in,Eq.} - \frac{\dot{Q}_{test}}{\dot{m}_{total}}\end{aligned} \tag{5.7}$$

5.5.2 Closure Equations

Equilibrium is assumed at the inlet of the test section and a heat duty corresponding to a partial condensation of the two-phase mixture was fixed, i.e., quality changes of 0.05 or 0.10. An energy balance conducted between the inlet enthalpy and the heat duty is used to calculate the outlet enthalpy, from which the enthalpies of the vapor and liquid phases can be determined, Eq. (5.7).

The following assumptions provide closure to the coupled equations and simplify the analysis:

1) Condensate sensible cooling is neglected, i.e., $T_{\text{liquid,out}} = T_{\text{interface,out}}$. Fronk (2014) showed that accounting for condensate subcooling can slightly improve the predictions from a nominal AAD of 14.6% to 12.9%; however, the conditions he investigated were for very high glide mixtures with LMTDs ~ 50K – the much smaller LMTDs used in this analysis (10K) imply that neglecting condensate subcooling will have a negligible impact on the results.
2) The condensate film is well mixed and no mass transfer resistance exists in liquid phase, i.e., $x_{\text{int,avg}} = x_{\text{ethane,avg}}$. Milkie (2014) showed that for similar operating conditions and tube diameters, the liquid condensate is a very rough film, which produces significant mixing, thus substantiating the well mixed concentration assumption.
3) The interfacial area between the vapor- and liquid- phases can be calculated directly from a void fraction correlation (the Baroczy (1963) correlation is used throughout this analysis), and by approximating the flow regime as annular flow only for the purpose of calculating interfacial area. However, the effect of the specific flow regimes inside the tubes on the heat transfer coefficient and condensation process is accounted for, i.e., the correlation used, presented in Chapter 4, to calculate the condensation heat transfer coefficient accounts for the expected flow regime present for a given set of conditions. Therefore, the different condensation characteristics of wavy and

annular flows are explicitly addressed, despite this approximation for the calculation of interfacial area.

4) Thermodynamic equilibrium is assumed at the interface.

5) The liquid film condensation heat transfer coefficients is calculated using the correlation developed specifically for pure propane in 7.75 mm and 14.45 mm diameter tubes in Chapter 4.

The condensation heat transfer coefficient and the test section heat duty are used to calculate the liquid phase temperature at the outlet of the test section (this is the driving temperature for condensation), and the length of tube required for the partial condensation, Eq. (5.8). Thus, the length of tube for both tube diameters is not identical.

$$\dot{Q}_{test} = h_{liquid\ film} \cdot \pi D_{in} L_{test} \cdot \frac{\left(T_{liquid,in} - T_{wall,in}\right) - \left(T_{\text{int},out} - T_{wall,out}\right)}{\ln\left(\frac{\left(T_{liquid,in} - T_{wall,in}\right)}{\left(T_{\text{int},out} - T_{wall,out}\right)}\right)} \tag{5.8}$$

5.5.3 Results and Discussion

The analysis was conducted for the two tube diameters and two mixture concentrations of ethane and propane that corresponded to the experimental portion of this work. The results of the analysis are shown in Figure 5.7a-d for the saturation pressures of the two fluid mixtures equivalent to a reduced pressure of 0.60 and at a mass flux of 150 kg m^{-2} s^{-1}. Figures 5.7a and 5.7d show that the concentration of ethane in both the liquid and vapor phases increases with condensation. At the inlet, the equilibrium concentration of ethane is higher in the vapor phase than in the liquid phase. The propane, which has a higher saturation temperature than ethane and is therefore a less volatile fluid, preferentially condenses from the vapor phase to the liquid phase, leaving

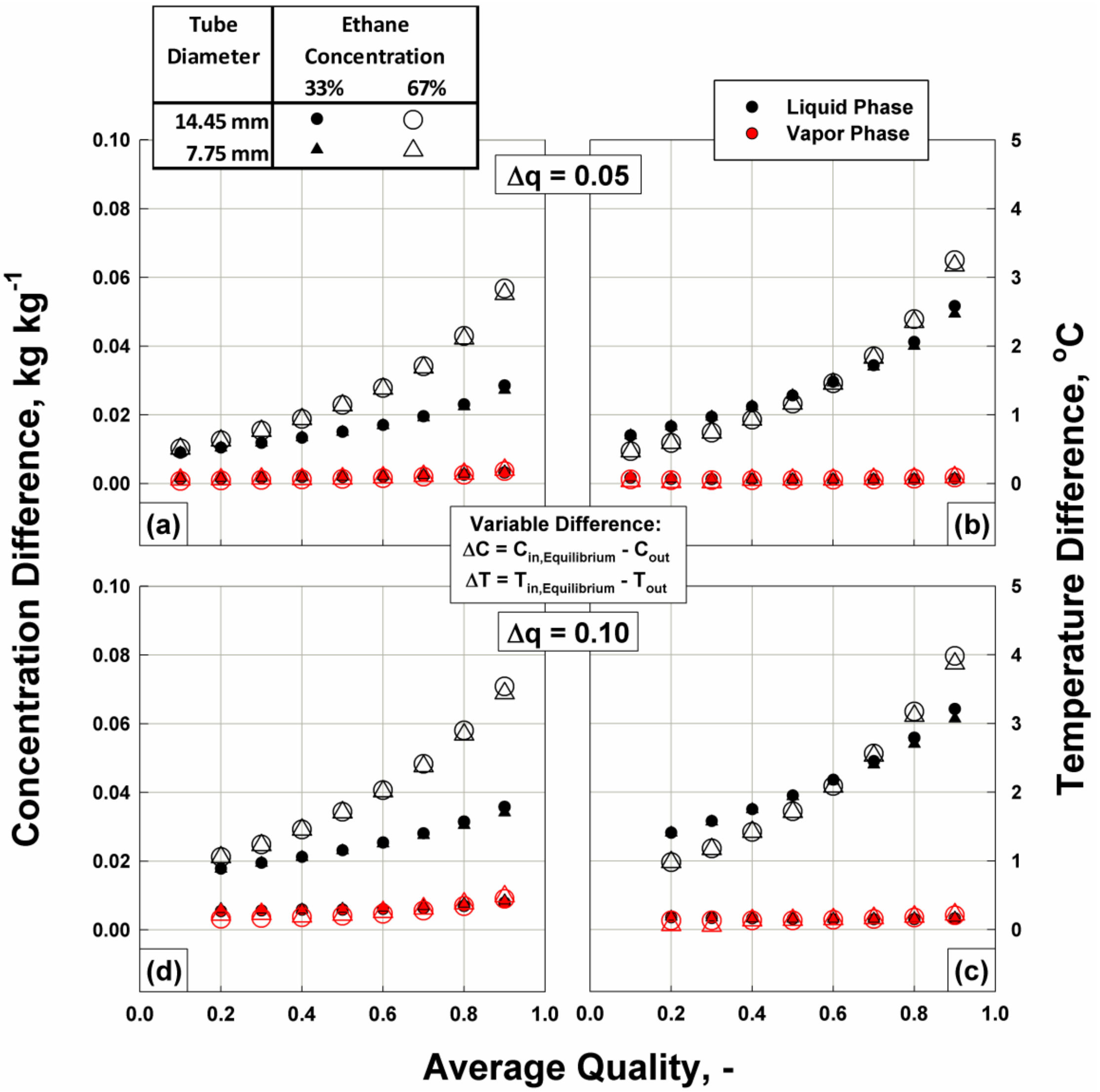

Figure 5.7: Concentration and temperature changes in a section length – Predictions of the study using the Colburn and Drew (1937) framework

the vapor phase richer in ethane at the outlet than at the inlet. Moreover, the condensing vapor has a higher concentration of ethane than the inlet liquid phase, which increases the concentration of ethane in the liquid phase during condensation. The increasing concentration of ethane in the liquid phase causes a decrease in the liquid phase temperature.

Figures 5.7a and 5.7d show that the concentration changes that happen in the vapor and liquid phases are greater for the 10% quality change; however, because mass transfer is an important consideration in the transfer processes, the concentration change is only marginally higher for the 10% quality change compared to the 5% quality change. For example, for the 33% ethane/67% propane mixture in the 7.75 mm tube diameter, the liquid phase concentration changes from 0.215 to 0.249 ($\Delta x = 0.034$) and from 0.212 to 0.239 ($\Delta x = 0.027$) for a vapor quality change of 10% and 5%, respectively. Thus, because the vapor quality changes have non-linear effects on the concentration changes in both phases, caution should be exercised when comparing the experimental heat transfer coefficients for the two tube diameters. However, if the quality changes in test sections are small, or in design calculations, if the segmental calculations are conducted with a fine enough grid to ensure $\Delta y \leq 10\%$, a comparison between tube diameters is more realistic.

The Churchill (1977 (b)) correlation predicts that the vapor phase heat and mass transfer coefficients are greatest at the higher quality points, where the vapor velocity is the highest. The higher mass transfer rates cause larger fractions of the ethane to be transferred from the vapor into the liquid. Thus, the higher quality points experience a larger decrease in the vapor-phase ethane concentration than the lower quality points. The greater shift in concentration at the high vapor quality points causes greater decreases in the vapor phase and the interface temperatures. Additionally, the vapor phases have higher ethane concentrations than the liquid phases, and more condensation of ethane from the vapor phase causes the equilibrium temperature of the liquid phase and interface to drop. The interface-to-wall temperature difference ($T_{\text{interface}}$ - T_{wall}) is the driving temperature difference for condensation. Therefore, decreases in this temperature difference decrease the condensation rate. A combination of both of these effects: a) the greater concentration shifts at higher quality points caused by greater transfer coefficients, and b) the condensation of a phase richer in a lower saturation temperature fluid (ethane) lead to the flatter slopes of the apparent heat transfer coefficient curves at the higher quality points shown above.

Figures 5.7a and 5.7d show that for both the 5% and 10% quality change, the concentration change is greater for the 67% ethane concentration; however, the liquid-phase temperature difference is comparable for both fluid mixtures. The liquid phase concentration changes (Δx) for the 10% quality change are 0.034 and 0.068 for the 33% and 67% ethane mixtures, respectively. At a quality of 0.9, the inlet liquid- and vapor-phase concentrations for the 33% ethane mixture are 0.215 and 0.352, respectively, while the corresponding phase concentrations for the 67% ethane mixture are 0.481 and 0.706, respectively. These values translate to a ratio of the vapor-to-liquid concentrations of 1.64 and 1.46 for the 33% and 67% ethane mixtures, respectively. Thus, despite the higher actual phase concentrations of the 67% ethane mixture and the greater increase in the absolute liquid phase concentration, the percentage phase concentration shifts are greater for the 33% ethane mixture. This causes the larger drop in the outlet temperature shown in Figure 5.7b and 5.7c, leading to the comparative temperature drops for significantly different changes in phase concentrations.

The importance of temperature glide on the heat transfer rate has been discussed in the experimental results section above and by several investigators (Koyama *et al.*, 1998; Shao and Granryd, 1998). The results above demonstrate that while the concentration imbalances are more extreme for the 67% ethane mixture, this is not the sole determining parameter when considering the degradation in condensation rate. Examination of Table

5.1 shows that, at a reduced pressure of 0.60, the 33% ethane mixture has a slightly larger temperature glide than the 67% ethane mixture (the temperature glides are 11.5°C and 9.6°C, respectively.) Therefore, the parameter that most strongly influences heat transfer degradation is the temperature glide. This result is confirmed by the experimental results, shown in Figure 5.4c, where a local minimum exists for the heat transfer coefficient at the 33% ethane concentration. Thus, the thermodynamic profile/temperature glide of the fluid mixture is an important consideration when predicting the effective condensation heat transfer coefficients of zeotropic mixtures.

5.6 Conclusions

The heat transfer coefficients for condensing mixtures of hydrocarbons were measured over a very wide range of conditions, the trends with mass flux, mixture concentration, tube diameter, and saturation pressure and vapor quality elucidated. A comparison with the Silver (1947) and Bell and Ghaly (1973) equilibrium approach was conducted using the correlation developed in Chapter 4 for the corresponding pure fluid propane. The use of that correlation in this equilibrium framework predicts the measured heat transfer coefficients well: 100% of the data points are predicted within ±25% of the measured values with an absolute average deviation of 8.5%. In addition, the progression of condensation from the vapor phase to the liquid phase was analyzed using this pure component correlation and the Colburn and Drew (1937) non-equilibrium framework to understand the effects of preferential condensation of the species and its effect on individual phase concentrations and temperature glides. Specifically, the gradients in concentration and temperature across different finite vapor quality changes along the condenser length were analyzed. The corresponding results provide guidance for the comparison of these calculated heat transfer coefficients with other values from the literature and also help prescribe the segment lengths in incremental calculations needed for accurate designs. The variations in degradation in heat transfer rate from the initial to the later stages of condensation were also documented and interpreted in terms of the temperature glide in the mixture from inlet to outlet. This study therefore presents a large hydrocarbon mixture condensation database, the relevant condensation heat transfer models, and framework for the design of zeotropic binary fluid mixture condensers.

CHAPTER 6 CRITERIA TO DETERMINE APPROPRIATE ZEOTROPIC MODELING TECHNIQUES

6.1 Introduction

Zeotropic mixtures are widely encountered in industry, as working fluids in power, refrigerant or separation cycles, or as the process fluid in the chemical industry. One of the key features of zeotropic mixtures is their non-isothermal condensation, leading to a temperature glide (T_{bubble} - T_{dew}), which stems from the different saturation temperatures of the individual components of the mixture. In general, the condensation rate (or heat transfer coefficient) of zeotropic mixtures is lower than the rate for either of the pure substances. This is due to two phenomena commonly referred to as the equilibrium effect and the non-equilibrium effect. The equilibrium effect is a result of the temperature decrease of the mixture that occurs as the quality decreases during condensation. The temperature glide/temperature decrease is due to the different bubble and dew points of the mixture components, and results in a decrease in the driving temperature for condensation, which in turn reduces the condensation rate. The non-equilibrium effect is due to a preferential condensation of one component (the less volatile component) from the vapor phase to the liquid phase. The condensation of the larger fraction of the more volatile component at the interface results in its depletion in the vapor phase and a corresponding increase in the liquid phase at the interface. This has two effects: a) it reduces the interfacial temperature (the more volatile component, which is now in a higher concentration at the interface, has a lower saturation temperature), and b) it creates a mass transfer resistance to condensation (the less volatile component must diffuse through the vapor phase before it can condense at the interface). Both the equilibrium and non-equilibrium effects independently act to decrease the condensation rate.

6.1.1 General Trends in Heat Transfer Coefficient

Experimental studies have confirmed the reduced heat transfer rates of zeotropic mixtures discussed above. However, while studies generally agree about the trends, the specific combination of operating conditions that leads to the greatest reductions in heat transfer rates is unclear. The operating conditions that have been shown to reduce the heat transfer rate are: a) fluid combination, b) concentration c) quality, d) mass flux, and e) saturation pressure. The temperature glide is often used as a "catch-all" measure to describe the combined influence of the fluid mixture, fluid concentration and saturation pressure. It has been shown in Chapter 5 and by several investigators (Afroz *et al.*, 2008; Fronk, 2014; Milkie, 2014) to generally be a good indicator of the likelihood of the mixture to have reduced condensation heat transfer rates. The temperature glide decreases at higher saturation pressures, and typically larger temperature glides undergo greater degradation in heat transfer rates than smaller temperature glides.

6.1.2 Published Experimental Studies

Studies by Shao and Granryd (1998) and Smit and Meyer (2002) have noted that the decrease in condensation rates is greatest at low mass fluxes. This is generally attributed to decreases in turbulence in the vapor and liquid phases at lower mass fluxes, which decreases mixing and results in larger concentration gradients, and greater non-equilibrium (mass transfer) effects. Some studies (Fronk, 2014) have noted that increasing quality causes greater reductions in the condensation rate. Higher heat and mass transfer conditions in the vapor phase at higher qualities accelerate the decrease in the vapor phase concentration of the less volatile component than is the case at lower qualities. The larger decrease in concentration results in greater changes in the interfacial temperature, and therefore a decrease in the condensation rate. Fronk (2014) noted that the quality at which significant decreases in condensation rates occur corresponds to the point where large changes in the equilibrium temperature of a zeotropic mixture occur. Few studies have investigated the effect of saturation pressure on the condensation rate. In Chapter 5 it was noted that at higher saturation pressures, the slope of the apparent heat transfer coefficient curve approached a constant value with increasing quality, indicating that mass transfer effects are increasingly important at higher saturation pressures. The vapor density increases significantly with saturation pressure, which leads to lower vapor velocities, in turn reducing the vapor-phase Reynolds number and mass transfer rates. Fronk (2014) highlighted the importance of accounting for subcooling of the condensate. This can occur when very large mass transfer resistances are built up in the vapor phase that inhibit phase change, and thus the continued cooling at the wall causes the condensate to cool below saturation conditions. This typically only occurs when the temperature glide is very large and mass transfer rates are low.

6.1.3 Binary Fluid Condensation Modeling Techniques

The most commonly used techniques for modeling the condensation of zeotropic mixtures are: a) the equilibrium method, b) non-equilibrium method and c) empirical correction factors. The equilibrium method was first proposed by Silver (1947) and later by Bell and Ghaly (1973). This approach involves adding an effective mass transfer resistance in series to the calculation of the condensation heat transfer coefficient. This approximate thermal resistance is modeled as the ratio of the sensible cooling heat duty in the vapor-phase to the total phase change heat duty. The resulting heat transfer coefficient of the mixture represents an apparent heat transfer coefficient that accounts for the combined effects of mass transfer and condensation. It assumes equilibrium conditions at the inlet and the outlet of the condenser section being modeled and is therefore termed the "equilibrium method." The non-equilibrium method was first outlined by Colburn and Drew (1937). A computational procedure for implementing this theory in a design code was later outlined by Price and Bell (1973). This method proposes modeling the species, mass and energy transfer through the vapor and liquid phases, and calculating the rate of each individual condensing species. It involves solving a series of coupled equations for transport within the vapor and liquid phases and across the interface, and cooling to accomplish the condensation. These coupled equations rely upon several closure relations and assumptions to obtain solutions. The fundamental basis for this approach provides some reassurances that the predictions depict correct physical representations of the condensation process; however, because it involves coupled equations, it can be cumbersome to implement in design codes. In some cases, empirical correction factors to pure fluid condensation correlations have also been recommended. This can have a form similar to the Silver (1947) and Bell and Ghaly (1973) approach, such as the method presented by Shao and Granryd (1998), or it can be a purely empirical correction factor such the method presented by Koyama *et al.* (1990).

Based on the above discussion, it can be seen that analysis the condensation of zeotropic mixtures, especially in the design of binary fluid condensation equipment, is not fully understood across different operating conditions. The design of such equipment is further complicated by the lack of an agreed upon framework for applying the available modeling techniques. It is also difficult to gauge when a simplified analysis can be applied without loss of accuracy, and when a more rigorous analysis is necessary. The present study addresses these deficiencies by proposing a framework that allows the user to determine:

a) When it is necessary to model the mixture effects during condensation, and
b) When a simplified model suffices, offering computational ease and design efficacy

6.2 Approach

6.2.1 Heat Transfer Database

An extensive database on condensation of zeotropic mixtures from recent experimental studies (Fronk, 2014; Milkie, 2014) and the results presented in Chapter 5 is used to guide the development of the guidelines in the present study. The database consists of heat transfer coefficient measurements for a mixture of refrigerant R245fa and pentane (45%/55%), three concentrations of ammonia and water (80%/20%, 90%/10% and 96%/4%,) and two mixtures of ethane and propane (33%/67% and 67%/33%). All concentrations noted here are on a mass basis. The database contains experimental conditions covering a wide range of reduced pressures (from 0.05 to 0.87), total mass fluxes of the fluid (from 50 kg m^{-2} s^{-1} to 600 kg m^{-2} s^{-1}), and tube diameters (from 0.98 mm to 14.45 mm). Additionally, this database covers operating conditions for temperature glides between 6°C and 93°C.

Two condensation heat transfer coefficients is calculated using the UA-LMTD method shown in Eq. (6.1).

$$\begin{aligned} UA &= \frac{Q_{\text{test}}}{\Delta T_{\text{LM}}} \\ UA &= \left(R_{\text{annulus}} + R_{\text{conduction}} + \frac{1}{h_{\text{Equilibrium}} A_{\text{in}}} \right)^{-1} \end{aligned} \tag{6.1}$$

The heat transfer coefficient can generally be defined as: a) an equilibrium, or apparent, heat transfer coefficient, and b) a film heat transfer coefficient. The apparent heat transfer coefficient assumes equilibrium throughout the condensation process; therefore it uses equilibrium temperatures in the ΔT_{LM} calculation of the heat transfer coefficient at the inlet and outlet of the heat exchange domain of interest. Equilibrium temperatures can be calculated using a bulk concentration (assumed constant throughout condensation), saturation pressures, and an equilibrium enthalpy/quality. This calculation is shown in Eq. (6.2).

$$\Delta T_{\text{LM - Equilibrium}} = \frac{\left(T_{\text{Eq. - in}} - T_{\text{coolant - out}}\right) - \left(T_{\text{Eq. - out}} - T_{\text{coolant - in}}\right)}{\ln \dfrac{\left(T_{\text{Eq. - in}} - T_{\text{coolant - out}}\right)}{\left(T_{\text{Eq. - out}} - T_{\text{coolant - in}}\right)}} \tag{6.2}$$

The film heat transfer coefficient represents the condensation heat transfer coefficient of the condensate. This heat transfer coefficient can be calculated using a similar ΔT_{LM} calculation. However, instead of using the equilibrium temperatures at the outlet of the test section, the interface temperatures are used. These temperatures represent the effective driving temperatures for condensation, and the film heat transfer coefficient represents the actual thermal resistance for condensation. This calculation is shown in Eq. (6.3).

$$\Delta T_{\text{LM - Film}} = \frac{\left(T_{\text{Eq. - in}} - T_{\text{coolant - out}}\right) - \left(T_{\text{interface - out}} - T_{\text{coolant - in}}\right)}{\ln \dfrac{\left(T_{\text{Eq. - in}} - T_{\text{coolant - out}}\right)}{\left(T_{\text{interface - out}} - T_{\text{coolant - in}}\right)}} \tag{6.3}$$

Throughout the present study, all reported heat transfer coefficients are the apparent heat transfer coefficients.

6.2.2 Proposed Framework

A framework that provides a structured approach to determining the importance of mass transfer during condensation is proposed here. Specifically, the degree to which mass transfer affects the design of a condenser is assessed. Two dimensionless numbers that serve as boundary conditions for determining when mass transfer is important during condensation, and which mass transfer model is most appropriate for the given conditions, are defined. The dimensionless numbers are used sequentially; thus, if the criterion for the first dimensionless number is satisfied, the criterion for the second dimensionless number is subsequently assessed.

6.2.3 Mass Transfer Coefficient – Criterion 1

The first dimensionless number, Ψ_1, determines whether mass transfer effects should be considered during condensation. It is defined in Eq. (6.4) and is a ratio of the rate of mass transfer in the vapor phase to the rate of vapor-phase thermal capacitance, and is the mass transfer equivalent of the Brinkman number. A critical value of 4.5×10^{-4} is defined for Ψ_1, below which mass transfer should be considered. Thus, for a given fluid mixture, saturation pressure and tube diameter, a critical mass transfer coefficient, $\lambda_{V,critical}$, where mass transfer must be considered, can be calculated. The denominator has units of kJ kg^{-1}, which are equivalent to m s^{-1}, making the Ψ_1 term dimensionless.

$$\Psi_1 = \frac{\lambda_{\mathrm{V,critical}}}{\sqrt{C_{\mathrm{p,V}} \cdot \Delta T_{\mathrm{Glide}}}} \mathrm{Sc}_{\mathrm{V}}^{1/2} = 4.5\times10^{-4} \qquad (6.4)$$

By applying the Chilton and Colburn (1934) heat and mass transfer analogy to the Dittus and Boelter (1930) correlation, the turbulent Sherwood number correlation, shown in Eq. (6.5) can be derived.

$$\begin{aligned} \mathrm{Sh}_{\mathrm{V}} &= \frac{\lambda_{\mathrm{V,critical}} d}{D_{1\rightarrow 2}} = 0.023\,\mathrm{Re}^{0.8}\,\mathrm{Sc}_{\mathrm{V}}^{1/3} \\ \mathrm{Re} &= \frac{G_{\mathrm{critical}} d}{\mu_{\mathrm{V}}} \end{aligned} \tag{6.5}$$

From Eq. (6.5), a critical mass flux can be calculated directly from the Sherwood and Reynolds number equations. This critical mass flux represents the limiting case below which mass transfer effects on condensation must be considered. At higher mass fluxes, the higher heat and mass transfer coefficients and greater turbulent mixing produce conditions where mass transfer effects can be largely neglected.

The critical value of the dimensionless number in Eq. (6.4) was determined by assessing the conditions at which the apparent heat transfer coefficient curve of the mixture as a function of quality begins to flatten. The database conditions for all three fluid pairs were considered and the value of the constant for Ψ_1 that best represented the points where flattening was observed was chosen.

Figure 6.1 shows the experimental results for a 45%/55% mixture of R245fa and n-Pentane conducted by Milkie (2014). Both the experimental results and the predictions of the Cavallini *et al.* (2006) correlation for the fluid mixture are shown. The Cavallini *et al.* (2006) model is calculated assuming equilibrium conditions. The predicted values are consistently larger than the experimental results. Pure fluids typically have a monotonically increasing heat transfer coefficient slope; thus deviations from this monotonic profile suggest that the condensation is being impacted by mass transfer resistances that decrease the apparent heat transfer coefficient. For example, for the R245fa/pentane mixture at a reduced pressure of 0.05, the slope of the apparent heat transfer coefficient flattens for all conditions below a mass flux of ~300 kg m^{-2} s^{-1}, while for a reduced pressure of 0.11, the flattening occurs below mass fluxes of ~500 kg m^{-2} s^{-1},

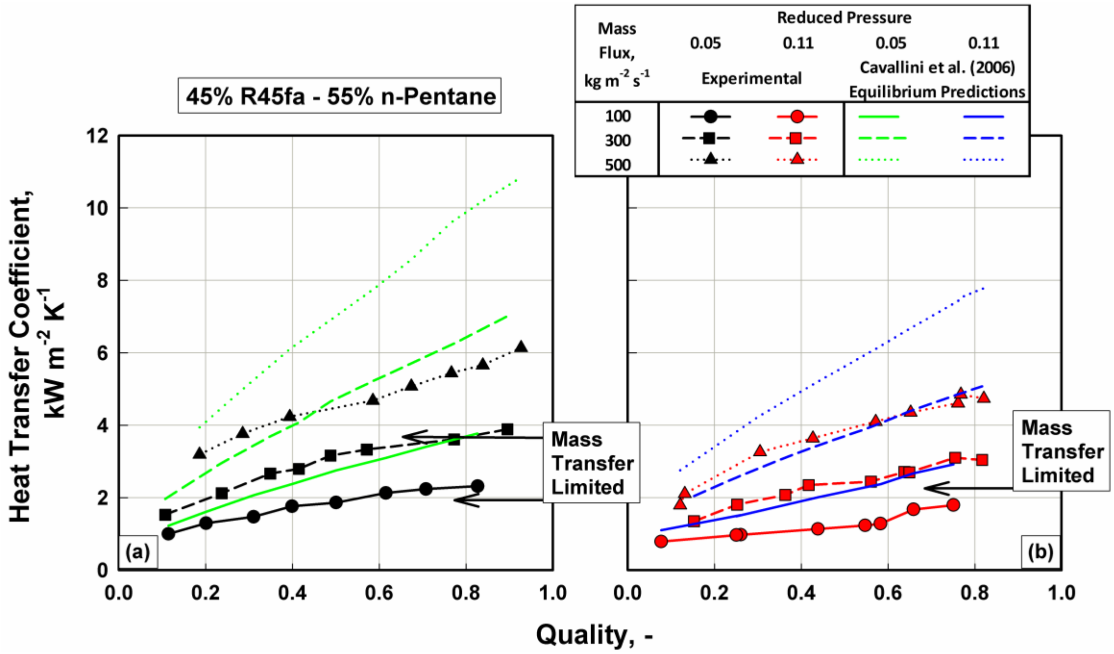

Figure 6.1: **Measured apparent heat transfer coefficients for 45% R245fa and 55% n-pentane and equilibrium heat transfer coefficient predictions of the Cavallini *et al.* (2006) correlation**

as shown in Figure 6.1a and b. These values are similar to the predictions of Eq. (6.4) and (6.5), where the critical mass fluxes where mass transfer can be neglected are ~350 kg m^{-2} s^{-1} and ~800 kg m^{-2} s^{-1}, respectively.

The heat transfer coefficients for a 33%/67% ethane- propane mixture condensing in a 14.45 mm diameter tube are shown in Figure 6.2a and 6.2b. The correlation that is shown in Figure 6.2 is the same as the one developed in Chapter 4 for pure fluid hydrocarbons. It predicts a monotonic increase in the heat transfer coefficient with quality, whereas the experimental results flatten slightly for all mass fluxes. The most extreme flattening occurs at the lowest mass flux case, and for the highest reduced pressure. At these conditions, the vapor phase is in almost laminar flow, which has negligible mixing and therefore experiences significant non-equilibrium effects that degrade the heat transfer. Equation (6.4) and (6.5) predict that mass transfer effects are

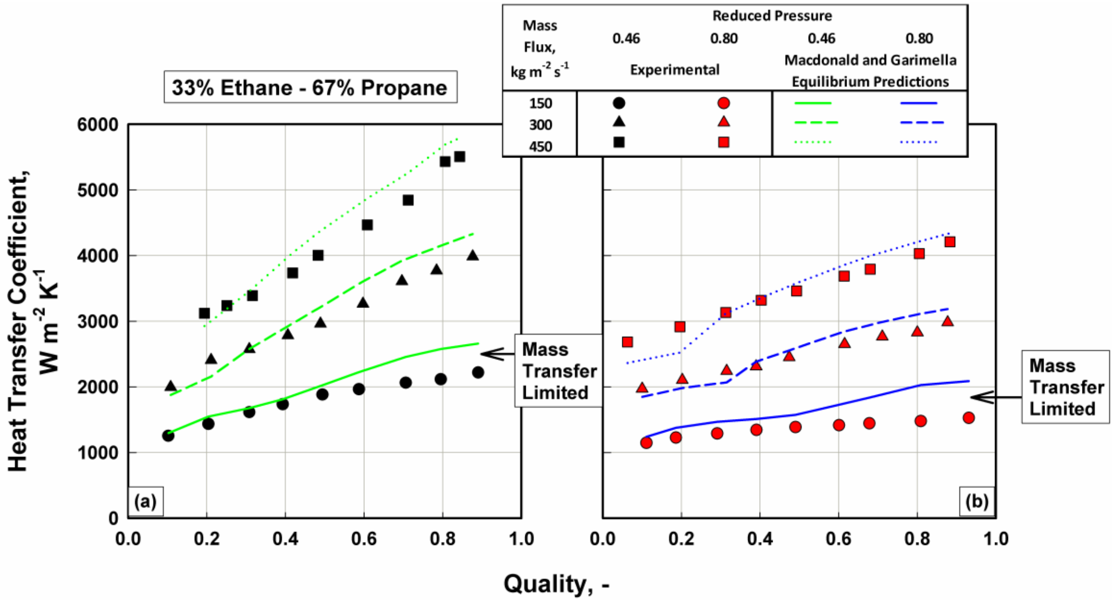

Figure 6.2: Measured apparent heat transfer coefficients for 33% ethane and 67% propane mixture and equilibrium heat transfer coefficient predictions of the proposed correlation

important for all of the conditions in the ethane-propane database. For the reduced pressure conditions shown in Figure 6.2, the critical mass flux is above 1000 kg m^{-2} s^{-1}.

Examination of Eq. (6.4) suggests that mass transfer effects should be considered at lower Schmidt numbers, where mass diffusion is slower than momentum diffusion and at lower diffusivities, both of which occur increasingly at higher pressures. Thus, notwithstanding a decreasing temperature glide at higher pressures, lower mass transfer rates at higher pressures lead to the increasing importance of mass transfer effects at higher pressures. Mass transfer was shown in Chapter 5 to have greater importance during condensation at higher saturation pressures. They noted flatter slope of the heat transfer coefficient with quality for higher qualities at high reduced pressures, suggesting that mass transfer is increasingly limiting the heat transfer process at these conditions. This is also confirmed by the results in Figures 6.1 and 6.2, where flattening of the slope occurs at lower vapor qualities for the 300 kg m^{-2} s^{-1} mass fluxes for the higher saturation pressure.

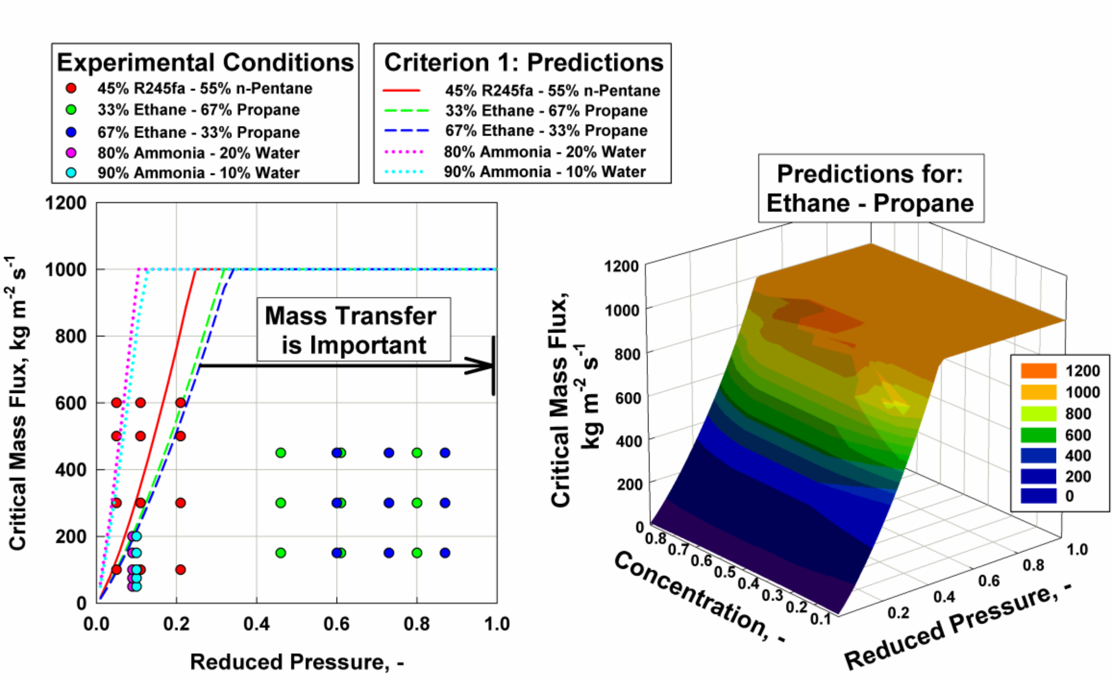

Figure 6.3: Sample predictions: a) Criterion 1 for the three fluid mixtures in the database and b) changes in predictions for the ethane and propane mixture at different concentration and reduced pressure

Figure 6.3 shows the predicted critical mass flux boundaries with changes in reduced pressure for the three fluid combinations in the database. The maximum critical mass flux shown in Figure 6.3 is capped at 1000 kg m^{-2} s^{-1} because the database used to develop this tool had data only under this mass flux. Therefore, application of this criterion beyond this point should be conducted with caution. Overlaid in Figure 6.3 are the experimental conditions of the database used to develop the criteria in the present study. Most of the test conditions are predicted to require consideration of mass transfer effects. Mass transfer is negligible only for the R245fa-n-Pentane mixture at the lowest reduced pressure. At these conditions, the flow is expected to be highly turbulent with large-scale mixing, and negligible non-equilibrium effects. Thus, mass transfer is not expected to pose an appreciable resistance during condensation and can be neglected during condenser design.

It is clear from Figure 6.3 that mass transfer is an important consideration for almost all conditions for the ammonia-water mixtures, including all of the test conditions in the Fronk (2014) database. This result should be expected of other binary mixtures with very high temperature glides. The temperature glide is on the denominator of Eq. (6.4), and thus fluid pairs with higher temperature glides have higher critical mass flux boundaries in Figure 6.3. A 3D graph that demonstrates the changes in the critical boundaries for different concentrations of the ethane-propane mixture is shown in Figure 6.3b. As concentration is increased from the pure fluid states, the reduced pressure at which mass transfer is an important consideration decreases. Thus, as the mixture becomes less like one of the pure fluids, mass transfer becomes an increasingly important consideration in the design process.

6.2.4 Sensible Cooling in the Vapor Phase - Criterion 2

The second dimensionless number, Ψ_2, is a ratio of the vapor phase sensible heat to the total enthalpy of phase change of the mixture, shown in Eq. (6.6).

$$\Psi_2 = \frac{C_{\text{p,V}} \cdot \Delta T_{\text{Glide}}}{i_{\text{fg}}} \quad \begin{cases} \Pi_2 < 0.05 & \rightarrow \text{Negligible Mass Transfer} \\ 0.05 \le \Pi_2 \le 0.15 & \rightarrow \text{Colburn and Drew Model} \\ 0.15 < \Pi_2 \le 0.20 & \rightarrow \text{Transition Region} \\ 0.20 < \Pi_2 & \rightarrow \text{Silver, Bell and Ghaly Model} \end{cases} \tag{6.6}$$

It is similar to the parameter outlined by Silver (1947) and Bell and Ghaly (1973), shown in Eq. (6.7).

$$h_{\text{Bell and Ghaly (1973)}} = \left(\frac{1}{h_{\text{pure fluid correlation}}} + \frac{y C_{\text{p,V}} \cdot \Delta T_{\text{Glide}} / i_{\text{fg}}}{h_{\text{single phase - vapor}}} \right)^{-1} \tag{6.7}$$

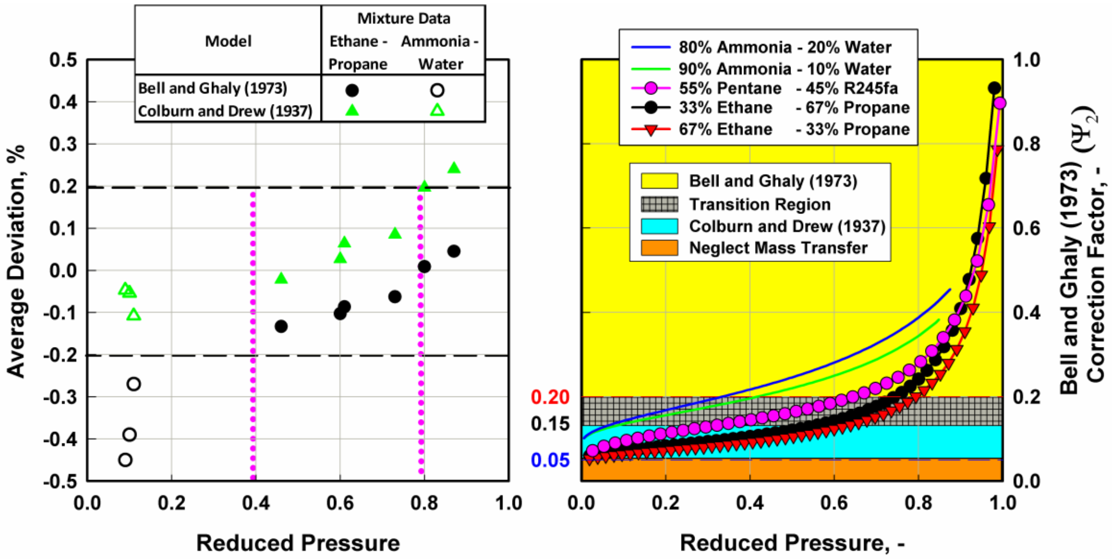

Figure 6.4: **Average deviations of the Colburn and Drew (1937) and Bell and Ghaly (1973) models using fluid in the database and corresponding values of the Bell and Ghaly correction factor with equivalent reduced pressures**

The correction factor used in the Bell and Ghaly (1973) method approximates the effect of mass transfer in the vapor phase on the total condensation rate. It varies from zero to one by multiplying the Ψ_2 term by the vapor quality. Zero indicates minimal vapor sensible heat and thus, minimal impact of mass transfer during condensation, while one indicates that the vapor phase sensible heat is the dominant transfer term. The Bell and Ghaly (1973) correction factor increases exponentially with increasing reduced pressure, as shown in Figure 6.4, this is because the vapor-phase kinematic viscosity increases while the Reynolds number decreases.

The average deviations between the predictions of the Bell and Ghaly method and the Colburn and Drew method are used to define the regions where each model is most applicable. Figure 6.4 shows that the average deviations between the measured and predicted heat duties are greater than 20% when the Colburn and Drew (1937) method is applied to reduced pressures greater than 0.80. In contrast, the average deviations decrease below -20% when the Bell and Ghaly (1973) method is used below a reduced pressure of 0.20. The conditions for the lower reduced pressures shown in Figure 6.3 correspond to larger temperature glides, and the larger deviations observed when using the Bell and Ghaly (1973) model at these conditions is due to an over dependence of this method on the temperature glide.

The trends in the average deviation are used to define the four regions shown in Figure 6.4. These regions define conditions where: a) mass transfer can be neglected, b) where it should be modeled using the Colburn and Drew (1937) framework, i.e., between Ψ_2 = 0.05 and 0.15, c) where it should be modeled using the Bell and Ghaly (1973) model, i.e., above Ψ_2 = 0.20, and d) where using either the Bell and Ghaly (1973) or Colburn and Drew (1937) approaches are appropriate, i.e., $0.15 < \Psi_2 < 0.20$. The lower bound, where mass transfer can be neglected, is specified using the lines for each of the mixtures shown in Figure 6.4. For these mixtures, the Ψ_2 correction factor asymptotically approaches 0.05 as the reduced pressure approaches zero. Other fluid mixtures can have Ψ_2 values lower than 0.05; however, for a Ψ_2 below 0.05, the effect of mass transfer on the condensation rate is expected to be minimal. Thus, applying the Bell and Ghaly (1973) correction factor will have little-to-no impact on the calculation of the apparent heat transfer coefficient, and the effect of mass transfer can be neglected without significant loss of accuracy in the calculation of the heat transfer coefficients.

The transition line from the Bell and Ghaly (1973) approach to the Colburn and Drew (1937) approach is determined by comparing the operating conditions where the predictions of the Bell and Ghaly (1973) model begin to deviate by greater than 20% when compared to the measured heat transfer coefficients. Figure 6.4 and Table 6.1 summarize the average deviations of the Bell and Ghaly (1973) model for the heat

Table 6.1. Average deviation with the Bell and Ghaly (1973) method

Reduced Pressure, -	Mixture	Fluid Concentration	Bell and Ghaly (1973) factor (Ψ_2), -	AD, %	Pure Fluid Model
0.05	R245fa pentane	55%/45%	0.08	3%	**Cavallini *et al.* (2006)**
0.11			0.10	11%	
0.21			0.11	16%	
0.09	ammonia water	80%/20%	0.14	-45%	**Keinath *et al.* (2012)**
0.10		90%/10%	0.14	-39%	
0.11		96%/ 4%	0.12	-27%	
0.46	ethane propane	33%/67%	0.11	-13.3%	**Model presented in Chapter 4**
0.60		67%/33%	0.12	-10.3%	
0.61		33%/67%	0.14	-8.7%	
0.73		67%/33%	0.16	-6.3%	
0.80		33%/67%	0.23	0.9%	
0.87		67%/33%	0.26	4.5%	

transfer database as a function of reduced pressure. The aggregate average deviations of all of the data are mostly less than the 20% threshold because the statistics are averaged over all qualities, and typically low qualities have smaller deviations from pure fluid conditions due to reduces mass transfer effects at these conditions.

The Bell and Ghaly (1973) model performs well for the ethane-propane mixtures at all reduced pressures, i.e., the average deviation is between ±20% for all points. It has the best agreement for the high reduced pressures where the Ψ_2 values are above 0.20, while at these conditions, the Colburn and Drew (1937) approach performs increasingly poorly. The dotted pink line shown in Figure 6.4 is used to denote the bounds of applicability of the Colburn and Drew (1937) framework, which corresponds to Ψ_2 values greater than 0.20, and the Bell and Ghaly (1973) model is recommended for these conditions.

Inspection of Figure 6.4b shows that the Bell and Ghaly (1973) model increasingly under-predicts the heat transfer coefficients for both ammonia-water and ethane-propane mixtures as the reduced pressure is decreased. As noted previously, this is a result of the increased dependence on the temperature glide in estimating the impact of mass transfer on the mixture heat transfer coefficient. The resulting over-estimation of the mass transfer resistance in Eq. (6.7) causes an under-prediction of the mixture heat transfer coefficient. This can also be seen by noting that the average deviations are greater than -20% for these conditions. The deviations are greater than -20% for the ethane-propane mixture for reduced pressures below 0.40, which corresponds to a Ψ_2 value of approximately ~0.10. The deviations are greater than -20% for the ammonia-water mixture for all of the reduced pressures studied; however, the agreement between the measured heat transfer coefficients and the Bell and Ghaly (1973) predictions increases with higher reduced pressures. At the highest reduced pressure studied (0.11), the average deviation is -27%. This reduced pressure corresponds to a Ψ_2 value of approximately ~0.10, similar to the value for the ethane-propane mixtures. Therefore, this information is used to define the lower bound of the Bell and Ghaly (1973) model, which is approximately ~0.10.

Both the Colburn and Drew (1937) and the Bell and Ghaly (1973) approaches perform well in the mid reduced pressure range (between 0.40 and 0.70), with average deviations close to 0% for the ethane-propane mixtures. Additionally, Fronk (2014) recommended the Colburn and Drew (1937) framework for all of the lower reduced pressure ammonia-water conditions. Thus, the Colburn and Drew (1937) framework and the Bell and Ghaly (1973) model are equally applicable for Ψ_2 values between 0.20 and

0.10. Therefore, a transition region is defined for these conditions where either model can be used with approximately similar accuracy.

Milkie (2014) noted that the Bell and Ghaly (1973) model showed good agreement with the data at the low reduced pressure conditions for the zeotropic mixture of R245fa/pentane. Table 6.1 shows that the reduced pressures of this mixture are between 0.05 and 0.21, which corresponds to Ψ_2 values between 0.08 and 0.11, respectively. However, it should be noted that the pure fluid data for each of the components of the 245fa and pentane mixture were consistently over-predicted by the Cavallini *et al.* (2006) pure fluid correlation. Therefore, when this pure fluid model is used with the Bell and Ghaly (1973) model to calculate the apparent heat transfer coefficient, the agreement may be subject to some positive skewing due to the initial over prediction of the pure fluid heat transfer coefficient. Nonetheless, Milkie (2014) showed that the Bell and Ghaly (1973) and Colburn and Drew (1937) approaches have average deviations of 9% and 20%, respectively, for the reduced pressures investigated for the R245fa/pentane mixture. These conditions are in the transition region outlined above.

Figure 6.5 demonstrates the implementation of this model in a flowchart format. In summary, if the mass flux calculated with Eq. (6.4) and (6.5) is lower than the critical mass flux, then mass transfer effects must be considered during zeotropic mixture condensation modeling. The Ψ_2 factor defined in Eq. (6.6) should then be calculated to determine which mass transfer model is most appropriate for the operating conditions under consideration.

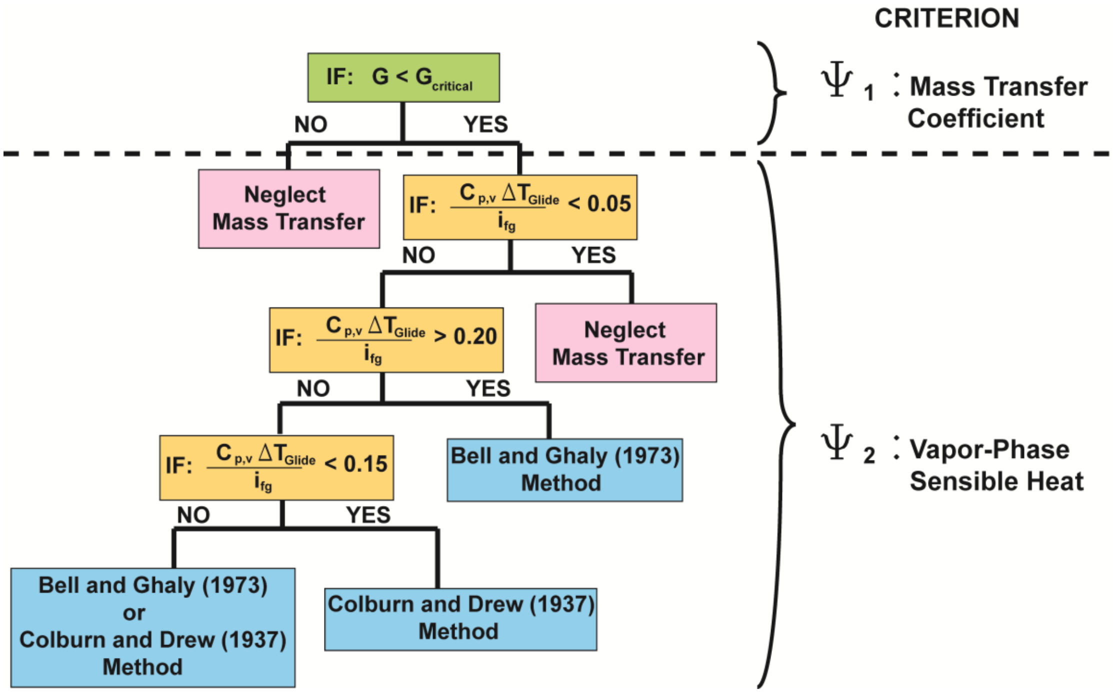

Figure 6.5: Flow chart demonstrating implementation of the outlined criteria

6.3 Conclusions

Two criteria are developed to improve the prediction of condensation of zeotropic mixtures. A large database of condensation of binary fluid mixtures of R245fa/n-pentane, ethane/propane and ammonia/water over a wide range of operating conditions is used as the basis to validate these criteria. The criteria are used sequentially; the first criterion assesses the importance of mass transfer during condensation, while the second criterion is used to select one of two established modeling techniques for the specific fluid mixture, concentrations and saturation conditions under consideration. The critical transition point for the first criterion is determined by inspection of the changes in the slope of the heat transfer coefficient from the experimental database. It is reasoned that mass transfer effects are dominant when the slope of the heat transfer coefficient is no longer monotonically increasing with quality and begins to flatten, or decrease.

It is noted that the Bell and Ghaly (1973) model can lead to large under-prediction in the mixture heat transfer coefficient at low reduced pressures, below 0.40. These pressures correspond to conditions where the temperature glide is greatest, and the Bell and Ghaly (1973) model results in an over-estimation of the vapor phase mass transfer resistance, and therefore an under-estimation of the zeotropic mixture heat transfer coefficient. Critical values of the Bell and Ghaly (1973) correction factor are defined to enable selection of the most applicable model. The Bell and Ghaly (1973) model is recommended for mid- and high- reduced pressures, above 0.40, where smaller temperature glides exist. It performs poorly at low reduced pressures, below 0.40 and for these conditions the Colburn and Drew (1937) approach is recommended. A transition region is defined where either modeling technique may be used with approximately similar degrees of accuracy.

CHAPTER 7 CONCLUSIONS AND RECOMMENDATIONS

A comprehensive study of pure and zeotropic mixtures of hydrocarbons during condensation in smooth horizontal tube across wide range of operating conditions was conducted. Condensation heat transfer coefficients and frictional pressure gradients were measured for pure propane with varying tube diameter (7.75 mm and 14.45 mm), mass flux (150, 300 and 450 kg m^{-2} s^{-1}), reduced pressure (0.25 – 0.95), quality and working fluid-to-coolant temperature difference (4, 7, 10 13°C). Experiments using zeotropic mixtures of hydrocarbons (ethane and propane) were conducted at two fluid concentrations (33/67 and 67/33), two tube diameters (7.75 and 14.45 mm), and three mass fluxes (150, 300 and 450 kg m^{-2} s^{-1}).

The trends in the pure fluid heat transfer coefficient were explained with reference to changes in flow regime, the competing influences of shear and gravity and changes in thermodynamics and transport properties. The heat transfer coefficient increased with mass flux, tube diameter, quality and working fluid-to-coolant temperature difference, and decreased at higher reduced pressures. The measured trends were compared to predictions of correlations from the literature. No correlation adequately predicted all of the observed trends, and the trends with tube diameter and working fluid-to-coolant temperature difference were not predicted correctly by any of the correlations. Notwithstanding this, the correlations that performed best were the Cavallini *et al.* (2002a) and Cavallini *et al.* (2006) correlations with AADs of 24% and 25%, respectively.

The frictional pressure drop increased with mass flux and quality and decreased at higher reduced pressures and tube diameters. Predictions of correlations from the literature demonstrated that the trends were correctly predicted, but the scaling with tube diameter and reduced pressure was not captured correctly by those correlations. The best performing among them were correlations by Andresen (2006) and Garimella *et al.* (2005) with AADs of 29% and 26%, respectively.

The investigation of the effect of working fluid-to-coolant temperature difference demonstrated that subcooling is increasingly important at higher reduced pressures. Subcooling becomes increasingly likely as the film thickness increases and turbulence mixing decreases, both of which occur at higher reduced pressures. The liquid subcooling increases the thermal conductivity of the liquid film, which increases the heat transfer coefficient. A correlation was developed that can be applied to existing correlations from the literature to account for the observed trends with temperature difference.

The trends from the experimental portion of this study were combined with physical insights from prior flow visualization studies to develop frictional pressure drop and condensing heat transfer coefficient correlations for pure fluid propane condensation. The pressure drop model accounts for the frictional pressure drops due to vapor and liquid flows as well as the additional frictional pressure drop due to liquid- and vapor- phase interactions. The model scales the individual contributions to the total pressure drop accurately based on changes in the velocities of the phases and the liquid inventory at given conditions inside the tube. A new technique that accurately models the evolution of the direction of flow of the upper liquid film with changes in quality for the prediction of heat transfer coefficients was introduced. The technique ensures a consistent physical representation of the conditions inside the tube throughout the condensation process, without the interpolations between flow regimes typically used by other correlations. The model was validated using a database containing only hydrocarbon data (propane and pentane), but is shown to also accurately predict synthetic refrigerant behavior. Special attention is paid to developing a model that is equally applicable to all of the operating conditions in the database, thus equal weighting is given to high pressure and low pressure conditions, and all mass fluxes and tube diameters. The models predict the frictional pressure drop and heat transfer coefficient for the propane database with average deviations of 3% and -1%, respectively.

The trends in heat transfer coefficient for the zeotropic mixture experiments with temperature glide, saturation pressure, concentration, mass flux, and quality and tube diameter are discussed with reference to the changing thermodynamic and physical phenomena across the condensing conditions. The heat transfer coefficient for the zeotropic mixtures has the same trend as for the pure fluid propane. The degradation in heat transfer coefficient that occurs with zeotropic mixtures due to equilibrium and non-equilibrium conditions was discussed. This degradation is most significant at large temperature glides and in the larger tube diameter, and is least significant at higher mass fluxes.

The modeling techniques most commonly used to account for the non-equilibrium conditions and changes in the bubble and dew point temperatures affecting the condensing heat transfer coefficient were assessed. The data were analyzed using the Silver (1947), Bell and Ghaly (1973) approach as well as the Colburn and Drew (1937) framework, using the correlation developed for the pure hydrocarbons as the film heat transfer coefficient model. The combination of the pure propane model and the Silver-Bell-Ghaly approach predicted the results very well, with all of the data predicted within ±25% and an AAD of 8.5%.

A set of criteria was proposed to provide guidelines on when the mass transfer effects that are present during zeotropic mixture condensation can be neglected, and when it is appropriate to apply established models in the literature. A condensation database containing fluid combinations of pairs of hydrocarbons, ammonia and water and synthetic refrigerants across large changes in operating conditions, tube diameters and concentrations is used to validate the approach. The proposed framework predicts that the Bell and Ghaly approach is valid for mid- and high- reduced pressures, i.e. above 0.40, while explicitly accounting for mass transfer using the Colburn and Drew framework is necessary at lower reduced pressures, i.e. below 0.40, where the influence of the temperature glide in the Bell and Ghaly method is weighted too strongly.

The findings of this study advance the understanding of condensation of pure and zeotropic mixtures of hydrocarbons. This work has direct application in the process industry where mixtures of hydrocarbons are inputs to a variety of cycles and refining processes. The results have further application in the HVAC industry, where propane is being considered as a working fluid due to its low GWP and improved transport properties over synthetic refrigerants.

7.1 Recommendation for Future Work

The present study has revealed several opportunities for future research that would provide insight on the condensation process, as summarized below:

1. The condensation flow regimes and flow structures at low (0.10), mid (0.40) and high (0.80) reduced pressures are assumed to be the same in the present study, which affects the delineation of annular and wavy flows. However, this assumption has not been substantiated by experimental studies in the literature. Moreover, flow regimes

other than wavy and annular flow such as intermittent flow, as the liquid inventory significantly increases, and mist flow as the phase densities of the vapor and liquid phases approach one another, may be more common at the higher reduced pressures,. A more detailed understanding of the flow regime and flow characteristics at these conditions will facilitate the development of the most appropriate condensation and pressure drop models at higher reduced pressures.

2. Some recent research (Scammell and Kim, 2015) has demonstrated the usefulness of infra-red cameras at describing the heat transfer characteristics of individual flow regimes and specific flow structures. A test setup that makes use of flow characteristics revealed by infra-red cameras, and an accurate measurement of the heat duty, would further substantiate the existence and extent the heat transfer enhancing flow structures, e.g., interfacial roughness and lower effective film thicknesses due to condensate entrained in the vapor core, at the conditions of interest in the present study.
3. The review of the literature shows that the trend in the heat transfer coefficients for tubes with diameters greater than 14.45 mm are not commonly studied. An expanded set of experiments for tube diameters both smaller and larger than the diameters investigated in the present study would provide a more comprehensive understanding of the trend with tube diameter, and enable the refinement of the model developed in Chapter 4 to make it applicable to a wide range of diameters.
4. The present study found a trend in the heat transfer coefficient with working fluid-to-coolant temperature difference that is different from the trends observed with Nusselt falling film condensation and several condensation heat transfer correlations. Thus,

here, the heat transfer coefficient was found to increase with the temperature difference, while several studies point to a decrease in heat transfer coefficient with an increasing temperature difference. Confirmation of this trend for other tube diameters, operating conditions and flow regimes would provide supporting evidence to the explanations provided in the present study.

5. The present study focused on the condensation of pure hydrocarbons and their zeotropic mixtures for the process industry. However, hydrocarbons are becoming increasingly popular as working fluids in HVAC applications, where they typically function in a cycle with a compressor that uses oil as a lubricant. The effect of small quantities of oil should be investigated to determine its effect on the pressure drop and heat transfer characteristics.
6. In the present study, the concentration of the binary fluid was assumed to be in equilibrium at the inlet to the test section and to have transitioned to a non-equilibrium state at the outlet. Additionally, the heat transfer behavior was derived directly from the measured heat duty. Direct measurement of the vapor- and liquid-phase concentrations at the inlet and outlet of the test section, and wall temperature measurements would provide a more detailed understanding of the heat and mass transfer during zeotropic mixture condensation.
7. An expanded set of zeotropic mixture test conditions with other working fluids would facilitate a confirmation of the approach outlined in Chapter 6 and a more refined definition of the boundaries for the application of each of the methods to model binary fluid condensation.

APPENDIX A COMPREHENSIVE LITERATURE REVIEW

This appendix describes in detail the experimental and modeling studies that are available in the literature on in-tube condensation of pure and zeotropic mixtures. A condensed version of the sections of this detailed literature review was presented in the pertinent chapters.

The tubes considered in the present study are considered macrochannels according to the Kandlikar (2002) classification, i.e., 7.75 mm and 14.45 mm; therefore, the studies reviewed here focus on similar tube diameters. The lower end of the tube range (8 mm) has been the focus of significant investigation over the last 30 years. The previous experimental work can be classified into three general categories: flow regime, pressure drop and heat transfer. Condensation heat transfer is greatly affected when more than one fluid is present. As such, this literature review is divided into the following sections:

- Flow regime classification
- Frictional pressure drop
- Pure fluid condensation heat transfer modeling
- Zeotropic mixture modeling

A.1 Flow Regime

A.1.1 Flow Regime Classification Studies

Taitel and Dukler (1976) developed an approach to determining the applicable flow regime that was based on a series of comparisons between dimensionless parameters that constituted ratios of the relevant physical forces for a given flow condition, i.e., momentum force ratios compared to Froude number and Froude number compared to the Martinelli parameter. This was the first modeling approach for two-phase flows that attempted to define flow regime boundaries as a balance between the competing forces causing the development of a given flow regime. The dimensionless parameters defined specific boundary lines on a flow regime map. As such, they did not provide any transition regions.

Breber *et al.* (1980) developed a flow regime map using the turbulent-turbulent Martinelli parameter that was originally develop for use in frictional pressure gradient predictions, Eq. (A.1), and the dimensionless gas velocity, Eq. (A.2), as the axes of this map.

$$X_{\mathrm{tt}} = \left(\frac{1-y}{y}\right)^{0.9} \left(\frac{\rho_{\mathrm{V}}}{\rho_{\mathrm{L}}}\right)^{0.5} \left(\frac{\mu_{\mathrm{L}}}{\mu_{\mathrm{V}}}\right)^{0.1} \tag{A.1}$$

$$J_{\mathrm{G}} = \frac{Gy}{\sqrt{Dg\rho_{\mathrm{V}}\left(\rho_{\mathrm{L}}-\rho_{\mathrm{V}}\right)}} \tag{A.2}$$

They identified four distinct zones on their map: annular/mist, bubble, wavy/stratified and slug/plug, with transition regions between each of the defined flow regimes. The flow regime boundaries lay between defined critical values for the Martinelli parameter and the dimensionless gas velocity, i.e., $1.0 < X_{\mathrm{tt}} < 1.5$ and $0.5 < J_{\mathrm{G}} < 1.5$.

Soliman (1982) proposed a modification (Eq. (A.3)) to the conventional definition of the Froude number that better characterized the competing gravitational and shear forces during two-phase flow. He compared the prediction of this criterion to his flow visualization database, and determined that a constant value of seven represented the transition point from wavy to annular flow.

$$Fr_{\mathrm{So}} = 1.26\cdot \mathrm{Re}_{\mathrm{L}}^{1.04}\left(\frac{1+1.09\cdot X_{\mathrm{tt}}^{0.039}}{X_{\mathrm{tt}}}\right)^{1.5} Ga^{-0.5} \tag{A.3}$$

Tandon *et al.* (1982) proposed a flow regime map with axes of dimensionless gas velocity and a ratio of the void fraction ($(1-\alpha)\ \alpha^{-1}$) as the axes. They outlined five distinct flow regimes on their map with no transition zones: spray, annular/semi-annular, wavy, slug and plug. A series of constant values for the void fraction ratio and the dimensionless gas velocity were identified and represent the flow regime boundaries.

Soliman (1983) and Soliman (1986) proposed transition criteria between annular and mist flow. He stated that mist flow occurs when the high shear forces that induce large-scale liquid entrainment in the vapor core, i.e., the vapor shear forces, are greater than the forces that cause adhesion of the liquid to the tube surface that are characteristic of annular flow, i.e., surface tension and liquid viscous forces.

Dobson and Chato (1998) proposed a constant Froude number, $Fr_{\mathrm{So}} = 20$, as the transition boundary point between the wavy and annular flow regimes. In defining a singular Froude number as the transition between wavy and annular flow, this approach is similar to the approach by Soliman (1982), described above. All points above a mass flux of 500 kg m^{-2} s^{-1} were defined as annular flow.

Cavallini *et al.* (2002a) proposed a modification to the Breber *et al.* (1980) map. They suggested using slightly different values as the transition lines for the flow regimes, i.e., $J_G = 2.5$, instead of 1.5, and $X_{tt} = 1.6$, instead of 1.5. This flow regime map was developed using only heat transfer data, as such flow regime changes were inferred from changes in the slope of the heat transfer coefficient when graphed as a function of quality. Thus, no visual confirmation of the changes in the flow regime was provided.

El Hajal *et al.* (2003) modified the flow regime map by Kattan *et al.* (1998) that was originally developed for boiling flows and applied it to condensation. In contrast to the dimensionless number approach that is typical of the previous investigators, they defined equations for critical values of mass flux where transitions between flow regimes occurred. A fixed value of the turbulent-turbulent Martinelli parameter, X_{tt} = 1.6, is defined for the transition between intermittent and annular flow.

Cavallini *et al.* (2006) defined a singular flow regime transition point using a critical dimensionless gas velocity equation, J_G^T, above which the flow is annular and below which, the flow is stratified. By using a single boundary and defining only two flow regimes this approach is similar to the approach defined by Dobson and Chato (1998). The critical dimensionless velocity uses the turbulent-turbulent Martinelli parameter and a constant, which has one value for hydrocarbons and another value for all other fluids, shown in Eq. (A.4).

$$
\begin{aligned}
&J_{\mathrm{G}}^{\mathrm{T}} = \left(\left(\frac{7.5}{4.3\mathrm{X}_{\mathrm{tt}}^{1.111} + 1} \right)^{-3} + C_{\mathrm{T}}^{-3} \right)^{-1/3} \\
&C_T = 1.6 \qquad \text{Hydrocarbons} \qquad (\mathrm{A.4}) \\
&C_T = 2.6 \qquad \text{Other refrigerants}
\end{aligned}
$$

Milkie (2014) conducted flow visualization studies with propane in 7.75 mm and 14.45 mm tubes for mass fluxes between 75 kg m^{-2} s^{-1} and 450 kg m^{-2} s^{-1}. He noted that Froude number defined by Soliman (1982) predicted the transition between wavy and annular flow regimes well. Critical values of the Froude number of 10 and 20 predicted the stratified and annular flow regime boundaries. This approach is similar to the approaches by Soliman (1982) and Dobson and Chato (1998) that were described above.

Table A.1 shows a summary of the models reviewed above.

Table A.1. Flow Regime Studies

Author	Diameter mm	Working Fluid	Range	Comments
Taitel and Dukler (1976)	13 - 50	Air/Water	T = 25°C - 38°C	Theoretical approach based on momentum force ratios and other dimensionless parameters
Breber *et al.* (1980)	4.8 - 50.8	R11, R12, R113, Steam, n-Pentane	G = 17-1600 kg m^{-2} s^{-1}	Map with Lockhart-Martinelli parameter and dimensionless gas velocity as axes
Soliman (1982)	4.8 - 15.9	R12, R113, Steam	T_{sat} = 27.6°C - 110°C	Proposed Fr = 7 as transition criterion between annular and wavy flow
Tandon *et al.* (1982 and 1985)	4.8 - 15.9	R12, R113		Proposed flow regime map with five distinct flow regimes. Transition regions outlined using dimensionless gas velocity and void fraction ratio
Soliman (1983 and 1986)	7.4 - 12.7	R12, R113, Steam	G = 80-1600 kg m^{-2} s^{-1} T_{sat} = 21°C - 310°C	Transition from annular to mist flow when destructive inertia force > stabilizing forces of surface tension and viscosity
Dobson and Chato (1998)	3.14 - 7.04	R12, R22, R134a, R32/R125 (50%/50% and 60%/40% concentrations)	G = 75-800 kg m^{-2} s^{-1} T_{sat} = 30°C - 60°C	Defined constant *Fr* as the transition between wavy and annular flow; flow annular for G > 500 kg m^{-2} s^{-1}
Cavallini *et al.* (2002)	8	R22, R134a, R125, R32, R236ea, R407C, R410A	G = 100-750 kg m^{-2} s^{-1}	Slight modification to the Breber et al. map
El Hajal *et al.* (2003)	3.14 - 21.4	R11, R12, R22, R32, R113, R132, R125, R134a, R236ea, R32/R125, R402A, R404A, R407C, R410A, R502, R290, R600	G = 16-1532 kg m^{-2} s^{-1} P_{sat} = 246 - 3140 kPa	Modified evaporation map. Mass flux transition lines defined for wavy, stratified, mist and bubbly regions. Fixed Martinelli parameter separates intermittent and annular regimes
Cavallini *et al.* (2006)	3.3 - 17	R22, R32, R123, R125, R134a, R142b, R236ea, R404A, R407C, R410A, R502, R507A, R717, R718, R744, R290, R600a	G = 18-1022 kg m^{-2} s^{-1}	Defined temperature dependent or temperature independent flow regimes. Gas velocity value different for halogenated refrigerants and hydrocarbons
Milkie (2014)	7.75 – 14.45	Propane	G = 75-450 kg m^{-2} s^{-1}	Proposed *Fr* of 10 and 20 as stratified and annular flow regime boundaries

A.2 Frictional Pressure Drop

A.2.1 Overview of Condensation Pressure Drop

For the condensation of a two-phase fluid, the total pressure drop has three components: the frictional, gravitational and acceleration. The present study focuses on horizontal tubes; thus, gravitational pressure drop is not important. The acceleration pressure drop arises due to the change in momentum of the liquid and vapor phases during condensation. This is due to the faster moving vapor, which has a lower density, condensing to a higher density and slower moving liquid. This results in an overall reduction in flow velocity. A simple analogy using the Bernoulli equation shows that this reduction in velocity results in an increase in the static pressure along the condensing path; as such, pressure recovery occurs due to condensation. The frictional pressure drop arises due to the vapor and liquid shear stresses exerted on the walls of the tube by these phases. An additional frictional pressure drop arises due to interactions between the phases, which move at different velocities.

The most common techniques for modeling the frictional pressure drop of a two-phase flow are outlined in this section.

A.2.2 Frictional Pressure Gradients

A common approach to modeling frictional pressure gradients is to relate the pressure drop of a two-phase fluid to either the liquid- or vapor- phase pressure drop using a two-phase multiplier that is applied to a liquid- or vapor- phase frictional pressure drop, Eq. (A.5). This equation can be written using the vapor or liquid phase velocities, or by assuming only vapor or liquid occupy the cross section of the tube diameter. In all cases the only parameter that changes is the form of the two-phase multiplier.

$$\left(\frac{dP}{dz}\right)_{\text{friction}} = \phi_{\text{V}}^2\left(\frac{dP}{dz}\right)_{\text{V}} = \phi_{\text{L}}^2\left(\frac{dP}{dz}\right)_{\text{L}} \tag{A.5}$$

Lockhart and Martinelli (1949) was one of the earliest studies to measure the pressure drop of a two-phase fluid. They conducted experiments with two immiscible fluids that were mixed at low pressure and passed through tubes of various sizes (1.48 mm and 25.83 mm). They then tabulated equations to use when calculating the two phase multipliers using the Martinelli parameter shown in Eq. (A.6).

$$X = \sqrt{\frac{\left({dP}/{dz}\right)_{\text{L}}}{\left({dP}/{dz}\right)_{\text{V}}}} \tag{A.6}$$

Chisholm and Sutherland (1969) developed a design tool that was a curve-fit of the original methodology developed by Lockhart and Martinelli. They defined two two-phase multipliers that could be applied to either the vapor or the liquid phases, Eq. (A.7) or Eq. (A.8), respectively.

$$\phi_{\text{L}}^2 = 1 + \frac{C}{\text{X}} + \frac{1}{\text{X}^2} \tag{A.7}$$

$$\phi_V^2 = 1 + CX + \text{X}^2 \tag{A.8}$$

The constant in both of these equations was specified using the same vapor and liquid criteria used by Lockhart and Martinelli, i.e., a defined constant was specified when either turbulent or laminar flow existed in the vapor or liquid phases, respectively.

Chisholm (1973) used the graphical procedure of Baroczy (1966) to develop a series of equations that could be applied to calculate a liquid only two-phase multiplier. The following equation was developed, where the exponent $n = 1$ is used for laminar flow and $n = 0.25$ for turbulent flow:

$$\phi_{\text{LO}}^2 = 1 + \left(\Gamma^2 - 1\right)\left(B \cdot y^{\frac{2-n}{2}}\left(1-y\right)^{\frac{2-n}{2}} + y^{2-n}\right) \tag{A.9}$$

The value of the Γ term is the ratio of the gas/vapor-only pressure drop to the liquid-only pressure drop, which is used to determine the value of the B term to be used in Eq. (A.9). The criteria outlined in Table A.2 are used to determine the equation for calculating the B term. The different criteria that he outlined for specific flow conditions resemble the flow regime dependent approach used to model the condensation heat transfer coefficient.

$$\Gamma = \sqrt{\frac{\left({dP}/{dz} \right)_{\mathrm{VO}}}{\left({dP}/{dz} \right)_{\mathrm{LO}}}} \tag{A.10}$$

Table A.2 Equations for *B* Chisholm (1973)

Γ	G, kg m^{-2} s^{-1}	B
≤9.5	≤500	4.8
	$500 < G < 1900$	$2400/G$
	≥1900	$55/G^{0.5}$
$9.5 < \Gamma < 28$	≤600	$520/(\Gamma G^{0.5})$
	>600	$21/\Gamma$
≥28		$15000/(\Gamma^2 G^{0.5})$

Friedel (1979b) developed a single-regime curve-fit to the liquid-only two-phase multiplier. He used a large database of conditions to determine the most appropriate values of the coefficients, as shown in Eq. (A.11) and (A.12).

$$\phi_{LO}^2 = C_{F1} + \frac{3.21 C_{F2}}{Fr^{0.045} We^{0.035}} \tag{A.11}$$

$$\begin{gathered} C_{F1} = (1-y)^2 + y^2 \left(\frac{\rho_{\mathrm{L}}}{\rho_{\mathrm{V}}} \right) \left(\frac{f_{\mathrm{VO}}}{f_{\mathrm{LO}}} \right) \\ C_{F2} = y^{0.78} (1-y)^{0.224} \left(\frac{\rho_{\mathrm{L}}}{\rho_{\mathrm{V}}} \right)^{0.91} \left(\frac{\mu_{\mathrm{L}}}{\mu_{\mathrm{V}}} \right)^{0.19} \left(1 - \frac{\mu_{\mathrm{L}}}{\mu_{\mathrm{V}}} \right)^{0.7} \end{gathered} \tag{A.12}$$

Müller-Steinhagen and Heck (1986) proposed a correlation that linearly interpolates between the all-vapor and all-liquid frictional pressure drop. They used a large database with wide variations in operating conditions to validate the predictions of their proposed method.

Garimella *et al.* (2005) used the pressure drop results from experiments on mini- and macro-channels with R134a between mass fluxes of 150 kg m^{-2} s^{-1} and 750 kg m^{-2} s^{-1} to develop a two-regime model for pressure drop in the intermittent and annular flow regimes. They proposed an interpolated technique for the pressure drop in the transition region. For annular flow, they proposed a friction factor for the vapor-liquid interface using the vapor cross section as the characteristic dimension. The interfacial friction factor was correlated to be a function of the Martinelli parameter, the liquid-phase Reynolds number and a dimensionless surface tension parameter, shown in Eq. (A.13).

$$\begin{aligned} \frac{f_{\mathrm{i}}}{f_{\mathrm{L}}} &= A \cdot \mathrm{X}_{\mathrm{tt}}^{a}\,\mathrm{Re}_{\mathrm{L}}^{b}\,\psi^{c} \\ \mathrm{Re}_{\mathrm{L}} &= \frac{GD(1-y)}{\left(1-\sqrt{\alpha}\right)\mu_{\mathrm{L}}} \\ \psi &= \frac{G(1-y)\,\mu_{\mathrm{L}}}{\rho_{\mathrm{L}}(1-\alpha)\,\sigma} \end{aligned} \tag{A.13}$$

In the intermittent regime, the pressure drop in the vapor, the annular liquid ring, the slug and due to slug transition was modeled separately. Each of these pressure drop terms was subsequently added together to determine the total pressure drop. Their model showed good agreement with their data with 82% of the data predicted within ±20%.

The Chisholm and Sutherland (1969) equation, Eq. (A.7), can be used with the definition for the Martinelli parameter to derive the two-phase multiplier expression shown in Eq. (A.14). This demonstrates that the total two-phase frictional pressure drop can be considered a combination of the pressure drop in the liquid, vapor and an additional pressure drop due to phase interactions.

$$\frac{dP}{dz} = \left(\frac{dP}{dz}\right)_{\mathrm{L}} + C\left[\left(\frac{dP}{dz}\right)_{\mathrm{L}}\left(\frac{dP}{dz}\right)_{\mathrm{V}}\right]^{0.5} + \left(\frac{dP}{dz}\right)_{\mathrm{V}} \tag{A.14}$$

Several authors have proposed correlations for the constant *C*, e.g., Mishima and Hibiki (1996) – Eq. (A.15), Ju Lee and Yong Lee (2001) – Eq. (A.16), and Andresen (2006) – Eq.(A.17).

$$C = a\,\mathrm{Re}_{\mathrm{LO}}^{b}\left(\frac{J\mu_{\mathrm{L}}}{\sigma}\right)^{c}\left(\frac{\mu_{\mathrm{L}}^{2}}{\sigma\rho_{\mathrm{L}}D}\right)^{d} \qquad \text{(A.15)}$$

$$C = 21\left(1-e^{-0.319D}\right) \qquad \text{(A.16)}$$

$$\begin{aligned} C &= 24\,\mathrm{Re}_{\mathrm{L}}^{-0.3}\,N_{\mathrm{conf}}^{-0.4} \\ N_{\mathrm{conf}} &= \frac{\left[\dfrac{\sigma}{g\left(\rho_{\mathrm{L}}-\rho_{\mathrm{V}}\right)}\right]^{0.5}}{D} \end{aligned} \qquad \text{(A.17)}$$

Mishima and Hibiki (1996) and Ju Lee and Yong Lee (2001) investigated pressure drop in microchannels, while Andresen (2006) investigated pressure drop in minichannels but included data from Jiang and Garimella (2003) and Mitra and Garimella (2003a), who conducted experiments on macrochannels. The database of Jiang and Garimella (2003), Mitra and Garimella (2003a) and Andresen (2006) is for high reduced pressures, $P_{\mathrm{r}} \geq 0.8$. He reported good agreement for his correlation with the database, with an average deviation of 14.1%.

Table A.3 shows a summary of the models reviewed above.

Table A.3. Frictional Pressure Drop Modeling Studies

Author	Diameter mm	Working fluid	Range	Comments
Lockhart and Martinelli (1949) / Chisholm and Sutherland (1969)	1.49 - 25.83	Air with: Benzene, Kerosene, Oil, Water		Proposed calculating pressure drop by applying two phase multiplier to gas or liquid only frictional pressure drop
Chisholm (1973)		Steam		Developed equations for graphical results of Baroczy for two-phase pressure drop
Friedel (1979)		Water, R12, Air/Water, Air/Oil	15 - 8250 kg m^{-2} s^{-1}	Single-regime two-phase multiplier from large database of adiabatic pressure drop
Müller-Steinhagen and Heck (1986)	14 - 24.3	R12, Steam, Argon, Hydrocarbons, Air/water, Air/oil, Nitrogen	50 - 2490 kg m^{-2} s^{-1}	Linearly interpolates between the all-vapor and all-liquid frictional pressure drop
Garimella *et al.* (2005)	0.5 - 4.91	R134a	150 - 750 kg m^{-2} s^{-1} T_{sat} = 52.3°C	Two regime model for intermittent and annular flow Pressure drop in annular regime modeled using interfacial friction factor and vapor core diameter
Andresen (2006)	0.76 - 9.4	R404A, R410A	200 - 800 kg m^{-2} s^{-1} $0.8 < P_r < 0.9$	Modeled pressure drop as combination of liquid, vapor and interaction between phases

A.3 Heat Transfer Coefficient

A.3.1 Overview of Condensation Heat Transfer

In-tube condensation begins when liquid forms on the inside surfaces of a tube/wall. For condensation to occur, the walls of the tube must be colder than the working fluid; as such, condensation occurs on the walls first and subsequently at a vapor-liquid interface. As condensation progresses, the accumulation of condensate at the walls presents a thermal resistance between the working fluid and the coolant. The liquid-film thermal resistance represents the dominant thermal resistance during in-tube condensation of pure component fluids. Therefore, the trends in heat transfer coefficient are often explained and modeled by describing the characteristics of the liquid film.

Some of the earliest models for horizontal in-tube condensation were developed by considering only annular flow throughout the condensation process. More recent studies have focused on modeling the dominant mechanisms in a given flow regime. This discussion is divided into two sections: experimental studies and modeling studies.

A.3.2 Experimental Studies

Synthetic Refrigerant and Water Studies

Traviss *et al.* (1973) conducted experiments on the condensation of R12 and R22 in horizontal tubes of 8-mm diameter for mass fluxes between 161 kg m^{-2} s^{-1} and 1530 kg m^{-2} s^{-1}. Jaster and Kosky (1976) investigated condensation of steam in horizontal tubes 12.5 mm in diameter for mass fluxes between 12.6 kg m^{-2} s^{-1} and 145 kg m^{-2} s^{-1}. The main conclusion of their work was that increasing vapor shear resulted in greater heat transfer coefficients. This conclusion is a direct result of their study being restricted primarily to the shear dominated region, i.e., annular flow.

The study by Soliman (1986) used heat transfer data from various researchers to develop a mist flow correlation. He noted that the rate of condensation in the mist flow regime is determined predominantly by the temperature difference and the mass flux of the condensing fluid. He noted that existing annular flow correlations predicted his data very poorly, with deviations typically greater than 50%. He did not independently vary the tube diameter as a variable in the heat transfer study; thus, the effect of diameter on the heat transfer coefficient for these mist flow conditions is not clear from this study.

Tandon *et al.* (1995) conducted experiments on the condensation of R12 and R22 in a horizontal tube with a 10-mm tube diameter between a mass flux range of 175 kg m^{-2} s^{-1} and 560 kg m^{-2} s^{-1}. They noted heat transfer coefficients increase with mass flux and quality, and are higher for R22, which has a higher liquid thermal conductivity and latent heat of condensation. They proposed that the increase in heat transfer coefficient with quality is due to the physical changes in the flow regimes from stratified flow to annular flow.

Dobson and Chato (1998) noted that the heat transfer coefficient remained approximately constant for an increase in mass flux from 75 - 150 kg m^{-2} s^{-1}. With a further increase in mass flux to 300 kg m^{-2} s^{-1} and at low vapor quality, the heat transfer coefficient also remained constant; however, at higher qualities, it increased with a distinct change in the slope of the heat transfer coefficient curve with quality. They attributed this to wavy flow dominating at the lower mass flux and low quality conditions at which the heat transfer mechanism is dominated by falling-film flow. At higher mass fluxes and higher qualities, annular flow dominates and is dramatically affected by vapor liquid shear. They noted that the effect the fluid and its thermophysical properties on the heat transfer coefficient changes with flow regime. In the stratified flow regime, they stated that R22 has the highest heat transfer coefficients. They attributed this to a higher wavy flow index, shown in Eq. (A.18), which is a combination of the thermophysical properties of the fluid.

$$\left(\frac{\rho_{\mathrm{L}}\left(\rho_{\mathrm{L}}-\rho_{\mathrm{V}}\right)k_{\mathrm{L}}^{3}i_{\mathrm{fg}}}{\mu_{\mathrm{L}}}\right)^{0.25} \tag{A.18}$$

In the annular flow regime, R134a has the highest heat transfer coefficients, which was attributed to R134a operating at a lower reduced pressure than the other fluids, and therefore having a higher phase-change enthalpy and flow velocities at the same mass flux. They conducted their experiments on three tube diameters (3.14, 4.57 and 7.04 mm), independently varying the mass flux and saturation temperature for each diameter. The main conclusion from this work was the quality at which the flow transitioned to annular flow, which manifested as a change in the slope of the heat transfer coefficient plotted as a function of quality.

Cavallini *et al.* (2001) conducted experiments on an 8-mm test section using R22, R134a, R236ea, R125, R32, R410A for several refrigerant-to-wall temperature differences, i.e., 2.5 - 17°C, and for mass fluxes between 100 kg m^{-2} s^{-1} and 750 kg m^{-2} s^{-1}. They noted a linear increase in the heat transfer coefficient with quality at the higher mass fluxes. At lower mass fluxes, the dependence of the heat transfer coefficient on quality is lower. Their experiments were for saturation temperatures between 30°C and 50°C, for which they noted only that lower saturation temperatures have a higher heat transfer coefficient. They also stated that the refrigerants in the low- and mid-range reduced pressures perform better than the high-pressure refrigerants. They attribute this to better thermo-physical properties at lower reduced pressures.

Milkie (2014) conducted experiments on 7.75 mm and 14.45 mm horizontal tubes with n-pentane and R245fa for mass fluxes between 100 and 600 kg m^{-2} s^{-1} at low reduced pressures, $P_r < 0.21$. He noted that there is a slight increase in heat transfer coefficient with tube diameter; however, there was a very large pressure drop in the test section. It should be noted that for the low pressure fluid (n-pentane), small changes in pressure result in large changes in the saturation temperature, thereby altering thermophysical properties, which may obscure these trends.

A.3.3 Modeling Studies

Nusselt (1916) derived an analytical expression for falling-film condensation on a flat surface. A slightly adjusted form of this analysis for curved surfaces is shown in Eq. (A.19). This analysis was originally developed for falling film condensation on the outside of tubes. The most notable change from the flat plate result is the length scale, which is the tube diameter, and not the distance along the plate. This analysis assumes a constant surface temperature, a linear temperature profile in the liquid film and laminar liquid-film flow, and assumes that no shear forces act on the vapor-liquid interface. The final assumption is generally true for falling films; however, for flows inside tubes, there can be significant axial shear stresses on the liquid film.

$$h_{\mathrm{Nusselt}} = 0.728\left(\frac{\rho_{\mathrm{L}}\left(\rho_{\mathrm{L}}-\rho_{\mathrm{V}}\right) g i_{\mathrm{fg}} k_{\mathrm{L}}{}^{3}}{\mu_{\mathrm{L}} D\cdot\Delta T}\right)^{1/4} \tag{A.19}$$

Several correlations have been developed by researchers that apply exclusively to the annular flow regime. They typically use the Dittus and Boelter (1930) single-phase turbulent flow convection correlation as their starting point and apply an additional term, called the two-phase multiplier, which accounts for two-phase flow effects. The key differentiating factors between the correlations proposed by researchers are the specific definition of the Reynolds number and the form of the two-phase multiplier used to account for two-phase effects.

Kosky and Staub (1971) outlined one of the first methods for calculating the local heat transfer coefficient for condensing flows in the annular regime. They derived a shear velocity from the frictional pressure drop and used the heat and momentum analogy to calculate the condensation heat transfer coefficient, which relates the turbulent momentum and the heat transfer, shown in Eq. (A.20). Equation (A.20) shows that their original formulation with the turbulent velocity can be written using an equation format that is similar to the Dittus and Boelter (1930) correlation for single-phase heat transfer. A dimensionless temperature is used to account for two-phase effects. This two-phase multiplier is a function of the dimensionless film thickness and Prandtl number. The dimensionless film thickness is in turn defined as a function of the liquid Reynolds number.

$$
\begin{aligned}
h_{\text{Kosky \& Staub}} &= \frac{\rho_{\mathrm{L}} C_{\mathrm{p,L}} u^{*}}{T^{+}\left(\delta^{+}, \mathrm{Pr}_{\mathrm{L}}\right)} \\
&\equiv \frac{\rho_{\mathrm{L}} u^{*} D}{\mu_{\mathrm{L}}} \cdot \frac{\mu_{\mathrm{L}} / \rho_{\mathrm{L}}}{k_{\mathrm{L}} / \left(\rho_{\mathrm{L}} C_{\mathrm{p,L}}\right)} \cdot \frac{1}{T^{+}\left(\delta^{+}, \mathrm{Pr}_{\mathrm{L}}\right)} \equiv \mathrm{Re}_{\mathrm{L}}\, \mathrm{Pr}_{\mathrm{L}} \cdot \frac{1}{T^{+}\left(\delta^{+}, \mathrm{Pr}_{\mathrm{L}}\right)} \\
u^{*} &= \sqrt{\frac{-D}{4\rho_{\mathrm{L}}}\left(\frac{dP}{dz}\right)_{\text{friction}}} \qquad \text{(A.20)} \\
T^{+} &= f\left(\delta^{+}, \mathrm{Pr}_{\mathrm{L}}\right) \\
\delta^{+} &= f\left(\mathrm{Re}_{\mathrm{L}}\right)
\end{aligned}
$$

Traviss *et al.* (1973) presented a correlation that followed the Kosky and Staub (1971) method for annular flows. However, they proposed a different exponent for the Reynolds number and used an additional two-phase multiplication factor, *F*, shown in Eq.

(A.21). Therefore, both the Kosky and Staub (1971) and the Traviss *et al.* (1973) correlations propose a direct link between the frictional pressure drop of the fluid and the rate of condensation heat transfer, and they both assume annular flow throughout the condensation process.

$$\begin{aligned} h_{\text{Traviss et al.}} &= \mathrm{Re}_{\mathrm{L}}^{0.9}\,\mathrm{Pr}_{\mathrm{L}} \cdot \frac{1}{T^{+}\left(\delta^{+}, \mathrm{Pr}_{\mathrm{L}}\right)} F \\ F &= \left[0.15 \cdot \left(\mathrm{X}_{\mathrm{tt}}^{-1} + 2.85 \cdot \mathrm{X}_{\mathrm{tt}}^{-0.476}\right)\right]^{a} \end{aligned} \tag{A.21}$$

Jaster and Kosky (1976) developed one of the first flow-regime-dependent heat transfer coefficient models. As such, they attempted applying correlations that modeled the modes of heat transfer for specific conditions inside the tube. Their correlation divided the flow into three regimes: stratified, annular, and transition between them. In the annular regime, they suggested using the Kosky and Staub (1971) model, Eq. (A.20). In the stratified regime, they recommended an adjustment to the constant in the Nusselt (1916) falling-film model, Eq. (A.19). In the transition region, they recommended a linear interpolation between the annular and stratified Nusselt numbers using Froude number based boundaries.

Shah (1979) developed an empirical curve fit from a large database of heat transfer coefficients for mass fluxes ranging between 11 kg m^{-2} s^{-1} and 211 kg m^{-2} s^{-1}, reduced pressured between 0.002 and 0.44, and liquid Prandtl numbers between 1 and 13. He applied a two-phase multiplier to the Dittus and Boelter (1930) single-phase correlation, as shown in Eq. (A.22). He notes that the correlation does not work well at higher qualities or when liquid entrainment in the vapor core should be considered. He reported good agreement between the 474 data points and his correlations with a mean deviation of 15.4%.

$$h_{\text{Shah}} = h_{\text{L}}\left[\left(1-y\right)^{0.8} + \frac{3.8q^{0.76}\left(1-y\right)^{0.04}}{P_r^{0.38}}\right]$$

$$h_{\text{L}} = 0.023\cdot \text{Re}_{\text{LO}}^{0.8}\cdot \text{Pr}_{\text{L}}^{0.4}\frac{k_{\text{L}}}{D} \tag{A.22}$$

Soliman (1986) proposed a correlation for the mist flow regime by assuming that the vapor and liquid phases move together and that they can be modeled using the equation shown in Eq. (A.23).

$$h_{\text{Soliman}} = 0.00345\,\text{Re}_{\text{m}}^{0.9}\left(\frac{\mu_{\text{V}} i_{\text{fg}}}{k_{\text{V}}\Delta T}\right)^{1/3}\frac{k_{\text{L}}}{D} \tag{A.23}$$

His original equation can be re-written as Eq. (A.24), which has the same form as the annular flow correlations described above, i.e., it uses the Dittus and Boelter (1930) correlation as the basis, with a two-phase multiplier that incorporates the Jakob number (temperature dependence). He defines a Reynolds number using a two-phase density and the total mass flux, and proposes using the vapor Prandtl number in his Nusselt number correlation, but defines the Nusselt number using the liquid thermal conductivity. Considering the phase that is in contact with the wall in mist flow is mostly vapor, using the vapor Prandtl number seems reasonable; however, the rationale for using the liquid thermal conductivity is unclear. Importantly, he notes that the correlation should not be used in the annular regime because of the substantial differences in the heat transfer mechanism in the two regimes, i.e., the development of a liquid layer on the surface of the tube in the annular regime is different from the combined flow of vapor and liquid that occurs in mist flow.

$$h_{\text{Soliman}} = 0.00345\,\text{Re}_{\text{m}}^{0.9}\,\text{Pr}_{\text{V}}^{1/3}\left(\frac{1}{Ja}\right)^{1/3}\frac{k_{\text{L}}}{D} \tag{A.24}$$

Tandon *et al.* (1995) proposed a correlation similar in form to the Soliman (1986) correlation, as shown in Eq. (A.25). However, they applied the correlation to all condensation conditions and suggested using the vapor Reynolds number and liquid Prandtl number. They divided the flow into either an annular/semi-annular or a wavy flow. The transition between the two regimes was defined by a vapor-phase Reynolds number. Different coefficients and exponents in the heat transfer coefficient correlation were proposed for the different flow regimes. Their model also includes the Jakob number to account for different working fluid-to-coolant temperature differences.

$$\begin{aligned} h_{\text{Tandon } et\ al.} &= 23.1\,\text{Re}_{\text{V}}^{1/8}\,\text{Pr}_{\text{L}}^{1/3}\left(\frac{1}{Ja}\right)^{1/6}\frac{k_{\text{L}}}{D} \qquad \text{Re}_{\text{V}} \le 30{,}000 \\ h_{\text{Tandon } et\ al.} &= 0.084\,\text{Re}_{\text{V}}^{0.67}\,\text{Pr}_{\text{L}}^{1/3}\left(\frac{1}{Ja}\right)^{1/6}\frac{k_{\text{L}}}{D} \qquad \text{Re}_{\text{V}} \ge 30{,}000 \end{aligned} \tag{A.25}$$

Dobson and Chato (1998) developed a two-regime model that divided the flow into either stratified or annular flow, as shown in Eq. (A.26), using the flow regime transition criteria discussed in Section 1.1.2.

$$\begin{aligned} h_{\text{Dobson \& Chato - stratified}} &= \left[0.23\frac{\text{Re}_{\text{VO}}{}^{0.12}}{1+1.11\text{X}_{\text{tt}}{}^{0.58}}\left(\frac{Ga\text{Pr}_{\text{L}}}{Ja_{\text{L}}}\right)^{0.25} + \left(1-\frac{\theta}{\pi}\right)\text{Nu}_{\text{forced}}\right]\frac{k_{\text{L}}}{D} \\ \text{Nu}_{\text{forced}} &= 0.0195\text{Re}_{\text{L}}{}^{0.8}\text{Pr}_{\text{L}}{}^{0.4}\sqrt{1.376+\frac{c_1}{X_{\text{tt}}^{c_2}}} \\ h_{\text{Dobson \& Chato - annular}} &= \left[0.023\text{Re}_{\text{L}}{}^{0.8}\text{Pr}_{\text{L}}{}^{0.4}\left(1+\frac{2.22}{\text{X}_{\text{tt}}{}^{0.89}}\right)\right]\frac{k_{\text{L}}}{D} \end{aligned} \tag{A.26}$$

In the stratified regime, they proposed using two models that account for the relative contributions to the total heat transfer, i.e., falling-film condensation in the upper portion of the tube, and forced convection in the pool of liquid at the base of the tube. The total heat transfer rate was calculated by adding the falling-film and convective heat transfer contributions. The contribution of the pool heat transfer was determined using the stratified film angle, which is a proxy for the exposed surface area of the liquid pool. The stratified film angle was measured from the top center of the tube to the height of the liquid pool at the base of the tube. Their annular regime model uses a two-phase multiplier with the Dittus and Boelter (1930) single-phase liquid correlation. Their model resulted in good agreement between their data and a database from other authors.

Moser *et al.* (1998) suggested an equivalent Reynolds number model that proposed using an all-liquid “equivalent” mass flux that has the same wall shear stress as the two-phase fluid. They used the heat and momentum analogy to relate the shear stress to the heat transfer coefficients. The equivalent Reynolds number calculated from the equivalent mass flux is then used in a single-phase heat transfer correlation to predict the condensing heat transfer coefficient, as shown in Eq. (A.27). Their correlation shows good agreement with their database, with an average deviation of 13.64%. However, they note that this correlation applies only to the annular flow regime.

$$\begin{aligned}
\mathrm{Re}_{\mathrm{equivalent}} &= \sqrt{-\left(\frac{dP}{dz}\right)_f \left(\frac{\rho_{\mathrm{L}} D^3}{2\mu_{\mathrm{L}}^2 f_{\mathrm{L},eq}}\right)} \\
h_{\mathrm{Moser}\ et\ al.} &= h_{\mathrm{Petukhov}} \cdot F \\
F &= 1.31\left(R^+\right)^{C1} \mathrm{Re}_{\mathrm{L}}^{\,C2}\, \mathrm{Pr}_{\mathrm{L}}^{-0.185} \qquad \text{(A.27)} \\
C1 &= 0.126\,\mathrm{Pr}_{\mathrm{L}}^{-0.448} \\
C2 &= -0.113\,\mathrm{Pr}_{\mathrm{L}}^{-0.563} \\
R^+ &= 0.0994\,\mathrm{Re}_{\mathrm{equivalent}}^{7/8}
\end{aligned}$$

Guo and Anand (2000) proposed a composite heat transfer model to calculate the heat transfer occurring in a rectangular channel with sides 12.7 mm × 25.4 mm and for low mass fluxes, between 74 and 178 kg m^{-2} s^{-1}. The model calculated the heat transfer occurring along the top, the walls and the base of the channel separately. The overall heat transfer coefficient of the tube is calculated from an area-averaged summation of heat transfer coefficients on the four sides. They used the von Karman universal velocity profile to calculate the heat transfer coefficient on the top of the tube, Nusselt falling-film condensation on the sides, and an all-liquid correlation for the base of the channel, as shown in Eq. (A.28). The model was applied to all flow regimes. The liquid pool depth at the base of the tube is calculated from the fluid accumulated from the walls and top of the channel. They noted very good agreement between their model and the data, with a mean deviation of 6.75%.

$$h_{\text{Guo \& Anand}} = \frac{h_{\text{von Karman}} A_{top} + h_{\text{Nusselt}} A_{vertical} + h_{\text{Dittus-Boelter}} A_{bottom}}{A_{top} + A_{vertical} + A_{bottom}} \tag{A.28}$$

Using experimental results of Cavallini *et al.* (2001), Cavallini *et al.* (2002a) proposed a heat transfer model for halogenated refrigerants in horizontal tube diameters between 3 mm and 21 mm. The approach is similar to the Dobson and Chato (1998) approach - in the stratified regime, they proposed a combination of a modified Nusselt falling-film heat transfer correlation and a modified Dittus and Boelter (1930) liquid pool convective correlation. In contrast to the Dobson and Chato (1998) method, they apply the Nusselt falling-film correlation only to the exposed surface area of the falling film and the pool contribution to the exposed surface area of the pool, as shown in Eq. (A.29).

$$h_{\text{Stratified}} = \frac{h_{\text{Nusselt}}\theta + \left(2\pi - \theta\right) h_{\text{Pool}}}{2\pi} \tag{A.29}$$

In the annular regime, they recommended using the Kosky and Staub (1971) correlation that was described above, Eq. (A.20). They proposed a modified Friedel (1979b) correlation for calculating the frictional pressure drop term and the resultant shear velocity. They used their modified Breber *et al.* (1980) flow regime map to determine the flow regime boundaries. Their model shows good agreement with the data with an average deviation of -2.2%.

Thome *et al.* (2003) developed a flow regime dependent correlation for stratified and annular flow. They used the flow regime map developed by El Hajal *et al.* (2003) to determine the applicable flow regimes. The approach they used to model the condensation heat transfer in the stratified regime model was similar to the Cavallini *et al.* (2002a) approach shown in Eq. (A.29). It models Nusselt falling-film condensation in the upper part of the tube and uses a convective correlation in the pool at the base of the tube. They introduced a new correlation for the annular flow regime heat transfer coefficient using the Dittus and Boelter (1930) root that has been used by several previous investigators and a new formulation of the two-phase multiplier. Their definition of the Reynolds number uses the liquid-film thickness, which is derived from the assumption that the vapor core is surrounded by a uniform annular liquid ring that adheres to the tube surface. The two-phase multiplier is modeled as an interfacial roughness term for the vapor-liquid interface. They note that by modeling the condensation heat transfer coefficient in this way, the heat transfer in the film can be modeled directly, and the increased heat transfer that occurs due to interfacial disturbances can be accounted for using the interfacial roughness term, as shown in Eq. (A.30).

$$\begin{aligned} h_{\text{Thome } et\ al.} &= \frac{k_{\text{L}}}{\delta} 0.003 \cdot \text{Re}_{\delta}{}^{0.74} \text{Pr}_{\text{L}}{}^{0.5} f_{\text{i}} \\ \text{Re}_{\delta} &= \frac{G(1-y)\delta}{\mu} \\ f_{\text{i}} &= 1 + \left(\frac{\Delta\rho g \delta}{\sigma} \right) \cdot \frac{u_{\text{V}}}{u_{\text{L}}} \end{aligned} \tag{A.30}$$

Cavallini *et al.* (2006) proposed a heat transfer correlation with temperature dependent (stratified) and temperature independent (annular) regions. They modeled the heat transfer in the stratified region using an approach similar to the (Cavallini *et al.*, 2002a) approach discussed above. However, instead of using the stratified film angle to attribute relative surface areas for the falling film and pool, the vapor quality was used. In the annular regime, they used the Dittus and Boelter (1930) single-phase heat transfer correlation and applied a two-phase multiplier to account for the increased heat transfer due to two-phase flow. In each regime, they proposed empirical curve-fits to the original models. The critical dimensionless gas velocity described above defined the transition between the stratified and annular flow regimes. They note that although some of the datasets show considerable scatter, the model shows generally good agreement with the data. While the correlation is validated against data with reduced pressures greater than 0.8, they note that caution should be exercised because only one data set was used for this validation.

ΔT dependent flow regime ($J_{\mathrm{G}} \le J_{\mathrm{G}}{}^{\mathrm{T}}$):

$$\begin{aligned}
h_{\text{Cavallini } et\ al.} &= \left(h_{\text{annular}} \left(\frac{J_{\mathrm{G}}^{\mathrm{T}}}{J_{\mathrm{G}}} \right)^{0.8} - h_{\text{stratified}} \right) \left(\frac{J_{\mathrm{G}}}{J_{\mathrm{G}}^{\mathrm{T}}} \right) + h_{\text{stratified}} \\
h_{\text{stratified}} &= 0.725 \left(1 + 0.741 \left(\frac{1-y}{y} \right)^{0.3321} \right)^{-1} \left(\frac{k_{\mathrm{L}}{}^{3} \rho_{\mathrm{L}} \left(\rho_{\mathrm{L}} - \rho_{\mathrm{V}} \right) g i_{\mathrm{fg}}}{\mu_{\mathrm{L}} D \mathit{\Delta} T_{\text{wall}}} \right)^{0.25} + \left(1 - y^{0.087} \right) h_{\mathrm{LO}} \\
h_{LO} &= 0.023 \, \mathrm{Re}^{0.8} \, \mathrm{Pr}^{0.4} \, \frac{k_{\mathrm{L}}}{D}
\end{aligned} \tag{A.31}$$

ΔT independent flow regime ($J_{\mathrm{G}} < J_{\mathrm{G}}{}^{\mathrm{T}}$):

$$h_{\text{Cavallini } et\ al.} = h_{\text{annular}} = h_{\mathrm{LO}} \left(1 + 1.128 q^{0.817} \left(\frac{\rho_{\mathrm{L}}}{\rho_{\mathrm{V}}} \right)^{0.3685} \left(\frac{\mu_{\mathrm{L}}}{\mu_{\mathrm{V}}} \right)^{0.2363} \left(1 - \frac{\mu_{\mathrm{V}}}{\mu_{\mathrm{L}}} \right)^{2.144} \mathrm{Pr}_{\mathrm{L}}{}^{-0.1} \right) \tag{A.32}$$

Figure A.1 summarizes the studies discussed. Table A.4 shows a summary of the modeling approaches reviewed above.

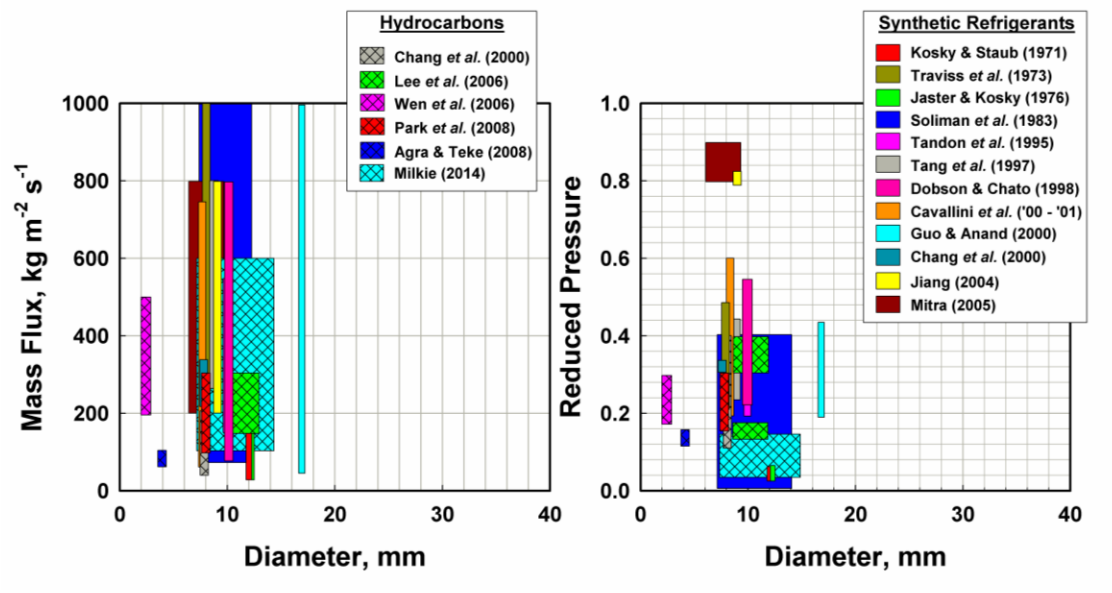

Figure A.1 Literature survey of pure fluids studies

Table A.4 Condensation Heat Transfer Coefficient Models

Author	Diameter mm	Working Fluid	Range	Comments
Kosky and Staub (1971)	12.57	Steam	2.7 - 150 kg m^{-2} s^{-1} 20 < P_{sat} < 156 kPa	Heat and mass transfer analogy to all-annular regime model
Traviss *et al.* (1973)	8	R12, R22	161 - 1530 kg m^{-2} s^{-1} 25°C < T_{sat} < 58°C	Heat and mass transfer analogy to all-annular regime model
Jaster & Kosky (1976)	12.5	Steam	12.6 - 145 kg m^{-2} s^{-1} 20 < P < 170 kPa	Flow regime dependent correlation for annular and stratified regimes
Soliman (1986)	7.4 - 12.7	R12, R113, Steam	80 - 1600 kg m^{-2} s^{-1} 21°C < T_{sat} < 310°C	Proposed shear-dominant mist flow regime model
Tandon *et al.* (1995)	10	R12, R22	175 - 560 kg m^{-2} s^{-1} 20°C < T_{sat} < 40°C	Adjusted Akers and Rosson correlation
Dobson and Chato (1998)	3.14 - 7.04	R12, R22, R134a, R32/R125	75 - 800 kg m^{-2} s^{-1} 30°C < T_{sat} < 60°C	Two-regime model: falling-film and convective for stratified; two-phase multiplier in annular
Moser *et al.* (1998)	3.14 - 20	R11, R12, R22, R113, R125, R134a, R410A	87 - 1533 kg m^{-2} s^{-1} 22°C < T_{sat} < 52°C	Equivalent *Re* model using heat-momentum analogy
Guo and Anand (2000)	16.9	R410A	30 - 2200 kg m^{-2} s^{-1} 3.7°C< T_{sat} < 36.7°C	von Karman analogy in upper section, falling film on walls and pool at base channel
Cavallini *et al.* (2002)	3 - 21	R22, R134a, R125, R32, R236ea, R407C, R410A	100 - 750 kg m^{-2} s^{-1} P_r < 0.75	Falling-film and convective correlations in stratified regime Annular regime Kosky and Staub (1971) model
Thome *et al.* (2003)	3.1 – 21.4	R11, R12, R22, R32, R113, R125, R134a, R236ea, R404A, R410A, R290, R600a,R32/R125	24 - 1022 kg m^{-2} s^{-1} P_r < 0.80	Two regime model. Annular regime uses two-phase multiplier to account for enhancement due to interfacial roughness
Cavallini *et al.* (2006)	3 - 17	R22, R134a, R410A, R125, R32, R236ea, R407C, R502, R507A, R404a, R142b, R744, R717, R718, R290, R600a,	100 - 750 kg m^{-2} s^{-1} P_r < 0.75	Two regime model similar to Cavallini *et al.* (2002)

A.4 Zeotropic Mixture Modeling

A.4.1 Equilibrium

The Silver (1947) and Bell and Ghaly (1973) method models two thermal resistances in series. The first thermal resistance is the condensation thermal resistance that is determined using any of the pure fluid correlations outlined above. The second thermal resistance approximates the effect of mass transfer on the condensation rate, as shown in Eq. (A.33).

$$\begin{gathered} h_{\text{Bell \& Ghaly}} = \left(\frac{1}{h_{\text{pure fluid}}} + \frac{Z}{h_{\text{vapor}}} \right)^{-1} = \left(R_{\text{pure fluid}} + R_{\text{mass transfer - vapor phase}} \right)^{-1} \\ Z = \frac{dQ_{\text{SV}}}{dQ_{\text{Total}}} \end{gathered} \tag{A.33}$$

The pure-fluid thermal resistance is based on condensation as a single-component fluid, i.e., at a constant temperature and in the absence of changes in concentration. The second thermal resistance simulates the mass transfer resistance by multiplying the thermal resistance due to heat transfer in the vapor phase by a ratio of the vapor phase sensible cooling to the total latent heat of phase change. This method is known as an "equilibrium" model because it assumes both vapor and liquid phases are in equilibrium throughout condensation. Thus, it neglects the specific details of the liquid- and vapor-phase concentrations and gradients.

A study by Webb *et al.* (1996) showed that this method might be "unsafe" when applied to Lewis numbers greater than unity, i.e., it under-predicts the size of condenser required for complete condensation of the working fluid. When Lewis numbers are less than 0.8, they deemed this approach "safe," i.e., it over-predicts the condenser size required for complete condensation of the working fluid. Therefore, they recommend that this method should only be used when Lewis numbers are below unity.

Shao and Granryd (1998) proposed an empirical adjustment to a pure-fluid heat transfer correlation to predict the local heat transfer coefficient of zeotropic mixtures, as shown in Eq. (A.34). The approach was to be applied only in the annular flow regime and they noted that this equation performs poorly in the stratified regime. Equation (A.34) is similar to the Silver (1947), Bell and Ghaly (1973) method. It models the mixture condensation heat transfer coefficient as a degraded equilibrium heat transfer coefficient of the pure fluid.

$$\begin{aligned} h_{\text{Shao \& Granryd}} &= h_{\text{pure fluid}} \cdot \frac{1}{1+A_1+A_2} \\ A_1 &= yZ_1\left(\frac{C_{\text{p,V}}}{C_{\text{p,w}}}\right)\left(\frac{h_{\text{pure fluid}}}{h_{\text{V}}}\right) \\ A_2 &= \left(1-y\right)Z_2\left(\frac{C_{\text{p,L}}}{C_{\text{p,w}}}\right)\left(\frac{h_{\text{pure fluid}}}{h_{\text{L}}}\right) \\ Z_1 &= 1.1y\left[1-e^{-10(1-y)}\right] \\ Z_2 &= 0.9\left(1-y\right) \end{aligned} \tag{A.34}$$

Del Col *et al.* (2005) developed an adjustment to the Bell and Ghaly (1973) model using data from Cavallini *et al.* (2000), Lee (1994) and Kim *et al.* (1996). They proposed using the Thome *et al.* (2003) correlation for condensation of a pure fluid and applying the following correction factors to account for mixture effects. The Bell and Ghaly (1973) method decreases the heat transfer coefficient from the pure fluid value at higher qualities and an additional empirical correction factor, F_{m}, decreases the heat transfer coefficient from the pure fluid values at lower qualities.

$$
\begin{aligned}
h_{\text{Del Col } et\ al.} &= F_{\text{m}}\left(\frac{1}{h_{\text{pure fluid}}}+R_f\right)^{-1} \\
R_f &= \frac{yC_{\text{p,V}}\Delta T_{\text{Glide}}}{i_{\text{fg - mixture}}}\frac{1}{h_{\text{V}}} \qquad \text{(A.35)} \\
F_{\text{m}} &= \exp\left[-0.25\left(1-y\right)\left(\frac{G_{\text{wavy}}}{G}\right)^{0.5}\frac{\Delta T_{\text{Glide}}}{T_{\text{sat}}-T_{\text{wall}}}\right]
\end{aligned}
$$

Empirical adjustments to pure-fluid correlations have been proposed by several researchers to account for the non-equilibrium conditions of zeotropic mixtures. Tandon *et al.* (1986) proposed the correlation shown in Eq. (A.36), Chang *et al.* (2000) proposed the correlation shown in Eq. (A.37) and Thonon and Bontemps (2002) proposed the correlation shown in Eq. (A.38).

$$
h_{\text{Tandon } et\ al.} = 2.82\,\text{Pr}^{1/3}\,\text{Re}^{0.14}\left(\frac{1}{Ja}\right)^{0.365}\frac{k_{\text{L}}}{D} \qquad \text{(A.36)}
$$

$$
\begin{aligned}
X_c &= \left(\frac{1-y}{y}\right)^{0.8}\left(\frac{P}{P_{crit}}\right)^{0.5} \\
h_{\text{l}} &= 0.023\,\text{Re}_{\text{l}}^{0.8}\,\text{Pr}_{\text{l}}^{0.4}\,\frac{k_{\text{l}}}{D} \qquad \text{(A.37)} \\
h_{\text{Chang } et\ al.} &= h_{\text{l}}\left(1+\frac{2.5}{X_c^{0.912}}\right)
\end{aligned}
$$

$$
h_{\text{Thonon \& Bontemps}} = h_{LO}\cdot 1564\,\text{Re}_{\text{eq}}^{-0.76} \qquad \text{(A.38)}
$$

A.4.2 Non-equilibrium

Colburn and Drew (1937) developed a framework of coupled equations to calculate the mass, species and energy fluxes of the individual components of a mixture as they condense. They proposed that the condensing flux of one component in the vapor phase, the more volatile component, could be modeled using Eq. (A.39), which is on a molar basis. This equation is integrated over the distance through which mass transfer occurs, i.e., the radial distance from the interface to the center of the tube, to obtain the total amount of both components that condense, Eq. (A.40).

$$\dot{N}_1 = \left(\dot{N}_1 + \dot{N}_2\right) \cdot z = \left(\dot{N}_1 + \dot{N}_2\right) \tilde{y}_1 + \beta_{\mathrm{V}} \frac{d\tilde{y}_1}{d\eta} \tag{A.39}$$

$$\left(\dot{N}_1 + \dot{N}_2\right) = \dot{N}_{\mathrm{T}} = \beta_{\mathrm{V}} \ln\left(\frac{z - \tilde{y}_{1,\mathrm{i}}}{z - \tilde{y}_{1,\mathrm{b}}}\right) \tag{A.40}$$

A similar integration of the energy equation allows the vapor sensible heat associated with condensation to be calculated. As with the mass flux equations in Eq. (A.39), the total vapor sensible heat flux is the summation of the heat transfer due to concentration shifts of the species and the transport of the species to the interface, Eq. (A.41). For this reason, the correction proposed by Ackerman (1937) is applied to the single-phase heat transfer equation shown in Eq. (A.42) to account for the non-zero species flux that should increase the sensible heat transfer rate.

$$q''_{\mathrm{S,V}} = \left(\dot{N}_1 \cdot \tilde{c}_{\mathrm{p},1} + \dot{N}_2 \cdot \tilde{c}_{\mathrm{p},2}\right)\left(T_{\mathrm{V}} - T_{\mathrm{i}}\right) + h_{\mathrm{V}} \frac{dT}{d\eta} \tag{A.41}$$

$$\begin{gathered} q''_{\mathrm{S,V}} = h_{\mathrm{V}}\left(T_{\mathrm{V}} - T_{\mathrm{i}}\right) \frac{a}{1 - \exp(-a)} \\ a = \frac{\left(\dot{N}_1 \cdot \tilde{c}_{\mathrm{p},1} + \dot{N}_2 \cdot \tilde{c}_{\mathrm{p},2}\right)}{h_{\mathrm{V}}} \end{gathered} \tag{A.42}$$

The condensing latent heat of the mixture is calculated from the condensing molar fluxes of each species and their corresponding latent heats, Eq. (A.43). The total heat duty in a section length is the summation of the latent and sensible heat terms, as shown in Eq. (A.44).

$$q''_{\lambda} = \dot{N}_1 \cdot i_{\mathrm{fg},1} + \dot{N}_2 \cdot i_{\mathrm{fg},2} \tag{A.43}$$

$$q''_{\mathrm{total}} = q''_{\lambda} + q''_{\mathrm{S,V}} \tag{A.44}$$

These equations are highly coupled and require a simultaneous solution of the species, mass and energy balance equations. However, the system of equations can only be solved by using several closure correlations. For example, correlations are required for: 1) the vapor-phase heat transfer coefficient, 2) the condensate-film heat transfer coefficient, and 3) the vapor-phase mass transfer coefficient. The Colburn and Drew (1937) methodology was originally formulated purely for film condensation, but Price and Bell (1973) described a procedure to adapt it as a design tool for heat exchanger design.

Fronk (2014) noted that, for high glide mixtures, sub-cooling of the liquid film can be an important consideration. He proposed that the liquid temperature could be calculated using a specified temperature profile, as shown in Eq. (A.45).

$$T_{\mathrm{L,out}} = T_{\mathrm{wall,out}} + \frac{1}{3}\left(T_{\mathrm{int,out}} - T_{\mathrm{wall,out}}\right) \tag{A.45}$$

Table A.5 summarizes the mixture condensation studies discussed above.

Table A.5. **Experimental Studies of Zeotropic Mixture Condensation**

Author	Diameter, mm	Working Fluid	Mass Flux, kg m^{-2} s^{-1}	Temperature Glide, K	Comments
Stoecker and McCarthy (1984)	12.7	R12/R114	165 - 190	3.5 - 7.3	Noted decrease in condensing heat transfer coefficient with increasing concentration of R114; greatest change between concentrations of 0 – 30%.
Tandon *et al.* (1986)	10	R12/R22	170 - 530	0.4 - 2.6	Heat transfer coefficients for mixtures varied between values for the two pure fluids. Proposed adjustment to pure fluid correlation to account for mixture effects
Koyama *et al.* (1990)	8.32	R22/R114	130 - 360	0 - 8.5	Proposed polytropic relationship for predicting changes in Nusselt number with increasing mass fraction of mixture
Shao and Granryd (1998)	6	R32/R134a	138 - 370	3.0 - 6.0	Greater decreases in mixture heat transfer coefficient at low mass flux Equilibrium correlation for annular regime to account for mass transfer effects on heat transfer coefficient Noted non-linear relationship with concentration
Chang *et al.* (2000)	8	R290/R600, R290/R600a	50 - 350	-	Polytropic-like relationship with increasing mass % of propane, with lowest heat transfer coefficient near 50/50 composition by mass
Cavallini *et al.* (2002)	8	R125/R236ea	400 - 750	16.9 – 21.9	Colburn-Drew approach to determine total heat duty of condenser section; shows good accuracy when compared to experimental total heat duty, ~9%.
Smit and Meyer (2002)	8.11	R22/R142b	40 - 800	0 - 4.6	Small reduction in heat transfer coefficient at $P_r \approx 0.48$ Heat transfer coefficient strongly affected by mass transfer only at $G < 300$ kg m^{-2} s^{-1}
Wen *et al.* (2006)	2.46	R290/R600	200-500	12	Mixture heat transfer coefficients between the two pure fluid values at similar conditions
Afroz *et al.* (2008)	4.35	CO_2/Dimethyl Ether (DME)	200 - 500	0 - 32.6	Increased mass transfer effects at higher qualities and with increasing CO_2 mass percentage, up to 39%
Milkie (2014)	7.75	Pentane/R245fa	150 - 600	7.6 - 15	Noted similar trends, but smaller magnitudes, for heat transfer coefficient of mixtures compared to pure fluid experiments Non-equilibrium conditions important at higher quality
Fronk (2014)	0.98 - 2.16	NH_3/H_2O	50 - 200	78 - 93	Significant degradation in heat transfer coefficient at higher qualities, local maxima or continual decrease in heat transfer coefficient with quality. Liquid subcooling important

APPENDIX B EXPERIMENTAL SETUP SPECIFICATIONS

The present test facility was used in a previous version by Milkie (2014) and several other previous researchers at the Sustainable Thermal Systems Laboratory at Georgia Institute of Technology. Several parts and features of the test facility are the same as those used by these previous researchers.

B.1 Main Loop Components

The dimensions of the pre- and post-condenser sections described in Chapter 2 are shown in Table B.1. The specifications for the pumps used to circulate the working fluid and the water in the coolant loops are shown in Table B.2.

B.2 Test Section Design

The test section schematic and a composite image of the built test section are shown in Figure B.1. It is a tube-in-tube condenser with the working fluid flowing through the inner tube and the primary loop coolant water flowing through the annulus. The coolant water flows countercurrent to the working fluid. The coolant enters and exits through a Tee junction, which also serves as the reducing section that seals the annulus to the test section.

The dimensions of the Tee section, the heat transfer length of the test section (annulus length) and the pressure drop length are outlined in Table B.3. Experiments were conducted for two test section inner diameters, 7.75 mm and 14.45 mm. The annulus length, and therefore the length exposed to cooling, was identical for both tube diameters, as was the pressure drop length. These test section dimensions correspond to aspect ratios ($L\ D^{-1}$) of 68 and 36, for the 7.75 mm and 14.45 mm tube diameters, respectively. The inner and outer tube walls were made of copper, which has a high

Table B.1 Pre- and Post- Condenser, and Evaporator specifications

Heat Exchanger Location	Exergy, Inc. Model	Serial No.	Tube Length, mm	Heat Transfer Area, m2	Shell		Tube		Tube / Baffle Count
					Outer Diameter, mm	Wall Thickness, mm	Outer Diameter, mm	Wall Thickness, mm	
Shell & Tube Heat Exchangers									
Pre-Condenser 1	35-00256-1	30178	508	0.27	38.1	1.65	3.18	0.032	55 / 11
Pre-Condenser 2		16870							
Post-Condenser 1		33819							
Post-Condenser 2		33820							
Secondary Loop	23-00540-6	33560	406	0.08	25.4	1.25	3.18	0.032	19 / 18
Tube-in-Tube Heat Exchanger					Outer Tube		Inner Tube		
Evaporator	528	13890	5900	-	12.7	1.65	25.4	1.65	-

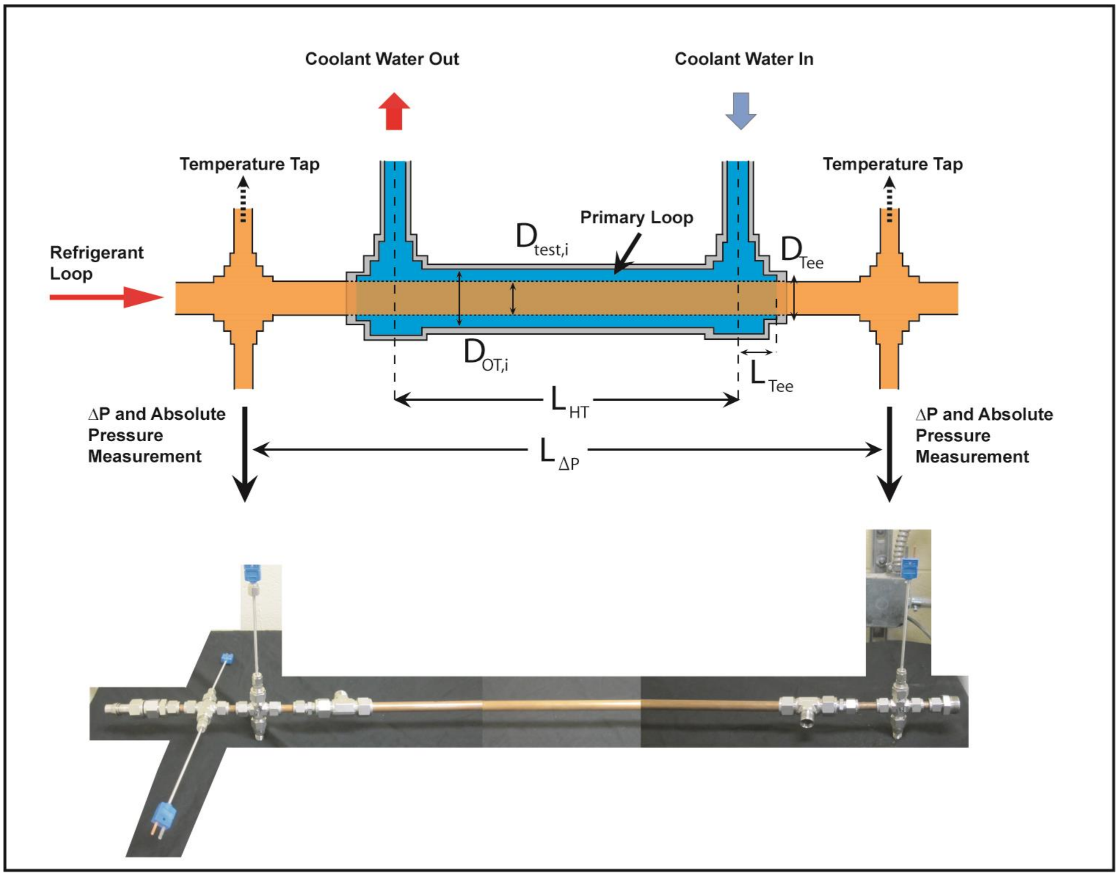

Figure B.1: Test section schematic and photograph

thermal conductivity and therefore results in a desirably small thermal resistance of the tube walls.

Temperatures are measured at the inlet and the outlet of the annulus. These temperatures are used: a) to ensure an approximately constant coolant temperature, which is also an indirect indication that the coolant flow rate is sufficiently high, and b) in the LMTD calculation to deduce the condensation heat transfer coefficient.

Temperature, pressure and differential pressure measurements of the working fluid are taken at the inlet to the test section, upstream of the test section, and again at the outlet of the test section, after exiting. During the pure fluid testing, the temperature measurements at these points are compared with the saturation temperatures based on the pressure transducer reading. This comparison serves as an additional check that verifies

Table B.2 Fluid loop pump specifications

Fluid Loop	Type	Model Number	Serial No.	Range	Manufacturer
Working fluid	Gear	GLHH25JVSEM	1074767	0 - 2.5 L min^{-1}	Micro Pump
Secondary	Gear	74011-21	912334	0 - 15.1 g s^{-1}	Cole Parmer
Pre-Condenser	Centrifugal	3680-975-95	1105	0 - 14 L min^{-1}	AMT
Post-Condenser	Centrifugal	3680-975-95	1106	0 - 14 L min^{-1}	AMT
Primary	Gear	5000.750/58C	365823	0 - 15 L min^{-1}	Micro Pump

the accuracy of both temperature measurement and the expected saturation condition inside the test section. It also verifies the absence of noncondensables. During zeotropic mixture testing, the temperature measurement at the inlet of the test section is compared with the equilibrium temperature calculated from the pressure transducer, measured concentration and deduced enthalpy. This comparison is used to validate the equilibrium assumption at the inlet to the test section, i.e., a well-mixed fluid enters the test section.

B.3 Control of Saturation Pressure in Loop

A piston accumulator, located downstream of the pump, facilitates precise control of the system pressure, as shown in Figure B.2. The piston accumulator has two chambers, the void space and the working fluid space. The working fluid space is continually occupied by some volume of working fluid (ideally subcooled liquid, because it is located immediately upstream of the evaporator) during facility operation. Initially the piston starts close to the bottom dead center position and a large void space exists. The void space is attached to a line that connects to both a nitrogen tank and the ambient as shown in Figure B.2. The working fluid loop without the accumulator has a constant volume; therefore, as the operating conditions in the test section transition to higher qualities, the volume of vapor contained within the working fluid loop increases because more vapor occupies the space in the pre-condenser and post-condenser sections. Therefore, to

Table B.3. Pressure drop and heat transfer test section dimensions

Test Section Dimensions			
Dimension	**Variable**	**7.75 mm**	**14.45 mm**
Test Section Inner Diameter, mm	$D_{test,i}$	7.75	14.45
Test Section Outer Diameter, mm	$D_{test,o}$	9.5	15.9
Outer Tube Inner Diameter, mm	$D_{OT,i}$	11.1	17.4
Outer Tube Outer Diameter, mm	$D_{OT,o}$	12.7	19.1
Heat Transfer Test Section Length, mm	L_{HT}	530	530
Differential Pressure Drop Length, mm	$L_{\Delta P}$	746	746
Tee Length, mm	L_{Tee}	13.2	15.0
Internal Diameter of Tee, mm	D_{Tee}	10.4	16.8

maintain the system pressure at a desired saturation condition, nitrogen is released from the void space and subcooled liquid enters the accumulator. The high pressure of the working fluid loop causes the piston inside the accumulator to shift upwards, allowing more liquid to occupy the working fluid space at the bottom of the accumulator. By allowing this adjustment in system charge, the targeted saturation pressure can be maintained in the working fluid loop.

B.4 Safety Precautions

The working fluids that were investigated in the present study were hydrocarbons, which are flammable at low concentrations in air and are denser than air. Therefore, precautions were taken to ensure that the facility was operated under safe conditions. The working fluid loop integrity was checked for pressures as high as 5000 kPa, which was 800 kPa above the highest pressure conditions under investigation. This was done to ensure that no conditions were reached during testing that would result in working fluid leaking from the working fluid loop to the surroundings. As a further precaution, the facility was surrounded by an acrylic wall that shielded the working fluid and coolant

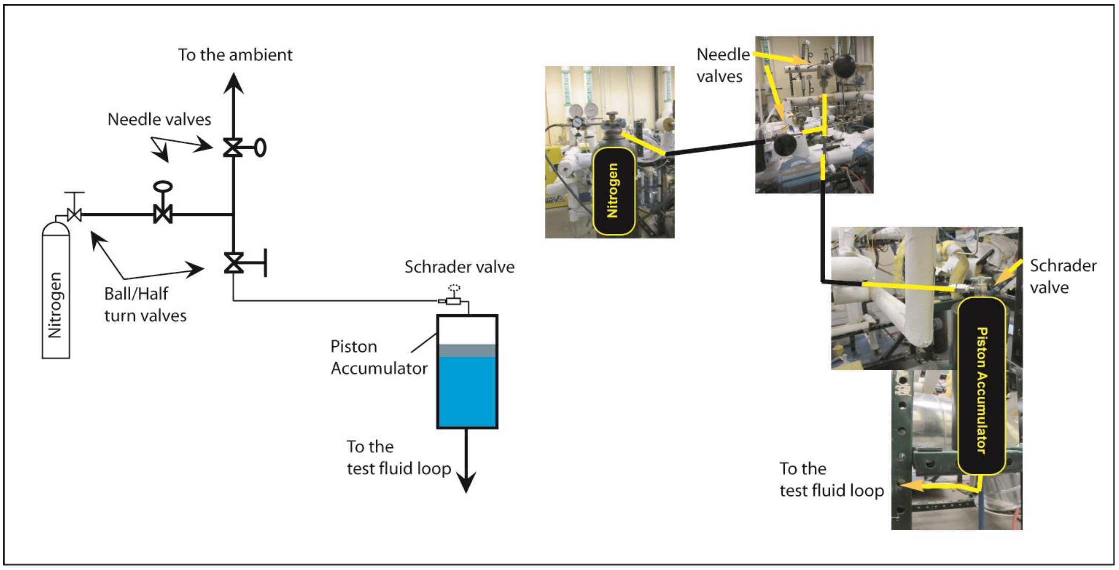

Figure B.2: Piston accumulator setup for saturation pressure regulation

loops from the lab, pump controllers, accumulator controllers and data acquisition setup. Therefore, any working fluid that might have leaked was contained within the test facility enclosure.

The hydrocarbons have saturation pressures significantly higher than ambient pressure; therefore, if they leaked from the facility, they would immediately vaporize, and accumulate at the base of the facility. This hazard was addressed by locating a ventilation hood at the base of the facility that continually extracted and transported air, and any leaked hydrocarbons, outside the lab. Additionally, the hydrocarbon concentration in the extracted air was monitored by sensors installed inside the ventilation hood and at two points on the facility. The sensor specifications are Honeywell MDA Scientific Midas, 10/72016 and 10/70012. These sensors provided real-time detection of leaked hydrocarbons inside the test facility enclosure. The detection limit of the monitors was set to 5% of the lower flammability limit of the hydrocarbons. If a leak was detected, the hydrocarbons monitors would trigger alarms inside the lab and

Table B.4. Pressure transducer specifications

Instrument Location	Reference Scale	Model	Serial No.	Range	Accuracy
Inlet to Pre-condenser	Absolute	Rosemount 3051TA4A2B21 AE5M5	1019352	0 - 5000 kPa	7 kPa (0.14 % F.S.)
Test Section Inlet			1019351		
Test Section Outlet			1019353		
Outlet of Post-condenser			1021623		
Test Section	Differential	Rosemount 3051CD3A22A 1AB4M5	687134	0 - 62.6 kPa	0.088 kPa (0.14% F.S.)
		Rosemount 3051CD1A22A 1AM5	687133	0 - 6.26 kPa	0.014 kPa (0.22% F.S.)
Coolant Water Loop	Absolute	Rosemount 2088A3M22A1 M7	138877	0 - 2413 kPa	2.4 kPa
Primary Loop			138874	0 - 5516 kPa	5.5 kPa
Primary Loop	Differential	Rosemount 3051CD4A22A 1AB4M5E5	2251309	0 - 2068 kPa	N/A

sent notifications to the Environmental Health and Safety department of Georgia Institute of Technology.

B.5 Test Facility Equipment Uncertainties

The uncertainties of the pressure transducers used throughout the test facility are shown in Table B.4. All absolute pressure transducers (Rosemount 3051T) have an uncertainty of ±0.14% of span (±7 kPa). The frictional pressure drop of the working fluid across the test section is measured using one of two differential pressure transducers (Rosemount 3051CD). Both transducers are located at the test section but are calibrated for high and low spans, i.e., 0 – 62 kPa and 0 – 6.26 kPa. These spans have uncertainties of ±0.14% (±0.088 kPa) and ±0.22% (±0.014 kPa) of the total calibration span, for the

Table B.5 Flow meter specifications

Fluid Loop			Model Number	Serial No.	Range	Accuracy, % of Reading	Manufacturer	Type
Working fluid		Sensor	CMF025M319NU	326974	0 - 100.0 g s^{-1}	±0.10%	MicroMotion	Coriolis
		Transmitter	IFT9701R6D3U	366359				
Secondary		Sensor	DS006S100SU	205104	0 - 15.1 g s^{-1}	±0.15%		
		Transmitter	IFT9701R6D3U	366366				
Pre-Condenser	High Flow Rate	Sensor	8711ASA30FR1E5G1	168079	0 - 14.0 L min^{-1}	±0.10%	Rosemount	Magnetic
		Transmitter	8712ESR1A1N5M4	310126				
	Low Flow Rate	Sensor	8711RRE15FS1	71955	0 - 2.5 L min^{-1}	±0.10%		
		Transmitter	8712CT12M4	63610				
Post-Condenser		Sensor	8711ASA30FR1E5G1	168080	0 - 14.0 L min^{-1}	±0.10%		
		Transmitter	8712ESR1A1N5M4	310125				
Primary		Sensor	8705TSA005S1W0N0M4	870119434	0 - 15.0 L min^{-1}	±0.50%		
		Transmitter	8732CT03N0M4	860199499				

high and low spans, respectively. The pressure drop across the pump in the primary loop is measured using a third differential pressure transducer (Rosemount 3051CD).

Thermocouples (Omega T-type Model No. TMQSS-125G-6) were used to measure the temperatures throughout the loop. They have calibrated uncertainties of ±0.3°C. The thermocouples were calibrated using a temperature controlled silicone oil bath (Hart Scientific Model No. 7340). The temperature of the bath was measured with a platinum RTD (Hart Scientific Model No. 5612), which has an accuracy of ±0.012°C.

The uncertainties of the flow meters used to measure the working fluid and coolant fluid flow rates are shown in Table B.5. The working fluid flow rate is measured using a Coriolis mass flow meter (MicroMotion CMF025) located downstream of the pump. The coolant water flow rates in the pre-condenser, post-condenser and primary loops are measured using magnetic volumetric flow meters (Rosemount 8711 series). The coolant flow rate in the secondary loop is measured using a Coriolis mass flow meter (MicroMotion DS006).

The subcooled state at the exit of the post-condenser is confirmed visually using a sight glass located downstream of the exit of the second post-condenser.

B.6 Charging the Test Facility with the Working fluid

This section describes evacuation of the working fluid loop followed by the introduction of working fluids.

To ensure that the values for the heat transfer coefficients and pressure drop measurements are reported accurately for a specific working fluid, it is critical that the working fluid loop contains as pure a concentration of that working fluid as possible. The first step in this process was ensuring that no contaminants, e.g., water or oil, were introduced into the working fluid loop at any stage of setup. These substances can be difficult to remove and can cause oxidation reactions in some of the components that can, over time, introduce debris and other particulates into the working fluid loop. In addition to maintaining a clean environment inside the working fluid loop, the sealed working fluid loop was evacuated before charging the loop with the working fluids. This was achieved by connecting a vacuum pump to the charging ports and running the pump for approximately eight hours. Fluids from previous tests can get trapped in crevices throughout the loop, for example in the small spaces between the isolation balls of the ball valves that are located throughout the test loop. These valves were opened and closed throughout the evacuation process to ensure that previous working fluids that may have been trapped were released and removed from the loop. A vacuum gauge was used to accurately measure the quality of the vacuum in the loop. When a pressure of 400 Pa was reached and sustained, it was assumed the working fluid loop had reached an acceptable point of purity. At this stage, the test loop was charged with the working fluids.

The volume of the loop was estimated from the length and cross sectional areas of the stainless steel tubing, the volume of the heat exchangers and a fraction of the volume of the accumulator, which was 0.00225 m^3. This volume was subsequently used to predict an approximate mass of working fluid required in the test loop that would enable the accumulator to pressurize the loop. To charge the loop, the chiller was set to a low temperature and the coolant pumps for the pre-condenser and post-condenser were turned on. This provided cooling throughout the loop and ensured that as the working fluid was introduced from the storage tanks to the low pressure loop and vaporized, the cooling provided throughout the loop would re-condense and depressurize the working fluid;

thereby facilitating continual and rapid charging of the loop from the working fluid cylinders. The cylinders containing the working fluids were placed on weighing scales and inverted. Inverting the cylinders ensured that liquid was forced through the valves of the cylinders and into the loop first, and that vapor was only introduced when the liquid level in the cylinders dropped below the valve height. The lines that connected the working fluid cylinders to the test loop were evacuated to ensure that no contaminants were introduced in the lines. The valves on the cylinders were opened slowly and the change in weight of the cylinders was monitored. After a reduction of approximately 1.125 kg was noted by the weighing scales, and the accumulator was able to pressurize the test loop above the saturation pressure corresponding to the room temperature (for propane $T_{\text{ambient}} = 20°\text{C} \approx P_{\text{sat}} = 830$ kPa), the valves of the working fluid cylinders were closed and charging was stopped.

The zeotropic mixture charging procedure was almost identical to the pure fluid procedure outlined above. However, for the zeotropic mixtures, the propane was introduced first, followed by ethane. Propane has a lower saturation pressure at room temperature than ethane; therefore, if ethane was introduced first, it would have been difficult to introduce propane into the loop because the pressure in the loop would be higher than that of the propane tanks.

The mass of propane that was introduced corresponded to the desired mass fraction of mixture. For example, for the 33% propane/67% ethane mixture, 0.37 kg of propane was introduced. In contrast to the procedures for charging the pure propane the ethane tanks were not inverted when charging. This ensured that vapor was introduced instead of liquid; thus a smaller mass flow rate of ethane passed through the charging ports and therefore the changes in the concentration of the two fluids could be more closely controlled. This ensured that the targeted concentration was slowly approached, and not overshot.

The concentration of the mixture was checked by first pressurizing and depressurizing the working fluid loop to promote mixing of the components, and then circulating the working fluid in a liquid state and taking a sample measurement with the gas chromatograph. Both the propane and ethane fluids used throughout the present study are instrument grade purity from Airgas, and each cylinder has a purity of 99.5%.

B.7 System Start-Up, Data Point Stability and Data Point Capture

The system was started by first circulating the chilled coolant water in both the pre- and post-condenser loops until the coolant temperature approached the lab chiller temperature. Next, the void space of the accumulator was pressurized to approximately 4000 kPa to ensure that as much of the liquid as possible was pushed from the accumulator to the working fluid loop, and therefore the working fluid loop was completely filled with liquid. The working fluid pump was then started and the working fluid was circulated until all points of the system achieved noticeable cooling. Finally, the valve of the steam loop was opened and steam at approximately ~100°C heated the working fluid in the evaporator, which subsequently increased the system pressure. The system pressure was then adjusted using the approach described above.

National Instruments LABView® software was used to observe the temperature, pressure, and flow rate conditions of the working fluid and coolant loops in real time. Instantaneous readings of the test conditions were reported over time spans of five, 30 and 60 minutes. These plots were used to assess the stability of the conditions and

Table B.6 Data acquisition Equipment

Instrument	Manufacturer	Model No.	Serial No.	Range
DAQ chassis	National Instruments	NI SCXI-1000	14223AE	0 - 24V
16 Bit Digitizer for USB		NI SCXI-1600	1423DE9	
32 Channel Thermocouple Amplifier		NI SCXI-1102	142E214	
Terminal Block		NI SCXI-1303	13C86A6	
32 Channel Analog Voltage		NI SCXI-1102	142E1EF	
Terminal Block		NI SCXI-1303	13F2AE6	

determine whether steady state had been reached in the various loops, which typically occurred between 20 and 60 minutes of transitioning between targeted conditions. Sample data points, typically consisting of 30 seconds of accumulated data, were taken to determine whether the targeted experimental conditions were reached. Complete data point sets were recorded for 300 seconds at a sample rate of 3 Hz; sampling over this long duration ensured that any short-term fluctuations in the facility did not adversely impact the fidelity of the heat transfer coefficient and pressure drop measurements. Each data point was then averaged over the sampled data and analyzed using *Engineering Equation Solver* software (EES) (Klein, 2012) to calculate the heat transfer coefficient and frictional pressure drop for that condition. The data points were graphed and compared to previous test conditions during testing. This was done to ensure that the facility was operating as expected and that reasonable data points were being collected. Table B.6 lists the data acquisition equipment used to report and record the temperature, pressure and flow rate measurements.

Each recorded data point had to pass three tests used to assess the quality of that data point. First, a comparison between the total evaporator heat duty calculated from the superheated state to the sub-cooled state was compared with the sum of the combined

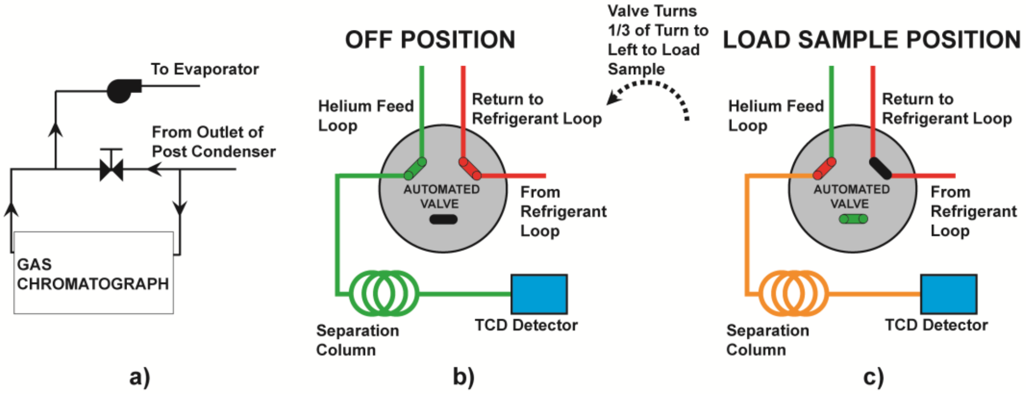

Figure B.3: Gas chromatograph sampling procedure

heat duties of partial condensation in the pre-condenser, test section and post-condenser - differences less than 2.5% were determined to be acceptable. Second, the resistance ratio, which is defined as the ratio of the condensation thermal resistance to all other thermal resistances in the heat transfer network, had to be above five. Resistance ratios above five ensured that the condensation heat transfer coefficient presented the dominant resistance in the thermal resistance network, which would ensure low uncertainties. Third, the quality change in the test section was kept below ~10%; this ensured that the reported heat transfer coefficient represents a local value, and not an averaged heat transfer coefficient over a wide quality range.

B.8 Mixture Concentration Measurement

This section describes the bulk mixture concentration measurement method. A schematic of the setup showing the sample being drawn from the working fluid loop is shown in Figure B.3a. The concentration of the mixture is measured using a gas chromatograph (Shimadzu GC-2014) that extracts a sample from the subcooled (all-liquid) section of the loop. The liquid sample is drawn from the loop downstream of the post-condenser section and upstream of the pump, which ensures that the drawn sample is always a liquid. An automated injector valve contained within the gas chromatograph

Table B.7 Thermal conductivity of the carrier gas and mixture components

Pressure, kPa	Thermal Conductivity, W m^{-1} K^{-1}		
	Helium	Ethane	Propane
2000	0.155	0.021	0.025
4000	0.156	0.040	0.060

contains links to two loops, one contains a continuous flow of a carrier gas that flows from the carrier gas tank to the thermal conductivity detector, and the other is connected to the pressurized working fluid loop, through which the liquid sample of the working fluid flows continuously.

A 100 μL sample is diverted from the working fluid loop into the carrier gas loop when the automated injector valve connecting the working fluid loop is turned from the position shown in Figure B.3b to position B.3c; the sample trapped within the valve volume at the time of the switch is the sample transferred to the carrier gas loop. The carrier gas carries the sample through a separation column (ResTek Rt-Alumina BOND/CFC; 30 m, ID = 0.53 mm, 10 μm; Serial No. 962866) where the two components are separated; the separated samples subsequently flow into the detector where the distinct peaks related to the two fluids (ethane and propane) are measured using a thermal conductivity detector. The mass concentrations are calculated from the relative areas beneath each peak using the LabSolutions Version 5.42 SP1 software from Shimadzu (2011).

The thermal conductivity of the carrier gas in the gas chromatograph loop is important; to allow accurate identification of the mixture components in the thermal conductivity detector, it must be significantly different from the thermal conductivity of the mixture components at the testing pressures. Table B.7 shows the thermal conductivity of the carrier gas that was chosen (helium) and the mixture components at the highest and lowest operating pressures investigated in the present study. For all saturation pressures studied, the thermal conductivity of the carrier gas was approximately five times the thermal conductivity of the individual mixture components.

The gas chromatograph was calibrated by injecting precise volumes of each fluid independently into the detector and recording the calculated mass of fluid; a detailed description of the calibration procedure is outlined in Appendix E. The procedure outlined in Appendix E was also used to determine the uncertainty of the concentration measurements, which is ±2% of the reading.

APPENDIX C PRIMARY LOOP PUMP HEAT ADDITION

This section describes the approach used to determine the heat addition to the primary loop due to the circulation of the single phase fluid in that loop. As previously noted, a precise estimation of this heat duty is necessary, because the primary loop operates as a closed loop. Any additions or losses of energy from this closed system must be correctly accounted for to determine the test section heat duty.

The work added by a pump to a closed loop that enables the circulation of the working fluid can be determined using the ideal pump work and an efficiency of the pump, shown in Eq. (C.1). This is typically referred to as the shaft work, W_{shaft}.

$$\begin{aligned} \dot{W}_{\text{ideal}} &= \eta \cdot \dot{W}_{\text{shaft}} \\ \dot{W}_{\text{shaft}} &= \frac{\left(\Delta P_{\text{primary}} \cdot \dot{V}_{\text{primary}}\right)}{\eta} \end{aligned} \tag{C.1}$$

The efficiency of the pump is not constant for all conditions. Moreover, typically pumps become less efficient with age. Therefore, if a constant efficiency of the pump is used, it can lead to an under-prediction of the total heat input to the system as the pump ages. To ensure an accurate estimation of the heat input from the pump for this specific set of experiments, experiments were conducted to measure the heat added by the pump at the present stage of its life-cycle. The 7.75 mm tube was used to conduct these experiments, where the heat added was directly measured as a function of the range of volumetric flow rates encountered in the present study. Using Eq. (C.2), the heat added to the primary loop by the pump can be measured when all other heat duties are known. The heat duty of the test section was measured by maintaining the working fluid as a liquid and measuring the temperature difference. The heat duty in the secondary loop is determined using temperature measurements at the inlet and outlet of the secondary loop heat exchanger.

$$\dot{Q}_{\text{test}} = \dot{Q}_{\text{secondary}} - \dot{Q}_{\text{pump}} + \dot{Q}_{\text{ambient}} \tag{C.2}$$

Equation (C.2) is equivalent to the equation used in the thermal amplification technique outlined in Chapter 2. However, instead of determining the test section heat duty with a known pump heat duty, here the test section heat duty is measured and the heat added by the pump is derived. The pump heat addition is measured for the range of flow rates encountered in the present study, i.e. 1.4 – 9.0 L min^{-1}. These results are shown in Figure C.1.

A curve fit of the measured heat addition data for the 7.75 mm tube was developed

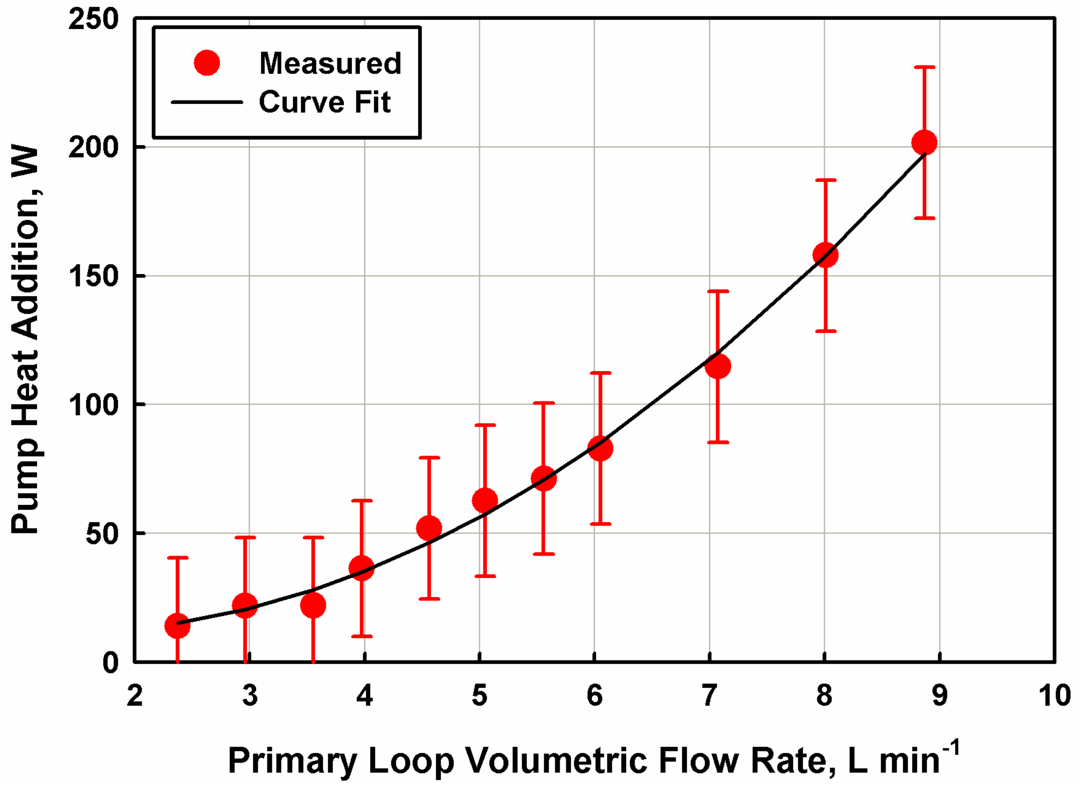

Figure C.1: **Measured pump heat addition using single phase fluids (The results from these tests conducted by the author were also used and reported by Milkie (2014))**

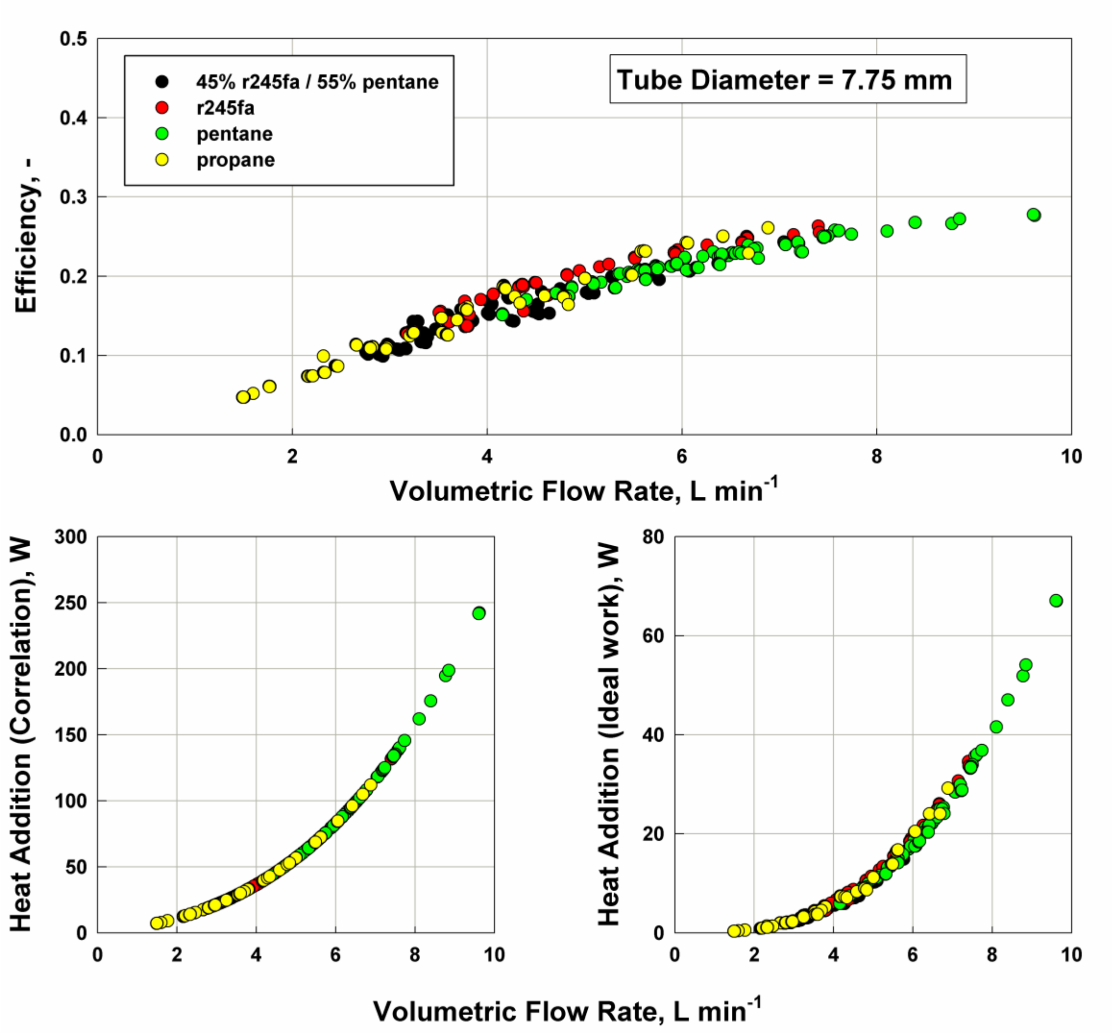

Figure C.2: Pump efficiency and work heat addition

and is shown in Eq. (C.3). The pump heat addition calculated in Eq. (C.3) was used to define an efficiency of the pump, η_{pump}, using the ideal work equation from Eq. (C.1). The efficiency curve fit is shown in Eq. (C.4). The predictions of Eq. (C.1), Eq. (C.3) and Eq. (C.4) are shown in Figure C.2.

$$\dot{Q}_{\text{pump - 7.75 mm}} = 0.1401 \cdot \dot{V}_{\text{primary}}^{3} + 0.9598 \cdot \dot{V}_{\text{primary}}^{2} + 3.025 \cdot \dot{V}_{\text{primary}} \tag{C.3}$$

$$\begin{gathered} \eta_{\text{pump}} = \frac{\dot{W}_{\text{ideal}}}{\dot{Q}_{\text{pump - 7.75 mm}}} \\ \eta_{\text{pump}} = 0.0205 + 0.0322 \cdot \dot{V}_{\text{primary}} \end{gathered} \tag{C.4}$$

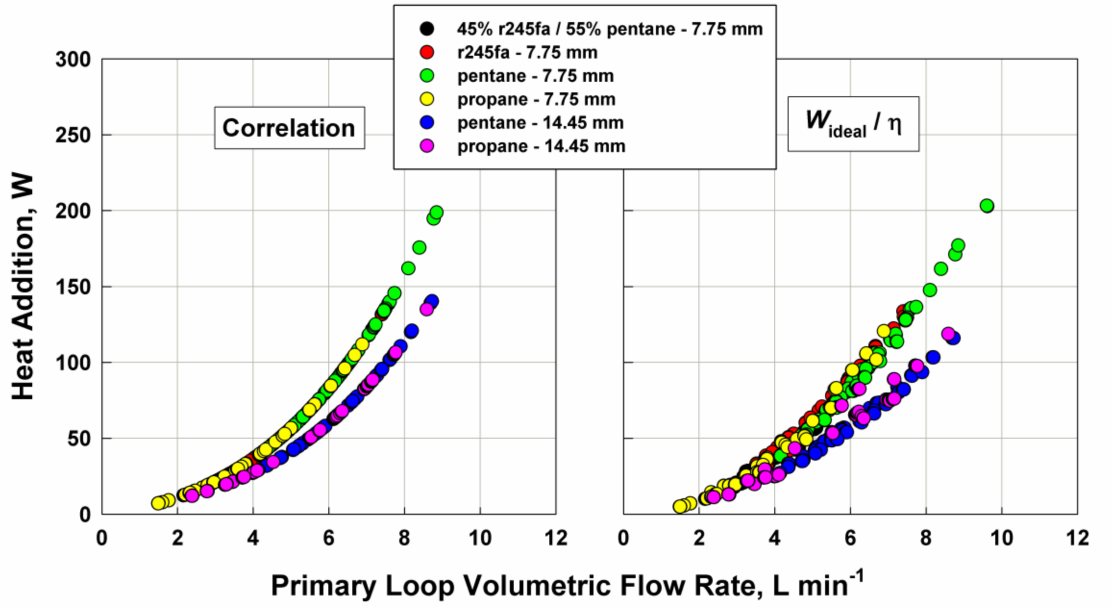

Figure C.3: Correlated and measured pump heat addition

The curve fit for the efficiency shown in Eq. (B4) was then used with the ideal work equation for the pump from Eq. (C.1) to calculate the shaft work for the 14.45 mm tube, which used the measured pressure drop and volumetric flow rates, Eq. (C.5). The heat addition from Eq. (C.5) was then curve fit as a function of flow rate for the 14.45 mm tube diameter, with the curve fit equation for this analysis shown in Eq. (C.6). A comparison between the heat additions predicted by using Eq. (C.5) and Eq. (C.6) is shown in Figure C.3.

$$\dot{Q}_{\text{pump - 14.45 mm}} = \dot{W}_{\text{shaft}} = \frac{\dot{W}_{\text{ideal}}}{\eta_{\text{pump}}} \tag{C.5}$$

$$\dot{Q}_{\text{pump - 14.45 mm}} = 0.1357 \cdot \dot{V}^3_{\text{primary}} + 0.2285 \cdot \dot{V}^2_{\text{primary}} + 3.7612 \cdot \dot{V}_{\text{primary}} \tag{C.6}$$

The pump heat addition to the primary loop for all of the data points of the present study is calculated using Eq. (C.3) and Eq. (C.6).

APPENDIX D SINGLE COMPONENT PHASE-CHANGE HEAT TRANSFER AND PRESSURE DROP: SAMPLE DATA ANALYSIS CALCULATIONS

Table D.1. Coolant loop measurements

Pre-Condenser	
$T_{\mathrm{w,Pre\ \#1,in}}\ (^{\circ}C)$	11.83
$T_{\mathrm{w,Pre\ \#1,out}}\ (^{\circ}C)$	57.60
$\dot{V}_{\mathrm{w,Pre}}\ (\mathrm{L\ min^{-1}})$	2.225
Post Condenser	
$T_{\mathrm{w,Post\ \#1,in}}\ (^{\circ}C)$	12.71
$T_{\mathrm{w,Post\ \#1,out}}\ (^{\circ}C)$	16.25
$T_{\mathrm{w,Post\ \#2,in}}\ (^{\circ}C)$	16.19
$T_{\mathrm{w,Post\ \#2,out}}\ (^{\circ}C)$	31.58
$\dot{V}_{\mathrm{w,Post}}\ (\mathrm{L\ min^{-1}})$	2.377
Secondary Loop	
$T_{\mathrm{w,Sec,in}}\ (^{\circ}C)$	13.17
$T_{\mathrm{w,Sec,out}}\ (^{\circ}C)$	48.01
$\dot{m}_{\mathrm{w,Sec}}\ (\mathrm{kg\ s^{-1}})$	0.002644
Primary Loop	
$T_{\mathrm{w,Test,in}}\ (^{\circ}C)$	46.38
$T_{\mathrm{w,Test,out}}\ (^{\circ}C)$	48.29
$\dot{V}_{\mathrm{w,Pri}}\ (\mathrm{L\ min^{-1}})$	3.234
$P_{\mathrm{w,Pri}}\ (\mathrm{kPa})$	271.1
$\Delta P_{\mathrm{w,Pri}}\ (\mathrm{kPa})$	58.65

Table D.2. Working fluid loop measurements

Working Fluid Loop	
$P_{\mathrm{f,Pre,in}}\ (\mathrm{kPa})$	2204
$P_{\mathrm{f,Test,in}}\ (\mathrm{kPa})$	2131
$P_{\mathrm{f,Test,out}}\ (\mathrm{kPa})$	2132
$P_{\mathrm{f,Post,out}}\ (\mathrm{kPa})$	2093
$\Delta P_{\mathrm{f,Test}}\ (\mathrm{kPa})$	1.078
$T_{\mathrm{f,Pre,in}}\ (^{\circ}C)$	107.30
$T_{\mathrm{f,Test,in,m}}\ (^{\circ}C)$	59.92
$T_{\mathrm{f,Test,out,m}}\ (^{\circ}C)$	59.95
$T_{\mathrm{f,Post,out}}\ (^{\circ}C)$	16.26
$\Delta T_{\mathrm{f,Pre,in,Sup}}\ (K)$	46.98
$\Delta T_{\mathrm{f,Test,in}}\ (K)$	-0.2182
$\Delta T_{\mathrm{f,Test,out}}\ (K)$	-0.2149
$\Delta T_{\mathrm{f,Post,out,Sub}}\ (K)$	43.80
$\dot{m}_{\mathrm{f}}\ (\mathrm{kg\ s^{-1}})$	0.02114

Table D.3. Data point identification and miscellaneous measurements

Data Point	
$P_{\mathrm{f,Test,Avg}}\ (\mathrm{kPa})$	2123.5
$P_{\mathrm{f,Critical}}\ (\mathrm{kPa})$	4230
P_{r}	0.501
$G\ (\mathrm{kg\ m^{-2}\ s^{-1}})$	448.2
$y_{\mathrm{f,Test,Avg}}$	0.118
$\mathrm{D_{Test,i}}$ (mm)	7.75
Experiment Date	6/21/2013
Assumed Variables	
$P_{\mathrm{Amb}}\ (\mathrm{kPa})$	101
$\varepsilon_{\mathrm{ins}}$	0.85
Misc. Measurements	
$P_{\mathrm{w}}\ (\mathrm{kPa})$	257.1
$T_{\mathrm{Amb}}\ (^{\circ}C)$	27.20

Table D.4. Propane data point heat transfer coefficient sample calculation

Heat Transfer Sample Calculations: Propane; 6/21/2013; Run 1		
Inputs	**Equations**	**Results**
Heat Loss in Fluid Line from Superheat Point to Pre-Condenser		
$P_{\mathrm{Amb}} = 101\,\mathrm{kPa}$ $T_{\mathrm{Amb}} = 27.20°\mathrm{C}$ $T_{\mathrm{f,Pre,line}} = 107.3°\mathrm{C}$ $D_{\mathrm{Pre,o}} = 12.7\,\mathrm{mm}$ $D_{\mathrm{Pre,i}} = 10.92\,\mathrm{mm}$ $D_{\mathrm{ins,o}} = 100\,\mathrm{mm}$ $L_{\mathrm{Pre}} = 0.1\mathrm{m}$ $k_{\mathrm{wall}} = 14.85\,\mathrm{W\,m^{-1}\,K^{-1}}$ $k_{\mathrm{ins}} = 0.043\,\mathrm{W\ m^{-1}\ K^{-1}}$ $\varepsilon_{\mathrm{ins}} = 0.85$ $\sigma_{\mathrm{SB}} = 5.67\times10^{-8}\ \mathrm{W\,m^{-2}K^{-4}}$ $g = 9.81\,\mathrm{kg\,m^{-1}\,s^{-2}}$	$R_{\mathrm{wall}} = \dfrac{\ln\left(D_{\mathrm{Pre,o}} / D_{\mathrm{Pre,i}}\right)}{2\cdot\pi\cdot k_{\mathrm{wall}}\cdot L_{\mathrm{Pre}}}$	$R_{\mathrm{wall}} = 0.01619\,\mathrm{K\,W^{-1}}$
	$R_{\mathrm{ins}} = \dfrac{\ln\left(D_{\mathrm{ins,o}} / D_{\mathrm{Pre,o}}\right)}{2\cdot\pi\cdot k_{\mathrm{ins}}\cdot L_{\mathrm{Pre}}}$	$R_{\mathrm{ins}} = 76.38\mathrm{K\ W^{-1}}$
	$R_{\mathrm{rad}} = \dfrac{1}{\varepsilon_{\mathrm{ins}}\cdot\pi\cdot D_{\mathrm{ins,o}}\cdot L_{\mathrm{Pre}}\cdot\sigma_{\mathrm{SB}}\cdot\left(\mathrm{T_{ins}}^2+\mathrm{T_{amb}}^2\right)\cdot\left(\mathrm{T_{ins}}+\mathrm{T_{amb}}\right)}$	$R_{\mathrm{rad}} = 5.978\,\mathrm{K\ W^{-1}}$ $T_{\mathrm{ins}} = 31.07°\mathrm{C}\left(\mathrm{Solved\ Iteratively}\right)$
	$T_{\mathrm{film}} = \left(T_{\mathrm{ins}} + T_{\mathrm{Amb}}\right)/2$	$T_{\mathrm{film}} = 29.14°\mathrm{C}$
	$T_{\mathrm{wall,i}} = T_{\mathrm{f,Pre,line}}$	$T_{\mathrm{wall,i}} = 107.3°\mathrm{C}$
	$\mathrm{Air\ Properties} = f\,(P = 101\,\mathrm{kPa}, T_{\mathrm{film}} = 29.14°\mathrm{C})$	$\alpha = 2.225\times10^{-5}\ \mathrm{m^2}\ s^{-1}$ $\beta = 0.003308\,\mathrm{K^{-1}}$ $k = 0.02616\,\mathrm{W\,m^{-1}\ K^{-1}}$ $\nu = 1.575\times10^{-5}\ \mathrm{m^2\ s^{-1}}$ $\mathrm{Pr} = 0.7193$ $\rho = 1.168\,\mathrm{kg\,m^{-3}}$
	$Ra_{\mathrm{air}} = \dfrac{g\cdot\beta\cdot\left(T_{\mathrm{ins}} - T_{\mathrm{amb}}\right)\cdot\left(D_{\mathrm{ins,o}}\right)^3}{\nu\cdot\alpha}$	$Ra_{\mathrm{air}} = 352500$
	$Nu_{\mathrm{D}} = \left(0.60 + 0.387\cdot\dfrac{Ra_{\mathrm{air}}^{\ 1/6}}{\left(1+\left(0.559/\mathrm{Pr}\right)^{9/16}\right)^{8/27}}\right)^2$	$Nu_{\mathrm{D}} = 10.91$ (Churchill and Chu, 1975)
	$h_{\mathrm{nat,conv}} = \dfrac{k_{\mathrm{air}}}{D_{\mathrm{ins,o}}}\cdot Nu_{\mathrm{D}}$	$h_{\mathrm{nat,conv}} = 2.854\,\mathrm{W\,m^{-2}\,k^{-1}}$
	$R_{\mathrm{conv}} = \dfrac{1}{h_{\mathrm{nat,conv}}\cdot\pi\cdot D_{\mathrm{ins,o}}\cdot L_{\mathrm{Pre}}}$	$R_{\mathrm{conv}} = 11.15\,\mathrm{K\,W^{-1}}$

<table>
<tr><th colspan="3">Heat Transfer Sample Calculations: Propane; 6/21/2013; Run 1</th></tr>
<tr><th>Inputs</th><th>Equations</th><th>Results</th></tr>
<tr><td></td><td>$\dot{Q}_{\text{loss}} = \dfrac{T_{\text{wall,i}} - T_{\text{amb}}}{R_{\text{wall}} + R_{\text{ins}} + \dfrac{R_{\text{conv}} \cdot R_{\text{rad}}}{\left(R_{\text{conv}} + R_{\text{rad}}\right)}}$</td><td>$\dot{Q}_{\text{loss,Superheat,Line}} = 0.9941\,\text{W}$</td></tr>
<tr><td colspan="3">Heat Loss in Pre-Condenser</td></tr>
<tr><td rowspan="9">$P_{\text{Amb}} = 101\,\text{kPa}$
$T_{\text{Amb}} = 27.20°\text{C}$
$T_{\text{w,Pre,in}} = 11.83°\text{C}$
$T_{\text{w,Pre,out}} = 57.6°\text{C}$
$D_{\text{Pre,o}} = 38.1\,\text{mm}$
$D_{\text{Pre,i}} = 34.8\,\text{mm}$
$D_{\text{ins,o}} = 100\,\text{mm}$
$L_{\text{Pre}} = 0.461\,\text{m}$
$k_{\text{wall}} = 13.54\,\text{W m}^{-1}\,\text{K}^{-1}$
$k_{\text{ins}} = 0.043\,\text{W m}^{-1}\,\text{K}^{-1}$
$\varepsilon_{\text{ins}} = 0.85$
$\sigma_{\text{SB}} = 5.67\times10^{-8}\,\text{W m}^{-2}\text{K}^{-4}$
$g = 9.81\,\text{kg m}^{-1}\,\text{s}^{-2}$</td><td>$R_{\text{wall}} = \dfrac{\ln\left(D_{\text{Pre,o}} / D_{\text{Pre,i}}\right)}{2\cdot\pi\cdot k_{\text{wall}}\cdot L_{\text{Pre}}}$</td><td>$R_{\text{wall}} = 0.00231\,\text{K W}^{-1}$</td></tr>
<tr><td>$R_{\text{ins}} = \dfrac{\ln\left(D_{\text{ins,o}} / D_{\text{Pre,o}}\right)}{2\cdot\pi\cdot k_{\text{ins}}\cdot L_{\text{Pre}}}$</td><td>$R_{\text{ins}} = 7.747\,\text{K W}^{-1}$</td></tr>
<tr><td>$R_{\text{rad}} = \dfrac{1}{\varepsilon_{\text{ins}}\cdot\pi\cdot D_{\text{ins,o}}\cdot L_{\text{Pre}}\cdot\sigma_{\text{SB}}\cdot\left(\text{T}_{\text{ins}}^{\;2} + \text{T}_{\text{amb}}^{\;2}\right)\cdot\left(\text{T}_{\text{ins}} + \text{T}_{\text{amb}}\right)}$</td><td>$R_{\text{rad}} = 1.317\,\text{K W}^{-1}$
$T_{\text{ins}} = 28.03°\text{C}\left(\text{Solved Iteratively}\right)$</td></tr>
<tr><td>$T_{\text{film}} = \left(T_{\text{ins}} + T_{\text{Amb}}\right)/2$</td><td>$T_{\text{film}} = 27.62°\text{C}$</td></tr>
<tr><td>$T_{\text{wall,i}} = \left(T_{\text{w,Pre,in}} + T_{\text{w,Pre,out}}\right)/2$</td><td>$T_{\text{wall,i}} = 34.72°\text{C}$</td></tr>
<tr><td>$\text{Air Properties} = f\,(P = 101\,\text{kPa}, T_{\text{film}} = 27.62°\text{C})$</td><td>$\alpha = 2.205\times10^{-5}\,\text{m}^2\,s^{-1}$ $\beta = 0.003325\,\text{K}^{-1}$
$k = 0.02605\,\text{W m}^{-1}\,\text{K}^{-1}$ $\nu = 1.575\times10^{-5}\,\text{m}^2\,\text{s}^{-1}$
$\text{Pr} = 0.7195$ $\rho = 1.174\,\text{kg m}^{-3}$</td></tr>
<tr><td>$Ra_{\text{air}} = \dfrac{g\cdot\beta\cdot\left(T_{\text{ins}} - T_{\text{amb}}\right)\cdot\left(D_{\text{ins,o}}\right)^3}{\nu\cdot\alpha}$</td><td>$Ra_{\text{air}} = 77522$</td></tr>
<tr><td>$Nu_{\text{D}} = \left(0.60 + 0.387\cdot\dfrac{Ra_{\text{air}}^{\;1/6}}{\left(1 + \left(0.559/\text{Pr}\right)^{9/16}\right)^{8/27}}\right)^2$</td><td>$Nu_{\text{D}} = 7.29$
(Churchill and Chu, 1975)</td></tr>
<tr><td>$h_{\text{nat,conv}} = \dfrac{k_{\text{air}}}{D_{\text{ins,o}}}\cdot Nu_{\text{D}}$</td><td>$h_{\text{nat,conv}} = 1.899\,\text{W m}^{-2}\,\text{k}^{-1}$</td></tr>
</table>

Heat Transfer Sample Calculations: Propane; 6/21/2013; Run 1		
Inputs	**Equations**	**Results**
	$R_{conv} = \frac{1}{h_{nat,conv}\cdot\pi\cdot D_{ins,o}\cdot L_{Pre}}$	$R_{conv} = 3.636\ K\ W^{-1}$
	$\dot{Q}_{loss} = \frac{T_{wall,i}-T_{amb}}{R_{wall}+R_{ins}+\frac{R_{conv}\cdot R_{rad}}{\left(R_{conv}+R_{rad}\right)}}$	$\dot{Q}_{loss,Pre} = 0.8601\ W$
Heat Loss in Line from Pre-Condenser to Test Section		
$P_{Amb} = 101\ kPa$ $T_{Amb} = 27.20°C$ $T_{f,Pre,out} = 60.18°C$ $D_{Tube,o} = 12.7\ mm$ $D_{Tube,i} = 10.92\ mm$ $D_{ins,o} = 100\ mm$ $L_{Pre\ to\ Test} = 0.615\ m$ $k_{wall} = 14.0\ W\ m^{-1}\ K^{-1}$ $k_{ins} = 0.043\ W\ m^{-1}\ K^{-1}$ $\varepsilon_{ins} = 0.85$ $\sigma_{SB} = 5.67\times10^{-8}\ W\ m^{-2}K^{-4}$ $g = 9.81\ kg\ m^{-1}\ s^{-2}$	$R_{wall} = \frac{\ln\left(D_{Tube,o}/D_{Tube,i}\right)}{2\cdot\pi\cdot k_{wall}\cdot L_{Pre\ to\ Test}}$	$R_{wall} = 0.002791\ K\ W^{-1}$
	$R_{ins} = \frac{\ln\left(D_{ins,o}/D_{Tube,o}\right)}{2\cdot\pi\cdot k_{ins}\cdot L_{Pre\ to\ Test}}$	$R_{ins} = 12.42\ K\ W^{-1}$
	$R_{rad} = \frac{1}{\varepsilon_{ins}\cdot\pi\cdot D_{ins,o}\cdot L_{Pre\ to\ Test}\cdot\sigma_{SB}\cdot\left(T_{ins}^{2}+T_{amb}^{2}\right)\cdot\left(T_{ins}+T_{amb}\right)}$	$R_{rad} = 0.9825\ K\ W^{-1}$ $T_{ins} = 28.92°C$ (Solved Iteratively)
	$T_{film} = \left(T_{ins}+T_{Amb}\right)/2$	$T_{film} = 28.06°C$
	$T_{wall,i} = T_{f,Pre,out}$	$T_{wall,i} = 60.18°C$
	Air Properties $= f\left(P = 101\ kPa, T_{film} = 28.06°C\right)$	$\alpha = 2.21\times10^{-5}\ m^2\ s^{-1}$ $\beta = 0.00332\ K^{-1}$ $k = 0.02608\ W\ m^{-1}\ K^{-1}$ $\nu = 1.575\times10^{-5}\ m^2\ s^{-1}$ $Pr = 0.7195$ $\rho = 1.172\ kg\ m^{-3}$
	$Ra_{air} = \frac{g\cdot\beta\cdot\left(T_{ins}-T_{amb}\right)\cdot\left(D_{ins,o}\right)^{3}}{\nu\cdot\alpha}$	$Ra_{air} = 158899$
	$Nu_{D} = \left(0.60+0.387\cdot\frac{Ra_{air}^{1/6}}{\left(1+\left(0.559/Pr\right)^{9/16}\right)^{8/27}}\right)^{2}$	$Nu_{D} = 8.802$ (Churchill and Chu, 1975)

Heat Transfer Sample Calculations: Propane; 6/21/2013; Run 1		
Inputs	**Equations**	**Results**
	$h_{\text{nat,conv}} = \dfrac{k_{\text{air}}}{D_{\text{ins,o}}} \cdot Nu_{\text{D}}$	$h_{\text{nat,conv}} = 2.296\ \text{W m}^{-2}\ \text{k}^{-1}$
	$R_{\text{conv}} = \dfrac{1}{h_{\text{nat,conv}} \cdot \pi \cdot D_{\text{ins,o}} \cdot L_{\text{Pre to Test}}}$	$R_{\text{conv}} = 2.255\ \text{K W}^{-1}$
	$\dot{Q}_{\text{loss}} = \dfrac{T_{\text{wall,i}} - T_{\text{amb}}}{R_{\text{wall}} + R_{\text{ins}} + \dfrac{R_{\text{conv}} \cdot R_{\text{rad}}}{\left(R_{\text{conv}} + R_{\text{rad}}\right)}}$	$\dot{Q}_{\text{loss,Pre to Test}} = 2.507\ \text{W}$
Heat Loss in Post-Condenser #2		
$P_{\text{Amb}} = 101\ \text{kPa}$ $T_{\text{Amb}} = 27.20°\text{C}$ $T_{\text{w,Post,2}} = 14.48°\text{C}$ $D_{\text{Post,2,o}} = 38.1\ \text{mm}$ $D_{\text{Post,2,i}} = 34.8\ \text{mm}$ $D_{\text{ins,o}} = 100\ \text{mm}$ $L_{\text{Post,2}} = 0.461\ \text{m}$ $k_{\text{wall}} = 13.05\ \text{W m}^{-1}\ \text{K}^{-1}$ $k_{\text{ins}} = 0.043\ \text{W m}^{-1}\ \text{K}^{-1}$ $\varepsilon_{\text{ins}} = 0.85$ $\sigma_{\text{SB}} = 5.67 \times 10^{-8}\ \text{W m}^{-2}\text{K}^{-4}$ $g = 9.81\ \text{kg m}^{-1}\ \text{s}^{-2}$	$R_{\text{wall}} = \dfrac{\ln\left(D_{\text{Post,2,o}} / D_{\text{Post,2,i}}\right)}{2 \cdot \pi \cdot k_{\text{wall}} \cdot L_{\text{Post,2}}}$	$R_{\text{wall}} = 0.002374\ \text{K W}^{-1}$
	$R_{\text{ins}} = \dfrac{\ln\left(D_{\text{ins,o}} / D_{\text{Post,2,o}}\right)}{2 \cdot \pi \cdot k_{\text{ins}} \cdot L_{\text{Post,2}}}$	$R_{\text{ins}} = 7.747\ \text{K W}^{-1}$
	$R_{\text{rad}} = \dfrac{1}{\varepsilon_{\text{ins}} \cdot \pi \cdot D_{\text{ins,o}} \cdot L_{\text{Post,2}} \cdot \sigma_{\text{SB}} \cdot \left(\text{T}_{\text{ins}}{}^{2} + \text{T}_{\text{amb}}{}^{2}\right) \cdot \left(\text{T}_{\text{ins}} + \text{T}_{\text{amb}}\right)}$	$R_{\text{rad}} = 1.331\ \text{K W}^{-1}$ $T_{\text{ins}} = 25.83°\text{C}\left(\text{Solved Iteratively}\right)$
	$T_{\text{film}} = \left(T_{\text{ins}} + T_{\text{Amb}}\right)/2$	$T_{\text{film}} = 26.52°\text{C}$
	$T_{\text{wall,i}} = T_{\text{w,Post,2}}$	$T_{\text{wall,i}} = 14.48°\text{C}$
	$\text{Air Properties} = f\left(P = 101\ \text{kPa}, T_{\text{film}} = 26.52°\text{C}\right)$	$\alpha = 2.19 \times 10^{-5}\ \text{m}^2\ s^{-1}$ $\beta = 0.003337\ \text{K}^{-1}$ $k = 0.02579\ \text{W m}^{-1}\ \text{K}^{-1}$ $\nu = 1.559 \times 10^{-5}\ \text{m}^2\ \text{s}^{-1}$ $\text{Pr} = 0.7197$ $\rho = 1.178\ \text{kg m}^{-3}$
	$Ra_{\text{air}} = \dfrac{g \cdot \beta \cdot \left(T_{\text{ins}} - T_{\text{amb}}\right) \cdot \left(D_{\text{ins,o}}\right)^{3}}{\nu \cdot \alpha}$	$Ra_{\text{air}} = 130069$

Heat Transfer Sample Calculations: Propane; 6/21/2013; Run 1

Inputs	**Equations**	**Results**
	$Nu_{\text{D}} = \left(0.60 + 0.387 \cdot \frac{Ra_{\text{air}}^{1/6}}{\left(1 + \left(0.559 / \Pr\right)^{9/16}\right)^{8/27}}\right)^2$	$Nu_{\text{D}} = 8.348$ (Churchill and Chu, 1975)
	$h_{\text{nat,conv}} = \frac{k_{\text{air}}}{D_{\text{ins,o}}} \cdot Nu_{\text{D}}$	$h_{\text{nat,conv}} = 2.168\,\text{W m}^{-2}\,\text{k}^{-1}$
	$R_{\text{conv}} = \frac{1}{h_{\text{nat,conv}} \cdot \pi \cdot D_{\text{ins,o}} \cdot L_{\text{Post,2}}}$	$R_{\text{conv}} = 3.185\,\text{K W}^{-1}$
	$\dot{Q}_{\text{loss}} = \frac{T_{\text{wall,i}} - T_{\text{amb}}}{R_{\text{wall}} + R_{\text{ins}} + \frac{R_{\text{conv}} \cdot R_{\text{rad}}}{\left(R_{\text{conv}} + R_{\text{rad}}\right)}}$	$\dot{Q}_{\text{loss,Post,2}} = -1.461\,\text{W}$
Heat Loss in Post-Condenser #1		
$P_{\text{Amb}} = 101\,\text{kPa}$ $T_{\text{Amb}} = 27.20°\text{C}$ $T_{\text{w,Post,1}} = 23.88°\text{C}$ $D_{\text{Post,1,o}} = 38.1\,\text{mm}$ $D_{\text{Post,1,i}} = 34.8\,\text{mm}$ $D_{\text{ins,o}} = 100\,\text{mm}$ $L_{\text{Post,1}} = 0.461\,\text{m}$ $k_{\text{wall}} = 13.35\,\text{W m}^{-1}\,\text{K}^{-1}$ $k_{\text{ins}} = 0.043\,\text{W m}^{-1}\,\text{K}^{-1}$ $\varepsilon_{\text{ins}} = 0.85$ $\sigma_{\text{SB}} = 5.67 \times 10^{-8}\,\text{W m}^{-2}\text{K}^{-4}$	$R_{\text{wall}} = \frac{\ln\left(D_{\text{Post,1,o}} / D_{\text{Post,1,i}}\right)}{2 \cdot \pi \cdot k_{\text{wall}} \cdot L_{\text{Post,1}}}$	$R_{\text{wall}} = 0.002343\,\text{K W}^{-1}$
	$R_{\text{ins}} = \frac{\ln\left(D_{\text{ins,o}} / D_{\text{Post,1,o}}\right)}{2 \cdot \pi \cdot k_{\text{ins}} \cdot L_{\text{Post,1}}}$	$R_{\text{ins}} = 7.747\,\text{K W}^{-1}$
	$R_{\text{rad}} = \frac{1}{\varepsilon_{\text{ins}} \cdot \pi \cdot D_{\text{ins,o}} \cdot L_{\text{Post,1}} \cdot \sigma_{\text{SB}} \cdot \left(\text{T}_{\text{ins}}^{2} + \text{T}_{\text{amb}}^{2}\right) \cdot \left(\text{T}_{\text{ins}} + \text{T}_{\text{amb}}\right)}$	$R_{\text{rad}} = 1.325\,\text{K W}^{-1}$ $T_{\text{ins}} = 26.82°\text{C}\left(\text{Solved Iteratively}\right)$
	$T_{\text{film}} = \left(T_{\text{ins}} + T_{\text{Amb}}\right)/2$	$T_{\text{film}} = 27.01°\text{C}$
	$T_{\text{wall,i}} = T_{\text{w,Post,1}}$	$T_{\text{wall,i}} = 23.88°\text{C}$
	$\text{Air Properties} = f\,(P = 101\text{kPa}, T_{\text{film}} = 27.01°\text{C})$	$\alpha = 2.196 \times 10^{-5}\,\text{m}^2\,s^{-1}$ $\beta = 0.003332\,\text{K}^{-1}$ $k = 0.026\,\text{W m}^{-1}\,\text{K}^{-1}$ $\Pr = 0.7196$ $\nu = 1.567 \times 10^{-5}\,\text{m}^2\,\text{s}^{-1}$ $\rho = 1.176\,\text{kg m}^{-3}$

Heat Transfer Sample Calculations: Propane; 6/21/2013; Run 1		
Inputs	**Equations**	**Results**
	$Ra_{\mathrm{air}} = \dfrac{g \cdot \beta \cdot (T_{\mathrm{ins}} - T_{\mathrm{amb}}) \cdot (D_{\mathrm{ins,o}})^3}{\nu \cdot \alpha}$	$Ra_{\mathrm{air}} = 36213$
	$Nu_{\mathrm{D}} = \left(0.60 + 0.387 \cdot \dfrac{Ra_{\mathrm{air}}^{1/6}}{\left(1 + (0.559 / \mathrm{Pr})^{9/16}\right)^{8/27}} \right)^2$	$Nu_{\mathrm{D}} = 6.002$ (Churchill and Chu, 1975)
	$h_{\mathrm{nat,conv}} = \dfrac{k_{\mathrm{air}}}{D_{\mathrm{ins,o}}} \cdot Nu_{\mathrm{D}}$	$h_{\mathrm{nat,conv}} = 1.561\,\mathrm{W\,m^{-2}\,k^{-1}}$
	$R_{\mathrm{conv}} = \dfrac{1}{h_{\mathrm{nat,conv}} \cdot \pi \cdot D_{\mathrm{ins,o}} \cdot L_{\mathrm{Post,1}}}$	$R_{\mathrm{conv}} = 4.424\,\mathrm{K\,W^{-1}}$
	$\dot{Q}_{\mathrm{loss}} = \dfrac{T_{\mathrm{wall,i}} - T_{\mathrm{amb}}}{R_{\mathrm{wall}} + R_{\mathrm{ins}} + \dfrac{R_{\mathrm{conv}} \cdot R_{\mathrm{rad}}}{(R_{\mathrm{conv}} + R_{\mathrm{rad}})}}$	$\dot{Q}_{\mathrm{loss,Post,1}} = -0.3774\,\mathrm{W}$
Heat Loss in Fluid Line from Post-Condenser # 1 to Post-Condenser # 2		
$P_{\mathrm{Amb}} = 101\,\mathrm{kPa}$ $T_{\mathrm{Amb}} = 27.20°\mathrm{C}$ $T_{\mathrm{f,Post,line}} = 26.49°\mathrm{C}$ $D_{\mathrm{Tube,o}} = 12.7\,\mathrm{mm}$ $D_{\mathrm{Tube,i}} = 10.92\,\mathrm{mm}$ $D_{\mathrm{ins,o}} = 100\,\mathrm{mm}$	$R_{\mathrm{wall}} = \dfrac{\ln(D_{\mathrm{Tube,o}} / D_{\mathrm{Tube,i}})}{2 \cdot \pi \cdot k_{\mathrm{wall}} \cdot L_{\mathrm{Post\ 1\ to\ 2}}}$	$R_{\mathrm{wall}} = 0.01794\,\mathrm{K\,W^{-1}}$
	$R_{\mathrm{ins}} = \dfrac{\ln(D_{\mathrm{ins,o}} / D_{\mathrm{Tube,i}})}{2 \cdot \pi \cdot k_{\mathrm{ins}} \cdot L_{\mathrm{Post\ 1\ to\ 2}}}$	$R_{\mathrm{ins}} = 76.38\,\mathrm{K\,W^{-1}}$
	$R_{\mathrm{rad}} = \dfrac{1}{\varepsilon_{\mathrm{ins}} \cdot \pi \cdot D_{\mathrm{ins,o}} \cdot L_{\mathrm{Post\ 1\ to\ 2}} \cdot \sigma_{\mathrm{SB}} \cdot (\mathrm{T_{ins}}^2 + \mathrm{T_{amb}}^2) \cdot (\mathrm{T_{ins}} + \mathrm{T_{amb}})}$	$R_{\mathrm{rad}} = 6.096\,\mathrm{K\,W^{-1}}$ $T_{\mathrm{ins}} = 27.16°\mathrm{C}$ (Solved Iteratively)
	$T_{\mathrm{film}} = (T_{\mathrm{ins}} + T_{\mathrm{Amb}})/2$	$T_{\mathrm{film}} = 27.18°\mathrm{C}$

Heat Transfer Sample Calculations: Propane; 6/21/2013; Run 1		
Inputs	**Equations**	**Results**
$L_{\text{Post 1 to 2}} = 0.1\text{m}$ $k_{\text{wall}} = 13.39\,\text{W m}^{-1}\,\text{K}^{-1}$ $k_{\text{ins}} = 0.043\,\text{W m}^{-1}\,\text{K}^{-1}$ $\varepsilon_{\text{ins}} = 0.85$ $\sigma_{\text{SB}} = 5.67\times10^{-8}\,\text{W m}^{-2}\text{K}^{-4}$ $g = 9.81\,\text{kg m}^{-1}\,\text{s}^{-2}$	$T_{\text{wall,i}} = T_{\text{f,Post,line}}$	$T_{\text{wall,i}} = 26.49°\text{C}$
	$\text{Air Properties} = f\left(P = 101\text{kPa}, T_{\text{film}} = 27.18°\text{C}\right)$	$\alpha = 2.199\times10^{-5}\,\text{m}^2\,s^{-1}$ $\beta = 0.00333\,\text{K}^{-1}$ $k = 0.02601\,\text{W m}^{-1}\,\text{K}^{-1}$ $\nu = 1.566\times10^{-5}\,\text{m}^2\,\text{s}^{-1}$ $\text{Pr} = 0.7196$ $\rho = 1.175\,\text{kg m}^{-3}$
	$Ra_{\text{air}} = \dfrac{g\cdot\beta\cdot\left(T_{\text{ins}} - T_{\text{amb}}\right)\cdot\left(D_{\text{ins,o}}\right)^3}{\nu\cdot\alpha}$	$Ra_{\text{air}} = 4247$
	$Nu_{\text{D}} = \left(0.60 + 0.387\cdot\dfrac{Ra_{\text{air}}^{\;1/6}}{\left(1+\left(0.559/\text{Pr}\right)^{9/16}\right)^{8/27}}\right)^2$	$Nu_{\text{D}} = 4.3$ (Churchill and Chu, 1975)
	$h_{\text{nat,conv}} = \dfrac{k_{\text{air}}}{D_{\text{ins,o}}}\cdot Nu_{\text{D}}$	$h_{\text{nat,conv}} = 0.9334\,\text{W m}^{-2}\,\text{K}^{-1}$
	$R_{\text{conv}} = \dfrac{1}{h_{\text{nat,conv}}\cdot\pi\cdot D_{\text{ins,o}}\cdot L_{\text{Post 1 to 2}}}$	$R_{\text{conv}} = 34.1\,\text{K W}^{-1}$
	$\dot{Q}_{\text{loss}} = \dfrac{T_{\text{wall,i}} - T_{\text{amb}}}{R_{\text{wall}} + R_{\text{ins}} + \dfrac{R_{\text{conv}}\cdot R_{\text{rad}}}{\left(R_{\text{conv}} + R_{\text{rad}}\right)}}$	$\dot{Q}_{\text{loss,f,Post,12}} = -0.008748\,\text{W}$

Heat Transfer Sample Calculations: Propane; 6/21/2013; Run 1		
Inputs	**Equations**	**Results**
Heat Loss in Line from Test Section to Post-Condenser #1		
$P_{\text{Amb}} = 101\,\text{kPa}$ $T_{\text{Amb}} = 27.20°\text{C}$ $T_{\text{f,Post,1,line}} = 60°\text{C}$ $D_{\text{Tube,o}} = 12.7\,\text{mm}$ $D_{\text{Tube,i}} = 10.92\,\text{mm}$ $D_{\text{ins,o}} = 100\,\text{mm}$ $L_{\text{Test to Post,1}} = 0.695\,\text{m}$ $k_{\text{wall}} = 14\,\text{W m}^{-1}\,\text{K}^{-1}$ $k_{\text{ins}} = 0.043\,\text{W m}^{-1}\,\text{K}^{-1}$ $\varepsilon_{\text{ins}} = 0.85$ $\sigma_{\text{SB}} = 5.67\times10^{-8}\,\text{W m}^{-2}\text{K}^{-4}$ $g = 9.81\,\text{kg m}^{-1}\,\text{s}^{-2}$	$R_{\text{wall}} = \dfrac{\ln\left(D_{\text{Tube,o}} / D_{\text{Tube,i}}\right)}{2\cdot\pi\cdot k_{\text{wall}}\cdot L_{\text{Test to Post,1}}}$	$R_{\text{wall}} = 0.002471\,\text{K W}^{-1}$
	$R_{\text{ins}} = \dfrac{\ln\left(D_{\text{ins,o}} / D_{\text{Tube,o}}\right)}{2\cdot\pi\cdot k_{\text{ins}}\cdot L_{\text{Test to Post,1}}}$	$R_{\text{ins}} = 10.99\,\text{K W}^{-1}$
	$R_{\text{rad}} = \dfrac{1}{\varepsilon_{\text{ins}}\cdot\pi\cdot D_{\text{ins,o}}\cdot L_{\text{Test to Post,1}}\cdot\sigma_{\text{SB}}\cdot\left(\text{T}_{\text{ins}}{}^{2}+\text{T}_{\text{amb}}{}^{2}\right)\cdot\left(\text{T}_{\text{ins}}+\text{T}_{\text{amb}}\right)}$	$R_{\text{rad}} = 0.8694\,\text{K W}^{-1}$ $T_{\text{ins}} = 28.91°\text{C}\left(\text{Solved Iteratively}\right)$
	$T_{\text{film}} = \left(T_{\text{ins}} + T_{\text{Amb}}\right)/2$	$T_{\text{film}} = 28.06°\text{C}$
	$T_{\text{wall,i}} = \left(T_{\text{f,Test,out}} + T_{\text{f,Post,1,in}}\right)/2$	$T_{\text{wall,i}} = 60°\text{C}$
	$\text{Air Properties} = f\left(P = 101\,\text{kPa}, T_{\text{film}} = 28.06°\text{C}\right)$	$\alpha = 2.221\times10^{-5}\,\text{m}^2\,s^{-1}$ $\beta = 0.00332\,\text{K}^{-1}$ $k = 0.02608\,\text{W m}^{-1}\,\text{K}^{-1}$ $\nu = 1.574\times10^{-5}\,\text{m}^2\,\text{s}^{-1}$ $\text{Pr} = 0.7195$ $\rho = 1.172\,\text{kg m}^{-3}$
	$Ra_{\text{air}} = \dfrac{g\cdot\beta\cdot\left(T_{\text{ins}} - T_{\text{amb}}\right)\cdot\left(D_{\text{ins,o}}\right)^{3}}{\nu\cdot\alpha}$	$Ra_{\text{air}} = 160443$
	$Nu_{\text{D}} = \left(0.60 + 0.387\cdot\dfrac{Ra_{\text{air}}{}^{1/6}}{\left(1+\left(0.559/\text{Pr}\right)^{9/16}\right)^{8/27}}\right)^{2}$	$Nu_{\text{D}} = 8.791$ (Churchill and Chu, 1975)
	$h_{\text{nat,conv}} = \dfrac{k_{\text{air}}}{D_{\text{ins,o}}}\cdot Nu_{\text{D}}$	$h_{\text{nat,conv}} = 2.293\,\text{W m}^{-2}\,\text{k}^{-1}$
	$R_{\text{conv}} = \dfrac{1}{h_{\text{nat,conv}}\cdot\pi\cdot D_{\text{ins,o}}\cdot L_{\text{Test to Post,1}}}$	$R_{\text{conv}} = 1.998\,\text{K W}^{-1}$

Heat Transfer Sample Calculations: Propane; 6/21/2013; Run 1

Inputs	Equations	Results
	$\dot{Q}_{\text{loss}} = \dfrac{T_{\text{wall,i}} - T_{\text{amb}}}{R_{\text{wall}} + R_{\text{ins}} + \dfrac{R_{\text{conv}} \cdot R_{\text{rad}}}{\left(R_{\text{conv}} + R_{\text{rad}}\right)}}$	$\dot{Q}_{\text{loss,f,Test to Post,1}} = 2.818\,\text{W}$
Heat Loss in Line from Post-Condenser #2 to Subcooled Point		
$P_{\text{Amb}} = 101\,\text{kPa}$ $T_{\text{Amb}} = 27.20°\text{C}$ $T_{\text{f,Subcool,Line}} = 16.26°\text{C}$ $D_{\text{Tube,o}} = 12.7\,\text{mm}$ $D_{\text{Tube,i}} = 10.92\,\text{mm}$ $D_{\text{ins,o}} = 100\,\text{mm}$ $L_{\text{Subcool,Line}} = 0.067\,\text{m}$ $k_{\text{wall}} = 13.21\,\text{W m}^{-1}\,\text{K}^{-1}$ $k_{\text{ins}} = 0.043\,\text{W m}^{-1}\,\text{K}^{-1}$ $\varepsilon_{\text{ins}} = 0.85$ $\sigma_{\text{SB}} = 5.67\times10^{-8}\,\text{W m}^{-2}\text{K}^{-4}$ $g = 9.81\,\text{kg m}^{-1}\,\text{s}^{-2}$	$R_{\text{wall}} = \dfrac{\ln\left(D_{\text{Tube,o}} / D_{\text{Tube,i}}\right)}{2\cdot\pi\cdot k_{\text{wall}}\cdot L_{\text{Test to Post,1}}}$	$R_{\text{wall}} = 0.02716\,\text{K W}^{-1}$
	$R_{\text{ins}} = \dfrac{\ln\left(D_{\text{ins,o}} / D_{\text{Tube,o}}\right)}{2\cdot\pi\cdot k_{\text{ins}}\cdot L_{\text{Test to Post,1}}}$	$R_{\text{ins}} = 114\,\text{K W}^{-1}$
	$R_{\text{rad}} = \dfrac{1}{\varepsilon_{\text{ins}}\cdot\pi\cdot D_{\text{ins,o}}\cdot L_{\text{Test to Post,1}}\cdot\sigma_{\text{SB}}\cdot\left(\text{T}_{\text{ins}}{}^2 + \text{T}_{\text{amb}}{}^2\right)\cdot\left(\text{T}_{\text{ins}} + \text{T}_{\text{amb}}\right)}$	$R_{\text{rad}} = 9.124\,\text{K W}^{-1}$ $T_{\text{ins}} = 26.59°\text{C}\left(\text{Solved Iteratively}\right)$
	$T_{\text{film}} = \left(T_{\text{ins}} + T_{\text{Amb}}\right)/2$	$T_{\text{film}} = 26.89°\text{C}$
	$T_{\text{wall,i}} = T_{\text{f,Subcool,Line}}$	$T_{\text{wall,i}} = 16.26°\text{C}$
	$\text{Air Properties} = f\left(P = 101\,\text{kPa}, T_{\text{film}} = 26.89°\text{C}\right)$	$\alpha = 2.195\times10^{-5}\,\text{m}^2\,s^{-1}$ $\beta = 0.003333\,\text{K}^{-1}$ $k = 0.02599\,\text{W m}^{-1}\,\text{K}^{-1}$ $\nu = 1.574\times10^{-5}\,\text{m}^2\,\text{s}^{-1}$ $\text{Pr} = 0.7196$ $\rho = 1.177\,\text{kg m}^{-3}$
	$Ra_{\text{air}} = \dfrac{g\cdot\beta\cdot\left(T_{\text{ins}} - T_{\text{amb}}\right)\cdot\left(D_{\text{ins,o}}\right)^3}{\nu\cdot\alpha}$	$Ra_{\text{air}} = 57999$
	$Nu_{\text{D}} = \left(0.60 + 0.387\cdot\dfrac{Ra_{\text{air}}{}^{1/6}}{\left(1 + \left(0.559 / \text{Pr}\right)^{9/16}\right)^{8/27}}\right)^2$	$Nu_{\text{D}} = 6.765$ (Churchill and Chu, 1975)
	$h_{\text{nat,conv}} = \dfrac{k_{\text{air}}}{D_{\text{ins,o}}}\cdot Nu_{\text{D}}$	$h_{\text{nat,conv}} = 1.758\,\text{W m}^{-2}\,\text{k}^{-1}$

Heat Transfer Sample Calculations: Propane; 6/21/2013; Run 1		
Inputs	**Equations**	**Results**
	$R_{\text{conv}} = \dfrac{1}{h_{\text{nat,conv}} \cdot \pi \cdot D_{\text{ins,o}} \cdot L_{\text{Test to Post,1}}}$	$R_{\text{conv}} = 27.02\,\text{K W}^{-1}$
	$\dot{Q}_{\text{loss}} = \dfrac{T_{\text{wall,i}} - T_{\text{amb}}}{R_{\text{wall}} + R_{\text{ins}} + \dfrac{R_{\text{conv}} \cdot R_{\text{rad}}}{\left(R_{\text{conv}} + R_{\text{rad}}\right)}}$	$\dot{Q}_{\text{loss,f,Subcool,Line}} = -0.09018\,\text{W}$
Heat Loss in Test Section		
$P_{\text{Amb}} = 101\,\text{kPa}$ $T_{\text{Amb}} = 27.20°\text{C}$ $T_{\text{w,Pri,Test,in}} = 46.38°\text{C}$ $T_{\text{w,Pri,Test,out}} = 48.29°\text{C}$ $D_{\text{OT,o}} = 12.7\,\text{mm}$ $D_{\text{OT,i}} = 11.06\,\text{mm}$ $D_{\text{ins,o}} = 100\,\text{mm}$ $L_{\text{Annulus}} = 0.53\,\text{m}$ $k_{\text{wall}} = 399.4\,\text{W m}^{-1}\,\text{K}^{-1}$ $k_{\text{ins}} = 0.043\,\text{W m}^{-1}\,\text{K}^{-1}$ $\varepsilon_{\text{ins}} = 0.85$ $\sigma_{\text{SB}} = 5.67 \times 10^{-8}\,\text{W m}^{-2}\text{K}^{-4}$ $g = 9.81\,\text{kg m}^{-1}\,\text{s}^{-2}$	$R_{\text{wall}} = \dfrac{\ln\left(D_{\text{OT,o}} / D_{\text{OT,i}}\right)}{2 \cdot \pi \cdot k_{\text{wall}} \cdot L_{\text{Annulus}}}$	$R_{\text{wall}} = 0.003016\,\text{K W}^{-1}$
	$R_{\text{ins}} = \dfrac{\ln\left(D_{\text{ins,o}} / D_{\text{OT,o}}\right)}{2 \cdot \pi \cdot k_{\text{ins}} \cdot L_{\text{Annulus}}}$	$R_{\text{ins}} = 14.41\,\text{K W}^{-1}$
	$R_{\text{rad}} = \dfrac{1}{\varepsilon_{\text{ins}} \cdot \pi \cdot D_{\text{ins,o}} \cdot L_{\text{Annulus}} \cdot \sigma_{\text{SB}} \cdot \left(\text{T}_{\text{ins}}{}^{2} + \text{T}_{\text{amb}}{}^{2}\right) \cdot \left(\text{T}_{\text{ins}} + \text{T}_{\text{amb}}\right)}$	$R_{\text{rad}} = 1.144\,\text{K W}^{-1}$ $T_{\text{ins}} = 28.29°\text{C}\left(\text{Solved Iteratively}\right)$
	$T_{\text{film}} = \left(T_{\text{ins}} + T_{\text{Amb}}\right)/2$	$T_{\text{film}} = 27.75°\text{C}$
	$T_{\text{wall,i}} = \left(T_{\text{w,Pri,Test,in}} + T_{\text{w,Pri,Test,out}}\right)/2$	$T_{\text{wall,i}} = 47.33°\text{C}$
	Air Properties $= f\,(P = 101\,\text{kPa}, T_{\text{film}} = 27.75°\text{C})$	$\alpha = 2.206 \times 10^{-5}\,\text{m}^2\,s^{-1}$ $\beta = 0.003323\,\text{K}^{-1}$ $k = 0.02606\,\text{W m}^{-1}\,\text{K}^{-1}$ $\text{Pr} = 0.7195$ $\nu = 1.572 \times 10^{-5}\,\text{m}^2\,\text{s}^{-1}$ $\rho = 1.173\,\text{kg m}^{-3}$
	$Ra_{\text{air}} = \dfrac{g \cdot \beta \cdot \left(T_{\text{ins}} - T_{\text{amb}}\right) \cdot \left(D_{\text{ins,o}}\right)^3}{\nu \cdot \alpha}$	$Ra_{\text{air}} = 101296$
	$Nu_{\text{D}} = \left(0.60 + 0.387 \cdot \dfrac{Ra_{\text{air}}{}^{1/6}}{\left(1 + \left(0.559 / \text{Pr}\right)^{9/16}\right)^{8/27}}\right)^2$	$Nu_{\text{D}} = 7.817$ (Churchill and Chu, 1975)

Heat Transfer Sample Calculations: Propane; 6/21/2013; Run 1		
Inputs	**Equations**	**Results**
	$h_{\text{nat,conv}} = \frac{k_{\text{air}}}{D_{\text{ins,o}}} \cdot Nu_{\text{D}}$	$h_{\text{nat,conv}} = 2.037\ \text{W m}^{-2}\,\text{k}^{-1}$
	$R_{\text{conv}} = \frac{1}{h_{\text{nat,conv}} \cdot \pi \cdot D_{\text{ins,o}} \cdot L_{\text{Annulus}}}$	$R_{\text{conv}} = 2.949\ \text{K W}^{-1}$
	$\dot{Q}_{\text{loss}} = \frac{T_{\text{wall,i}} - T_{\text{amb}}}{R_{\text{wall}} + R_{\text{ins}} + \frac{R_{\text{conv}} \cdot R_{\text{rad}}}{\left(R_{\text{conv}} + R_{\text{rad}}\right)}}$	$\dot{Q}_{\text{loss,Test}} = 1.321\text{W}$
Heat Loss in Primary Loop		
$P_{\text{Amb}} = 101\text{kPa}$ $T_{\text{Amb}} = 27.20°\text{C}$ $T_{\text{w,Pri,Test,in}} = 46.38°\text{C}$ $T_{\text{w,Pri,Test,out}} = 48.29°\text{C}$ $D_{\text{Tube,o}} = 12.7\ \text{mm}$ $D_{\text{Tube,i}} = 10.2\ \text{mm}$ $D_{\text{ins,o}} = 100\ \text{mm}$ $L_{\text{Pri, Effective}} = 5.703\ \text{m}$ $k_{\text{wall}} = 13.77\ \text{W m}^{-1}\ \text{K}^{-1}$ $k_{\text{ins}} = 0.043\ \text{W m}^{-1}\ \text{K}^{-1}$ $\varepsilon_{\text{ins}} = 0.85$ $\sigma_{\text{SB}} = 5.67 \times 10^{-8}\ \text{W m}^{-2}\text{K}^{-4}$ $g = 9.81\text{kg m}^{-1}\ \text{s}^{-2}$	$R_{\text{wall}} = \frac{\ln\left(D_{\text{Tube,o}} / D_{\text{Tube,i}}\right)}{2 \cdot \pi \cdot k_{\text{wall}} \cdot L_{\text{Pri,Effective}}}$	$R_{\text{wall}} = 0.0004443\ \text{K W}^{-1}$
	$R_{\text{ins}} = \frac{\ln\left(D_{\text{ins,o}} / D_{\text{Tube,o}}\right)}{2 \cdot \pi \cdot k_{\text{ins}} \cdot L_{\text{Pri,Effective}}}$	$R_{\text{ins}} = 1.339\ \text{K W}^{-1}$
	$R_{\text{rad}} = \frac{1}{\varepsilon_{\text{ins}} \cdot \pi \cdot D_{\text{ins,o}} \cdot L_{\text{Pri,Effective}} \cdot \sigma_{\text{SB}} \cdot \left(\text{T}_{\text{ins}}{}^{2} + \text{T}_{\text{amb}}{}^{2}\right) \cdot \left(\text{T}_{\text{ins}} + \text{T}_{\text{amb}}\right)}$	$R_{\text{rad}} = 0.1063\ \text{K W}^{-1}$ $T_{\text{ins}} = 28.29°\text{C}\left(\text{Solved Iteratively}\right)$
	$T_{\text{film}} = \left(T_{\text{ins}} + T_{\text{Amb}}\right)/2$	$T_{\text{film}} = 27.74°\text{C}$
	$T_{\text{wall,i}} = \left(T_{\text{w,Pri,Test,in}} + T_{\text{w,Pri,Test,out}}\right)/2$	$T_{\text{wall,i}} = 47.33°\text{C}$
	$\text{Air Properties} = f\left(P = 101\text{kPa}, T_{\text{film}} = 27.74°\text{C}\right)$	$\alpha = 2.206 \times 10^{-5}\ \text{m}^2\ s^{-1}$ $\beta = 0.003323\text{K}^{-1}$ $k = 0.02606\ \text{W m}^{-1}\ \text{K}^{-1}$ $\nu = 1.572 \times 10^{-5}\ \text{m}^2\ \text{s}^{-1}$ $\text{Pr} = 0.7195$ $\rho = 1.173\text{kg m}^{-3}$
	$Ra_{\text{air}} = \frac{g \cdot \beta \cdot \left(T_{\text{ins}} - T_{\text{amb}}\right) \cdot \left(D_{\text{ins,o}}\right)^{3}}{\nu \cdot \alpha}$	$Ra_{\text{air}} = 100944$

Heat Transfer Sample Calculations: Propane; 6/21/2013; Run 1		
Inputs	**Equations**	**Results**
	$Nu_D = \left(0.60 + 0.387 \cdot Ra_{air}^{1/6} \Big/ \left(1 + \left(0.559 / \mathrm{Pr} \right)^{9/16} \right)^{8/27} \right)^2$	$Nu_D = 7.809$ (Churchill and Chu, 1975)
	$h_{nat,conv} = \dfrac{k_{air}}{D_{ins,o}} \cdot Nu_D$	$h_{nat,conv} = 2.035\,\mathrm{W\,m^{-2}\,k^{-1}}$
	$R_{conv} = \dfrac{1}{h_{nat,conv} \cdot \pi \cdot D_{ins,o} \cdot L_{Annulus}}$	$R_{conv} = 0.2743\,\mathrm{K\,W^{-1}}$
	$\dot{Q}_{loss} = T_{wall,i} - T_{amb} \Big/ R_{wall} + R_{ins} + \dfrac{R_{conv} \cdot R_{rad}}{\left(R_{conv} + R_{rad} \right)}$	$\dot{Q}_{loss,Pri} = 14.16\,\mathrm{W}$
Heat Loss in Secondary Heat Exchanger		
$P_{Amb} = 101\,\mathrm{kPa}$ $T_{Amb} = 27.20°\mathrm{C}$ $T_{w,Pri,Sec,in} = 48.11°\mathrm{C}$ $T_{w,Pri,Sec,out} = 46.41°\mathrm{C}$ $D_{Sec,o} = 25.4\,\mathrm{mm}$ $D_{Sec,i} = 22.9\,\mathrm{mm}$ $D_{ins,o} = 100\,\mathrm{mm}$ $L_{sec} = 0.376\,\mathrm{m}$ $k_{wall} = 13.77\,\mathrm{W\,m^{-1}\,K^{-1}}$ $k_{ins} = 0.043\,\mathrm{W\,m^{-1}\,K^{-1}}$ $\varepsilon_{ins} = 0.85$	$R_{wall} = \dfrac{\ln\left(D_{Sec,o} / D_{Sec,i} \right)}{2 \cdot \pi \cdot k_{wall} \cdot L_{Sec}}$	$R_{wall} = 0.003186\,\mathrm{K\,W^{-1}}$
	$R_{ins} = \dfrac{\ln\left(D_{ins,o} / D_{Sec,o} \right)}{2 \cdot \pi \cdot k_{ins} \cdot L_{Sec}}$	$R_{ins} = 13.49\,\mathrm{K\,W^{-1}}$
	$R_{rad} = \dfrac{1}{\varepsilon_{ins} \cdot \pi \cdot D_{ins,o} \cdot L \cdot \sigma_{SB} \cdot \left(\mathrm{T_{ins}}^2 + \mathrm{T_{amb}}^2 \right) \cdot \left(\mathrm{T_{ins}} + \mathrm{T_{amb}} \right)}$	$R_{rad} = 1.608\,\mathrm{K\,W^{-1}}$ $T_{ins} = 28.75°\mathrm{C}\,(\text{Solved Iteratively})$
	$T_{film} = \left(T_{ins} + T_{Amb} \right) / 2$	$T_{film} = 27.97°\mathrm{C}$
	$T_{wall,i} = \left(T_{w,Pri,Sec,in} + T_{w,Pri,Sec,out} \right) / 2$	$T_{wall,i}{}^* = 47.26°\mathrm{C}$
	$\text{Air Properties} = f\,(P = 101\,\mathrm{kPa}, T_{film} = 26.5°\mathrm{C})$	$\alpha = 2.209 \times 10^{-5}\,\mathrm{m^2}\,s^{-1}$ $\beta = 0.003321\,\mathrm{K^{-1}}$ $k = 0.02607\,\mathrm{W\,m^{-1}\,K^{-1}}$ $\nu = 1.571 \times 10^{-5}\,\mathrm{m^2\,s^{-1}}$ $\mathrm{Pr} = 0.7195$ $\rho = 1.172\,\mathrm{kg\,m^{-3}}$

Heat Transfer Sample Calculations: Propane; 6/21/2013; Run 1		
Inputs	**Equations**	**Results**
$\sigma_{SB} = 5.67\times10^{-8}\ \mathrm{W\,m^{-2}K^{-4}}$ $g = 9.81\ \mathrm{kg\,m^{-1}\,s^{-2}}$	$Ra_{air} = \frac{g\cdot\beta\cdot(T_{ins}-T_{amb})\cdot(D_{ins,o})^3}{\nu\cdot\alpha}$	$Ra_{air} = 143291$
	$Nu_D = \left(0.60+0.387\cdot\frac{Ra_{air}^{1/6}}{\left(1+(0.559/\mathrm{Pr})^{9/16}\right)^{8/27}}\right)^2$	$Nu_D = 8.564$ (Churchill and Chu, 1975)
	$h_{nat,conv} = \frac{k_{air}}{D_{ins,o}}\cdot Nu_D$	$h_{nat,conv} = 2.233\ \mathrm{W\,m^{-2}\,k^{-1}}$
	$R_{conv} = \frac{1}{h_{nat,conv}\cdot\pi\cdot D_{ins,o}\cdot L}$	$R_{conv} = 3.791\ \mathrm{K\,W^{-1}}$
	$\dot{Q}_{loss} = \frac{T_{wall,i}-T_{amb}}{R_{wall}+R_{ins}+\frac{R_{conv}\cdot R_{rad}}{(R_{conv}+R_{rad})}}$	$\dot{Q}_{loss,Sec} = 1.368\ \mathrm{W}$
Average Test Section Quality		
$T_{w,Pre,in} = 11.83^{\circ}\mathrm{C}$ $T_{w,Pre,out} = 57.6^{\circ}\mathrm{C}$ $T_{w,Post\,\#1,in} = 12.71^{\circ}\mathrm{C}$ $T_{w,Post\,\#1,out} = 16.25^{\circ}\mathrm{C}$ $T_{w,Post\,\#2,in} = 16.19^{\circ}\mathrm{C}$ $T_{w,Post\,\#2,out} = 31.58^{\circ}\mathrm{C}$	$i_{f,Pre,in} = f\left(P_{f,Pre,in}, T_{f,Pre,in}\right)$	$i_{f,Pre,in} = 743.6\ \mathrm{kJ\,kg^{-1}}$
	$T_{f,Saturation} = f\left(P_{f,Test,in}, q=1\right)$	$T_{f,Saturation} = 60.32^{\circ}\mathrm{C}$
	$\Delta T_{f,Pre,in,Sup} = T_{f,Pre,in} - T_{f,Saturation}$	$\Delta T_{f,Pre,in,Sup} = 46.98\mathrm{K}$
	$i_{w,Pre,in} = f\left(P_w, T_{w,Pre,in}\right)$	$i_{w,Pre,in} = 49.95\ \mathrm{kJ\,kg^{-1}}$
	$i_{w,Pre,out} = f\left(P_w, T_{w,Pre,out}\right)$	$i_{w,Pre,out} = 241.3\ \mathrm{kJ\,kg^{-1}}$
	$\rho_{w,Pre,in} = f\left(P_w, T_{w,Pre,in}\right)$	$\rho_{w,Pre,in} = 999.6\ \mathrm{kg\,m^{-3}}$
	$\dot{m}_{w,Pre} = \dot{V}_{w,Pre}\cdot\rho_{w,Pre,in}$	$\dot{m}_{w,Pre} = 0.03707\ \mathrm{kg\,s^{-1}}$
	$\dot{Q}_{Pre} = \dot{m}_{w,Pre}\left(i_{w,Pre,out}-i_{w,Pre,in}\right)+\dot{Q}_{loss,Pre}$	$\dot{Q}_{Pre} = 7097\ \mathrm{W}$

Heat Transfer Sample Calculations: Propane; 6/21/2013; Run 1

Inputs	Equations	Results
$T_{\text{f,Pre,in}} = 107.30^\circ\text{C}$ $T_{\text{f,Test,in,m}} = 59.92^\circ\text{C}$ $T_{\text{f,Test,out,m}} = 59.95^\circ\text{C}$ $T_{\text{f,Post,out}} = 16.26^\circ\text{C}$ $P_{\text{f,Test,in}} = 2123\,\text{kPa}$ $P_{\text{f,Test,out}} = 2124\,\text{kPa}$ $P_{\text{w}} = 271.1\,\text{kPa}$ $\dot{V}_{\text{w,Pre}} = 2.225\,\text{L min}^{-1}$ $\dot{V}_{\text{w,Post}} = 2.377\,\text{L min}^{-1}$ $\dot{m}_{\text{f}} = 0.02114\,\text{kg s}^{-1}$ $\dot{Q}_{\text{loss,f,Superheat,Line}} = 0.994\,\text{W}$ $\dot{Q}_{\text{loss,Pre}} = 0.8601\,\text{W}$ $\dot{Q}_{\text{loss,Post,1}} = -0.3774\,\text{W}$ $\dot{Q}_{\text{loss,Post,2}} = -1.461\,\text{W}$ $\dot{Q}_{\text{loss,f,Post,12}} = -0.00875\,\text{W}$ $\dot{Q}_{\text{loss,f,Subcool,Line}} = -0.0902\,\text{W}$ $\dot{Q}_{\text{loss,Pre to Test}} = 2.507\,\text{W}$ $\dot{Q}_{\text{loss,Test to Post}} = 2.818\,\text{W}$	$i_{\text{f,Test,in}} = i_{\text{f,Pre,in}} - \left(\dot{Q}_{\text{Pre}} + \dot{Q}_{\text{loss,Pre to Test}} + \dot{Q}_{\text{loss,f,Superheat,Line}}\right) / \dot{m}_{\text{f}}$	$i_{\text{f,Test,in}} = 407.8\,\text{kJ kg}^{-1}$
	$y_{\text{f,Test,in}} = f\left(i_{\text{f,Test,in}}, P_{\text{f,Test,in}}\right)$	$y_{\text{f,Test,in}} = 0.15$
	$i_{\text{f,Post,out}} = f\left(P_{\text{f,Post,out}}, T_{\text{f,Post,out}}\right)$	$i_{\text{f,Post,out}} = 242.1\,\text{kJ kg}^{-1}$
	$i_{\text{w,Post \#1,in}} = f\left(P_{\text{w}}, T_{\text{w,Post \#1,in}}\right)$	$i_{\text{w,Post \#1,in}} = 53.65\,\text{kJ kg}^{-1}$
	$i_{\text{w,Post \#1,out}} = f\left(P_{\text{w}}, T_{\text{w,Post \#1,out}}\right)$	$i_{\text{w,Post \#1,out}} = 68.44\,\text{kJ kg}^{-1}$
	$i_{\text{w,Post \#2,in}} = f\left(P_{\text{w}}, T_{\text{w,Post \#2,in}}\right)$	$i_{\text{w,Post \#2,in}} = 68.2\,\text{kJ kg}^{-1}$
	$i_{\text{w,Post \#2,out}} = f\left(P_{\text{w}}, T_{\text{w,Post \#2,out}}\right)$	$i_{\text{w,Post \#2,out}} = 132.6\,\text{kJ kg}^{-1}$
	$\rho_{\text{w,Post,in}} = f\left(P_{\text{w}}, T_{\text{w,Post,in}}\right)$	$\rho_{\text{w,Post,in}} = 999.5\,\text{kg m}^{-3}$
	$\dot{m}_{\text{w,Post}} = \dot{V}_{\text{w,Post}} \cdot \rho_{\text{w,Post,in}}$	$\dot{m}_{\text{w,Post}} = 0.0396\,\text{kg s}^{-1}$
	$\dot{Q}_{\text{loss,Post}} = \dot{Q}_{\text{loss,Post,1}} + \dot{Q}_{\text{loss,Post,2}} + \dot{Q}_{\text{loss,f,Post,12}} + \dot{Q}_{\text{loss,f,Subcool,Line}}$	$\dot{Q}_{\text{loss,Post}} = -1.937\,\text{W}$
	$\dot{Q}_{\text{Post}} = \dot{m}_{\text{w,Post}}\left(\left(i_{\text{w,Post \#1,out}} - i_{\text{w,Post \#1,in}}\right) + \left(i_{\text{w,Post \#2,out}} - i_{\text{w,Post \#2,in}}\right)\right) + \dot{Q}_{\text{loss,Post}}$	$\dot{Q}_{\text{Post}} = 3133\,\text{W}$
	$i_{\text{f,Test,out}} = i_{\text{f,Post,out}} + \dot{Q}_{\text{Post}} / \dot{m}_{\text{f}} + \dot{Q}_{\text{loss,Test to Post}} / \dot{m}_{\text{f}}$	$i_{\text{f,Test,out}} = 390.4\,\text{kJ kg}^{-1}$
	$y_{\text{f,Test,out}} = f\left(i_{\text{f,Test,out}}, P_{\text{f,Test,out}}\right)$	$y_{\text{f,Test,out}} = 0.08$
	$i_{\text{f,Test,Avg}} = \left(i_{\text{f,Test,in}} + i_{\text{f,Test,out}}\right)/2$	$i_{\text{f,Test,Avg}} = 399.1\,\text{kJ kg}^{-1}$
	$y_{\text{f,Test,Avg}} = \left(y_{\text{f,Test,in}} + y_{\text{f,Test,out}}\right)/2$	$y_{\text{f,Test,Avg}} = 0.118$

Heat Transfer Sample Calculations: Propane; 6/21/2013; Run 1

Inputs	**Equations**	**Results**
Test Section Heat Duty Calculation		
$T_{\text{w,Sec,in}} = 13.17°\text{C}$ $T_{\text{w,Sec,out}} = 48.01°\text{C}$ $P_{\text{w}} = 257.1\,\text{kPa}$ $\Delta P_{\text{w,Pri}} = 58.65\,\text{kPa}$ $\dot{V}_{\text{w,Pri}} = 3.234\,\text{L min}^{-1}$ $\dot{m}_{\text{w,Sec}} = 0.002644\,\text{kg s}^{-1}$ $\dot{Q}_{\text{loss,Sec}} = 1.368\,\text{W}$ $\dot{Q}_{\text{loss,Pri}} = 14.16\,\text{W}$ $\dot{Q}_{\text{loss,Test}} = 1.321\,\text{W}$	$i_{\text{w,Sec,in}} = f\left(P_{\text{w}}, T_{\text{w,Sec,in}}\right)$	$i_{\text{w,Sec,in}} = 55.57\,\text{kJ kg}^{-1}$
	$i_{\text{w,Sec,out}} = f\left(P_{\text{w}}, T_{\text{w,Sec,out}}\right)$	$i_{\text{w,Sec,out}} = 201.2\,\text{kJ kg}^{-1}$
	$\dot{Q}_{\text{Sec}} = \dot{m}_{\text{w,Sec}} \cdot \left(i_{\text{w,Sec,out}} - i_{\text{w,Sec,in}}\right)$	$\dot{Q}_{\text{Sec}} = 386.6\,\text{W}$
	$\dot{Q}_{\text{Pump}} = 0.1401 \cdot \dot{V}_{\text{primary}}^{3} + 0.9598 \cdot \dot{V}_{\text{primary}}^{2} + 3.025 \cdot \dot{V}_{\text{primary}}$	$\dot{Q}_{\text{Pump}} = 24.56\,\text{W}$
	$\dot{Q}_{\text{loss,Amb}} = \dot{Q}_{\text{loss,Test}} + \dot{Q}_{\text{loss,Pri}} + \dot{Q}_{\text{loss,Sec}}$	$\dot{Q}_{\text{loss,Amb}} = 16.849\,\text{W}$
	$\dot{Q}_{\text{Test}} = \dot{Q}_{\text{Sec}} + \dot{Q}_{\text{loss,Amb}} - \dot{Q}_{\text{Pump}}$	$\dot{Q}_{\text{Test}} = 378.9\,\text{W}$
Test Section Annulus Heat Transfer Coefficient		
$T_{\text{w,Pri,Test,in}} = 46.38°\text{C}$ $T_{\text{w,Pri,Test,out}} = 48.29°\text{C}$ $P_{\text{w,Pri}} = 271.1\,\text{kPa}$ $D_{\text{Test,o}} = 9.525\,\text{mm}$ $D_{\text{OT,i}} = 11.06\,\text{mm}$ $\dot{V}_{\text{w,Pri}} = 3.234\,\text{L min}^{-1}$	$T_{\text{w,Pri,Avg}} = \left(T_{\text{w,Pri,Test,in}} + T_{\text{w,Pri,Test,out}}\right)/2$	$T_{\text{w,Pri,Avg}} = 47.33°\text{C}$
	Primary Loop Water Properties $= f\left(T_{\text{w,Pri,Avg}}, P_{\text{w,Pri}}\right)$	$\mu = 5.719\times10^{-4}\,\text{kg m}^{-1}\,\text{s}^{-1}$ $k = 0.640\,\text{W m}^{-1}\,\text{K}^{-1}$ $\rho = 989.3\,\text{kg m}^{-3}$ $\text{Pr} = 3.733$
	$A_{\text{c,Annulus}} = \pi\left(D_{\text{OT,i}}^{2} - D_{\text{Test,o}}^{2}\right)/4$	$A_{\text{c,Annulus}} = 2.48\times10^{-5}\,\text{m}^{2}$
	$\dot{m}_{\text{Annulus}} = \rho_{\text{w,Pri}} \cdot \dot{V}_{\text{w,Pri}}$	$\dot{m}_{\text{Annulus}} = 0.0533\,\text{kg s}^{-1}$
	$D_{\text{h,Annulus}} = D_{\text{OT,i}} - D_{\text{Test,o}}$	$D_{\text{h,Annulus}} = 1.54\,\text{mm}$

Heat Transfer Sample Calculations: Propane; 6/21/2013; Run 1

Inputs	Equations	Results
	$\mathrm{Re}_{\text{Annulus}} = \dot{m}_{\text{Annulus}} \cdot D_{\text{h,Annulus}} / A_{\text{c,annulus}} \cdot \mu$	$\mathrm{Re}_{\text{Annulus}} = 5767$
	$r^{*} = D_{\text{Test,o}} / D_{\text{OT,i}}$	$r^{*} = 0.8612$
	$\mathrm{Re}_{\text{tt}} = 2963.02 + 334.16 \cdot r^{*}$	$\mathrm{Re}_{\text{tt}} = 3251$
	$Nu_{\text{Annulus}} = 0.025 \cdot \left(\mathrm{Re}_{\text{Annulus}}^{0.78} \cdot \mathrm{Pr}^{0.48} \cdot r^{*\,-0.14} \right)$	$Nu_{\text{Annulus}} = 41.23$ (Garimella and Christensen, 1995b)
	$h_{\text{w,Annulus}} = Nu_{\text{Annulus}} \cdot k / D_{\text{h,Annulus}}$	$h_{\text{w,Annulus}} = 17,200\ \mathrm{W\ m^{-2}\ K^{-1}}$
Test Section Working Fluid Heat Transfer Coefficient		
$T_{\text{f,Test,in,m}} = 60.14^{\circ}\mathrm{C}$ $T_{\text{f,Test,out,m}} = 60.16^{\circ}\mathrm{C}$ $T_{\text{w,Pri,Test,in}} = 46.38^{\circ}\mathrm{C}$ $T_{\text{w,Pri,Test,out}} = 48.29^{\circ}\mathrm{C}$ $h_{\text{w,Annulus}} = 17,200\ \mathrm{W\ m^{-2}\ K^{-1}}$ $D_{\text{Test,o}} = 9.525\ \mathrm{mm}$ $D_{\text{Test,i}} = 7.75\mathrm{mm}$ $D_{\text{Tee}} = 10.4\mathrm{mm}$ $L_{\text{Annulus}} = 0.53\mathrm{m}$ $L_{\text{Tee}} = 0.0132\mathrm{m}$ $k_{\text{test}} = 398.3\mathrm{W\ m^{-1}\ K^{-1}}$ $\dot{Q}_{\text{Test}} = 378.9\ \mathrm{W}$	$\Delta T_{LM} = \left(T_{\text{f,Test,in}} - T_{\text{w,Pri,Test,out}}\right) - \left(T_{\text{f,Test,out}} - T_{\text{w,Pri,Test,in}}\right) \Big/ ln\left(\dfrac{T_{\text{f,Test,in}} - T_{\text{w,Pri,Test,out}}}{T_{\text{f,Test,out}} - T_{\text{w,Pri,Test,in}}}\right)$	$\Delta T_{LM} = 12.8\ \mathrm{K}$
	$R_{\text{Annulus}} = 1 / h_{\text{w,Annulus}} \cdot \pi \cdot D_{\text{Test,o}} \cdot L_{\text{Annulus}}$	$R_{\text{Annulus}} = 0.003666\ \mathrm{K\ W^{-1}}$
	$R_{\text{TS,wall}} = ln\left(D_{\text{Test,o}} / D_{\text{Test,i}}\right) / 2 \cdot \pi \cdot k_{\text{test}} \cdot \left(L_{\text{Annulus}} + 2 \cdot \left(L_{\text{Tee}}\right)\right)$	$R_{\text{Test,wall}} = 0.0001481\ \mathrm{K\ W^{-1}}$
	$R_{\text{Tee}} = \dfrac{ln\left(D_{\text{Tee}} / D_{\text{Test,o}}\right)}{2 \cdot \pi \cdot k_{\text{eff,tee}} \cdot L_{\text{Tee}}}$	$R_{\text{Tee}} = 1.665\ \mathrm{K\ W^{-1}}$
	$R_{\text{Conv,Equiv.}} = \left(1 / R_{\text{Annulus}} + 2 \cdot \left(1 / R_{\text{Tee}}\right)\right)^{-1}$	$R_{\text{Conv,Equiv.}} = 0.00365\ \mathrm{K\ W^{-1}}$
	$UA_{\text{T}} = \dot{Q}_{\text{test}} / \Delta \mathrm{T}_{\text{LM}}$	$UA_{\text{T}} = 29.62\ \mathrm{K\ W^{-1}}$
	$h_{\text{WF,test}} = \dfrac{1}{\pi \cdot D_{\text{Test,i}} \cdot \left(L_{\text{Annulus}} + 2 \cdot \left(L_{\text{Tee}}\right)\right) \cdot \left(1 / UA_{\text{T}} - R_{\text{Test,wall}} - R_{\text{Conv,Equiv}}\right)}$	$h_{\text{WF,test}} = 2464\ \mathrm{W\ m^{-2}\ K^{-1}}$

Heat Transfer Sample Calculations: Propane; 6/21/2013; Run 1		
Inputs	**Equations**	**Results**
Working Fluid-to-Coolant Resistance Ratio		
$h_{\mathrm{WF,test}} = 2464\ \mathrm{W\ m^{-2}\ K^{-1}}$ $D_{\mathrm{Test,i}} = 7.75\mathrm{mm}$ $L_{\mathrm{Annulus}} = 0.53\mathrm{m}$ $L_{\mathrm{Tee}} = 0.0132\mathrm{m}$ $R_{\mathrm{Conv,Equiv.}} = 0.00365\ \mathrm{K\ W^{-1}}$ $R_{\mathrm{TS,wall}} = 0.0001481\ \mathrm{K\ W^{-1}}$	$R_{\mathrm{f}} = \dfrac{1}{h_{\mathrm{WF,test}} \cdot \pi \cdot D_{\mathrm{Test,i}} \cdot \left(L_{\mathrm{Annulus}} + 2 \cdot \left(L_{\mathrm{Tee}}\right)\right)}$	$R_{\mathrm{f}} = 0.02996\ \mathrm{K\ W^{-1}}$
	$\text{Resistance Ratio} = \dfrac{R_{\mathrm{f}}}{R_{\mathrm{TS,wall}} + R_{\mathrm{Conv,Equiv.}}}$	$\text{Resistance Ratio} = 7.9$
Evaporator Energy Balance		
$T_{\mathrm{f,Pre,in}} = 107.3°\mathrm{C}$ $T_{\mathrm{f,Post,out}} = 16.26°\mathrm{C}$ $P_{\mathrm{f,Pre,in}} = 2131\,\mathrm{kPa}$ $P_{\mathrm{f,Post,out}} = 2119\,\mathrm{kPa}$ $\dot{m}_{\mathrm{f}} = 0.02114\,\mathrm{kg\ s^{-1}}$ $\dot{Q}_{\mathrm{Test}} = 378.9\mathrm{W}$ $\dot{Q}_{\mathrm{Pre}} = 7097\mathrm{W}$ $\dot{Q}_{\mathrm{Post}} = 3133\mathrm{W}$ $\dot{Q}_{\mathrm{loss,Pre\ to\ Test}} = 2.507\mathrm{W}$ $\dot{Q}_{\mathrm{loss,Test\ to\ Post}} = 2.818\mathrm{W}$	$i_{\mathrm{f,Pre,in}} = f\left(P_{\mathrm{f,Pre,in}}, T_{\mathrm{f,Pre,in}}\right)$	$i_{\mathrm{f,Pre,in}} = 743.6\,\mathrm{kJ\ kg^{-1}}$
	$i_{\mathrm{f,Post,out}} = f\left(P_{\mathrm{f,Post,out}}, T_{\mathrm{f,Post,out}}\right)$	$i_{\mathrm{f,Post,out}} = 242.1\mathrm{kJ\ kg^{-1}}$
	$\dot{Q}_{\mathrm{Evap}} = \dot{m}_{\mathrm{f}} \cdot \left(i_{\mathrm{f,Pre,in}} - i_{\mathrm{f,Post,out}}\right)$	$\dot{Q}_{\mathrm{Evap}} = 10{,}601\,\mathrm{W}$
	$\dot{Q}_{\mathrm{Loop}} = \dot{Q}_{\mathrm{Pre}} + \dot{Q}_{\mathrm{loss,Pre\ to\ Test}} + \dot{Q}_{\mathrm{Test}} + \dot{Q}_{\mathrm{loss,Test\ to\ Post}} + \dot{Q}_{\mathrm{Post}}$	$\dot{Q}_{\mathrm{Loop}} = 10{,}608\,\mathrm{W}$
	$\Delta\dot{Q}_{\mathrm{Evap}} = \dot{Q}_{\mathrm{Evap}} - \dot{Q}_{\mathrm{Loop}}$	$\Delta\dot{Q}_{\mathrm{Evap}} = -7.39\,\mathrm{W}$
	$\%_{\mathrm{Error}} = \dfrac{\Delta\dot{Q}_{\mathrm{Evap}}}{\dot{Q}_{\mathrm{Evap}}}$	$\%_{\mathrm{Error}} = -0.07\%$
Test Section Quality Change		
$y_{\mathrm{f,Test,in}} = 0.15$ $y_{\mathrm{f,Test,out}} = 0.08$	$\Delta y_{\mathrm{f,Test}} = y_{\mathrm{f,Test,in,Pri}} - y_{\mathrm{f,Test,out,Pri}}$	$\Delta y_{\mathrm{f,Test}} = 0.069$

Table D.5. Propane data point pressure drop sample calculation

Pressure Drop Sample Calculations: Propane; 6/21/2013; Run 1		
Inputs	**Equations**	**Results**
$\dot{m}_{\mathrm{f}} = 0.02114\,\mathrm{kg\,s^{-1}}$ $P_{\mathrm{f,Test,in}} = 2123\,\mathrm{kPa}$ $P_{\mathrm{f,Test,out}} = 2124\,\mathrm{kPa}$ $\Delta P_{\mathrm{f,Measured}} = 1.0787\,\mathrm{kPa}$ $i_{\mathrm{f,Test,in,Pri}} = 407.8\,\mathrm{kJ\,kg^{-1}}$ $i_{\mathrm{f,Test,out,Pri}} = 390.4\,\mathrm{kJ\,kg^{-1}}$ $y_{\mathrm{f,Test,in,Pri}} = 0.15$ $y_{\mathrm{f,Test,out,Pri}} = 0.08$ $\dot{Q}_{\mathrm{Test}} = 378.9\,\mathrm{W}$ $D_{\mathrm{Test,i}} = 7.75\,\mathrm{mm}$ $L_{\Delta \mathrm{P}} = 0.746\,\mathrm{m}$	$\text{Inlet Liquid Properties} = f\left(i_{\mathrm{f,Test,in,Pri}}, P_{\mathrm{f,Test,in}}\right)$	$\rho_{\mathrm{l,in}} = 427.7\,\mathrm{kg\,m^{-3}}$
	$\text{Inlet Liquid Properties} = f\left(P_{\mathrm{f,Test,in}}, y = 0\right)$	$\mu_{\mathrm{l,in}} = 6.554\times10^{-5}\,\mathrm{kg\,m^{-1}\,s^{-1}}$
	$\text{Inlet Vapor Properties} = f\left(i_{\mathrm{f,Test,in,Pri}}, P_{\mathrm{f,Test,in}}\right)$	$\rho_{\mathrm{v,in}} = 49.66\,\mathrm{kg\,m^{-3}}$
	$\text{Inlet Vapor Properties} = f\left(P_{\mathrm{f,Test,in}}, y = 1\right)$	$\mu_{\mathrm{v,in}} = 1.005\times10^{-5}\,\mathrm{kg\,m^{-1}\,s^{-1}}$
	$\text{Outlet Liquid Properties} = f\left(i_{\mathrm{f,Test,out,Pri}}, P_{\mathrm{f,Test,out}}\right)$	$\rho_{\mathrm{l,out}} = 427.6\,\mathrm{kg\,m^{-3}}$
	$\text{Outlet Liquid Properties} = f\left(P_{\mathrm{f,Test,out}}, y = 0\right)$	$\mu_{\mathrm{l,out}} = 6.552\times10^{-5}\,\mathrm{kg\,m^{-1}\,s^{-1}}$
	$\text{Outlet Vapor Properties} = f\left(i_{\mathrm{f,Test,out,Pri}}, P_{\mathrm{f,Test,out}}\right)$	$\rho_{\mathrm{v,out}} = 49.69\,\mathrm{kg\,m^{-3}}$
	$\text{Outlet Vapor Properties} = f\left(P_{\mathrm{f,Test,out}}, y = 1\right)$	$\mu_{\mathrm{v,out}} = 1.004\times10^{-5}\,\mathrm{kg\,m^{-1}\,s^{-1}}$
	$\alpha_{\mathrm{f,Test,in}} = \left(1 + \left(\frac{1 - y_{\mathrm{f,Test,in,Pri}}}{y_{\mathrm{f,Test,in,Pri}}}\right)^{0.74} \left(\frac{\rho_{\mathrm{v,in}}}{\rho_{\mathrm{l,in}}}\right)^{0.65} \left(\frac{\mu_{\mathrm{l,in}}}{\mu_{\mathrm{v,in}}}\right)^{0.13}\right)^{-1}$	$\alpha_{\mathrm{f,Test,in}} = 0.4713$ (Baroczy, 1965)
	$\alpha_{\mathrm{f,Test,out}} = \left(1 + \left(\frac{1 - y_{\mathrm{f,Test,out,Pri}}}{y_{\mathrm{f,Test,out,Pri}}}\right)^{0.74} \left(\frac{\rho_{\mathrm{v,out}}}{\rho_{\mathrm{l,out}}}\right)^{0.65} \left(\frac{\mu_{\mathrm{l,out}}}{\mu_{\mathrm{v,out}}}\right)^{0.13}\right)^{-1}$	$\alpha_{\mathrm{f,Test,out}} = 0.3498$ (Baroczy, 1965)
	$\left\lvert \Delta P_{\mathrm{f,Decel}} \right\rvert = \left\lvert \left. G^2 \left(\frac{y^2}{\rho_{\mathrm{v,out}}\alpha} + \frac{(1-y)^2}{\rho_{\mathrm{l,out}}(1-\alpha)}\right)\right\rvert_{\substack{\alpha=\alpha_{\mathrm{Test,out}} \\ y=y_{\mathrm{Test,out}}}} - \left. G^2 \left(\frac{y^2}{\rho_{\mathrm{v,in}}\alpha} + \frac{(1-y)^2}{\rho_{\mathrm{l,in}}(1-\alpha)}\right)\right\rvert_{\substack{\alpha=\alpha_{\mathrm{Test,in}} \\ y=y_{\mathrm{Test,in}}}} \right\rvert$	$\left\lvert \Delta P_{\mathrm{f,Decel}} \right\rvert = 0.150\,\mathrm{kPa}$ $\left(13.93\%\text{ of Measured}\right)$ (Carey, 2008)
	$\Delta P_{\mathrm{f,Measured}} = \Delta P_{\mathrm{fr}} - \left\lvert \Delta P_{\mathrm{f,Decel}} \right\rvert$	$\Delta P_{\mathrm{fr}} = 1.228\,\mathrm{kPa}\left(113.8\%\text{ Measured}\right)$
	$\nabla P_{\mathrm{fr}} = \frac{\Delta P_{\mathrm{fr}}}{L_{\Delta \mathrm{P}}}$	$\nabla P_{\mathrm{fr}} = 1.65\,\mathrm{kPa\,m^{-1}}$

APPENDIX E SINGLE COMPONENT PHASE-CHANGE HEAT TRANSFER AND PRESSURE DROP: MODEL SAMPLE CALCULATIONS

Table E.1. Heat transfer coefficient model sample calculation

Heat Transfer Model Sample Calculations: Propane		
Inputs	**Equations**	**Results**
$\Delta T_{\mathrm{LM}} = 10.2°\mathrm{C}$ $T_{\mathrm{ref}} = 75.2°\mathrm{C}$ $P_{\mathrm{ref}} = 2860\,\mathrm{kPa}$ $D = 0.01445\ \mathrm{m}$ $\mathrm{G} = 150\,\mathrm{kg\ m^{-2}s^{-1}}$ $q = 0.400$ $\left.\frac{dP}{dz}\right\rvert_{\mathrm{frictional}} = 81.45\ \mathrm{Pa\ m^{-1}}$	Propane Saturated Properties $= f\left(P_{\mathrm{sat}}\right)$	$C_{\mathrm{p,L}} = 4.07\ \mathrm{kJ\,kg^{-1}\ K^{-1}}$ $i_{\mathrm{fg}} = 209.84\ \mathrm{kJ\,kg^{-1}}$ $k_{\mathrm{L}} = 0.07\ \mathrm{W\ m^{-1}\ K^{-1}}$ $\mathrm{Pr_L} = 2.98$ $\rho_{\mathrm{L}} = 388.9\ \mathrm{kg\ m^{-3}}$ $\rho_{\mathrm{V}} = 73.5\ \mathrm{kg\ m^{-3}}$ $\mu_{\mathrm{L}} = 5.3\times10^{-5}\ \mathrm{kg\ m^{-1}\ s^{-1}}$ $\mu_{\mathrm{V}} = 1.1\times10^{-5}\ \mathrm{kg\ m^{-1}\ s^{-1}}$ $\sigma = 0.0016\ \mathrm{N\ m^{-1}}$
Calculation of Void Fraction		
$q = 0.400$ $\rho_{\mathrm{L}} = 388.9\ \mathrm{kg\ m^{-3}}$ $\rho_{\mathrm{V}} = 73.5\ \mathrm{kg\ m^{-3}}$ $\mu_{\mathrm{L}} = 5.3\times10^{-5}\ \mathrm{kg\ m^{-1}\ s^{-1}}$ $\mu_{\mathrm{V}} = 1.1\times10^{-5}\ \mathrm{kg\ m^{-1}\ s^{-1}}$	$\varepsilon = \left(1+\left(\frac{1-q}{q}\right)^{0.74}\cdot\left(\frac{\rho_{\mathrm{V}}}{\rho_{\mathrm{L}}}\right)^{0.65}\cdot\left(\frac{\mu_{\mathrm{L}}}{\mu_{\mathrm{V}}}\right)^{0.13}\right)^{-1}$ **(Baroczy, 1965)**	$\varepsilon = 0.647$
Calculation of Liquid Entrainment Fraction		
$D = 0.01445\ \mathrm{m}$ $\mathrm{G} = 150\,\mathrm{kg\ m^{-2}s^{-1}}$ $q = 0.400$ $\rho_{\mathrm{L}} = 388.9\ \mathrm{kg\ m^{-3}}$ $\rho_{\mathrm{V}} = 73.5\ \mathrm{kg\ m^{-3}}$ $\sigma = 0.0016\ \mathrm{N\ m^{-1}}$ $\varepsilon = 0.647$	$j_{\mathrm{L}} = \frac{G(1-q)}{\rho_{\mathrm{L}}(1-\varepsilon)}$ $j_{\mathrm{V}} = \frac{Gq}{\rho_{\mathrm{V}}\varepsilon}$ $\mathrm{Bo} = \frac{\Delta\rho g D^2}{\sigma}$ $Fr = \frac{u_{\mathrm{L}}}{\sqrt{gD}}$	$j_{\mathrm{L}} = 0.645\ \mathrm{m\ s^{-1}}$ $j_{\mathrm{V}} = 1.278\ \mathrm{m\ s^{-1}}$ $\mathrm{Bo} = 405$ $Fr = 1.712$
$j_{\mathrm{L}} = 0.645\ \mathrm{m\ s^{-1}}$ $j_{\mathrm{V}} = 1.278\ \mathrm{m\ s^{-1}}$ $\mathrm{Bo} = 405$ $Fr = 1.712$	$E = 0.0003\left(\frac{j_{\mathrm{V}}}{j_{\mathrm{L}}}\right)^{1.15}\mathrm{Bo}^{0.75}Fr^{0.5}$	$E = 0.078$

Inputs	**Equations**	**Results**
Calculation of Dimensionless Parameters		
$q = 0.400$ $\rho_\text{L} = 388.9 \text{ kg m}^{-3}$ $\rho_\text{V} = 73.5 \text{ kg m}^{-3}$ $\mu_\text{L} = 5.3\times10^{-5} \text{ kg m}^{-1} \text{ s}^{-1}$ $\mu_\text{V} = 1.1\times10^{-5} \text{ kg m}^{-1} \text{ s}^{-1}$	$\text{Re}_\text{L} = \frac{G(1-q)D}{\mu_\text{L}}$ $Ga = \frac{gD^3\rho_\text{L}^2}{\mu_\text{L}^2}$ $X_{tt} = \left(\frac{\rho_\text{V}}{\rho_\text{L}}\right)^{0.5} \cdot \left(\frac{\mu_\text{L}}{\mu_\text{V}}\right)^{0.1} \cdot \left(\frac{1-q}{q}\right)^{0.9}$ $Fr_{So} = 1.26 \cdot \text{Re}_\text{L}^{1.04} \cdot \left(\frac{1+1.09\cdot X_{tt}^{0.039}}{X_{tt}}\right)^{1.5} \cdot \left(\frac{1}{Ga^{0.5}}\right)$	$\text{Re}_\text{L} = 24150$ $Ga = 1.59\times10^9$ $X_{tt} = 0.711$ $Fr_{So} = 5.69$
Calculation of Upper Film Thickness		
$D = 0.01445 \text{ m}$ $\text{G} = 150 \text{ kg m}^{-2}\text{s}^{-1}$	$\eta = 1-\left(1+0.1\cdot Fr_\text{So}^{2.5}\right)^{-0.05}$	$\eta = 0.103$
$\varepsilon = 0.647$ $E = 0.078$ $\eta = 0.103$	$\theta = 2\pi - 2\left[\begin{array}{l}\pi(1-\varepsilon)+ \\ \frac{3\pi}{2}\left(1-2(1-\varepsilon)+(1-\varepsilon)^{1/3}-\varepsilon^{1/3}\right) \\ -\frac{1}{200}(1-\varepsilon)\varepsilon\left(1-2(1-\varepsilon)\right)\cdot \\ \left(1+4\left((1-\varepsilon)^2+\varepsilon^2\right)\right)\end{array}\right]$	$\theta = 3.61 \text{ radians}$
$D = 0.01445 \text{ m}$ $\varepsilon = 0.647$ $E = 0.078$ $\theta = 3.61 \text{ radians}$ $\eta = 0.103$	$\eta(1-\varepsilon)(1-E)\frac{\pi D^2}{4} = \frac{\theta}{2\pi}\pi\left(\frac{D^2}{4}-\left[\frac{D}{2}-\delta_\text{wavy}\right]^2\right)$	$\delta_\text{stratified} = 0.23 \text{ mm}$
$D = 0.01445 \text{ m}$ $\delta_\text{stratified} = 0.00023 \text{ m}$	$\varepsilon_\text{effective} = \frac{\left(D/2-\delta_\text{stratified}\right)^2}{D^2/4}$	$\varepsilon_\text{stratified} = 0.937$
Calculation of Annular Film Thickness & Effective Annular Film Thickness		
$D = 0.01445 \text{ m}$ $\varepsilon = 0.647$	$\delta_\text{annular} = \frac{D}{2}\left(1-\sqrt{\varepsilon}\right)$	$\delta_\text{annular} = 1.42 \text{ mm}$
$D = 0.01445 \text{ m}$ $\varepsilon = 0.647$ $E = 0.078$	$\delta_\text{entrainment} = \frac{D}{2}\left(1-\sqrt{E(1-\varepsilon)+\varepsilon}\right)$	$\delta_\text{entrainment} = 1.29 \text{ mm}$

<table>
<tr><th>Inputs</th><th colspan="2">Equations</th><th>Results</th></tr>
<tr><td colspan="4">Assignment of Film Thicknesses, Void Fraction and Fraction of Flow in Axial Film</td></tr>
<tr><td rowspan="3">$Fr_{So} = 5.69$
$\eta = 0.103$
$\delta_{\text{stratified}} = 0.23 \text{ mm}$
$\delta_{\text{annular}} = 1.42 \text{ mm}$
$\delta_{\text{entrainment}} = 1.29 \text{ mm}$
$\varepsilon_{\text{stratified}} = 0.937$
$\varepsilon = 0.647$</td><td colspan="2">IF</td><td rowspan="3">$\delta_{\text{film}} = 0.23 \text{ mm}$
$\delta = 0.23 \text{ mm}$
$\eta = 0.103$
$\varepsilon_{\text{void}} = 0.937$</td></tr>
<tr><td>$Fr_{So} \le 7$
Apply film thickness, void fraction and fraction of flow from: “Upper Film Thickness” method</td><td>$Fr_{So} > 7$
Apply film thickness, void fraction and fraction of flow from: “Idealized Annular Flow” method</td></tr>
<tr><td>$\delta_{\text{film}} = \delta_{\text{stratified}}$
$\delta_{\text{effective}} = \delta_{\text{stratified}}$
$\eta = \eta_{\text{up}}$
$\varepsilon_{\text{void}} = \varepsilon_{\text{stratified}}$</td><td>$\delta_{\text{film}} = \delta_{\text{annular}}$
$\delta_{\text{effective}} = \delta_{\text{entrainment}}$
$\eta = 1$
$\varepsilon_{\text{void}} = \varepsilon$</td></tr>
<tr><td colspan="4">Calculation of Heat Transfer Coefficient Parameters</td></tr>
<tr><td>$D = 0.01445 \text{ m}$
$\text{G} = 150 \text{ kg m}^{-2}\text{s}^{-1}$
$q = 0.400$
$\rho_{\text{L}} = 388.9 \text{ kg m}^{-3}$
$\rho_{\text{V}} = 73.5 \text{ kg m}^{-3}$
$\mu_{\text{L}} = 5.3\times10^{-5} \text{ kg m}^{-1} \text{ s}^{-1}$
$\sigma = 0.0016 \text{ N m}^{-1}$
$\delta_{\text{film}} = 0.00023 \text{ m}$
$\eta = 0.103$
$\varepsilon_{\text{void}} = 0.937$
$\varepsilon = 0.647$</td><td colspan="2">$\text{Re}_{\delta} = \dfrac{4G(1-q)\eta\delta_{\text{film}}}{(1-\varepsilon_{\text{void}})\mu_{\text{L}}}$
$\text{Bo}_{\text{film}} = \dfrac{\Delta\rho g \delta_{\text{film}}^2}{\sigma}$
$u_{\text{L,upper}} = \dfrac{G(1-q)\eta}{\rho_{\text{L}}(1-\varepsilon_{\text{void}})}$
$u_{\text{V}} = \dfrac{Gq}{\rho_{\text{V}}\varepsilon}$</td><td>$\text{Re}_{\delta} = 2159$
$\text{Bo}_{\text{film}} = 0.104$
$u_{\text{L,upper}} = 0.371 \text{ m s}^{-1}$
$u_{\text{V}} = 1.278 \text{ m s}^{-1}$</td></tr>
<tr><td>$\text{Re}_{\delta} = 2519$
$\text{Bo}_{\text{film}} = 0.104$
$u_{\text{L,upper}} = 0.371 \text{ m s}^{-1}$
$u_{\text{V}} = 1.278 \text{ m s}^{-1}$
$k_{\text{L}} = 0.07 \text{ W m}^{-1} \text{ K}^{-1}$
$\text{Pr}_{\text{L}} = 2.98$
$\delta_{\text{film}} = 0.23 \text{ mm}$</td><td colspan="2">$\kappa_i = 1 + \text{Bo}_{\text{film}}^{0.1}\left(\dfrac{u_{\text{V}}}{u_{\text{L,upper}}}\right)^{0.5}$
$\kappa_e = \left(\dfrac{\delta_{\text{film}}}{\delta_{\text{effective}}}\right)$
$h_{\text{annular}} = 0.0039\,\text{Re}_{\delta}^{0.775}\,\text{Pr}_{\text{L}}^{0.3}\,\kappa_i\kappa_e\,\dfrac{k_{\text{L}}}{\delta_{\text{film}}}$</td><td>$\kappa_i = 2.481$
$\kappa_e = 1$
$h_{\text{annular}} = 1811 \text{ W m}^{-2} \text{ K}^{-1}$</td></tr>
</table>

Inputs	**Equations**	**Results**
Calculation of Falling Film Heat Transfer Coefficient		
$k_{\mathrm{L}} = 0.07\ \mathrm{W\ m^{-1}\ K^{-1}}$ $\rho_{\mathrm{L}} = 388.9\ \mathrm{kg\ m^{-3}}$ $\mu_{\mathrm{L}} = 5.3\times10^{-5}\ \mathrm{kg\ m^{-1}\ s^{-1}}$ $\kappa_i = 2.481$ $\kappa_e = 1$	$l_{\mathrm{FF}} = \left[\dfrac{\left(\mu_{\mathrm{L}}/\rho_{\mathrm{L}}\right)^2}{g}\right]^{1/3}$ $h_{\mathrm{FF}} = 0.2\,\mathrm{Re}_{\delta}^{-0.08}\,\kappa_i\kappa_e\,\dfrac{k_{\mathrm{L}}}{l_{\mathrm{FF}}}$	$l_{\mathrm{FF}} = 0.0124\ \mathrm{mm}$ $h_{\mathrm{FF}} = 1547\ \mathrm{W\ m^{-2}\ K^{-1}}$
Calculation of Relative Contributions of Falling Film and Annular Flow		
$\left.\dfrac{dP}{dz}\right\rvert_{\mathrm{frictional}} = 81.45\ \mathrm{Pa\ m^{-1}}$ $\rho_{\mathrm{L}} = 388.9\ \mathrm{kg\ m^{-3}}$ $\rho_{\mathrm{V}} = 73.5\ \mathrm{kg\ m^{-3}}$ $\delta_{\mathrm{film}} = 0.23\ \mathrm{mm}$	$\tau_{\mathrm{vertical}} = \Delta\rho g \delta_{\mathrm{film}}$ $\tau_{\mathrm{horizontal}} = \left.\dfrac{dP}{dz}\right\rvert_{\mathrm{frictional}} \dfrac{\pi D^2/4}{\pi D}$	$\tau_{\mathrm{vertical}} = 0.716\ \mathrm{Pa}$ $\tau_{\mathrm{horizontal}} = 0.294\ \mathrm{Pa}$
$\tau_{\mathrm{vertical}} = 0.716\ \mathrm{Pa}$ $\tau_{\mathrm{horizontal}} = 0.294\ \mathrm{Pa}$	$\tau_{\mathrm{resultant}} = \sqrt{\tau_{\mathrm{vertical}}^2 + \tau_{\mathrm{horizontal}}^2}$	$\tau_{\mathrm{resultant}} = 0.774\ \mathrm{Pa}$
$\tau_{\mathrm{vertical}} = 0.716\ \mathrm{Pa}$ $\tau_{\mathrm{horizontal}} = 0.294\ \mathrm{Pa}$ $\tau_{\mathrm{resultant}} = 0.774\ \mathrm{Pa}$	$A = \dfrac{\tau_{\mathrm{vertical}}}{\tau_{\mathrm{resultant}}}$ $B = \dfrac{\tau_{\mathrm{horizontal}}}{\tau_{\mathrm{resultant}}}$	$A = 0.92$ $B = 0.38$
Calculation of Total Film Heat Transfer Coefficient		
$A = 0.92$ $B = 0.38$ $h_{\mathrm{FF}} = 1547\ \mathrm{W\ m^{-2}\ K^{-1}}$ $h_{\mathrm{annular}} = 1811\ \mathrm{W\ m^{-2}\ K^{-1}}$	$h_{\mathrm{film}} = A\cdot h_{\mathrm{FF}} + B\cdot h_{\mathrm{annular}}$	$h_{\mathrm{film}} = 2119\ \mathrm{W\ m^{-2}\ K^{-1}}$
Calculation of Liquid Pool Heat Transfer Coefficient		
$\mathrm{Re}_{\mathrm{L}} = 24150$ $k_{\mathrm{L}} = 0.07\ \mathrm{W\ m^{-1}\ K^{-1}}$ $\mathrm{Pr}_{\mathrm{L}} = 2.98$ $D = 0.01445\ \mathrm{m}$	$h_{\mathrm{Pool}} = 0.023\,\mathrm{Re}_{\mathrm{L}}^{0.8}\,\mathrm{Pr}_{\mathrm{L}}^{0.3}\,\dfrac{k_{\mathrm{L}}}{D}$	$h_{\mathrm{Pool}} = 512\ \mathrm{W\ m^{-2}\ K^{-1}}$
Calculation of Total Condensation Heat Transfer Coefficient		
$h_{\mathrm{Pool}} = 512\ \mathrm{W\ m^{-2}\ K^{-1}}$ $h_{\mathrm{film}} = 2119\ \mathrm{W\ m^{-2}\ K^{-1}}$ $\theta = 3.61\ \mathrm{radians}$	$h_{\mathrm{model}} = \dfrac{h_{\mathrm{film}}\theta + h_{\mathrm{pool}}\left(2\pi - \theta\right)}{2\pi}$	$h_{\mathrm{model}} = 1435\ \mathrm{W\ m^{-2}\ K^{-1}}$

Table E.2. Adjustment for Subcooled Liquid sample calculation

Subcooling Adjustment Parameter Model Sample Calculations: Propane		
Inputs	**Equations**	**Results**
Calculation of Dimensionless Parameters		
$P_{\mathrm{red}} = 0.673$ [-] $k_{\mathrm{l,wall}} = 0.077\ \mathrm{W\ m^{-1}\ K^{-1}}$ $k_{\mathrm{l,sat}} = 0.072\ \mathrm{W\ m^{-1}\ K^{-1}}$	$\chi_{\mathrm{subcool}} = \left(\left(\dfrac{k_{\mathrm{l,wall}}}{k_{\mathrm{l,sat}}}\right)^{2} - 0.3\right)\dfrac{1}{P_{\mathrm{red}}^{0.1}}$	$\chi_{\mathrm{subcool}} = 0.874$
Calculation of Condensation Heat Transfer Coefficient Adjusted for Subcooled Liquid		
$h_{\mathrm{model}} = 1435\ \mathrm{W\ m^{-2}\ K^{-1}}$ $\chi_{\mathrm{subcool}} = 0.874$	$h_{\mathrm{condensation}} = \chi_{\mathrm{subcooling}} \cdot h_{\mathrm{model}}$	$h_{\mathrm{condensation}} = 1255\ \mathrm{W\ m^{-2}\ K^{-1}}$

Table E.3. Frictional Pressure Gradient sample calculation

Frictional Pressure Drop Model Sample Calculations: Propane		
Inputs	**Equations**	**Results**
Calculation of Phase Interaction Parameters		
$\mathrm{G}=150\,\mathrm{kg\ m^{-2}s^{-1}}$ $D=0.01445\ \mathrm{m}$ $q=0.407$ $\rho_{\mathrm{L}}=388.9\ \mathrm{kg\ m^{-3}}$ $\rho_{\mathrm{V}}=73.5\ \mathrm{kg\ m^{-3}}$ $\mu_{\mathrm{L}}=5.3\times10^{-5}\ \mathrm{kg\ m^{-1}\ s^{-1}}$ $\mu_{\mathrm{V}}=1.1\times10^{-5}\ \mathrm{kg\ m^{-1}\ s^{-1}}$ $\varepsilon=0.647$	$\mathrm{Re}_{\mathrm{L}}=\frac{G(1-q)D}{\mu_{\mathrm{L}}}$ $\mathrm{Re}_{\mathrm{V}}=\frac{GqD}{\mu_{\mathrm{V}}}$ $\mathrm{Bo}=\frac{\Delta\rho g D^2}{\sigma}$ $u_{\mathrm{L}}=\frac{G(1-q)}{\rho_{\mathrm{L}}(1-\varepsilon)}$ $u_{\mathrm{V}}=\frac{Gq}{\rho_{\mathrm{V}}\varepsilon}$ $S_r=\frac{u_{\mathrm{V}}}{u_{\mathrm{L}}}$	$\mathrm{Re}_{\mathrm{L}}=24150$ $\mathrm{Re}_{\mathrm{V}}=76884$ $\mathrm{Bo}=405$ $u_{\mathrm{L}}=0.645\ \mathrm{m\ s^{-1}}$ $u_{\mathrm{V}}=1.278\ \mathrm{m\ s^{-1}}$ $S_r=1.983$
Calculation of Vapor and Liquid Friction Factors		
$D=0.01445\ \mathrm{m}$ $\varsigma=0.0015\ \mathrm{mm}$ $\mathrm{Re}_{\mathrm{L}}=24150$ $\mathrm{Re}_{\mathrm{V}}=76884$	$f_{\mathrm{L\,\&\,V}}=8\left(\left(\frac{8}{\mathrm{Re}_{\mathrm{L/V}}}\right)^{12}+\left(\left(2.457\ln\left(\frac{1}{\left(\frac{7}{\mathrm{Re}_{\mathrm{L/V}}}\right)^{0.9}+0.27\left(\frac{\varsigma}{D}\right)}\right)\right)^{16}+\left(\frac{37530}{\mathrm{Re}_{\mathrm{L/V}}}\right)^{16}\right)^{-1.5}\right)^{1/12}$	$f_{\mathrm{L}}=0.025$ $f_{\mathrm{V}}=0.019$
Calculation of Vapor and Liquid Pressure Gradients		
$\mathrm{G}=150\,\mathrm{kg\ m^{-2}s^{-1}}$ $D=0.01445\ \mathrm{m}$ $q=0.407$ $\rho_{\mathrm{L}}=388.9\ \mathrm{kg\ m^{-3}}$ $\rho_{\mathrm{V}}=73.5\ \mathrm{kg\ m^{-3}}$ $f_{\mathrm{L}}=0.025$ $f_{\mathrm{V}}=0.019$	$\left.\frac{dP}{dz}\right\vert_{\mathrm{L}}=\frac{1}{2}f_{\mathrm{L}}\frac{(G(1-q))^2}{\rho_{\mathrm{L}}D}$ $\left.\frac{dP}{dz}\right\vert_{\mathrm{V}}=\frac{1}{2}f_{\mathrm{V}}\frac{(Gq)^2}{\rho_{\mathrm{V}}D}$	$\left.\frac{dP}{dz}\right\vert_{\mathrm{L}}=17.5\ \mathrm{Pa\ m^{-1}}$ $\left.\frac{dP}{dz}\right\vert_{\mathrm{V}}=33.7\ \mathrm{Pa\ m^{-1}}$

Inputs	Equations	Results
Calculation of Total Frictional Pressure Gradient		
$\left.\frac{dP}{dz}\right\|_{\mathrm{L}} = 17.5\ \text{Pa m}^{-1}$ $\left.\frac{dP}{dz}\right\|_{\mathrm{V}} = 33.7\ \text{Pa m}^{-1}$ $\mathrm{Re_L} = 24150$ $\mathrm{Bo} = 405$ $S_r = 1.983$	$\left.\frac{dP}{dz}\right\|_{\mathrm{frictional}} = \left.\frac{dP}{dz}\right\|_{\mathrm{L}} + \left.\frac{dP}{dz}\right\|_{\mathrm{V}} + \left\{20\,\mathrm{Re_L}^{-0.15}\,\mathrm{Bo}^{-0.2} S_r^{\ 1.15}\right\}\sqrt{\left.\frac{dP}{dz}\right\|_{\mathrm{L}} \cdot \left.\frac{dP}{dz}\right\|_{\mathrm{V}}}$	$\left.\frac{dP}{dz}\right\|_{\mathrm{frictional}} = 122\ \text{Pa m}^{-1}$

APPENDIX F GAS CHROMATOGRAPH CALIBRATION

This section details the procedures followed to calibrate the gas chromatograph. The calibration procedure was conducted independently for both fluids.

A balloon was filled with a sample of the pure fluid. Known volumes of the pure fluid were extracted from the balloon by piercing the balloon using a syringe and extracting a specific volume of the pure fluid. The mass of the sample in the syringe was calculated from a reading of the volume of the syringe and the density of the gas. The density of each fluid was calculated assuming the balloon and syringe are at ambient temperature and pressure, as shown in Eq. (F.1).

$$\begin{aligned} \rho &= f\left(T,P\right) = f\left(T = 20°C, P = 100\text{ kPa}\right) \\ \rho_{\text{propane}} &= 1.83\text{ kg m}^{-3} \\ \rho_{\text{ethane}} &= 1.23\text{ kg m}^{-3} \end{aligned} \tag{F.1}$$

The sample was subsequently injected into the top of the gas chromatograph. The sample passed through the separation column and the output signal was recorded. Two pieces of information were extracted from this procedure, the retention time and the area of the curve. The retention time was recorded for both samples to ensure that there were sufficient gaps in the retention time between the two fluids. This ensured that distinct peaks were displayed when the mixture was sampled during regular testing. The area under the curve that corresponded to the mass of the sample injected was recorded and tabulated.

Table F.1 Pure Fluid Gas Chromatograph Calibration Data

Propane			Ethane		
Mass, mg	Volume, mL	Area	Mass, mg	Volume, mL	Area
0.009	0.005	3347	0.006	0.005	2867
0.018	0.010	7586	0.012	0.010	5389
0.092	0.050	40353	0.062	0.050	36325
0.229	0.125	100872	0.111	0.090	63575
0.458	0.250	205189	0.302	0.245	170377
0.915	0.500	422847	0.617	0.500	352493
1.144	0.625	521444	0.772	0.625	441161

Table F.1 shows the volume, mass and corresponding areas for each fluid. The information in this table was subsequently used as the calibration curve in the gas chromatograph. The tabulated data are shown in Figure F.1. The agreement between the injected volume and the area calculated using the GC is very good: for both fluids, the R^2 value is 0.999.

The standard deviation of the samples injected using the syringe and the GC readings was 1346 and 1509 for propane and ethane, respectively. A sample reading of each mixture concentration was used to calculate the uncertainty of the GC. Figure F.2 shows a sample output reading of the GC for a mixture concentration of 33% ethane/67%

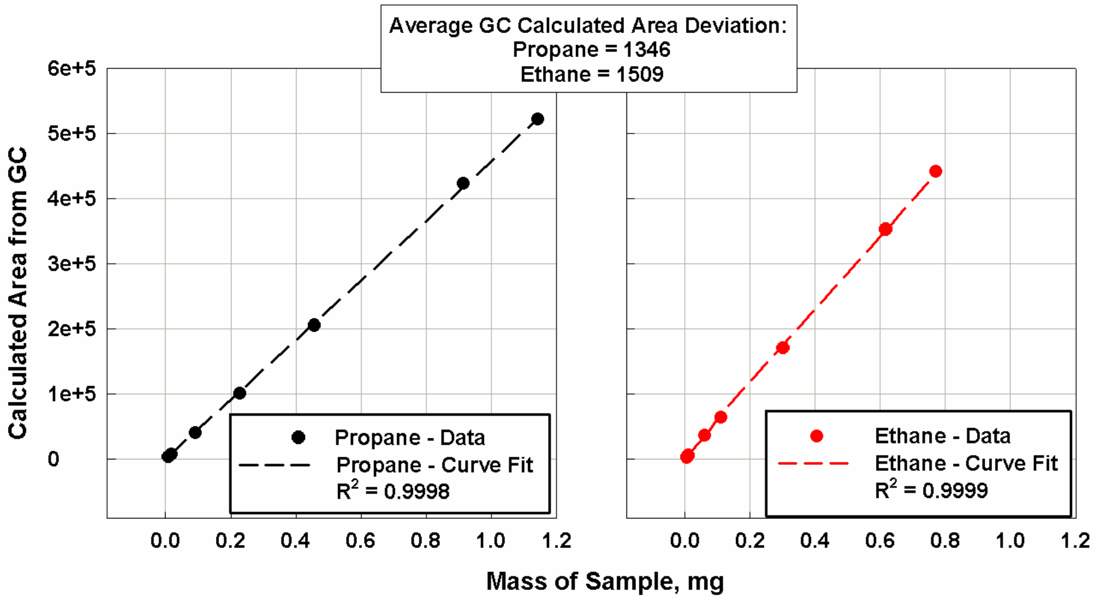

Figure F.1: Gas chromatograph calibration curves

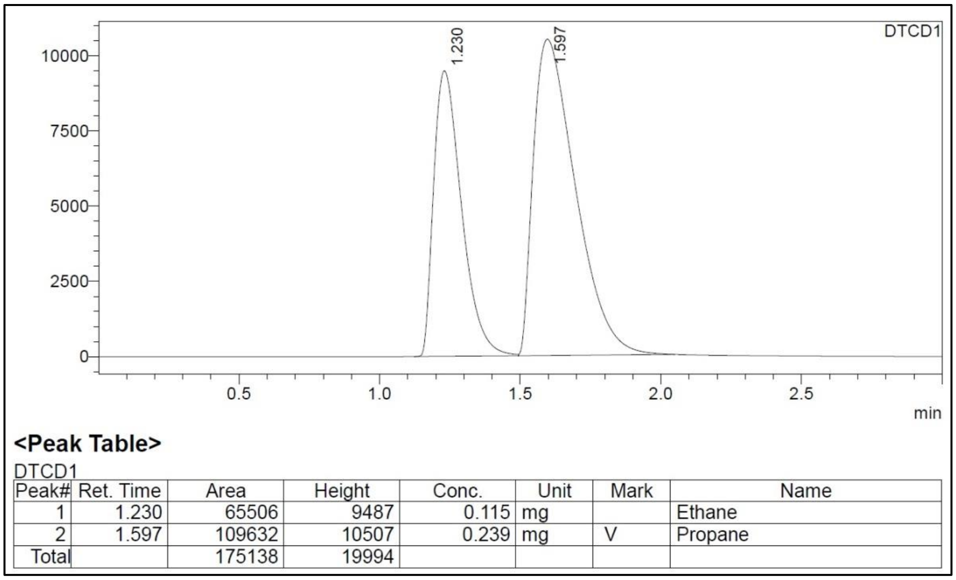

<Peak Table>

DTCD1

Peak#	Ret. Time	Area	Height	Conc.	Unit	Mark	Name
1	1.230	65506	9487	0.115	mg		Ethane
2	1.597	109632	10507	0.239	mg	V	Propane
Total		175138	19994				

Figure F.2: Sample output reading of the gas chromatograph: 33% ethane – 67% propane mixture

propane. The area output for each fluid calculated using the GC was divided by the standard deviation, as shown in Eq. (F.3), to calculate the percent uncertainty for each fluid. This percent uncertainty was subsequently used in the uncertainty propagation analysis for each data point. Similarly, a sample reading for the 67% ethane/33% propane mixture concentration, Figure F.3, was used to calculate the percent uncertainty for that mixture, as shown in Eq. (F.4). However, in the uncertainty propagation calculation, only the uncertainty of the ethane concentration is specified. Therefore, the largest uncertainty of the two mixtures, which was 2% was used for all uncertainty calculations.

$$\text{Uncertainty} = \frac{\text{Standard Deviation}}{\text{Reading}} \times 100\% \tag{F.2}$$

33% Ethane - 67% Propane

$$\text{Ethane:}\quad \text{Uncertainty} = \frac{1509}{65506} \times 100\% = 2.03\% \tag{F.3}$$

$$\text{Propane: Uncertainty} = \frac{1346}{109632} \times 100\% = 1.23\%$$

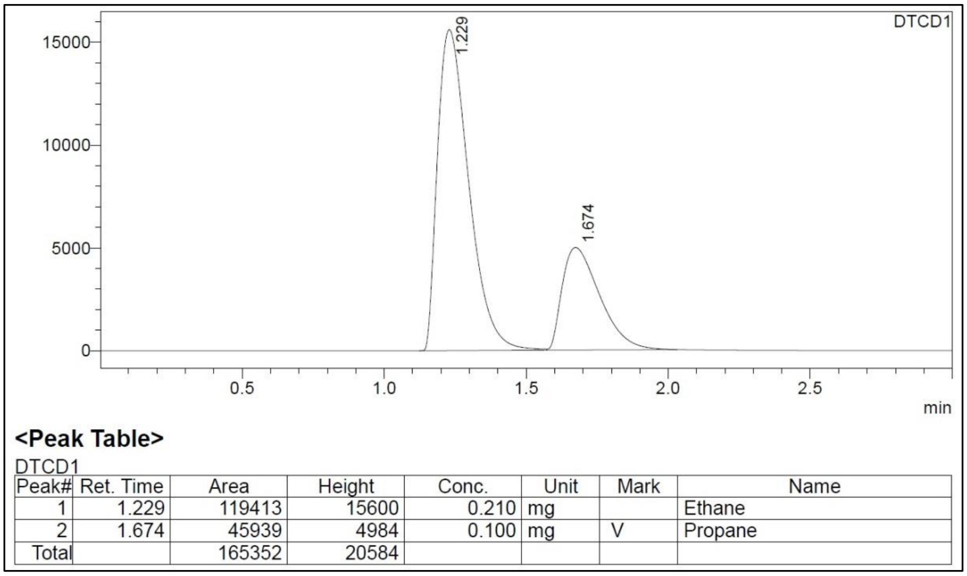

<Peak Table>

DTCD1

Peak#	Ret. Time	Area	Height	Conc.	Unit	Mark	Name
1	1.229	119413	15600	0.210	mg		Ethane
2	1.674	45939	4984	0.100	mg	V	Propane
Total		165352	20584				

Figure F.3 Sample output reading of the gas chromatograph: 67% ethane – 33% propane mixture

67% Ethane - 33% Propane

$$\text{Ethane:}\quad \text{Uncertainty} = \frac{1509}{119413} \times 100\% = 1.26\% \tag{F.4}$$

$$\text{Propane: Uncertainty} = \frac{1346}{45939} \times 100\% = 2.93\%$$

REFERENCES

Ackermann, G., 1937. Heat transfer and molecular mass transfer in the same field at high temperatures and large partial pressure differences, Forsch. Ing. Wes. VDI, Forschungesheft 8, 232.

Afroz, H.M., Miyara, A., Tsubaki, K., 2008. Heat transfer coefficients and pressure drops during in-tube condensation of CO2/DME mixture refrigerant, International Journal of Refrigeration 31, 1458-1466.

Agarwal, R., Hrnjak, P., 2015. Condensation in two phase and desuperheating zone for R1234ze(E), R134a and R32 in horizontal smooth tubes, International Journal of Refrigeration 50, 172-183.

Ağra, Ö., Teke, İ., 2008. Experimental investigation of condensation of hydrocarbon refrigerants (R600a) in a horizontal smooth tube, International Communications in Heat and Mass Transfer 35, 1165-1171.

Akers, W., Rosson, H., 1960. Condensation inside a horizontal tube, Chemical Engineering Progress Symposium Series, pp. 145-150.

Altman, M., Staub, F., Norris, R., 1960. Local heat transfer and pressure drop for Refrigerant-22 condensing in horizontal tubes, Chemical Engineering Progress Symposium Series, pp. 151-159.

Andresen, U.C., 2006. Supercritical gas cooling and near-critical-pressure condensation of refrigerant blends in microchannels, PhD, Georgia Institute of Technology.

Baroczy, C.J., 1963. Correlation of liquid fraction in two-phase flow with application to liquid metals. Atomics International. Div. of North American Aviation, Inc., Canoga Park, Calif.

Baroczy, C.J., 1965. Correlation of liquid fraction in two-phase flow with applications to liquid metals, Chem. Eng. Prog. Symp. Series 61, 179-191.

Baroczy, C.J., 1966. A systematic correlation for two-phase pressure drop, Chem. Eng. Prog. Symp. Series 62, 287-289.

Bejan, A., 1980. Second law analysis in heat transfer, Energy 5, 720-732.

Bell, K., Ghaly, M., 1973. An approximate generalized design method for multicomponent/partial condensers, AIChE Symp. Ser, pp. 72-79.

Breber, G., Palen, J.W., Taborek, J., 1980. Prediction of Horizontal Tubeside Condensation of Pure Components Using Flow Regime Criteria, Journal of Heat Transfer 102, 471-476.

Bromley, L.A., 1952. Effect of heat capacity of condensate, Industrial & Engineering Chemistry 44, 2966-2969.

Carey, V.P., 1992. Liquid-vapor phase-change phenomena. CRC Press.

Carey, V.P., 2008. Liquid-Vapor Phase-Change Phenomena: An Introduction to the Thermophysics of Vaporization and Condensation Processes in Heat Transfer Equipment, Second ed. Taylor and Francis, New York, NY.

Cavallini, A., Censi, G., Del Col, D., Doretti, L., Longo, G.A., Rossetto, L., 2001. Experimental investigation on condensation heat transfer and pressure drop of new HFC refrigerants (R134a, R125, R32, R410A, R236ea) in a horizontal smooth tube, International Journal of Refrigeration 24, 73-87.

Cavallini, A., Censi, G., Del Col, D., Doretti, L., Longo, G.A., Rossetto, L., 2002a. Condensation of halogenated refrigerants inside smooth tubes, HVAC&R Research 8, 429-451.

Cavallini, A., Censi, G., Del Col, D., Doretti, L., Longo, G.A., Rossetto, L., 2002b. A tube-in-tube water/zeotropic mixture condenser: design procedure against experimental data, Experimental Thermal and Fluid Science 25, 495-501.

Cavallini, A., Censi, G., Del Col, D., Doretti, L., Rossetto, L., Zilio, C., Longo, G.A., Giugno, V.X., 2000. Analysis and prediction of condensation heat transfer of the zeotropic mixture R-125/236ea, ASME PUBLICATIONS HTD 366, 103-110.

Cavallini, A., Del Col, D., Doretti, L., Matkovic, M., Rossetto, L., Zilio, C., Censi, G., 2006. Condensation in Horizontal Smooth Tubes: A New Heat Transfer Model for Heat Exchanger Design, Heat Transfer Engineering 27, 31-38.

Chamra, L., Webb, R.L., 1995. Condensation and evaporation in micro-fin tubes at equal saturation temperatures, Journal of Enhanced Heat Transfer 2.

Chang, Y., Kim, M., Ro, S., 2000. Performance and heat transfer characteristics of hydrocarbon refrigerants in a heat pump system, International Journal of Refrigeration 23, 232-242.

Chen, S., Gerner, F., Tien, C., 1987. General film condensation correlations, Experimental Heat Transfer 1, 93-107.

Chilton, T.H., Colburn, A.P., 1934. Mass transfer (absorption) coefficients prediction from data on heat transfer and fluid friction, Industrial & Engineering Chemistry 26, 1183-1187.

Chisholm, D., 1967. A theoretical basis for the Lockhart-Martinelli correlation for two-phase flow, International Journal of Heat and Mass Transfer 10, 1767-1778.

Chisholm, D., 1973. Pressure gradients due to friction during the flow of evaporating two-phase mixtures in smooth tubes and channels, International Journal of Heat and Mass Transfer 16, 347-358.

Chisholm, D., Sutherland, L., 1969. Prediction of pressure gradients in pipeline systems during two-phase flow, Proceedings of the Institution of Mechanical Engineers, Conference Proceedings. SAGE Publications, pp. 24-32.

Churchill, S.W., 1977 (a). Friction Factor Equation Spans all Fluid-Flow Regimes, Chemical Engineering.

Churchill, S.W., 1977 (b). Comprehensive Correlating Equations for Heat, Mass and Momentum Transfer in Fully Developed Flow in Smooth Tubes, Industrial & Engineering Chemistry Fundamentals 16, 109-116.

Churchill, S.W., Chu, H.H.S., 1975. Correlating equations for laminar and turbulent free convection from a horizontal cylinder, International Journal of Heat and Mass Transfer 18, 1049-1053.

Colburn, A.P., Drew, T.B., 1937. The condensation of mixed vapors. American Institute of Chemical Engineers.

Coleman, J.W., Garimella, S., 2000. Two-phase flow regime transitions in microchannel tubes: the effect of hydraulic diameter, ASME PUBLICATIONS HTD 366, 71-84.

Coleman, J.W., Garimella, S., 2003. Two-phase flow regimes in round, square and rectangular tubes during condensation of refrigerant R134a, International Journal of Refrigeration 26, 117-128.

Del Col, D., Cavallini, A., Thome, J.R., 2005. Condensation of zeotropic mixtures in horizontal tubes: new simplified heat transfer model based on flow regimes, Journal of heat transfer 127, 221-230.

Del Col, D., Torresin, D., Cavallini, A., 2010. Heat transfer and pressure drop during condensation of the low GWP refrigerant R1234yf, International Journal of Refrigeration 33, 1307-1318.

Dittus, F., Boelter, L., 1930. University of California Publications on Engineering, University of California Publications in Engineering, p. 371.

Dobson, M.K., 1994. Heat transfer and flow regimes during condensation in horizontal tubes. Air Conditioning and Refrigeration Center. College of Engineering. , University of Illinois at Urbana-Champaign.

Dobson, M.K., Chato, J.C., 1998. Condensation in Smooth Horizontal Tubes, Journal of Heat Transfer 120, 193-213.

Edwards, D.K., Denny, V.E., Mills, A.F., 1978. Transfer processes. an introduction to diffusion, convection and radiation, Series in Thermal and Fluids Engineering, New York: McGraw-Hill, and Washington: Hemisphere Publication Co., 1978, 2nd ed. 1.

El Hajal, J., Thome, J.R., Cavallini, A., 2003. Condensation in horizontal tubes, part 1: two-phase flow pattern map, International Journal of Heat and Mass Transfer 46, 3349-3363.

Fernando, P., Palm, B., Ameel, T., Lundqvist, P., Granryd, E., 2008. A minichannel aluminium tube heat exchanger–Part III: Condenser performance with propane, International Journal of Refrigeration 31, 696-708.

Friedel, L., 1979a. Improved friction pressure drop correlation for horizontal and vertical two phase flow, 3R International 18, 485-491.

Friedel, L., 1979b. Improved friction pressure drop correlations for horizontal and vertical two-phase pipe flow, European two-phase flow group meeting, Paper E, p. 1979.

Fronk, B.M., 2014. Coupled heat and mass transfer during condensation of high-temperature-glide zeotropic mixtures in small diameter channels, PhD, Georgia Institute of Technology.

Fujita, T., Ueda, T., 1978. Heat transfer to falling liquid films and film breakdown—I: Subcooled liquid films, International Journal of Heat and Mass Transfer 21, 97-108.

Garimella, S., Agarwal, A., Killion, J., 2005. Condensation pressure drop in circular microchannels, Heat Transfer Engineering 26, 28-35.

Garimella, S., Bandhauer, T.M., 2001. Measurement of condensation heat transfer coefficients in microchannel tubes, ASME PUBLICATIONS HTD 369, 243-250.

Garimella, S., Christensen, R., 1995a. Heat transfer and pressure drop characteristics of spirally fluted annuli. II: Heat transfer, Journal of Heat Transfer 117, 61-68.

Garimella, S., Christensen, R.N., 1995b. Heat Transfer and Pressure Drop Characteristics of Spirally Fluted Annuli, Part II: Heat Transfer, ASME Journal of Heat Transfer 117, 61-68.

Ghiaasiaan, S.M., 2007. Two-phase flow, boiling, and condensation: in conventional and miniature systems. Cambridge University Press.

Govan, A., Hewitt, G., Owen, D., Burnett, G., 1989. Wall shear stress measurements in vertical air-water annular two-phase flow, International Journal of Multiphase Flow 15, 307-325.

Granryd, E., 2001. Hydrocarbons as refrigerants—an overview, International Journal of Refrigeration 24, 15-24.

Gstöhl, D., 2004. Heat transfer and flow visualization of falling film condensation on tube arrays with plain and enhanced surfaces, PhD, École Polytechnique Fédérale de Lausanne.

Guo, Z., Anand, N., 2000. An analytical model to predict condensation of R-410A in a horizontal rectangular channel, Journal of Heat Transfer 122, 613-620.

Jaster, H., Kosky, P., 1976. Condensation heat transfer in a mixed flow regime, International Journal of Heat and Mass Transfer 19, 95-99.

Jiang, Y., Garimella, S., 2003. Heat transfer and pressure drop for condensation of refrigerant R-404 A at near-critical pressures, ASHRAE Transactions 109, 677-688.

Ju Lee, H., Yong Lee, S., 2001. Pressure drop correlations for two-phase flow within horizontal rectangular channels with small heights, International Journal of Multiphase Flow 27, 783-796.

Jung, D., Chae, S., Bae, D., Oho, S., 2004. Condensation heat transfer coefficients of flammable refrigerants, International journal of refrigeration 27, 314-317.

Jung, D., Song, K.-h., Cho, Y., Kim, S.-j., 2003. Flow condensation heat transfer coefficients of pure refrigerants, International Journal of Refrigeration 26, 4-11.

Kandlikar, S.G., 2002. Fundamental issues related to flow boiling in minichannels and microchannels, Experimental Thermal and Fluid Science 26, 389-407.

Kattan, N., Thome, J.R., Favrat, D., 1998. Flow boiling in horizontal tubes: Part 1—Development of a diabatic two-phase flow pattern map, Journal of Heat Transfer 120, 140-147.

Keinath, B., Garimella, S., 2011. Void Fraction and Pressure Drop During Condensation of Refrigerants in Minichannels, 6th International Berlin Workshop on Transport Phenomena with Moving Boundaries, Berlin, Germany.

Keinath, B.L., 2012. Void fraction, pressure drop, and heat transfer in high pressure condensing flows through microchannels, PhD, Georgia Institute of Technology.

Kim, M., Chang, Y., Ro, S., 1996. Performance and heat transfer of hydrocarbon refrigerants and their mixtures in a heat pump system, Proc. of IIR Meeting of Comm. B, p. B2.

Klein, S.A., 2012. Engineering Equation Solver (EES) for Microsoft Windows Operating System: Academic Professional Version.

Kosky, P.G., Staub, F.W., 1971. Local condensing heat transfer coefficients in the annular flow regime, AIChE Journal 17, 1037-1043.

Koyama, S., Miyara, A., Takamatsu, H., Fujii, T., 1990. Condensation heat transfer of binary refrigerant mixtures of R22 and R114 inside a horizontal tube with internal spiral grooves, International Journal of Refrigeration 13, 256-263.

Koyama, S., Yu, J., Ishibashi, A., 1998. Condensation of binary refrigerant mixtures in a horizontal smooth tube, Thermal Science and Engineering 6, 123-129.

Le Fevre, E., Rose, J., 1965. An experimental study of heat transfer by dropwise condensation, International Journal of Heat and Mass Transfer 8, 1117-1133.

Lee, C.-C., 1994. Investigation of Condensation Heat Transfer of R124/22 Nonazeotropic Refrigerant Mixtures in Horizontal Tubes, PhD, National Chiao Tung University, Taiwan.

Lee, H.-S., Yoon, J.-I., Kim, J.-D., Bansal, P., 2006. Condensing heat transfer and pressure drop characteristics of hydrocarbon refrigerants, International Journal of Heat and Mass Transfer 49, 1922-1927.

Lee, H.J., Lee, S.Y., 2001. Pressure drop correlations for two-phase flow within horizontal rectangular channels with small heights, International Journal of Multiphase Flow 27, 783-796.

Lee, W.C., Rose, J.W., 1984. Forced convection film condensation on a horizontal tube with and without non-condensing gases, International Journal of Heat and Mass Transfer 27, 519-528.

Lemmon, E., Huber, M., McLinden, M., 2013. NIST Standard Reference Database 23: Reference Fluid Thermodynamic and Transport Properties-REFPROP, Version 9.1, Standard Reference Data Program; National Institute of Standards and Technology: Gaithersburg, MD, 2013.

Lemmon, E.W., McLinden, M.O., Wagner, W., 2009. Thermodynamic Properties of Propane. III. A Reference Equation of State for Temperatures from the Melting Line to 650 K and Pressures up to 1000 MPa, Journal of Chemical Engineering Data, 3141-3180.

Lockhart, R., Martinelli, R., 1949. Proposed correlation of data for isothermal two-phase, two-component flow in pipes, Chemical Engineering Progress 45, 39-48.

Milkie, J.A., 2014. Condensation of Hydrocarbons and Zeotropic Hydrocarbon/Refrigerant Mixtures in Horizontal Tubes, Georgia Institute of Technology, Atlanta.

Mishima, K., Hibiki, T., 1996. Some characteristics of air-water two-phase flow in small diameter vertical tubes, International Journal of Multiphase Flow 22, 703-712.

Mitra, B., Garimella, S., 2003a. Heat transfer and pressure drop for condensation of refrigerant R410A at near-critical pressures. ASME.

Mitra, B., Garimella, S., 2003b. Heat transfer and pressure drop for condensation of refrigerant R410A at near-critical pressures, ASME 2003 International Mechanical Engineering Congress and Exposition. American Society of Mechanical Engineers, pp. 87-97.

Miyara, A., 2008. Condensation of hydrocarbons–A review, International Journal of Refrigeration 31, 621-632.

Moser, K., Webb, R., Na, B., 1998. A new equivalent Reynolds number model for condensation in smooth tubes, Journal of Heat Transfer 120, 410-417.

Mudawwar, I., El-Masri, M., 1986. Momentum and heat transfer across freely-falling turbulent liquid films, International Journal of Multiphase Flow 12, 771-790.

Müller-Steinhagen, H., Heck, K., 1986. A simple friction pressure drop correlation for two-phase flow in pipes, Chemical Engineering and Processing: Process Intensification 20, 297-308.

Nema, G., Garimella, S., Fronk, B.M., 2014. Flow regime transitions during condensation in microchannels, International Journal of Refrigeration 40, 227-240.

Nusselt, W., 1916. The surface condensation of water vapor, Zetrschr. Ver. Deutch. Ing. 60, 541-546.

Park, K.-J., Jung, D., Seo, T., 2008. Flow condensation heat transfer characteristics of hydrocarbon refrigerants and dimethyl ether inside a horizontal plain tube, International Journal of Multiphase Flow 34, 628-635.

Park, K.-J., Kang, D.G., Jung, D., 2011. Condensation heat transfer coefficients of R1234yf on plain, low fin, and Turbo-C tubes, International Journal of Refrigeration 34, 317-321.

Price, B.C., Bell, K.J., 1973. Design of binary vapor condensers using the Colburn-Drew equations. Oklahoma State University.

Rohsenow, W., 1956. Heat transfer and temperature distribution in laminar film condensation, Transactions of the ASME 78, 1645-1648.

Rose, J., 2002. Dropwise condensation theory and experiment: a review, Proceedings of the Institution of Mechanical Engineers, Part A: Journal of Power and Energy 216, 115-128.

Scammell, A., Kim, J., 2015. Heat transfer and flow characteristics of rising Taylor bubbles, International Journal of Heat and Mass Transfer 89, 379-389.

Shah, M.M., 1979. A general correlation for heat transfer during film condensation inside pipes, International Journal of Heat and Mass Transfer 22, 547-556.

Shao, D.W., Granryd, E.G., 1998. Experimental and theoretical study on flow condensation with non-azeotropic refrigerant mixtures of R32/R134a, International Journal of Refrigeration 21, 230-246.

Shimadzu, 2011. LabSolutions, 5.42 SP2.

Silver, L., 1947. Gas cooling with aqueous condensation, Transactions of the Institute of Chemical Engineers 25, 30-42.

Smit, F., Meyer, J., 2002. Condensation heat transfer coefficients of the zeotropic refrigerant mixture R-22/R-142b in smooth horizonal tubes, International Journal of Thermal Sciences 41, 625-630.

Soliman, H., 1982. On the annular-to-wavy flow pattern transition during condensation inside horizontal tubes, The Canadian Journal of Chemical Engineering 60, 475-481.

Soliman, H., 1983. Correlation of mist-to-annular transition during condensation, The Canadian Journal of Chemical Engineering 61, 178-182.

Soliman, H., 1986. The mist-annular transition during condensation and its influence on the heat transfer mechanism, International Journal of Multiphase Flow 12, 277-288.

Souza, A., Chato, J., Jabardo, J., Wattelet, J., Panek, J., Christoffersen, B., Rhines, N., 1992. Pressure drop during two-phase flow of refrigerants in horizontal smooth tubes. Air Conditioning and Refrigeration Center. College of Engineering. University of Illinois at Urbana-Champaign.

Stoecker, W., McCarthy, C., 1984. Simulation and performance of a system using an R-12/R-114 refrigerant mixture. Illinois Univ., Urbana (USA). Dept. of Mechanical and Industrial Engineering.

Taitel, Y., Dukler, A., 1976. A model for predicting flow regime transitions in horizontal and near horizontal gas-liquid flow, AIChE Journal 22, 47-55.

Tandon, T., Varma, H., Gupta, C., 1982. A new flow regimes map for condensation inside horizontal tubes, Journal of Heat Transfer 104, 763.

Tandon, T., Varma, H., Gupta, C., 1986. Generalized correlation for condensation of binary mixtures inside a horizontal tube, International Journal of Refrigeration 9, 134-136.

Tandon, T., Varma, H., Gupta, C., 1995. Heat transfer during forced convection condensation inside horizontal tube, International Journal of Refrigeration 18, 210-214.

Thome, J.R., El Hajal, J., Cavallini, A., 2003. Condensation in horizontal tubes, part 2: new heat transfer model based on flow regimes, International Journal of Heat and Mass Transfer 46, 3365-3387.

Thonon, B., Bontemps, A., 2002. Condensation of pure and mixture of hydrocarbons in a compact heat exchanger: experiments and modelling, Heat transfer engineering 23, 3-17.

Traviss, D., Rohsenow, W., Baron, A., 1973. Forced convection condensation inside tubes: a heat transfer equation for condenser design, ASHRAE Transactions 79, 157-165.

Uehara, H., Kinoshita, E., 1994. Wave and Turbulent Film Condensation on a Vertical Surface. Correlation for Local Heat-Transfer Coefficient, Transactions of the Japan Society of Mechanical Engineers Series B 60, 3109-3116.

Wallis, G.B., 1969. One-dimensional two-phase flow. McGraw-Hill New York.

Webb, D., Fahrner, M., Schwaab, R., 1996. The relationship between the Colburn and Silver methods of condenser design, International Journal of Heat and Mass Transfer 39, 3147-3156.

Wen, M.-Y., Ho, C.-Y., Hsieh, J.-M., 2006. Condensation heat transfer and pressure drop characteristics of R-290 (propane), R-600 (butane), and a mixture of R-290/R-600 in the serpentine small-tube bank, Applied Thermal Engineering 26, 2045-2053.

Yang, C., Webb, R., 1996. Condensation of R-12 in small hydraulic diameter extruded aluminum tubes with and without micro-fins, International Journal of Heat and Mass Transfer 39, 791-800.